UNIVERSITY OF CALIFORNIA
Los Angeles

Collisional and Electromagnetic Physics in Gyrokinetic Models

A dissertation submitted in partial satisfaction
of the requirements for the degree
Doctor of Philosophy in Physics

by

Paul Charles Crandall

2019

ABSTRACT OF THE DISSERTATION

Collisional and Electromagnetic Physics in Gyrokinetic Models

by

Paul Charles Crandall
Doctor of Philosophy in Physics
University of California, Los Angeles, 2019
Professor Frank Jenko, Co-chair
Professor Troy Carter, Co-chair

One of the most challenging problems facing plasma physicists today involves the modeling of plasma turbulence and transport in magnetic confinement experiments. The most successful model to this end so far is the reduced gyrokinetic model. Such a model cannot be solved analytically, but can be used to simulate the plasma behavior and transport with the help of present-day supercomputers. This has lead to the development of many different codes which simulate the plasma using the gyrokinetic model in various ways. These models have achieved a large amount of success in describing the core of the plasma for conventional tokamak devices. However, numerous difficulties have been encountered when applying these models to more extreme parameter regimes, such as the edge and scrape-off layer of the tokamak, and high plasma β devices, such as spherical tokamaks. The development and application of the gyrokinetic model (specifically with the gyrokinetic code, GENE) to these more extreme parameter ranges shall be the focus of this thesis.

One of the main accomplishments during this thesis project is the development of a more advanced collision operator suitable for studying the low temperature plasma edge. The previous collision operator implemented in the code was found to artificially create free energy at high collisionality, leading to numerical instabilities when one attempted to model the plasma edge. This made such an analysis infeasible. The newly implemented collision

operator conserves particles, momentum, and energy to machine precision, and is guaranteed to dissipate free energy, even in a nonisothermal scenario. Additional finite Larmor radius correction terms have also been implemented in the local code, and the global code version of the collision operator has been adapted for use with an advanced block-structured grid scheme, allowing for more affordable collisional simulations.

The GENE code, along with the newly implemented collision operator developed in this thesis, has been applied to study plasma turbulence and transport in the edge ($\rho_{\mathrm{tor}} = 0.9$) of an L-mode magnetic confinement discharge of ASDEX Upgrade. It has been found that the primary microinstabilities at that radial position are electron drift waves destabilized by collisions and electromagnetic effects. At low toroidal mode numbers, ion temperature gradient driven modes and microtearing modes also seem to exist. In nonlinear simulations with the nominal experimental parameters, the simulated electron heat flux was four times higher than the experimental reconstruction, and the simulated ion heat flux was twice as high. However, both the ion and electron simulated heat flux could be brought into agreement with experimental values by lowering the input logarithmic electron temperature gradient by 40%. It was also found that the cross-phases between the electrostatic potential and the moments agreed well for the part of the binormal spectrum where the dominant transport occurred, and was fairly poor at larger scales where minimal transport occurred.

Finally, a new scheme for evaluating the electromagnetic fields has been developed to address the instabilities occurring in nonlinear local and global gyrokinetic simulations at high plasma β. This new scheme is based on evaluating the electromagnetic induction explicitly, and constructing the gyrokinetic equation based on the original distribution, rather than the modified distribution which implicitly takes into account the induction. This new scheme removes the artificial instability occurring in global simulations, enabling the study of high β scenarios with GENE. The new electromagnetic scheme can also be generalized to a full-f implementation, however, it would require updating the field matrix every time-step to avoid the cancellation problem. The new scheme (including the parallel nonlinearity) does not remove the local instability, suggesting that that instability (caused by magnetic field perturbations shorting out zonal flows) is part of the physics of the local model.

The dissertation of Paul Charles Crandall is approved.

Warren Mori

Christoph Niemann

Frank Jenko, Committee Co-chair

Troy Carter, Committee Co-chair

University of California, Los Angeles

2019

To my mother, father, and brother, Ross ...

for their incredible love and support

Table of Contents

Acknowledgments

I would like to extend my deepest gratitude for all of those who have helped me over the course of my PhD thesis. I would like to thank Frank Jenko for giving me the opportunity to work with him at UCLA and for also giving me the opportunity to work at the Max Planck Institute, and for all of the advice and assistance he has provided throughout my PhD. I would like to thank Troy Carter and David Salzburg for their advice, and I would also like to thank Troy for helping me to smoothly transition from UCLA to the Max Planck Institute. I would like to thank the members of my committee, Frank Jenko, Troy Carter, Warren Mori, and Chris Niemann for their time and feedback. I would like to thank the postdoctoral scientists from UCLA who also greatly assisted me in becoming a far better scientist than I was when I started the PhD. These include: Daniel Told, Alejandro Bañón Navarro, and Gabriele Merlo. I would also like to thank all of my friends and colleagues from UCLA who helped me throughout the PhD, including: David Cesar, Arjun Rana, Nayana Sumanga Rajapakse, Tom Neiser, Patrick Astfalk, Daniel Groselj, Qingjiang Pan, and Maurice Maurer. I would also like to thank Stephanie Krilov for helping me numerous times when I had questions about paperwork or degree requirements.

There are also many people who I would like to thank from the Max Planck institute who helped me throughout the PhD. These include: Nicola Bonanomi, Karl Stimmel, Hauke Doerk, Patrick Astfalk, Daniel Groselj, Daniel Told, Alejandro Bañón Navarro, Denis Jarema, Maurice Maurer, Alessandro Di Siena, Andres Cathey, Francesco Vannini, Ivan Novikau, Vladimir Zholobenko, Dominik Michels, Felipe Nathan de Oliveira, Bobby Brzozowski, Cole Stephens, as well as many others. I would especially like to thank Tobias Görler for helping me with GENE on numerous occasions. It was truly an honor to be surrounded by so many talented and friendly people. I would additionally like to thank Frank Jenko, Tobias Görler, Nicola Bonanomi, and Gabriele Merlo for their extensive help with editing this thesis. A difficult task for which their work is greatly appreciated.

I would also like to thank my friends and family back in Minnesota for their significant support throughout my PhD. Thank you Andrew, Jason, Matt, Ross, Mom, and Dad.

Curriculum Vitae

2009 – 2013	B.S. in Physics and Engineering Physics, University of Wisconsin-Madison, Madison, Wisconsin.
2013 – Present	Ph.D. student in Physics, University of California, Los Angeles (UCLA).

Publications

[1] Alejandro Bañón Navarro, Bogdan Teaca, Daniel Told, Daniel Groselj, Paul Crandall, and Frank Jenko, "Structure of Plasma Heating in Gyrokinetic Alfvénic Turbulence" Phys. Rev. Lett. **117** 245101 (2016)

[2] Nicola Bonanomi, Clemente Angioni, Paul Crandall, Alessandro Di Siena, Costanza Maggi, and Philip Schneider, the ASDEX Upgrade Team, the EUROFusion NST1 Team, and JET Contributors, "Effect of the isotope mass on the turbulent transport at the edge of L-mode plasmas in ASDEX Upgrade and JET-ILW" Nuclear Fusion **59** 126025 (2019)

[3] Tom Neiser, Frank Jenko, Troy Carter, Lothar Schmitz, Daniel Told, Gabriele Merlo, Alejandro Bañón Navarro, Paul Crandall, Ginger Mckee, and Zheng Yan, "Gyrokinetic GENE simulations of DIII-D near-edge L-mode plasmas" Physics of Plasmas **26** 092510 (2019)

CHAPTER 1

Introduction

1.1 Nuclear fusion

Some of the most significant scientific and engineering challenges in the 21st century concern the sustainability and scalability of humanity's energy consumption, and the issue of climate change caused by anthropogenic greenhouse gases from the burning of fossil fuels. Over the last several decades, energy production, including that produced by fossil fuels, has increased. Fig. 1.1 displays the amount of energy production by various sources in the United States over time. In 2017, the burning of fossil fuels accounted for 77.6% of the domestic energy produced in the United States. That includes 31.8% from natural gas, 28% from petroleum, and 17.8% from coal. Nuclear fission energy was responsible for 9.6% of the energy produced, while renewables made up 12.7% [1]. Nearly all of these resources are finite. And with world-wide energy consumption expected to increase over the coming decades, it is vital to implement a sustainable energy resource that can be scaled up to meet the increasing demands of humanity. It is particularly important to replace fossil fuels which contribute to climate change. The problems associated with climate change are numerous and profound. They include widespread droughts, wildfires, flooding, hurricanes, crop failures, sea-level rise, and mass extinction events [2, 3, 4]. To mitigate the damage from climate change, it is essential to replace fossil fuels with a clean, sustainable energy source.

One candidate for replacement is the extension of existing renewable energy sources, such as wind and solar. The share of energy production by renewable energy sources has been increasing, and the costs of these sources continue to fall. According to the International Renewable Energy Agency (IRENA), the price of solar energy has fallen by 69% between

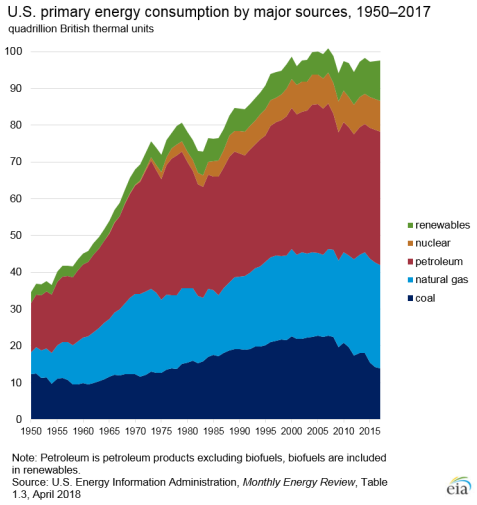

Figure 1.1: Energy consumption in the United States from various sources over time.

2010 and 2016, and the price of wind has fallen by 23% during the same period [5]. There is also more than enough energy from the wind and the sun to meet humanity's energy needs. However, even though enormous energy could be gained from renewables, these sources do not operate constantly, and the energy would have to be stored when the sun is not shining and the wind is not blowing. Creating the infrastructure to store this energy and distribute it efficiently without a supplemental energy source that operates constantly may prove to be a significant challenge and a limitation of the scalability of such resources.

Another possibility is the extension of existing nuclear fission energy sources. Nuclear fission could easily meet the world's energy needs, if not indefinitely, then at least for a very long period of time. In addition, there are no greenhouse gas emissions from fission reactions. Nevertheless, there are problematic aspects of such an energy source. The use of nuclear fission carries with it the risk of cataclysmic accidents. Examples include the disaster at Chernobyl, where a catastrophic meltdown occurred after control over the nuclear chain reactions were lost, as well as the disaster at Fukushima Daiichi, where a tsunami disabled the generators that were used to pump water to cool the reactor vessel after the nuclear reactor was shut down. There is also the problem of how to deal with the waste from nuclear reactors. Such waste can last hundreds of thousands of years, and must be stored securely and safeguarded against accidents and terrorism.

The problems and challenges associated with fossil fuels, conventional renewable resources, and nuclear fission motivate the study and consideration of nuclear fusion as an energy source. The energy output from a nuclear fusion reaction is about an order of magnitude higher than a nuclear fission reaction, and roughly a million times higher than a combustion chemical reaction. Also, there are practically limitless supplies of materials available for nuclear fusion (although it depends on the fusion reaction utilized), so the energy output from nuclear fusion plants could always be scaled to meet the world's energy needs, no matter how large those needs could grow in practical terms. Unlike solar and wind power, prospective fusion reactors would reliably operate 24/7, so incorporating a fusion reactor into an energy grid should not constitute a significant infrastructural challenge. Such an energy source would also create no greenhouse gas emissions or long-lived nuclear waste. Due to neutron emissions in fusion reactions, the reactor elements could become activated. However, the materials for the reactor walls could be chosen such that the period of activation is relatively short (decades) as opposed to nuclear waste from fission reactions (hundreds of thousands of years). So the radioactive elements associated with nuclear fusion could be stored for short-term periods in buildings as opposed to long-term permanent repositories. Furthermore, there is no risk of uncontrolled chain reactions leading to meltdowns, like there is in nuclear fission. For these reasons, it is worthwhile to invest significant time and energy towards the study of potential fusion reactors, despite the substantial scientific and engineering challenges associated with such pursuits.

The main challenge is exciting a macroscopic collection of atoms to a high enough energy such that a large number of fusion reactions take place. The easiest fusion reaction to achieve in this regard (because of its favorable cross-section) is the fusion of deuterium and tritium into helium and neutron particles,

$$ {}^{2}_{1}D + {}^{3}_{1}T \rightarrow {}^{4}_{2}He + {}^{1}_{0}n + 17.6\text{MeV}. $$

Deuterium is a highly prolific isotope of hydrogen found in nature. It can be obtained from ocean water in the form of HDO and D_2O molecules. Tritium can be bred from lithium

by bombardment with neutral particles,

$$^{6}_{3}Li +^{1}_{0} n \rightarrow^{4}_{2} He +^{3}_{1} T + 4.8\text{MeV}.$$

The tritium required for fusion reactions can therefore be regenerated by lining the reactor walls with lithium. In this way, the tritium can then be continually recycled. In order to achieve fusion, the system must be at such a high temperature, that it can only exist as a plasma. In such a system, nearly all of the atoms are fully ionized, and respond to the collective electromagnetic fields associated with the bulk motion of the particles, and the small-angle scattering affiliated with occasional discrete particle interactions (to be described in more detail later). The density of the plasma species, n, the temperature, T, and the energy confinement time, τ_E (the time-scale on which the energy can be maintained in a fusion plasma), must all be large enough such that the energy output from the fusion reactions exceeds the energy that it takes to heat the plasma to the ignition state. This requires that the triple product of the aforementioned quantities exceeds a critical value, as expressed by the Lawson Criterion for the deuterium-tritium reaction [6],

$$nT\tau_E \geq 3 * 10^{21} \frac{\text{keV} * \text{s}}{\text{m}^3}.$$

So to achieve meaningful energy output, a deuterium/tritium plasma with a high enough density and temperature must be confined for a long enough period of time to satisfy the Lawson Criterion. Some of the most popular schemes to this end are based on magnetic confinement.

1.2 Magnetic confinement fusion

Because of the enormously high temperatures of fusion plasmas, confinement cannot be maintained by material walls. Any such material would melt or corrode upon exposure to such a hot plasma. This motivates the use of magnetic fields as a means of confinement. Charged particles tend to go in helical orbits about field lines. This suggests the use of a

toroidal magnetic field to trap the charged particles in helical orbits about closed field lines. However, inhomogeneities in the magnetic field due to the curvature of the field lines and the changing strength of the magnetic field lead to charge dependent drifts that separate the ions and the electrons in the vertical direction (imagine the closed circular field lines lying in a horizontal plane). This creates a vertical electric field, which, when combined with the toroidal magnetic field, leads to an $\mathbf{E} \times \mathbf{B}$ drift of the charged particles outside of the device.

This confinement problem could be mitigated with the use of a poloidal magnetic field component, which would help to remedy the drifts resulting in charge separation. This can be done in different ways. One method would be to drive a rapidly changing magnetic flux through the center of the toroidal confinement device. This changing magnetic flux would induce a toroidal electric field via Faraday's law, which would create a toroidal current, which would then generate the desired poloidal magnetic field via Ampére's law. The class of magnetic confinement devices encompassing this philosophy are called tokamaks [6]. Alternatively, the field coils that generate the toroidal magnetic field can be twisted into new shapes such that they generate a stabilizing poloidal component as well. The class of magnetic confinement devices encompassing this philosophy are called stellarators [7]. The configuration of tokamaks and stellarators are shown in Figure 1.2.

One of the main drawbacks of standard tokamaks (without external current drive) is that they can only operate in the pulsed regime (because it is based on the transformer principle and needs a continually increasing magnetic flux in order to operate). This is in contrast to the stellarator, which can operate continuously. However, the design and construction of a stellarator is a more complicated task due to the complex shape of the field coils which must be designed and manufactured to high precision.

While power loads and complexity of design are certainly factors to be considered in the design of a prototype fusion reactor, one of the most important considerations is the confinement time of the plasma. The goal of enhancing the macroscopic stability of the plasma and minimizing the transport of heat and particles outside of the device is the main criterium used to judge the effectiveness of different confinement schemes. This is the reason for the devotion of large amounts of time and resources toward studying different devices.

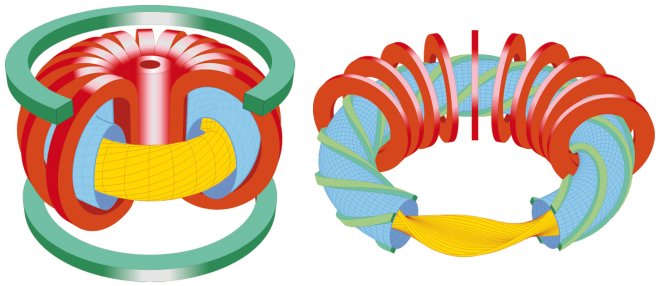

Figure 1.2: Magnetic field configuration for a tokamak (left) and a stellarator (right). Source: Max Planck Institute for Plasma Physics

As a first approximation, one could assume that the plasma is inherently stable and that a charged particle in the device will travel in a helical trajectory along an orbit determined by the drifts associated with an inhomogeneous magnetic field while occasionally experiencing collisions that will move the particle to a different orbit. The transport of plasma would then be a result of these collective particles moving towards orbits that progressively take them farther to the edge of the device until eventually they reach an orbit that would result in contact with the wall or divertor. Such a transport mechanism is known as neoclassical transport.

While neoclassical transport can sometimes make up a significant portion of the overall loss of confinement in some situations (particularly in transport barriers), it is found that models based off of neoclassical predictions usually significantly under-predict the experimentally observed level of particle and heat transport. This is because another important transport mechanism has to be considered: anomalous transport. Anomalous transport describes the transport associated with plasma turbulence arising from the small scale instabilities (microinstabilities) resulting from the free-energy source of the temperature and density gradients in the plasma discharge.

Deriving a comprehensive model for anomalous transport in magnetic confinement devices is one of the major unsolved problems in plasma physics research. The equations that describe the physics in a fusion reactor are nonlinear partial integro-differential equations that

cannot be solved analytically to give the transport fluxes. One could determine confinement quality by constructing a reactor, determining if the plasma discharges are stable, and if so, measuring the transport fluxes of heat and particles out of the device. This is already being done, but it requires enormous time and money. The devices of interest for future studies will have an even larger size. Current magnetic confinement devices achieve densities of $n \sim 10^{20}\mathrm{m}^{-3}$, temperatures of $T \sim 10\mathrm{keV}$, and confinement times on the order of $\sim 0.1-0.3\mathrm{s}$, where the confinement time is defined as energy contained in the plasma discharge divided by the steady-state heating power required to maintain such a state. The densities and temperatures required to achieve fusion have already been reached in present-day devices, and current attempts to satisfy the Lawson criteria are based on designing devices to increase the plasma confinement time. Both theory and experiment suggest that the confinement time of a discharge can be increased by scaling up the size of the device, motivating the design and construction of large scale experiments such as ITER (International Thermonuclear Experimental Reactor), currently under construction in Cadarache, France. The largest device until now has been the JET tokamak, with a plasma volume of $200m^3$. ITER will have a volume of $800m^3$, and first plans for an actual demonstration power plant assume a volume of $\sim 1200m^3$.

In fields such as aerodynamics and hydrodynamics, to determine if a large-scale system (such as an airfoil or turbine) will work as expected, it is common to design a smaller scale system operating in a different fluid, conduct tests of different aspects of the design, and if successful, scale up the smaller system to the large-scale design originally planned. This saves a lot of time and effort from constructing expensive large-scale experiments that could potentially fail. The reason that this can be done is that the equations which govern fluid flows in aerodynamics and hydrodynamics are often characterized by a single dimensionless number. For instance, one equation used to characterize the dynamics of fluids is the incompressible Navier-Stokes equation [8],

$$\frac{\partial \mathbf{u}}{\partial t} + (\mathbf{u} \cdot \nabla)\mathbf{u} = -\frac{\nabla p}{\rho} + \nu \nabla^2 \mathbf{u} + \mathbf{g}.$$

In the above equation, t represents time, $\mathbf{u}$ denotes the vector field representing the flow at each point, p represents the pressure scalar field, ρ represents the mass density of the incompressible fluid, ν denotes the kinematic viscosity, and $\mathbf{g}$ denotes the vector field representing the acceleration that the fluid experiences at each point due to external forces (typically gravity). A characteristic velocity and length scale (v and L respectively) can then be defined and all of the dimensional quantities can be normalized to units based on combinations of v, L, and ρ. The dimensionless incompressible Navier-Stokes equation can then be derived:

$$\frac{\partial \mathbf{u}}{\partial t} + (\mathbf{u} \cdot \nabla)\mathbf{u} = -\nabla p + \frac{1}{Re}\nabla^2 \mathbf{u} + \mathbf{g}.$$

In the above equation, all quantities are in dimensionless units, and the Reynolds number is defined as $Re = Lv/\nu$. Since the above equation is in dimensionless units, this means that the fluid can span a large range of flow, length, and mass density scales, and as long as the Reynolds number is the same (and assuming the Navier-Stokes equation still describes the fluid under consideration), the behavior of the fluid should be the same. This is an enormous benefit to the researcher. If one wanted to study fluid flow over a hypothetical large scale wing design, rather than constructing a large wing, one could build a smaller wing, and study fluid flow over the wing using a fluid with a smaller viscosity than air. The behavior of the fluid should then be the same as in the larger case.

The plasma physicist is not so lucky. The equations of plasma physics are not governed by a single dimensionless parameter, such as a Reynolds number. Instead, there are numerous dimensionless quantities characterizing plasma models, such as the normalized gyroradius, the ratio of magnetic to kinetic pressure, the collisionality, etc. So one could not build a small-scale magnetic confinement device to study the stability and transport properties of a large-scale magnetic confinement device, because one could not reduce the scale while keeping all dimensionless quantities constant and meeting the necessary criteria of a plasma. Some scalings have been inferred based off of various existing experiments. However, if one wanted to conduct definitive experiments related to large-scale magnetic confinement devices, one

would have to build the large-scale device.

There is an alternative to solving analytical models and constructing large experimental devices to model the stability and transport of different confinement schemes. One could also construct numerical models of the plasma and carry out high performance computing (HPC) simulations to determine the plasma characteristics associated with a given device. While such simulations can be very expensive (on the order of tens of millions of CPU hours), they are still far cheaper and can be done much more quickly than building large-scale confinement devices. In addition to being faster and cheaper, such models can also give great insight into the physics of the system because it is much easier and less error-prone to construct high-resolution diagnostics of simulated data than experimental data, and there are still many poorly understood phenomena that simulations can help elucidate.

One example is the existence of the H-mode plasma [9, 10]. It has been discovered experimentally that when the external heating power of the plasma exceeds a certain critical value, then a transport barrier forms in the edge of the plasma near the separatrix (the area where the field lines go from closed to open), accompanied by steep density and temperature gradients, and the plasma goes from a lower confinement (L-mode) regime to a higher confinement (H-mode) regime, as shown in figure 1.3. The H-mode plasma has a confinement time which is about twice as high as the confinement time of an L-mode discharge. The reason why the plasma transitions from an L-mode discharge to an H-mode discharge is still a mystery, and it is difficult to discern the dynamics of such a transition from experimental diagnostics. This example (and many others) provide a motivation for studying such discharges with simulated models. However, in order to be successful with such an approach, it is important to choose a comprehensive and tractable model of the plasma for the construction of a code.

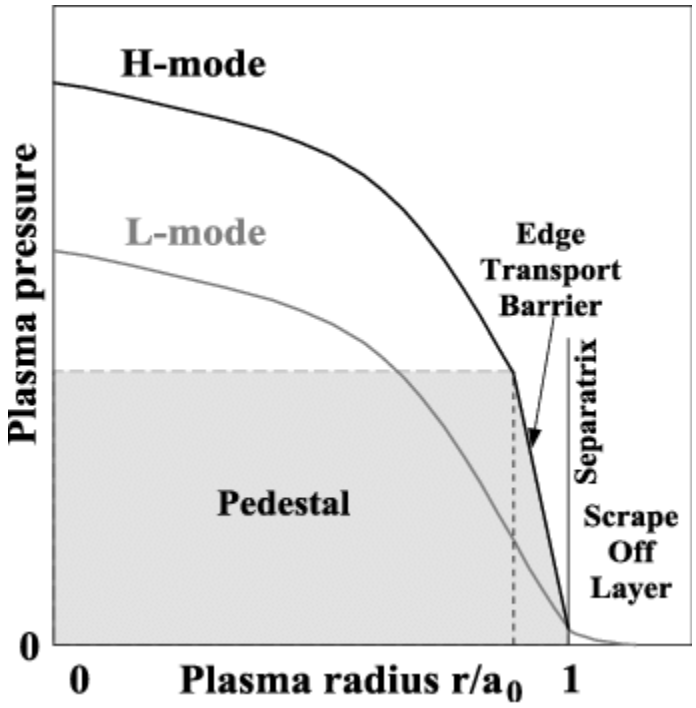

Figure 1.3: The plasma pressure profiles associated with L-mode and H-mode discharges [11]. The H-mode is associated with longer confinement times and a steep transport barrier in the edge of the plasma. Understanding the L-H transition is one of many mysteries in magnetic confinement plasma physics that simulations may help resolve.

1.3 Plasma physics models

1.3.1 Plasma kinetic equation

The equation describing the evolution of the exact, microscopic distribution of all particles (in the parameter range where quantum and relativistic effects can be neglected) is the Klimontovich equation [12],

$$\frac{\partial \mathcal{F}_a}{\partial t} + \mathbf{v} \cdot \nabla \mathcal{F}_a + \frac{q_a}{m_a}(\mathbf{E} + \mathbf{v} \times \mathbf{B}) \cdot \frac{\partial \mathcal{F}_a}{\partial \mathbf{v}} = 0.$$

In the above equation, t, $\mathbf{x}$, and $\mathbf{v}$ parameterize time, configuration space, and velocity space respectively. The microscopic distribution, $\mathcal{F}_p = \mathcal{F}_p(\mathbf{x}, \mathbf{v}, t)$, provides information about the location and velocity of particle p at a given time, t. The charge and mass corresponding to particle p are given by q_p and m_p. The microscopic electric and magnetic fields, $\mathbf{E} = \mathbf{E}(\mathbf{x}, t)$ and $\mathbf{B} = \mathbf{B}(\mathbf{x}, t)$, are evaluated from the Maxwell Equations,

$$\nabla \cdot \mathbf{E} = \sum_p \int d^3v q_p \mathcal{F}_p(\mathbf{x}, \mathbf{v}, t)$$

$$\nabla \cdot \mathbf{B} = 0$$

$$\nabla \times \mathbf{E} = -\frac{1}{c}\frac{\partial \mathbf{B}}{\partial t}$$

$$\nabla \times \mathbf{B} = \frac{4\pi}{c} \sum_p \int d^3v q_p \mathbf{v} \mathcal{F}_p(\mathbf{x}, \mathbf{v}, t) - \frac{1}{c}\frac{\partial \mathbf{E}}{\partial t}.$$

While the above equations contain complete information about the plasma, they cannot be evaluated numerically. There are too many particles in the plasma for a computer to simulate, and the required resolution for the configuration and velocity space grid to model the particle dynamics would be too high. Furthermore, one does not care about the micro-

scopic particle distributions, because only the macroscopic quantities (such as the densities or heat fluxes) are meaningful and can be compared to experimental data. To obtain a more tractable equation, one can take an ensemble average of the Klimontovich equation over all of the different microscopic states corresponding to a particular macroscopic system to obtain an equation for the one-particle distribution function, $f =< \mathcal{F} >_{\text{ensemble}}$. Doing this, one would arrive at the standard kinetic equation in plasma physics,

$$\frac{\partial f_a}{\partial t} + \mathbf{v} \cdot \nabla f_a + \frac{q_a}{m_a}(\mathbf{E} + \mathbf{v} \times \mathbf{B}) \cdot \frac{\partial f_a}{\partial \mathbf{v}} = C_a.$$

In the above equation, $f_a = f_a(\mathbf{x}, \mathbf{v}, t)$ represents the smooth six-dimensional macroscopic distribution function which represents the phase-space density of the charged particle species, a. For this equation, a represents a collection of charged particles belonging to a particular species such as ions or electrons. It does not correspond to individual particles. In addition, the electric and magnetic fields, $\mathbf{E}$ and $\mathbf{B}$, are the smooth macroscopic fields that are determined by the bulk plasma particles, and it does not incorporate the fields that would be observed on small microscopic distances close to a charged particle. The term on the right-hand side is referred to as the collision operator, and its exact expression is given by

$$C_a = \frac{q_a}{m_a}(\mathbf{E}_{\text{macro}} + \mathbf{v} \times \mathbf{B}_{\text{macro}}) \cdot \frac{\partial f_a}{\partial \mathbf{v}} - \left\langle \frac{q_a}{m_a}(\mathbf{E}_{\text{micro}} + \mathbf{v} \times \mathbf{B}_{\text{micro}}) \cdot \frac{\partial \mathcal{F}_a}{\partial \mathbf{v}} \right\rangle_{\text{ensemble}}.$$

The collision operator acts as a correction term to the six-dimensional kinetic equation, incorporating microscopic discrete particle effects. The extreme case in which the collision operator is zero would correspond to the case where the large-scale electromagnetic fields are determined by the bulk motion of many particles. This would mean that particle interactions (through microscopic fields) are exceedingly rare and have little influence on the system as a whole. This is a reasonable approximation in a hot and dilute plasma. When the density is low, there are fewer particles to interact in a given volume, and when the temperature

is higher, the cross-section for interaction is much lower, and particles tend to travel right by each other, unless they happen to come very close. The case where collisions can be neglected altogether is referred to as the Vlasov equation.

The necessary assumption for neglecting the collision operator (or using a simplified form) can be expressed mathematically through the idea of the Debye length, λ_D, and the distance of closest approach, λ_c. In a plasma near statistical equilibrium, the Debye length corresponds to the length scale over which the electric field from a charge perturbation is damped (or shielded). For a quasi-neutral plasma, the Debye length is given by

$$\lambda_D = \sqrt{T/(4\pi n e^2)}.$$

In the above formula, e denotes the magnitude of charge associated with a proton or electron. The distance of closest approach refers to the inter-particle spacing at which the total energy of one particle in the electrostatic field of the other, $U = \frac{1}{2}mv^2 - e^2/r$, would vanish. For a plasma at a temperature of T, this would correspond to

$$\lambda_c = \frac{e^2}{T}.$$

λ_D corresponds to the length scale of the fields resulting from the collective plasma particles. It exists independent of particle correlations. λ_c corresponds to the length scale of the discrete particle interactions. If $\lambda_D >> \lambda_c$, then the charged particles will for the most part undergo acceleration from the collective electromagnetic fields, and only occasionally experience short range collisions. This is the necessary assumption for a weakly coupled plasma, and can be encompassed by what is called the plasma parameter,

$$\Lambda = \frac{\lambda_D}{\lambda_c} = \sqrt{\frac{T^3}{4\pi n e^6}} \gg 1.$$

The plasma parameter must be significantly large to justify modeling the plasma with a six-dimensional distribution function. The plasma parameter increases with increasing temperature and decreasing density as expected. In a tokamak, typical values of the plasma

parameter are around $\Lambda \sim 10^8$ [13], which is used as justification to model the plasma dynamics with kinetic theory. The plasma parameter (and the criterion for a weakly coupled plasma) is also related to the number of particles in a Debye sphere,

$$\Lambda = 4\pi n \lambda_D^3 \gg 1.$$

It is convenient, and in many cases justified, to neglect the collision operator modeling the discrete particle effects in the plasma. Nevertheless, collisional effects can be important in some regimes, such as the plasma edge and scrape-off layer in a magnetic confinement device. Collisions act to smooth out the velocity space part of the six-dimensional distribution function, and act as an important sink of free energy in the system (the Vlasov equation conserves entropy). Even though it is practically impossible to model particle correlations completely, a perturbative model acting as an operator on the six-dimensional distribution function can be used to capture the most important collisional effects. An in-depth discussion of the theory of collision operators and a description of the collision operator used in the GENE code shall be given in chapter 3.

While the six-dimensional kinetic equation is far simpler than the Klimontovich equation, it is still too expensive to use for modeling magnetic confinement devices such as tokamaks and stellarators. The kinetic equation is used for the study of some plasma systems, such as systems involving laser plasma interactions. But this is because the dynamics of such systems occur on very fast time-scales. The important dynamics that occur in magnetically confined plasmas exist over long time and space scales. The kinetic equation just derived can be used to model very fast phenomena (on the order of the plasma frequency), and very small-scale phenomena (on the order of the Debye length). Using such a model to study magnetic confinement plasmas would be akin to trying to view a large photo at an extremely high resolution. Doing so would be incredibly computationally expensive (impractically so), and past a certain point, higher resolution provides no benefit.

In Chapter 2, a new, more computationally tractable kinetic model shall be obtained by eliminating the fast and short-scale dynamics, in addition to one of the velocity space di-

mensions. This is analogous to how the more computationally tractable kinetic equation was derived from the Klimontovich equation by eliminating the extremely short-scales necessary to model the particle interactions and the enormous number of degrees of freedom necessary to track each particle. But first, more traditional reduced models based on treating the plasma as a fluid shall be discussed.

1.3.2 Plasma fluid models

Plasma fluid models have no velocity space dependence and are obtained by taking moments of the kinetic equation. To derive fluid models, one would multiply the kinetic equation by v^m, where m is a non-negative integer, and integrate over velocity space to obtain equations for moments (such as density, flow, temperature, etc.) depending only on configuration space. One would obtain an infinite set of equations for each m. Each equation which solves for a given moment requires information about a higher order moment. So there is an infinite hierarchy of equations which are all coupled. To obtain a finite set of equations which could be solved, some closure condition must be applied to one of the higher order moments (preferably based on a reasonable assumption applied to the plasma). Typically, it is assumed that the distribution function is close to a local Maxwellian (which depends on the lower order moments of density, flow, and temperature), and the higher order moments which need to be obtained are derived by taking certain velocity space integrals of this distribution which depends on the lower order moments. Thus, one would obtain a closed set of equations which would be valid at high collisionality, since one used the assumption that the distribution was close to a Maxwellian to apply the closure conditions. These equations are called plasma fluid equations because they resemble the traditional equations used to study fluid behavior (such as the Navier-Stokes equation). The notable distinction is the effect of electric and magnetic fields on the fluid moments (which are still calculated from the Maxwell equations, where the fluid moments are used for the charge and current density).

By assuming quasi-neutrality and neglecting the electron inertia and Finite Larmor Ra-

dius (FLR) effects, one can obtain the single fluid magnetohydrodynamic (MHD) equations. This is a highly computationally tractable model which is commonly used to study macroscopic plasma stability. A given discharge can be studied to determine if it is stable according to the MHD equations. MHD stability is a necessary but not sufficient condition for plasma stability, meaning that if a given discharge is unstable according to the MHD model, then the plasma is almost certainly unstable. However, if the discharge is MHD stable, then the plasma could be unstable due to factors that are not incorporated into the MHD model. Furthermore, there are phenomena that are observed both in magnetic confinement experiments and MHD simulations such as sawteeth crashes and disruptions, and due to the relative simplicity and computational tractability of the model, MHD simulations are a useful tool for understanding the dynamics of such phenomena.

While fluid models may be a useful tool for investigating plasma stability and studying certain plasma phenomena, they are not applicable to studying small-scale plasma turbulence and transport, especially in the core of the discharge where the collisionality is very low. For this, it is essential to have a model which includes important kinetic effects, such as Landau damping, particle trapping, FLR effects, etc. Given that the standard plasma kinetic model is too computationally expensive for this task, it is necessary to derive a new reduced kinetic model, known as gyrokinetics.

1.4 Thesis outline

This thesis shall be devoted to the topic of collisional and electromagnetic gyrokinetic models, as well as the study of how the gyrokinetic model behaves when going from the core (where the gyrokinetic model has been well validated in modeling the plasma turbulence and transport) to the edge of a plasma discharge. The remainder of this thesis shall be outlined in this subsection.

In chapter 2, a description of gyrokinetic theory and the gyrokinetic model used in the GENE code shall be given, with the topic of collisions deferred until later. The assumptions and ordering of gyrokinetics shall be presented, along with the full-f gyrokinetic equation.

From there, the delta-f gyrokinetic equation shall be derived, a background Maxwellian will be assumed, and the vector expressions shall be expanded based on the field-aligned coordinate system. The equations used to solve for the fields shall also be derived from the Maxwell equations using the pull-back operator and the gyrokinetic ordering. From there, the normalization of the equations shall be detailed, the boundary conditions shall be examined, and the numerical discretization of each coordinate in the GENE code shall be described.

In chapter 3, a description of the linearized Sugama delta-f collision operator newly implemented in the GENE code shall be given. The linearized Landau-Boltzmann collision operator shall be derived starting from the full nonlinear Landau-Boltzmann operator. This collision operator does not guarantee free energy dissipation in the nonisothermal case, and a new operator shall be derived which satisfies this essential property. This derivation shall follow the one outlined in ref. [14]. Following this, the FLR corrections to the collision operator shall be derived for the local gyrokinetic model. Then the numerical implementation of the collision operator shall be given. A set of tests shall be conducted to prove that the collision operator conserves particles, momentum, and energy, and dissipates free energy. Finally, benchmarks shall be performed to ensure correct implementation of the collision operator.

In chapter 4, the local version of the GENE code shall be applied to study the edge of an L-mode plasma discharge. First, the physical scenario under investigation shall be described. Afterwards, the linear microinstabilities present at that radial position shall be examined. Finally, the nonlinear turbulence simulations shall be discussed, with the focus being on the transport levels, and the degree of nonlinearity in the system.

In chapter 5, a new implementation of the electromagnetic fields shall be described. This implementation will then be linearly benchmarked, examined for stability in the Rosenbluth-Hinton test, and then tested to see if such a model can mitigate the nonlinear instabilities that occur at high plasma β.

Conclusions and an outline for potential future work shall be given in chapter 6.

CHAPTER 2

Fundamentals of gyrokinetic theory and simulation

The six-dimensional collisional kinetic equation described in the previous chapter should be capable of simulating the transport in any practical magnetic confinement fusion device owing to the hot and dilute nature of fusion plasmas. Such an equation could also simulate the extremely fast phenomena of laser-plasma interactions, or the physics occurring in the interstellar medium, the solar wind, or the sun. Unfortunately, a model which is so powerful so as to be capable of describing such a diverse range of physical systems often has the downside of being too computationally heavy to be useful in practical applications. A model which has the capability of simulating the incredibly fast dynamics of light waves in plasmas must also use very small time-steps in a simulation to resolve such phenomena, even if they are irrelevant to the slower physics of the system. A model which has the capability of simulating the small-scale dynamics along a strong magnetic field must have a high enough resolution to capture this, even if the structures along the magnetic field tend to be very large. This motivates the construction of a reduced model which is capable of simulating the small-scale turbulence and transport occurring in a magnetic confinement fusion device, and which is also computationally tractable on present-day supercomputers.

The most successful model to this end is the gyrokinetic model. The premise behind gyrokinetics is that when a plasma is very strongly magnetized (in a magnetic confinement device such as a tokamak or stellarator, the magnetic field strength is between 1-5 T) and the transport and turbulent dynamics of interest are on long time-scales compared to the ion cyclotron resonance, then the cyclotron motion can be regarded as instantaneous. In this scenario, the particle which has six degrees of freedom (three degrees in configuration space and three degrees in velocity space) can effectively be replaced with a ring which has five

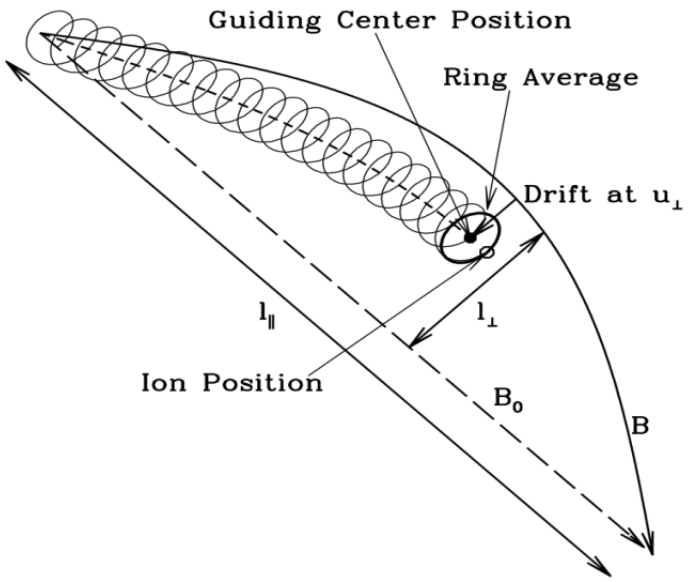

Figure 2.1: Depiction of gyromotion in a strong magnetic field. This figure has been taken from ref. [15]

degrees of freedom (three degrees to specify the guiding center position of the ring, one degree to specify the velocity along the magnetic field, and one degree to specify the perpendicular speed or the size of the ring). Such a ring then experiences the typical drifts ($\mathbf{E} \times \mathbf{B}$, ∇B, and curvature drifts) perpendicular to the magnetic field, and also undergoes different drifts and acceleration forces along the magnetic field. However, the magnetic moment for the ring is conserved as an adiabatic invariant in the collisionless limit. This is depicted with a diagram in Fig. 2.1. This model eliminates the time scales above the ion cyclotron resonance, the gyrophase angle dependence, and allows for a separation of scales along and across the magnetic field. This gyrokinetic model allows for computationally tractable simulations of plasma turbulence and transport.

Many different codes have been developed based on the gyrokinetic model to simulate turbulence and transport. The discussion and results laid out in this thesis shall pertain to the Eulerian gyrokinetic code, GENE (Gyrokinetic Electromagnetic Numerical Experiment) [16, 17, 18]. GENE solves the 5D delta-f gyrokinetic equations on a fixed grid in phase space. Only the perturbation is solved for, and all of the terms are evaluated with explicit time-stepping schemes. GENE can operate as a local flux-tube model (which simulates a small

radial domain of the plasma discharge using periodic boundary conditions) or as a global model which takes into account the radial variation of the plasma profiles. Additionally, a new version of the code which can utilize 3D boundary conditions is in development. GENE has been highly optimized (especially relative to codes that do not rely upon field aligned coordinates), is well benchmarked, and can efficiently scale up to tens of thousands of processors. This makes GENE an ideal tool for the study of plasma turbulence and transport.

This chapter is outlined in the following way: First, the underlying assumptions and ordering of gyrokinetics shall be discussed in section 2.1. After that, the full gyrokinetic equation shall be presented, as well as a physical interpretation of each of the terms in section 2.2. The full derivation shall not be given, only described qualitatively. In section 2.3, the distribution function shall be split into a background and a perturbation. The perturbation will be assumed to vary on the gyrokinetic ordering, and the original gyrokinetic equation shall be expanded to first order to obtain the delta-f gyrokinetic equation. In section 2.4, the background distribution shall be taken to be a Maxwellian, and the delta-f equation shall be simplified according to this assumption. In section 2.5, the field-aligned coordinate system shall be presented, and the vector expressions shall be expanded based on this coordinate choice to obtain a scalar partial differential equation. In section 2.6, the gyrokinetic field equations shall be obtained by transforming the distribution function from gyrocenter coordinates to particle coordinates in the moments for the charge and current density. In section 2.7, the diagnostic quantities relating to turbulent transport shall be discussed. The normalization of the equations shall be given in section 2.8. The boundary conditions for each dimension will be given in section 2.9, and the numerical discretization applied to each coordinate of the 5D phase space will be given in section 2.10. This shall be done for both the local flux-tube model and the global model. Finally, conclusions will be drawn in section 2.11. Much of the discussion in this chapter shall be specific to the GENE code. It must also be emphasized that this chapter does not include a discussion of collisions. Because much of the work developed in this thesis relates to collision models, and because collisions can be a very exhaustive topic which is treated on a different footing than the rest

of the gyrokinetic model, chapter 3 is exclusively devoted to the topic of collision operators.

2.1 Assumptions and ordering of gyrokinetics

In order to obtain a simulation which can easily resolve the time, configuration space, and velocity space scales of interest, one must first prescribe an ordering related to the system under examination. One can then construct a Lagrangian based around that ordering and discard higher order terms to build a model which is specifically tailored to the physics at hand. In this section, the specific ordering relating to the gyrokinetic model in the GENE code (there are several different gyrokinetic orderings leading to different model approximations) shall be discussed. It must be emphasized that the ordering used to construct the gyrokinetic model is based upon experimental observations of plasma turbulence and transport occurring within a magnetic confinement device. The ordering is as follows:

- The microturbulent fluctuations in the plasma are assumed to be highly anisotropic. The correlation lengths of fluctuations across the magnetic field are about 10-100 gyroradii, while the correlation lengths along the magnetic field can be on the order of several meters. This can be expressed mathematically as $k_\parallel/k_\perp \sim \epsilon_\parallel \ll 1$. Here, $k_\parallel$ and $k_\perp$ correspond to the typical parallel and perpendicular wavenumbers of the turbulent fluctuations. Here, and for the remainder of the thesis, the words *parallel* and *perpendicular* shall be used in reference to the background magnetic field unless otherwise specified.

- The Larmor radius ($\rho_a = v_\perp/\Omega_a = v_\perp m_a c/q_a B$) is very small compared to the length scales corresponding to magnetic field variations ($1/L_B = (1/B)dB/dx$) and variations of the background equilibrium distribution ($1/L_F = (1/F_0)dF_0/dx$). This can be expressed mathematically as $\rho_a/L_B \sim \epsilon_B \ll 1$ and $\rho_a/L_F \sim \epsilon_F \ll 1$.

- The fluctuations of the field perturbations against the background profiles are all very small. Additionally, it is assumed in the GENE code (and many other codes) that the perturbations of the distribution function are very small compared to the background

equilibrium distribution, although this constraint can be removed for a full-f code. This ordering is expressed mathematically as $\delta f/F_0 \sim q\delta\phi/T_e \sim q(v_\parallel/c)A_\parallel/T_e \sim \delta B_\parallel/B_0 \sim \epsilon_\delta \ll 1$.

- The frequency spectra of the turbulence and transport is very low compared to the ion cyclotron frequency. This is essential if particles are going to be replaced by rings of charge for a simulation modeling turbulence and transport. This ordering is expressed mathematically as $\omega/\Omega_a \sim \epsilon_t \ll 1$. Here, ω denotes the relevant frequency scale of the plasma microturbulence and Ω_a denotes the cyclotron frequency of species a.

- The time scales over which collisions alter the distribution function are very long in comparison to the ion cyclotron gyration time. This is necessary if particles are going to be replaced by rings of charge for the modeling of weakly collisional turbulence and transport. This ordering is expressed mathematically as $\nu_a/\Omega_a \sim \epsilon_\nu \ll 1$.

The above assumptions (in addition to the assumptions of the standard six dimensional kinetic equation) are the only ones needed to be able to apply the gyrokinetic model. While fluctuation amplitudes have been found to be on the order of $\epsilon_\delta \sim 10\%$ in the edge, and the slow timescale assumption ($\epsilon_t \ll 1$) makes a self-consistent study of the kinetics of ion/electron cyclotron heating completely impossible, these assumptions have been found to be broadly applicable for the study of transport in fusion plasmas. One thing that should also be emphasized is that even though the variations of the background profiles must be large compared to the ion/electron gyroradius, turbulent fluctuations with perpendicular correlation lengths comparable to gyroradius scales can be handled by gyrokinetics. Mathematically speaking, $k_\perp \rho_{i/e} \sim 1$ is allowed, as would be required to model microturbulent transport. For the following discussion, all of the different ordering parameters $(\epsilon_\parallel, \epsilon_B, \epsilon_F, \epsilon_\delta, \epsilon_t, \epsilon_\nu)$ shall be taken to be roughly the same size, ϵ.

2.2 The full-f gyrokinetic equation

To derive the gyrokinetic equation, one would start with the Lagrangian and Hamiltonian of charged particles in electromagnetic fields. One could then derive the one-form, $\gamma(\mathbf{x}, \mathbf{v})$, associated with that Lagrangian. The one-form is just the integrand of the action integral $\left(\int \gamma(\mathbf{x}, \mathbf{v}) = \int L(\mathbf{x}, \mathbf{v}) dt\right)$ and is useful for facilitating coordinate transformations. One could then transform the one-form from particle coordinates to guiding-center coordinates, where the guiding-center is taken according a strong background magnetic field. At this point, there is an equilibrium background part and a perturbed part associated with the one-form. The equilibrium part is averaged over the gyroangle, and the perturbed part is operated on by a Lie (near-identity) transformation based on the gyrokinetic ordering. The result is a new gyrocenter one-form where the gyrophase dependence can be eliminated. The gyrocenter is the same as the guiding-center, but is adjusted to account for field perturbations and inhomogeneities. From this one-form, the gyrokinetic Lagrangian can be obtained. This Lagrangian can then be plugged into the Euler-Lagrange equations to obtain the final gyrokinetic Vlasov equation. The derivation of the gyrokinetic equation shall not be repeated here. Rather, the full equation shall simply be given and discussed. A highly simplified derivation of the gyrokinetic equations for the reduced case of a straight, uniform background magnetic field is given in ref. [15]. The complete derivation of modern gyrokinetic theory is given in ref. [19, 20, 21, 22]. This theory is summarized in the review paper in ref. [23]. A description of the mathematical perturbation theory necessary for the derivation of gyrokinetics is given in ref. [24, 25]. A good overview of the derivation has been given in PhD theses associated with the development of the GENE code in ref. [26, 27].

The full-f gyrokinetic Vlasov equation is given by

$$\frac{\partial F_a}{\partial t} + \frac{\partial \mathbf{X}}{\partial t} \cdot \nabla F_a + \frac{\partial v_\parallel}{\partial t} \frac{\partial F_a}{\partial v_\parallel} = 0, \tag{2.1}$$

where $F_a = F_a(\mathbf{x}, v_\parallel, \mu)$ is the full gyrocenter distribution function for species a in the full 5D phase space. A particle in the gyrokinetic framework is advected through configuration space by the various plasma drifts, and accelerated along the magnetic field. However,

the magnetic moment is conserved as an adiabatic invariant in the (collisionless) system. This is reflected in the equation by the fact that there is no $((\partial\mu/\partial t)\partial F_a/\partial\mu)$ term because $(\partial\mu/\partial t) = 0$. The velocity which advects the plasma particles, $\partial\mathbf{X}/\partial t$, is given by

$$\frac{\partial \mathbf{X}}{\partial t} = \mathbf{v}_D = \left(v_\parallel \hat{\mathbf{b}}_0 + \frac{B_0}{B^*_{0\parallel}} (\mathbf{v}_{\overline{\chi}} + \mathbf{v}_{\nabla B} + \mathbf{v}_c) \right),$$

where the new gyrokinetic potential, χ, has been introduced. The gyrokinetic potential has the form,

$$\overline{\chi} = \overline{\phi} - \frac{v_\parallel}{c} \overline{A_\parallel} + \frac{\mu}{q_a} \overline{B_\parallel},$$

and the newly defined magnetic field, $B^*_{0\parallel}$, has an expression given by

$$B^*_{0\parallel} = B_0 + \frac{m_a c}{q_a} v_\parallel \hat{\mathbf{b}}_0 \cdot \left(\nabla \times \hat{\mathbf{b}}_0 \right).$$

The over-bar on the fields denotes an average over the gyroradius,

$$\overline{\psi} = \int \frac{d\theta}{2\pi} \psi(\mathbf{X} + \rho_a), \tag{2.2}$$

where $\mathbf{X}$ denotes the guiding center position, ρ_a denotes the gyroradius vector, and θ denotes the gyroangle coordinate.

The advection term is a drift velocity which is a superposition of four different terms. There is the standard parallel motion along the magnetic field, $v_\parallel \hat{\mathbf{b}}_0$, the $\mathbf{E} \times \mathbf{B}$ drift, $\mathbf{v}_{\overline{\chi}}$, the drift due to the varying magnetic field strength, $\mathbf{v}_{\nabla B_0}$, and the drift due to the curvature of the magnetic field lines, $\mathbf{v}_c$. The expressions for these drift velocities are

$$\mathbf{v}_{\overline{\chi}} = \frac{c}{B_0^2} \mathbf{B}_0 \times \nabla \overline{\chi}$$

$$\mathbf{v}_{\nabla B_0} = \frac{\mu c}{q_a B_0^2} \mathbf{B}_0 \times \nabla B_0$$

$$\mathbf{v}_c = \frac{v_\parallel^2}{\Omega_a}\big(\nabla \times \hat{\mathbf{b}}_0\big)_\perp.$$

The expression for the curvature drift velocity, $\mathbf{v}_c$, can be simplified using the Ampére relation, $\nabla \times \mathbf{B} = (4\pi/c)\mathbf{J}$, the MHD equilibrium expression, $\nabla p_0 = (\mathbf{J}_0 \times \mathbf{B}_0)/c$, and the vector identity, $\mathbf{A} \times (\mathbf{B} \times \mathbf{C}) = (\mathbf{A} \cdot \mathbf{C})\mathbf{B} - (\mathbf{A} \cdot \mathbf{B})\mathbf{C}$,

$$\mathbf{v}_c = \frac{v_\parallel^2}{\Omega_a}\left(\hat{\mathbf{b}}_0 \times \left(\frac{\nabla B_0}{B_0} + \frac{\beta}{2}\frac{\nabla p_0}{p_0}\right)\right),$$

where β denotes the ratio of the plasma pressure to magnetic field strength,

$$\beta = \frac{8\pi p}{B_0^2}.$$

Finally, the expression for the acceleration along the magnetic field is given by

$$\frac{\partial v_\parallel}{\partial t} = \frac{1}{m_a v_\parallel}\mathbf{v}_D \cdot \mathfrak{F}_a.$$

The acceleration along the field lines is the most complicated term, and is given by the dot product of a force, $\mathfrak{F}_a$, with the drift velocity normalized with respect to the parallel velocity. The expression for $\mathfrak{F}_a$ is given by

$$\mathfrak{F}_a = -\left(q_a \nabla \overline{\phi} + \frac{q_a}{c}\frac{\partial \overline{A_\parallel}}{\partial t}\hat{\mathbf{b}}_0 + \mu \nabla\big(B_0 + \overline{B_\parallel}\big)\right).$$

The force contributing to the parallel acceleration consists of the parallel electric field due to both the electrostatic drive term and the induced electric field along the magnetic field lines due to changing perpendicular magnetic fields, as well as the magnetic mirror force that results from an inhomogeneous magnetic field.

The drifts and accelerations appearing in the gyrokinetic equation are more complex than the drifts and accelerations appearing in the standard Vlasov equation. While the equations are more complex, they are nevertheless easier to solve computationally. There

is one less dimension in the system, a much larger time-step can be used to evolve the system's dynamics, and fewer grid points are needed to resolve the configuration space. If one was to simulate transport using the standard 6D Vlasov model, the fast gyration and the drifts associated with the electric field, the inhomogeneous magnetic field, and the field line curvature would be become apparent in a simulation for which the gyrokinetic ordering was accurate. This would be a "brute force" approach to resolving those features, and would require an impossibly enormous amount of computational resources. One can dramatically reduce the required resolution by working with a simulation where the drifts, magnetic moment conservation, etc. are already explicitly part of the model. The complexity of the model leading to drift motion and μ conservation is handled analytically to eliminate the computational resources needed to handle such complexity. This is highly similar to the derivation of the 6D kinetic equation from the Klimontovich equation. It is easy to understand all of the parts of the Klimontovich equation, and deriving a 6D kinetic equation from the Klimontovich equation results in a collision operator which can have a much more complicated expression than any part of the Klimontovich equation. Nevertheless, such an equation is far more suited to computational analysis.

2.3 The delta-f gyrokinetic model

While the full-f gyrokinetic equation (Eq. 2.1) can be used for modeling the plasma, there are still several difficulties associated with such a model. The full distribution function by definition must be a positive definite quantity. However, it has been found that the distribution function can occasionally become negative after numerical discretization is applied. It is not trivial to come up with a computationally efficient numerical scheme which enforces positive-definiteness on the distribution function. Furthermore, using the full distribution function would require the implementation of a nonlinear field-solver for the field equations, which is no trivial task. Also, the full-f Landau-Boltzmann collision operator is nonlocal in velocity space, and would require a convolution integral, unlike the linearized model collision operator (discussed in chapter 3). These difficulties (and several others) can be mitigated by

separating the full distribution into a background part and a smaller perturbed part. One can then approximately neglect higher order terms in the gyrokinetic ordering to obtain the delta-f gyrokinetic equation,

The full-f gyrokinetic equation can be written in a more detailed form:

$$\frac{\partial}{\partial t}(F_{0a}+f_a)+$$

$$\left(v_\parallel\hat{\mathbf{b}}_0+\frac{B_0}{B^*_{0\parallel}}(\mathbf{v}_{\overline{\chi}}+\mathbf{v}_{\nabla B}+\mathbf{v}_c)\right)\cdot\left(\nabla(F_{0a}+f_a)-\frac{1}{m_a v_\parallel}\left(\mu\nabla B_0+q_a\nabla\overline{\chi}\right)\frac{\partial}{\partial v_\parallel}(F_{0a}+f_a)\right)$$

$$-\frac{q_a}{m_a c}\frac{\partial\overline{A_\parallel}}{\partial t}\frac{\partial}{\partial v_\parallel}(F_{0a}+f_a)=0.$$

In the above expression, the full distribution, F_a, has been split into a background distribution, F_{0a}, and a perturbed distribution, f_a. The perturbed distribution is smaller than the background by a factor of the gyrokinetic ordering, $f_a/F_{0a}\sim O(\epsilon)$. It will be assumed that the background distribution is stationary in time (the evolution of the background occurs on the heating time-scale which is far slower than the turbulent transport time-scale). It will also be assumed that the background distribution varies along and across the magnetic field on the macroscopic length-scale $(\hat{\mathbf{z}}\cdot\nabla F_{0a})\sim|\hat{\mathbf{z}}\times\nabla F_{0a}|\sim O(F_{0a}/L_F)$. The perturbation varies along the magnetic field on the macroscopic length scale, $(\hat{\mathbf{z}}\cdot\nabla f_a)\sim O(f_a/L_F)$, but varies across the magnetic field on the scale of the gyroradius, $|\hat{\mathbf{z}}\times\nabla f_a|\sim O(f_a/\rho_a)$. This equation can be expanded to various orders in ϵ based on the gyrokinetic ordering discussed in section 2.1. The full-f gyrokinetic equation to zeroth order in ϵ gives the equilibrium constraint for the background distribution,

$$v_\parallel\hat{\mathbf{b}}_0\cdot\left(\nabla F_{0a}-\frac{\mu}{m_a v_\parallel}\frac{\partial F_{0a}}{\partial v_\parallel}\nabla B_0\right)=0. \tag{2.3}$$

The background distribution can in principle be anything as long as it satisfies the equi-

librium constraint (Eq. 2.3). Expanding the equation to first order in ϵ gives the complete delta-f gyrokinetic equation,

$$\frac{\partial f_a}{\partial t} + \frac{B_0}{B_{0\|}^*}\left(\mathbf{v}_{\overline{\chi}} + \mathbf{v}_{\nabla B} + \mathbf{v}_c\right) \cdot \left(\nabla(F_{0a} + f_a) - \frac{1}{m_a v_\|}\left(\mu \nabla B_0 + q_a \nabla \overline{\chi}\right)\frac{\partial F_{0a}}{\partial v_\|}\right)$$

$$+ v_\| \hat{\mathbf{b}}_0 \cdot \left(\nabla f_a - \frac{q_a}{m_a v_\|}\frac{\partial F_{0a}}{\partial v_\|}\nabla \overline{\chi} - \frac{\mu}{m_a v_\|}\frac{\partial f_a}{\partial v_\|}\nabla B_0\right) - \frac{q_a}{m_a c}\frac{\partial \overline{A_\|}}{\partial t}\frac{\partial F_{0a}}{\partial v_\|} = 0. \tag{2.4}$$

The second order terms in ϵ are generally neglected, but could be included in the model relatively easily. These terms result in the parallel nonlinearity term:

$$\left(-\frac{B_0}{B_{0\|}^*}\left(\mathbf{v}_{\overline{\chi}} + \mathbf{v}_{\nabla B} + \mathbf{v}_c\right) \cdot \left(\frac{1}{m_a v_\|}\left(\mu \nabla B_0 + q_a \nabla \overline{\chi}\right)\right) + \frac{q_a}{m_a}\left(\frac{B_0}{B_{0\|}^*}\hat{\mathbf{b}}_0 \cdot \nabla \overline{\chi} - \frac{1}{c}\frac{\partial \overline{A_\|}}{\partial t}\right)\right)\frac{\partial f_a}{\partial v_\|}.$$

2.4 Equilibrium background distribution

Any background distribution that meets the constraint in Eq. 2.3 can be utilized in the gyrokinetic model. This could be a Maxwellian, bi-Maxwellian, kappa distribution, bump-on-tail distribution, or an arbitrary distribution based on experimental measurements. Non-maxwellian background distributions have also been incorporated as a feature in the GENE code. However, in most cases, GENE is deployed with Maxwellian background distributions for all species in a simulation,

$$F_{0a} = F_{Ma} = \frac{n_{0a}(\mathbf{x})}{\pi^{3/2} v_{Ta}^3(\mathbf{x})} \exp\left(-\frac{m_a v_\|^2/2 + \mu B_0(\mathbf{x})}{T_{0a}(\mathbf{x})}\right). \tag{2.5}$$

In the above formula, $n_{0a}(\mathbf{x})$ denotes the density of species a, $T_{0a}(\mathbf{x})$ denotes the temperature and $v_{Ta}(\mathbf{x}) = \sqrt{2T_{0a}(\mathbf{x})/m_a}$ denotes the thermal velocity. The Maxwellian distribution is commonly used because it is the solution to the gyrokinetic equations for thermalized plasmas and because it only requires information about the density, temperature, and mag-

netic field strength associated with the background profiles. Experimentalists can construct profiles of the density and temperature for ions and electrons based on experimental measurements. The magnetic field strength and geometry information can be reconstructed from an MHD equilibrium either from the Grad-Shafranov equation [28] or from an MHD equilibrium code [29, 30]. Obtaining more detailed information, and thereby constructing more elaborate backgrounds closer to reality, is much harder. However, many different distributions are acceptable as a background distribution, as long as the delta-f approximation and the equilibrium constraint (Eq. 2.3) still holds to a satisfactory degree. Non-Maxwellian background distributions have recently been implemented in the GENE code and used to study fast particle effects [31]. For the remainder of this thesis, the Maxwellian distribution shall be taken as the background for discussions of theory and simulation. The derivatives of the background are as follows:

$$\nabla F_{Ma} = \left(\frac{\nabla n_{0a}}{n_{0a}} + \frac{\nabla T_{0a}}{T_{0a}} \left(\frac{m_a v_\parallel^2/2 + \mu B_0}{T_{0a}} - \frac{3}{2} \right) - \frac{\nabla B_0}{B_0} \frac{\mu B_0}{T_{0a}} \right) F_{Ma}$$

$$\frac{\partial F_{Ma}}{\partial v_\parallel} = -\frac{m_a v_\parallel}{T_{0a}} F_{Ma}$$

$$\frac{\partial F_{Ma}}{\partial \mu} = -\frac{B_0}{T_{0a}} F_{Ma}.$$

When these derivatives are plugged into the delta-f gyrokinetic equation, the simplified formula for the delta-f equation is obtained,

$$\frac{\partial f_a}{\partial t} + \frac{B_0}{B_{0\parallel}^*} \left(\mathbf{v}_{\overline{\chi}} + \mathbf{v}_{\nabla B} + \mathbf{v}_c \right) \cdot \left(\frac{\nabla n_{0a}}{n_{0a}} + \frac{\nabla T_{0a}}{T_{0a}} \left(\frac{m_a v_\parallel^2/2 + \mu B_0}{T_{0a}} - \frac{3}{2} \right) - \frac{\nabla B_0}{B_0} \frac{\mu B_0}{T_{0a}} \right) F_{Ma}$$

$$+ \frac{B_0}{B_{0\parallel}^*} \left(\mathbf{v}_{\overline{\chi}} + \mathbf{v}_{\nabla B} + \mathbf{v}_c \right) \cdot \left(\nabla f_a + \left(\mu \nabla B_0 + q_a \nabla \overline{\chi} \right) \frac{F_{Ma}}{T_{0a}} \right)$$

$$+ v_\parallel \hat{\mathbf{b}}_0 \cdot \left(\nabla f_a + q_a \frac{F_{Ma}}{T_{0a}} \nabla \overline{\chi} - \frac{\mu}{m_a v_\parallel} \frac{\partial f_a}{\partial v_\parallel} \nabla B_0 \right) + \frac{q_a v_\parallel}{c} \frac{\partial \overline{A_\parallel}}{\partial t} \frac{F_{Ma}}{T_{0a}} = 0. \tag{2.6}$$

2.5 Expansion of vector expressions

In order to implement the gyrokinetic equation numerically, a coordinate system must be chosen, and the vector expressions appearing in the equation must be expanded with regards to that coordinate system in configuration space. The following scalar partial differential equation can then be discretized and implemented as computer code. The coordinate system implemented in the GENE code is the field-aligned coordinate system. In an MHD equilibrium configuration, the magnetic field lines lie on surfaces that enclose a given amount of magnetic flux, called flux surfaces. The radial coordinate that parameterizes the flux surface in the simulation is denoted by x. The coordinate parameterizing the surface which is perpendicular to the field lines is denoted by y, and z is taken to be the coordinate which is parallel to the field lines. By using this more complex non-orthonormal coordinate system, one can use fewer points in the z dimension because of the natural separation of scales occurring in the highly-anisotropic plasma. Since the correlation length of structures along the magnetic field are ~ 1000 times larger than structures perpendicular to the magnetic field, this coordinate system makes simulations ~ 1000 times less expensive in terms of resolution. The downside of this approach is that such a coordinate system becomes singular at the separatrix (where the field lines go from closed to open) and at the very inner points in the core of the plasma where the flux surface encloses vanishingly small flux. Nevertheless, such a coordinate system has been highly beneficial for studying transport in the core. For more information, ref. [32] is a highly useful source for understanding non-orthonormal flux coordinates. The background magnetic field is regarded as being proportional to the cross product of the gradients of the two perpendicular coordinates,

$$\mathbf{B}_0 = C \nabla x \times \nabla y,$$

where C is the constant of proportionality. The geometry of the coordinate system can be described with the set of contravariant metric coefficients,

$$g^{ij} = (\nabla u^i \cdot \nabla u^j) = \begin{pmatrix} g^{xx} & g^{xy} & g^{xz} \\ g^{yx} & g^{yy} & g^{yz} \\ g^{zx} & g^{zy} & g^{zz} \end{pmatrix}.$$

In the above expression, u^i can correspond to the x, y, or z coordinate. The indices which loop over all configuration space variables are denoted by i and j. The coordinate system also has the Jacobian, $\mathfrak{J}$, expressed as

$$\frac{1}{\mathfrak{J}} = (\nabla x \times \nabla y) \cdot \nabla z = \frac{\mathbf{B}_0 \cdot \nabla z}{C}.$$

As will become clear very soon, it is useful to group the contravariant metric tensor elements together into certain expressions,

$$\gamma_1 = g^{xx} g^{yy} - g^{yx} g^{xy}$$

$$\gamma_2 = g^{xx} g^{yz} - g^{yx} g^{xz}$$

$$\gamma_3 = g^{xy} g^{yz} - g^{yy} g^{xz}.$$

The magnetic field strength can be expressed as

$$B_0^2 = \mathbf{B}_0 \cdot \mathbf{B}_0 = C^2 (g^{xx} g^{yy} - g^{xy} g^{yx}) = C^2 \gamma_1.$$

There are two types of vector expressions appearing in the gyrokinetic equation: $\mathbf{B}_0 \cdot \nabla$ and $(1/B_0^2)(\mathbf{B}_0 \times \nabla\psi) \cdot \nabla$. These can be expressed for the field-aligned coordinate system as

$$\mathbf{B}_0 \cdot \nabla = C\big(\nabla x \times \nabla y\big) \cdot \nabla u^i \frac{\partial}{\partial u^i} = \frac{C}{\mathfrak{J}} \frac{\partial}{\partial z} \tag{2.7}$$

$$\frac{1}{B_0^2}\big(\mathbf{B}_0 \times \nabla\psi\big) \cdot \nabla = \frac{C}{B_0^2}\Big(\big(\nabla x \times \nabla y\big) \times \frac{\partial \psi}{\partial u^i}\nabla u^i\Big) \cdot \nabla u^j \frac{\partial}{\partial u^j} = \frac{1}{C}\frac{g^{xi}g^{yj} - g^{yi}g^{xj}}{\gamma_1}\frac{\partial \psi}{\partial u^i}\frac{\partial}{\partial u^j}$$

$$= \frac{1}{C}\bigg(- \bigg(\frac{\partial \psi}{\partial y} + \frac{\gamma_2}{\gamma_1}\frac{\partial \psi}{\partial z}\bigg)\frac{\partial}{\partial x} + \bigg(\frac{\partial \psi}{\partial x} - \frac{\gamma_3}{\gamma_1}\frac{\partial \psi}{\partial z}\bigg)\frac{\partial}{\partial y} + \bigg(\frac{\gamma_2}{\gamma_1}\frac{\partial \psi}{\partial x} + \frac{\gamma_3}{\gamma_1}\frac{\partial \psi}{\partial y}\bigg)\frac{\partial}{\partial z}\bigg). \tag{2.8}$$

Before plugging these expressions into the gyrokinetic equation, it is worth noting the following configuration space derivatives of the background Maxwellian distribution:

$$\frac{\partial F_{Ma}}{\partial x} = \bigg(\frac{1}{n_{0a}}\frac{\partial n_{0a}}{\partial x} + \frac{1}{T_{0a}}\frac{\partial T_{0a}}{\partial x}\bigg(\frac{m_a v_\parallel^2/2 + \mu B_0}{T_{0a}} - \frac{3}{2}\bigg) - \frac{1}{B_0}\frac{\partial B_0}{\partial x}\frac{\mu B_0}{T_{0a}}\bigg)F_{Ma}$$

$$\frac{\partial F_{Ma}}{\partial y} = -\frac{1}{B_0}\frac{\partial B_0}{\partial y}\frac{\mu B_0}{T_{0a}}F_{Ma}$$

$$\frac{\partial F_{Ma}}{\partial z} = -\frac{1}{B_0}\frac{\partial B_0}{\partial z}\frac{\mu B_0}{T_{0a}}F_{Ma}.$$

The density and temperature profiles do not have a y or z dependence because it is assumed that these values are constant on a flux surface (although this would change for the code version which allows for 3D boundary conditions). Furthermore, it is useful to define the following variable:

$$\Gamma_{a,i} = \frac{\partial f_a}{\partial u^i} + \bigg(q_a\frac{\partial \overline{\phi}}{\partial u^i} + \mu\frac{\partial \overline{B_\parallel}}{\partial u^i}\bigg)\frac{F_{Ma}}{T_{0a}}. \tag{2.9}$$

Using these expressions, it is now possible to write down the gyrokinetic equation, free from vector expressions, for the field-aligned coordinate system,

$$\frac{\partial f_a}{\partial t} = \frac{c}{C}\frac{B_0}{B^*_{0\|}}\left(\frac{1}{n_{0a}}\frac{\partial n_{0a}}{\partial x} + \frac{1}{T_{0a}}\frac{\partial T_{0a}}{\partial x}\left(\frac{m_a v_\|^2/2 + \mu B_0}{T_{0a}} - \frac{3}{2}\right)\right)F_{Ma}\frac{\partial \overline{\chi}}{\partial y}$$

$$+\frac{c}{C}\frac{B_0}{B^*_{0\|}}\frac{\mu B_0 + m_a v_\|^2}{q_a B_0}\left(\frac{\partial B_0}{\partial y} + \frac{\gamma_2}{\gamma_1}\frac{\partial B_0}{\partial z}\right)\Gamma_{a,x}$$

$$-\frac{c}{C}\frac{B_0}{B^*_{0\|}}\left(\frac{\partial \overline{\chi}}{\partial x}\Gamma_{a,y} - \frac{\partial \overline{\chi}}{\partial y}\Gamma_{a,x}\right) - \frac{C}{\mathfrak{J}B_0}v_\|\Gamma_{a,z} + \frac{C}{\mathfrak{J}B_0}\frac{\mu}{m_a}\frac{\partial B_0}{\partial z}\frac{\partial f_a}{\partial v_\|}$$

$$-\frac{c}{C}\frac{B_0}{B^*_{0\|}}\left(\frac{\mu B_0 + m_a v_\|^2}{q_a B_0}\left(\frac{\partial B_0}{\partial x} - \frac{\gamma_3}{\gamma_1}\frac{\partial B_0}{\partial z}\right) + \frac{m_a v_\|^2}{q_a}\frac{\beta}{2}\frac{1}{p_0}\frac{\partial p_0}{\partial x}\right)\Gamma_{a,y}$$

$$+\frac{c}{C}\frac{B_0}{B^*_{0\|}}\frac{m_a v_\|^2 + \mu B_0}{q_a B_0}\left(\frac{\partial B_0}{\partial y} + \frac{\gamma_2}{\gamma_1}\frac{\partial B_0}{\partial z}\right)\left(\frac{1}{n_{0a}}\frac{\partial n_{0a}}{\partial x} + \frac{1}{T_{0a}}\frac{\partial T_{0a}}{\partial x}\left(\frac{m_a v_\|^2/2 + \mu B_0}{T_{0a}} - \frac{3}{2}\right)\right)F_{Ma}. \tag{2.10}$$

2.6 Gyrokinetic field equations

In order to evaluate the gyrokinetic equation, the electromagnetic fields must also be evaluated. Appropriate field equations must be derived from the original Maxwell equations for the electrostatic potential, ϕ, and the magnetic vector potential, $\mathbf{A}$,

$$-\nabla^2\phi = 4\pi\rho(\mathbf{x}) = 4\pi\sum_a q_a n_a(\mathbf{x})$$

$$-\nabla^2\mathbf{A} = \frac{4\pi}{c}\mathbf{J}(\mathbf{x}) = \frac{4\pi}{c}\sum_a q_a n_a(\mathbf{x})\mathbf{u}_a(\mathbf{x}).$$

In the equation for the magnetic vector potential, $\mathbf{A}$, the Coulomb gauge is utilized ($\nabla\cdot\mathbf{A} = 0$). The moments that are used to evaluate the fields are obtained from integrals of the distribution function,

$$n_a(\mathbf{x}) = \int d^3v f_a(\mathbf{x}, \mathbf{v})$$

$$\mathbf{u}_a(\mathbf{x}) = \frac{1}{n_a(\mathbf{x})} \int d^3v \mathbf{v} f_a(\mathbf{x}, \mathbf{v})$$

$$T_a(\mathbf{x}) = \frac{1}{n_a(\mathbf{x})} \int d^3v \frac{1}{2} m_a (\mathbf{v} - \mathbf{u}_a)^2 f_a(\mathbf{x}, \mathbf{v}).$$

These moments represent the density, flow, and temperature respectively. All that is needed to obtain the gyrokinetic field equations is to transform the distribution function from gyrocenter coordinates to guiding-center coordinates with the pull-back operator, T^*, evaluate the integrals in guiding-center coordinates rather than particle coordinates, and to eliminate higher order terms from the equations based on the gyrokinetic ordering (see refs. [26, 27, 23] for more details). The necessary moments can be evaluated from the distribution in particle, guiding-center, and gyrocenter coordinates:

$$M_{mn,a}(\mathbf{x}) = \int d^3v v_\parallel^m v_\perp^n f_a^{(\text{particle})}(\mathbf{x}, \mathbf{v})$$

$$M_{mn,a}(\mathbf{x}) = \int d^3X dv_\parallel d\mu d\theta \delta(\mathbf{X} - (\mathbf{x} - \rho)) f_a^{(\text{guiding-center})}(\mathbf{X}, \mathbf{V}) v_\parallel^m v_\perp^n \frac{B_{0\parallel}^*(\mathbf{x}, \mathbf{v})}{m_a}$$

$$M_{mn,a}(\mathbf{x}) = \int d^3X dv_\parallel d\mu d\theta \delta(\mathbf{X} - (\mathbf{x} - \rho)) T^* \{ f_a^{(\text{gyrocenter})}(\mathbf{X}, \mathbf{V}) \} v_\parallel^m v_\perp^n \frac{B_{0\parallel}^*(\mathbf{x}, \mathbf{v})}{m_a}$$

$$M_{mn,a}(\mathbf{x}) = \int d^3X dv_\parallel d\mu d\theta \delta(\mathbf{X} - (\mathbf{x} - \rho)) \cdot$$

$$\left(f_a(\mathbf{X},\mathbf{V}) - \left(q_a\phi(\mathbf{x}) - q_a\overline{\phi}(\mathbf{X}) - \mu\overline{B_\parallel}(\mathbf{X})\right)\frac{F_{Ma}}{T_{0a}}\right)v_\parallel^m v_\perp^n \frac{B^*_{0\parallel}(\mathbf{x},\mathbf{v})}{m_a}. \tag{2.11}$$

In the last expression, the pull-back operator has been applied to the distribution function,

$$T^*\{f_a\} = f_a - (q_a\phi(\mathbf{x}) - q_a\overline{\phi} - \mu\overline{B_\parallel})\frac{F_{Ma}}{T_{0a}}.$$

The following simplification shall also be made regarding $B^*_{0\parallel}$ in the field solver:

$$B^*_{0\parallel} = B_0 + \frac{m_a c}{q_a} v_\parallel \hat{\mathbf{b}}_0 \cdot \left(\nabla \times \hat{\mathbf{b}}_0\right) \simeq B_0.$$

The additional term in $B^*_{0\parallel}$ is considered to be $O(\epsilon_B)$ compared to B_0 and is neglected, thereby simplifying the analysis. In addition to the original gyroaverage definition introduced in Eq. 2.2, an additional gyroaveraging procedure must also be defined,

$$\langle\psi\rangle = \int d^3X \frac{d\theta}{2\pi}\delta(\mathbf{X} - (\mathbf{x} - \rho_a))\psi(\mathbf{X}). \tag{2.12}$$

With the proper expressions for the moments and gyroaveraging procedures defined, the field solver for ϕ, $A_\parallel$, and $B_\parallel$ can now be obtained. The gyrokinetic field equation for ϕ is as follows:

$$\nabla^2_\perp\phi(\mathbf{x}) = -4\pi\sum_a q_a M_{00,a}(\mathbf{x})$$

$$\nabla^2_\perp\phi(\mathbf{x}) = -8\pi^2\sum_a \frac{q_a}{m_a}\int dv_\parallel d\mu\left(\langle f_a B_0\rangle - \frac{q_a B_0 F_{Ma}}{T_{0a}}\phi(\mathbf{x}) + q_a\langle\frac{B_0 F_{Ma}}{T_{0a}}\overline{\phi}\rangle + \mu\langle\frac{B_0 F_{Ma}}{T_{0a}}\overline{B_\parallel}\rangle\right)$$

$$\nabla^2_\perp\phi(\mathbf{x}) + 8\pi^2\sum_a \frac{q_a}{m_a}\int dv_\parallel d\mu\left(q_a\langle\frac{B_0 F_{Ma}}{T_{0a}}\overline{\phi}\rangle - \frac{q_a B_0 F_{Ma}}{T_{0a}}\phi\right) =$$

$$-8\pi^2 \sum_a \frac{q_a}{m_a} \int dv_\parallel d\mu \left(\langle f_a B_0 \rangle + \mu \langle \frac{B_0 F_{Ma}}{T_{0a}} \overline{B_\parallel} \rangle \right).$$

The parallel part of the Laplacian has been discarded based on the gyrokinetic ordering. Additionally, it was assumed that the plasma was quasineutral ($\sum_a q_a n_{0a} = 0$) so that only the perturbed distribution has to be considered. The equation for the parallel magnetic vector potential is given as follows (the parallel part of the Laplacian has once again been excluded):

$$\nabla_\perp^2 A_\parallel = -\frac{4\pi}{c} J_\parallel = -\frac{4\pi}{c} \sum_a q_a M_{10,a}(\mathbf{x})$$

$$\nabla_\perp^2 A_\parallel = -\frac{8\pi^2}{c} \sum_a \frac{q_a}{m_a} \int dv_\parallel d\mu v_\parallel \langle f_a B_0 \rangle.$$

Finally, the parallel magnetic field can also be obtained,

$$\left(\nabla \times \delta \mathbf{B}\right)_\perp = \frac{\partial B_\parallel}{\partial y} \hat{\mathbf{x}} - \frac{\partial B_\parallel}{\partial x} \hat{\mathbf{y}} = \frac{4\pi}{c} \mathbf{J}_\perp$$

$$= \frac{4\pi^2}{c} \sum_a q_a \left(\frac{2}{m_a} \right)^{3/2} \int dv_\parallel d\mu \sqrt{\mu} \left\langle \hat{\mathbf{v}}_\perp B_0^{3/2} \left(f_a + \frac{q_a F_{Ma}}{T_{0a}} \overline{\phi} + \frac{q_a F_{Ma}}{T_{0a}} \overline{B_\parallel} \right) \right\rangle,$$

where the perpendicular velocity vector is defined (in local orthogonal coordinates) as

$$\hat{\mathbf{v}}_\perp = -\sin(\theta) \hat{\mathbf{x}} - \cos(\theta) \hat{\mathbf{y}}.$$

These equations can be used to determine the electromagnetic fields utilized in the gyrokinetic equation. The only complication is that the equations for ϕ and $B_\parallel$ are coupled together. This problem can be remedied in the local version of the code where the derivatives are replaced by wavenumbers and the gyroaveraging is replaced with Bessel functions. In that case it is easy to rewrite the equations so they are decoupled. It is not as straightforward for the global version of the code where the gyroaveraging and the derivatives have a

more complicated form. For this reason, $B_\parallel$ fluctuations have been implemented in the local version of the code, but implementing them into the global version is a work in progress.

2.7 Turbulent transport observables

A description of the gyrokinetic integro-differential equations implemented in the GENE code has been given (with a discussion of collisions deferred until chapter 3). However, the fundamental quantities related to plasma transport (the radial particle, heat, and momentum fluxes) have not been expressed. These are calculated as moments of the distribution function and then occasionally output from the code as a diagnostic (how often they are output can be set by the user). In order to have an expression for the radial fluxes, the flux-surface average definition must be used,

$$\left\{\Phi\right\}(x) = \frac{\int\int\int \mathfrak{J}\Phi(\mathbf{x}')\delta(x-x')dx'dy'dz'}{\int\int\int \mathfrak{J}\delta(x-x')dx'dy'dz'}.$$

This represents the average of an arbitrary quantity, Φ, over a flux surface located at a particular radial position. The radial transport of particles, heat, and parallel momentum are associated with the radial drift velocity, v_D^r, and are defined as

$$\Gamma_a(x) = \left\{ \int d^3v v_D^r f_a(\mathbf{x},\mathbf{v}) \right\}$$

$$Q_a(x) = \left\{ \int d^3v \frac{m_a}{2} v^2 v_D^r f_a(\mathbf{x},\mathbf{v}) \right\}$$

$$\Pi_a(x) = \left\{ \int d^3v m_a v_\parallel v_D^r f_a(\mathbf{x},\mathbf{v}) \right\}.$$

The total drift velocity in the gyrokinetic model is associated with three different drift velocities: the drift due to field fluctuations ($\mathbf{E}\times\mathbf{B}$ drift), the drift due to the inhomogeneous magnetic field strength (∇B drift), and the drift due to the curvature of the field lines

(v_c drift). For the case of turbulent transport, only the drift due to the field fluctuations contributes. The other drifts exist independent of the perturbed distribution function, and can be considered in a neoclassical code (in a neoclassical model, turbulence is not considered and the transport is due entirely to collisions and field line curvature). While GENE can operate as a neoclassical code, the code is mainly used to simulate the anomalous transport, which is typically the dominant transport occurring in the plasma. The discussion here shall be specific to turbulent transport. For more information on measurements of neoclassical transport with GENE, see ref. [33]. The radial $\mathbf{E} \times \mathbf{B}$ drift velocity, v_χ^r, is the advection mechanism responsible for turbulent transport,

$$v_\chi^r = \mathbf{v}_\chi \cdot \nabla x = -\frac{c}{C}\left(\frac{\partial \chi}{\partial y} + \frac{\gamma_2}{\gamma_1}\frac{\partial \chi}{\partial z}\right) \simeq -\frac{c}{C}\frac{\partial \chi}{\partial y} \equiv v_{\chi,y}^r.$$

It has been assumed that the $\partial\chi/\partial z$ term can be neglected due to the scale separation along and across the magnetic field. The transport can also be decomposed into an electrostatic and an electromagnetic part because the same separation property exists in the drift velocity,

$$v_{\chi,y}^r = \frac{1}{C}\left(- c\frac{\partial \phi}{\partial y} + v_\parallel \frac{\partial A_\parallel}{\partial y} + \mathbf{v}_\perp \cdot \frac{\partial \mathbf{A}_\perp}{\partial y}\right).$$

The turbulent transport fluxes can now be expressed more specifically,

$$\Gamma_a^{\text{turbulent}}(x) = \left\{ \int d^3v v_{\chi,y}^r f_a(\mathbf{x}, \mathbf{v}) \right\}$$

$$Q_a^{\text{turbulent}}(x) = \left\{ \int d^3v \frac{m_a}{2} v^2 v_{\chi,y}^r f_a(\mathbf{x}, \mathbf{v}) \right\}$$

$$\Pi_a^{\text{turbulent}}(x) = \left\{ \int d^3v m_a v_\parallel v_{\chi,y}^r f_a(\mathbf{x}, \mathbf{v}) \right\}.$$

In the absence of $B_\parallel$ fluctuations (this is not included in the global code version, for information on the implementation in the local code version, see ref. [33]) the transport

fluxes can be expressed in terms of the moments in Eq. 2.11,

$$\Gamma_a^{\text{turbulent}}(x) = \left\{ -\frac{c}{C}\frac{\partial \phi}{\partial y} M_{00,a} + \frac{1}{C}\frac{\partial A_\parallel}{\partial y} M_{10,a} \right\} \tag{2.13}$$

$$Q_a^{\text{turbulent}}(x) = \frac{m_a}{2}\left\{ -\frac{c}{C}\frac{\partial \phi}{\partial y}\big(M_{20,a} + M_{02,a}\big) + \frac{1}{C}\frac{\partial A_\parallel}{\partial y}\big(M_{30,a} + M_{12,a}\big) \right\} \tag{2.14}$$

$$\Pi_a^{\text{turbulent}}(x) = m_a\left\{ -\frac{c}{C}\frac{\partial \phi}{\partial y} M_{10,a} + \frac{1}{C}\frac{\partial A_\parallel}{\partial y} M_{20,a} \right\}. \tag{2.15}$$

The radial drift velocity can also be evaluated as $v_\chi^r = \mathbf{v}_\chi \cdot \nabla x/|\nabla x|$ as opposed to $v_\chi^r = \mathbf{v}_\chi \cdot \nabla x$ which has the benefit of removing the radial dependence of the integration element (and is the default option in GENE prerelease-1.6). This would modify the fluxes by an additional factor of $1/\sqrt{g^{xx}}$. However, evaluating the radial drift velocity as $v_\chi^r = \mathbf{v}_\chi \cdot \nabla x$ leads to a more relevant definition of the flux as far as the transport equations are concerned, and is the default option in the current version of the GENE code. This option can be changed with the norm_flux_projection parameter.

2.8 Normalization

Now that the fundamental equations and diagnostics have been derived, the next important step is normalization. This must be done prior to discretization because computers can only work with unitless quantities. All quantities can be normalized with appropriate combinations of 5 input terms with units that are specific to the discharge under investigation: A reference length scale, L_{ref}, a reference magnetic field strength, B_{ref}, a reference temperature, T_{ref}, a reference mass, m_{ref}, and a reference density, n_{ref}. With these five reference quantities, it is useful to derive the following constants:

$$c_{\text{ref}} = \sqrt{T_{\text{ref}}/m_{\text{ref}}} \qquad \Omega_{\text{ref}} = eB_{\text{ref}}/(cm_{\text{ref}}) \qquad \rho_{\text{ref}} = c_{\text{ref}}/\Omega_{\text{ref}}$$

$$\rho^*_{\rm ref} = \frac{\rho_{\rm ref}}{L_{\rm ref}} \qquad \beta_{\rm ref} = \frac{8\pi n_{\rm ref} T_{\rm ref}}{B^2_{\rm ref}} \qquad \nu_c = \frac{\pi e^4 n_{\rm ref} L_{\rm ref} \ln(\Lambda)}{2^{3/2} T^2_{\rm ref}}.$$

The constants $c_{\rm ref}$, $\Omega_{\rm ref}$, and $\rho_{\rm ref}$ define the scales for the sound speed, the cyclotron frequency, and gyroradius in the system. In addition, ρ^*, $\beta_{\rm ref}$, and ν_c are the three parameters in the normalized gyrokinetic equation that depend on the external reference quantities. Besides these three parameters, the reference quantities are only used for computing the diagnostics in meaningful units. The magnetic field, density, and temperature profiles are normalized as

$$B_0 = B_{\rm ref}\hat{B}_0(x) \qquad n_{0a} = n_{\rm ref}\hat{n}_{0a}(x_0)\hat{n}_{pa}(x) \qquad T_{0a} = T_{\rm ref}\hat{T}_{0a}(x_0)\hat{T}_{pa}(x).$$

The variables $\hat{n}_{0a}(x_0)$ and $\hat{T}_{0a}(x_0)$ are the normalized values at the center of the flux-tube, and $\hat{n}_{pa}(x)$ and $\hat{T}_{pa}(x)$ contain the profile dependence and vary with radial position. The reason the profiles are defined this way is so that GENE can more easily act as either a local or global code. The configuration space coordinates are normalized as

$$x = \rho_{\rm ref}\hat{x} \qquad y = \rho_{\rm ref}\hat{y} \qquad z = \hat{z}$$

$$k_x = \frac{1}{\rho_{\rm ref}}\hat{k}_x \qquad k_y = \frac{1}{\rho_{\rm ref}}\hat{k}_y.$$

Since x and y parameterize the region perpendicular to the magnetic field, it makes sense to normalize these coordinates with respect to the gyroradius. z is interpreted as a straight field-line angle, and considered unitless (the units are carried by the Jacobian). The magnetic field line geometry is normalized as

$$\gamma_1 = \hat{\gamma}_1 \qquad \gamma_2 = \frac{1}{L_{\rm ref}}\hat{\gamma}_2 \qquad \gamma_3 = \frac{1}{L_{\rm ref}}\hat{\gamma}_3$$

$$C = B_{\rm ref}\hat{C} \qquad \mathfrak{F} = L_{\rm ref}\hat{\mathfrak{J}}.$$

The normalization of the various parameters associated with the gyromotion is straightforward,

$$q_a = e\hat{q}_a \qquad m_a = m_{\rm ref}\hat{m}_a$$

$$\rho_a = \rho_{\rm ref}\hat{\rho}_a \qquad \Omega_a = \Omega_{\rm ref}\hat{\Omega}_a.$$

The velocity space is normalized with respect to the thermal velocity of a given species,

$$v_\parallel = c_{\rm ref}\sqrt{\frac{2\hat{T}_{0a}(x_0)}{\hat{m}_a}}\hat{v}_\parallel \qquad v_\perp = c_{\rm ref}\sqrt{\frac{2\hat{T}_{0a}(x_0)}{\hat{m}_a}}\hat{v}_\perp \qquad \mu = \frac{T_{\rm ref}}{B_{\rm ref}}\hat{T}_{0a}(x_0)\hat{\mu}.$$

The background distribution is normalized such that its velocity space integral provides the density. The perturbed distribution is normalized the same way, except that there is an additional $\rho_{\rm ref}/L_{\rm ref}$ factor due to the delta-f gyrokinetic ordering,

$$F_{0a} = \frac{n_{\rm ref}\hat{n}_{0a}(x_0)}{c_{\rm ref}^3\hat{v}_{Ta}^3(x_0)}\hat{F}_{0a} \qquad f_a = \frac{n_{\rm ref}\hat{n}_{0a}(x_0)}{c_{\rm ref}^3\hat{v}_{Ta}^3(x_0)}\frac{\rho_{\rm ref}}{L_{\rm ref}}\hat{f}_a.$$

Time is normalized as

$$t = \frac{L_{\rm ref}}{c_{\rm ref}}\hat{t} \qquad \frac{\partial f_a}{\partial t} = \frac{c_{\rm ref}}{L_{\rm ref}}\frac{n_{\rm ref}\hat{n}_{0a}(x_0)}{c_{\rm ref}^3\hat{v}_{Ta}^3(x_0)}\frac{\rho_{\rm ref}}{L_{\rm ref}}\hat{f}_a.$$

The velocity space integration elements are normalized with respect to the reference sound velocity and the thermal velocity,

$$\int d^3v\big(...\big) = \int d^3\hat{v}c_{\rm ref}^3\hat{v}_{Ta}^3(x_0)\big(...\big) = \int_0^\infty d\hat{\mu}\int_{-\infty}^\infty d\hat{v}_\parallel \pi\hat{B}_0\big(...\big).$$

The fields are normalized as

$$\phi = \frac{T_{\text{ref}}}{e}\frac{\rho_{\text{ref}}}{L_{\text{ref}}}\hat{\phi} \qquad A_{\parallel} = \rho_{\text{ref}} B_{\text{ref}} \frac{\rho_{\text{ref}}}{L_{\text{ref}}}\hat{A}_{\parallel} \qquad B_{\parallel} = B_{\text{ref}}\frac{\rho_{\text{ref}}}{L_{\text{ref}}}\hat{B}_{\parallel}.$$

The $\Gamma_{a,i}$'s defined in Eq. 2.9 are normalized as

$$\left(\Gamma_{a,x}, \Gamma_{a,y}, \Gamma_{a,z}\right) = \frac{n_{\text{ref}}\hat{n}_{0a}(x_0)}{c_{\text{ref}}^3 L_{\text{ref}}\hat{v}_{Ta}^3(x_0)}\left(\hat{\Gamma}_{a,x}, \hat{\Gamma}_{a,y}, \rho_{\text{ref}}\hat{\Gamma}_{a,z}\right).$$

And finally, $B_{0\parallel}^*$ is normalized as

$$\hat{B}_{0\parallel}^* = \hat{B}_0 + \beta_{\text{ref}}\sqrt{\frac{\hat{m}_a \hat{T}_{0a}(x_0)}{2}}\frac{\hat{j}_{0\parallel}\hat{v}_{\parallel}}{\hat{q}_a \hat{B}_0}.$$

Putting all of these terms together, the normalized gyrokinetic equation becomes

$$\frac{\partial \hat{f}_a}{\partial \hat{t}} = -\frac{1}{\hat{C}}\frac{\hat{B}_0}{\hat{B}_{0\parallel}^*}\left(\hat{\omega}_{na} + \hat{\omega}_{Ta}\left(\frac{\hat{v}_{\parallel}^2 + \hat{\mu}\hat{B}_0}{\hat{T}_{pa}} - \frac{3}{2}\right)\right)\hat{F}_{Ma}\frac{\partial \hat{\overline{\chi}}}{\partial \hat{y}}$$

$$-\frac{\hat{B}_0}{\hat{B}_{0\parallel}^*}\frac{\hat{T}_{0a}}{\hat{q}_a}\frac{2\hat{v}_{\parallel}^2 + \hat{\mu}\hat{B}_0}{\hat{B}_0}\hat{\kappa}_x\hat{\Gamma}_{a,x} - \frac{\hat{v}_{\parallel}}{\hat{T}_{0a}\hat{T}_{pa}}\frac{\partial \hat{\overline{A}}_{\parallel}}{\partial \hat{t}}\hat{F}_{Ma}$$

$$-\frac{\hat{B}_0}{\hat{B}_{0\parallel}^*}\frac{\hat{T}_{0a}}{\hat{q}_a\hat{B}_0}\left(\left(2\hat{v}_{\parallel}^2 + \hat{\mu}\hat{B}_0\right)\hat{\kappa}_y - \beta_{ref}\frac{\hat{v}_{\parallel}^2}{\hat{C}}\frac{\hat{p}_0}{\hat{B}_0}\hat{\omega}_{pa}\right)\hat{\Gamma}_{a,y}$$

$$-\sqrt{\frac{2\hat{T}_{0a}}{\hat{m}_a}}\frac{\hat{C}}{\hat{\mathfrak{J}}\hat{B}_0}\left(\hat{v}_{\parallel}\hat{\Gamma}_{a,z} - \frac{\hat{\mu}}{2}\frac{\partial \hat{B}_0}{\partial \hat{z}}\frac{\partial \hat{f}_a}{\partial \hat{v}_{\parallel}}\right)$$

$$+\frac{\hat{B}_0}{\hat{B}_{0\parallel}^*}\frac{\hat{T}_{0a}}{\hat{q}_a}\frac{2\hat{v}_{\parallel}^2 + \hat{\mu}\hat{B}_0}{\hat{B}_0}\hat{\kappa}_x\left(\hat{\omega}_{na} + \hat{\omega}_{Ta}\left(\frac{\hat{v}_{\parallel}^2 + \hat{\mu}\hat{B}_0}{\hat{T}_{pa}} - \frac{3}{2}\right)\right)\hat{F}_{Ma}$$

$$-\frac{\hat{B}_0}{\hat{C}\hat{B}_{0\parallel}^*}\left(\frac{\partial \hat{\overline{\chi}}}{\partial \hat{x}}\hat{\Gamma}_{a,y} - \frac{\partial \hat{\overline{\chi}}}{\partial \hat{y}}\hat{\Gamma}_{a,x}\right).$$

Where the normalized logarithmic gradients are defined as

$$\hat{\omega}_{na} = -\frac{L_{\text{ref}}}{n_a(x)}\frac{\partial n_a(x)}{\partial x} \qquad \hat{\omega}_{Ta} = -\frac{L_{\text{ref}}}{T_a(x)}\frac{\partial T_a(x)}{\partial x} \qquad \hat{\omega}_{pa} = -\frac{L_{\text{ref}}}{p_{0a}(x)}\frac{\partial p_{0a}(x)}{\partial x}.$$

And normalized curvature terms have also been defined for convenience,

$$\hat{\kappa}_x = -\frac{1}{\hat{C}}\frac{L_{\text{ref}}}{B_{\text{ref}}}\left(\frac{\partial B_0}{\partial y} + \frac{\gamma_2}{\gamma_1}\frac{\partial B_0}{\partial z}\right) \qquad \hat{\kappa}_y = \frac{1}{\hat{C}}\frac{L_{\text{ref}}}{B_{\text{ref}}}\left(\frac{\partial B_0}{\partial x} - \frac{\gamma_3}{\gamma_1}\frac{\partial B_0}{\partial z}\right).$$

The normalized gyrokinetic Poisson equation is given by

$$\hat{\lambda}_D^2\hat{\nabla}_\perp^2\hat{\phi} - \pi\sum_a \frac{\hat{q}_a^2\hat{n}_{0a}}{\hat{T}_{0a}}\int d\hat{v}_\parallel d\hat{\mu}\left(\hat{\phi}\hat{B}_0\frac{\hat{F}_{Ma}}{\hat{T}_{pa}} - \left\langle\hat{\bar{\phi}}\hat{B}_0\frac{\hat{F}_{Ma}}{\hat{T}_{pa}}\right\rangle\right)$$

$$= -\pi\sum_a \hat{q}_a\hat{n}_{0a}\int d\hat{v}_\parallel d\hat{\mu}\left(\left\langle\hat{B}_0\hat{f}_a\right\rangle + \hat{\mu}\left\langle\hat{\bar{B}}_\parallel\hat{B}_0\frac{\hat{F}_{Ma}}{\hat{T}_{pa}}\right\rangle\right),$$

where the normalized Debye length is defined as

$$\hat{\lambda}_D = \frac{\lambda_D}{\rho_{\text{ref}}} = \frac{B_{\text{ref}}}{\sqrt{4\pi n_{\text{ref}} m_{\text{ref}} c^2}}.$$

Similarly, the normalized perpendicular Ampére law is given by

$$\hat{\nabla}_\perp^2\hat{A}_\parallel = -\frac{\pi\beta_{\text{ref}}}{2}\sum_a \hat{q}_a\hat{n}_{0a}\sqrt{\frac{2\hat{T}_{0a}}{\hat{m}_a}}\int d\hat{v}_\parallel d\hat{\mu}\hat{v}_\parallel\left\langle\hat{B}_0\hat{f}_a\right\rangle,$$

and the normalized parallel Ampére law is given by

$$\frac{\partial\hat{B}_\parallel}{\partial\hat{y}}\hat{\mathbf{x}} - \frac{\partial\hat{B}_\parallel}{\partial\hat{x}}\hat{\mathbf{y}} =$$

$$\frac{\pi\beta_{\text{ref}}}{2}\sum_a \hat{q}_a\hat{n}_{0a}\sqrt{\frac{2\hat{T}_{0a}}{\hat{m}_a}}\int d\hat{v}_\parallel d\hat{\mu}\sqrt{\hat{\mu}}\left(\left\langle\hat{\mathbf{v}}_\perp\hat{B}_0^{3/2}\hat{f}_a\right\rangle + \left\langle\hat{\mathbf{v}}_\perp\hat{B}_0^{3/2}\frac{\hat{q}_a\hat{F}_{Ma}}{\hat{T}_{0a}\hat{T}_{pa}}\hat{\phi}\right\rangle\right)$$

$$+\frac{\pi\beta_{\rm ref}}{2}\sum_a \hat{q}_a\hat{n}_{0a}\sqrt{\frac{2\hat{T}_{0a}}{\hat{m}_a}}\int d\hat{v}_\parallel d\hat{\mu}\sqrt{\hat{\mu}}\Big\langle \hat{\mathbf{v}}_\perp \hat{B}_0^{3/2}\hat{\mu}\hat{\overline{B}}_\parallel\frac{\hat{F}_{Ma}}{\hat{T}_{pa}}\Big\rangle.$$

Finally, the transport quantities are normalized with respect to gyrobohm units, which are computed from the reference units,

$$\Gamma_{GB}=n_{\rm ref}c_{\rm ref}\left(\frac{\rho_{\rm ref}}{L_{\rm ref}}\right)^2 \qquad Q_{GB}=n_{\rm ref}T_{\rm ref}c_{\rm ref}\left(\frac{\rho_{\rm ref}}{L_{\rm ref}}\right)^2 \qquad \Pi_{GB}=n_{\rm ref}m_{\rm ref}\left(\frac{c_{\rm ref}\rho_{\rm ref}}{L_{\rm ref}}\right)^2$$

$$\frac{\Gamma_a^{\rm turbulent}(x)}{\Gamma_{GB}}=\hat{n}_{0a}\Big\{-\frac{1}{\hat{C}}\frac{\partial\hat{\phi}}{\partial\hat{y}}\hat{M}_{00,a}+\frac{\sqrt{2\hat{T}_{0a}/\hat{m}_a}}{\hat{C}}\frac{\partial\hat{A}_\parallel}{\partial\hat{y}}\hat{M}_{10,a}\Big\}$$

$$\frac{Q_a^{\rm turbulent}(x)}{Q_{GB}}=-\hat{n}_{0a}\hat{T}_{0a}\Big\{\frac{1}{\hat{C}}\frac{\partial\hat{\phi}}{\partial\hat{y}}\big(\hat{M}_{20,a}+\hat{M}_{02,a}\big)-\frac{\sqrt{2\hat{T}_{0a}/\hat{m}_a}}{\hat{C}}\frac{\partial\hat{A}_\parallel}{\partial\hat{y}}\big(\hat{M}_{30,a}+\hat{M}_{12,a}\big)\Big\}$$

$$\frac{\Pi_a^{\rm turbulent}(x)}{\Pi_{GB}}=\hat{n}_{0a}\hat{m}_a\sqrt{\frac{2\hat{T}_{0a}}{\hat{m}_a}}\Big\{-\frac{1}{\hat{C}}\frac{\partial\hat{\phi}}{\partial\hat{y}}\hat{M}_{10,a}+\frac{\sqrt{2\hat{T}_{0a}/\hat{m}_a}}{\hat{C}}\frac{\partial\hat{A}_\parallel}{\partial\hat{y}}\hat{M}_{20,a}\Big\}.$$

2.9 Boundary conditions

With the fundamental integro-differential equations given, the only remaining step before discretization is to provide boundary conditions in each of the five phase space dimensions. Starting with configuration space, the flux-tube coordinates (x,y,z) can be written in terms of the traditional toroidal coordinates $(\rho_{\rm tor},\Psi,\theta)$,

$$x=\rho_{\rm tor} \qquad y=C_y\big(q(\rho_{\rm tor})\theta-\Psi\big) \qquad z=\theta, \tag{2.16}$$

where $\rho_{\rm tor}$ is the flux surface label, Ψ is the toroidal angle, θ is the straight field line angle, and C_y is a constant length given by $C_y=\rho_0/q_0$, where ρ_0 is the radial position and q_0

is the safety factor at the center of the radial domain. These coordinate expressions shall make it easier to derive the appropriate boundary conditions in flux-tube coordinates. The boundary conditions for each coordinate shall be summarized in turn.

2.9.1 Binormal coordinate

The distribution function and the fields are periodic in the toroidal angle, Ψ. Using Eq. 2.16, this translates to the periodicity condition,

$$f(\rho_{\mathrm{tor}}, \Psi, \theta) = f(\rho_{\mathrm{tor}}, \Psi + 2\pi, \theta) \rightarrow f(x, y, z) = f(x, y - 2\pi C_y, z).$$

The velocity space coordinates in the above expression have been excluded for convenience. While this condition enforces periodicity across the entire toroidal domain of the tokamak ($2\pi C_y$), in most cases, the turbulent correlation lengths are much smaller than the device size. It is desirable to enforce periodicity over a smaller domain ($2\pi C_y/n_0$) to avoid having to resolve small wavenumbers. Therefore, the periodicity constraint is the binormal boundary condition,

$$L_y = \frac{2\pi C_y}{n_0} \qquad f(x, y, z) = f(x, y - L_y, z),$$

where n_0 denotes the minimum integer toroidal mode number in a simulation. Because of the periodic boundary conditions, the binormal coordinate is evaluated in Fourier space for both the local and x-global code versions,

$$f(x, y, z) = \sum_{k_y} f(x, k_y, z) e^{i k_y y}.$$

The toroidal modes in a GENE simulation are all integer multiples of the minimum toroidal wavenumber,

$$k_y = m k_{y,\mathrm{min}} = m \frac{2\pi}{L_y} = \frac{m n_0}{C_y} \qquad m = 0, 1, ..., n_{k_y} - 1.$$

2.9.2 Radial coordinate

The boundary conditions for the radial coordinate are different depending on whether the local or global code version is utilized. In the local code version, a thin annulus of the plasma is simulated at a particular radial position. It is assumed that the profiles and their gradients are constant across the radial domain, and the boundary condition is periodic with the radial box size set by the user to resolve the turbulent structures. Since the boundary conditions are periodic, the radial direction is resolved in Fourier space. This simplifies the field equations and the gyroaveraging dramatically.

In the global code version, a larger radial section of the device can be simulated, and the radial variations of the temperature, density, safety factor, and magnetic field geometry can be taken into account. The only limitation is that the very center of the device, as well as the separatrix cannot be simulated as the field aligned coordinate system becomes singular there. The most commonly used boundary condition for the global code is the Dirichlet boundary condition, where the perturbed distribution function and fields are set to zero outside of the radial domain. There is also the option of using a Neumann boundary condition, which is the same as the Dirichlet boundary condition, except that the flux-surface averaged distribution function is allowed to have a finite value at the inner surface, so long as the derivative of the flux-surface average is zero. In addition, Krook-type buffer zones exist near the boundaries, where the distribution is damped by Krook terms in an attempt to smooth the transition of the distribution to zero at the Dirichlet boundaries.

2.9.3 Parallel coordinate

The distribution and fields are periodic in the straight field line angle as well, which translates to the following boundary condition in the flux-tube coordinates (from Eq. 2.16):

$$f(\rho_{\text{tor}}, \Psi, \theta) = f(\rho_{\text{tor}}, \Psi, \theta + 2\pi) \rightarrow f(x, y, z) = f(x, y + 2\pi q C_y, z + 2\pi).$$

Since the binormal direction is evaluated in Fourier space, a Fourier decomposition must be utilized,

$$f(x,y,z) = \sum_{k_y} f(x,k_y,z)e^{ik_y y} = \sum_{k_y} f(x,k_y,z+2\pi)e^{ik_y(y+2\pi q C_y)}.$$

So the parallel boundary condition can be expressed as

$$f(x,k_y,z) = f(x,k_y,z+2\pi)\exp(i2\pi m n_0 q(x)).$$

This shifted periodic boundary condition is utilized in the global code version. However, it must be modified for the local code version since the full safety factor profile is not accessible through a local simulation. This problem can be mitigated by Taylor expanding the safety factor profile,

$$q(x) \simeq q_0 + \frac{\partial q}{\partial x} = q_0\left(1 + \frac{x-x_0}{x_0}\hat{s}\right),$$

where the local shear factor is defined as

$$\hat{s} = \frac{x_0}{q_0}\frac{\partial q}{\partial x}.$$

To derive the suitable parallel boundary condition for the local flux-tube model, the distribution must be Fourier decomposed in the radial coordinate, and the local expansion of the safety factor must be utilized,

$$f(x,k_y,z) = \sum_{k_x} f(k_x,k_y,z)\exp(ik_x x)$$

$$= \sum_{k_x} f(k_x,k_y,z+2\pi)\exp(ik_x x)\exp(i2\pi m n_0 \hat{s}(x-x_0)/C_y)\exp(i2\pi m n_0 q_0).$$

Assuming all modes are summed over, each k_x value in the summation can be shifted: $k_x \rightarrow k_x - 2\pi m n_0 \hat{s}/C_y$. The boundary condition can then be obtained by matching the

coefficients in $\exp(ik_x x)$,

$$f(k_x, k_y, z) = f(k_x - 2\pi m n_0 \hat{s}/C_y, k_y, z + 2\pi) \exp\left(i2\pi m n_0 (q_0 - x_0 \hat{s}/C_y)\right).$$

In addition to requiring a phase shift in the boundary condition, different k_x modes must also be accessed. In order for these modes to be accessed, the following k_x modes must be present in the simulation,

$$k_x' = k_x - 2\pi \hat{s} k_y,$$

where the definition of $k_y = m n_0 / C_y$ has been utilized. This condition can be met by ensuring that each $2\pi \hat{s} k_y$ is an integer multiple of some k_x present in the system. This places the following constraint on local flux-tube simulations:

$$k_{x,\min} = 2\pi \frac{\hat{s} k_{y,\min}}{N},$$

where N is some integer value greater than or equal to one. Using the definition of the perpendicular wave numbers in terms of the size of the radial and binormal domains leads to a constraint on the radial domain size in terms of the binormal domain size,

$$N = 2\pi \hat{s} L_x / L_y.$$

The radial domain is always adjusted to meet this quantization condition.

2.9.4 Velocity coordinates

The velocity space of the distribution function is typically resolved on a grid which goes from -3 to 3 in $\hat{v}_\parallel$, and from 0 to 9 in $\widehat{\mu}$ (however, this domain is adjustable by the user). The perturbed distribution function is assumed to go to zero outside of this domain, so Dirichlet boundary conditions are used.

2.10 Numerical implementation

Now that the normalized equations have been obtained, the only remaining step before code implementation is the numerical discretization of the underlying equations. In this section, the discussion of discretization shall be divided by the different coordinates in the equations. The discussion of the discretization applied to the collision operator shall be deferred until chapter 3.

2.10.1 Time

The delta-f gyrokinetic equation can be written as

$$\frac{\partial f}{\partial t} = L\{f\} + N\{f\} + K_0,$$

where in the above expression, L denotes the linear terms in the equation, N denotes the nonlinear term, and K_0 denotes the constant terms that exist independent of the perturbation. GENE can be used as a nonlinear initial value solver, a linear initial value solver, a linear eigenvalue solver, or as a neoclassical solver.

When operating as a linear solver, only a single k_y mode is typically chosen at a time (the different toroidal modes only interact with each other through the nonlinearity). This makes the linear simulations more computationally affordable due to optimal time-stepping and allows one to get a sense of the different microinstabilities present at different toroidal mode numbers in the system for both the local and global code versions. The linear solver can act as an initial value solver, or as an eigenvalue solver. When acting as an initial value solver, the perturbation is initialized to a particular distribution (typically a Maxwellian uniform across configuration space) and advanced in time using a fourth order Runge-Kutta scheme (with a separate explicit time-stepping scheme applied to the collision operator, to be discussed in chapter 3) in accordance with the linear terms. Eventually, the system will evolve into one mode which grows exponentially in time with a particular frequency and growth rate (the largest growth rate in the system). The configuration and velocity

space structure of the mode can then be examined and used to identify and characterize the dominant mode. Since all of the terms are linear, the maximum possible time step that can be used to evolve the system can be calculated from the spectra of the linear operator. When operating as an eigenvalue solver, the system is not evolved in time using an explicit time-stepping scheme. Rather, all of the linear terms are grouped together as a matrix, and then the system is analyzed to determine the eigenvalue with the largest growth rate of the system and its associated eigenvector. The eigenvalue corresponds to the growth rate and frequency and the eigenvector corresponds to the mode structure of the dominant mode in the system. However, such an approach can also be utilized to determine the subdominant modes in the system, which is useful because sometimes subdominant instabilities can play a large role in the nonlinear dynamics. The neoclassical solver can also act as either an initial value or eigenvalue solver. The only difference is that for the neoclassical case, only the zeroth toroidal mode number can be considered and an additional term proportional to F_{0a} is considered (which is neglected in local simulations, because it can be considered part of the neoclassical transport). The topic of neoclassical transport is beyond the scope of this thesis. For more information on utilizing GENE as a neoclassical code, see refs. [34, 33].

The nonlinear initial value solver operates in the same way as the linear initial value solver, except that rather than evolving into an exponentially increasing mode, the system saturates at a particular level of transport via the perpendicular nonlinearity (or potentially, if activated, the parallel nonlinearity). In addition, the maximum possible time-step cannot be directly calculated from the linear terms. Rather, the linear time-step limit is taken as an estimate, and it is then adjusted based on an estimate from the advection velocity of the nonlinearity to meet the Courant-Friedrichs-Lewy time-step limit. For more information, see ref. [35].

2.10.2 Magnetic moment

In the collisionless limit, there are no derivatives of μ since it is a conserved quantity in the gyrokinetic equation. Therefore, the only numerical error that comes from discretizing μ is

integration error when the electromagnetic fields are computed. The best way to minimize this type of error is to use a Gauss-Laguerre grid for the points in the μ domain. With this discretization, the number of points in the magnetic moment can be typically be confined to between 8 and 16 points. This situation changes when collisions are present, as will be discussed in the next chapter.

2.10.3 Parallel configuration and parallel velocity space

The parts of the gyrokinetic equation that contain the z and $v_\parallel$ derivatives are given by

$$\left(\frac{\partial f_a}{\partial t}\right)_{z,v_\parallel} = -\frac{C v_\parallel}{\mathfrak{J} B_0}\left(\frac{\partial f_a}{\partial z} + \frac{e F_{Ma}}{T_{0a}}\frac{\partial \overline{\chi}}{\partial z}\right) + \frac{\mu C}{m_a \mathfrak{J} B_0}\frac{\partial B_0}{\partial z}\frac{\partial f_a}{\partial v_\parallel}.$$

These derivatives can be analyzed with a fourth order finite difference stencil. However, an alternative discretization can be utilized by rewriting the equations using the definitions of the non-adiabatic part of the distribution function, h_a, and the unperturbed Hamiltonian, H_0,

$$h_a = f_a + \frac{e\overline{\phi}}{T_{0a}}F_{Ma} + \frac{\mu \overline{B}_\parallel}{T_{0a}}F_{Ma}$$

$$H_0 = \frac{1}{2}m_a v_\parallel^2 + \mu B_0.$$

With these definitions, the relevant part of the gyrokinetic equation can be expressed in terms of a Poisson bracket between the Hamiltonian and non-adiabatic part of the distribution function,

$$\left(\frac{\partial f_a}{\partial t}\right)_{z,v_\parallel} = -\frac{C}{\mathfrak{J} B_0}\frac{1}{m_a}\frac{\partial H_0}{\partial v_\parallel}\frac{\partial h_a}{\partial z} + \frac{C}{m_a \mathfrak{J} B_0}\frac{\partial H_0}{\partial z}\frac{\partial h_a}{\partial v_\parallel} = \frac{C}{m_a \mathfrak{J} B_0}\left\{H_0, h_a\right\}_{z,v_\parallel},$$

where the 2D Poisson bracket is defined as

$$\left\{H_0, h_a\right\}_{z,v_\parallel} = \frac{\partial H_0}{\partial z}\frac{\partial h_a}{\partial v_\parallel} - \frac{\partial H_0}{\partial v_\parallel}\frac{\partial h_a}{\partial z}.$$

The Poisson bracket has many conservation properties which can be satisfied numerically with an Arakawa discretization scheme. One of the most desirable conservation properties is the conservation of free energy, F, with the free energy defined as

$$F = \int dz dv_\parallel \frac{h_a^*}{F_{Ma}}\frac{\partial f_a}{\partial t}.$$

The free energy associated with this term can be conserved to machine precision by expressing it in the following way and applying an Arakawa discretization scheme [36]:

$$\frac{\partial f_a}{\partial t} = \frac{T_{oa} C F_{Ma}}{m_a \mathfrak{J} B_0}\left\{\frac{1}{F_{Ma}}, h_a\right\}_{z,v_\parallel}.$$

There are two different options for the parallel configuration and velocity space discretization in GENE. One could use simple fourth order finite difference schemes or a fourth order Arakawa scheme which conserves free energy to machine precision. The default implementation is the Arakawa scheme. This is almost always used for the local code version. However, it has been found for the global code version that in some cases a higher resolution is needed for the Arakawa scheme.

2.10.4 Perpendicular configuration space

The discretization of the x and y coordinates are different depending on whether the local or global version of the GENE code is being utilized. For the linear terms in the gyrokinetic equation, the derivatives in the y coordinate are represented in Fourier space and correspond to multiplication by the binormal wavenumber. An analogous procedure is done for the x coordinate in the local code version. For the global code version, the linear terms with x-derivatives are analyzed with fourth order centered finite difference schemes. The field equations are also evaluated differently for the local and global code versions. For the local code version, the derivatives are replaced with a simple multiplication by the wavenumbers,

and the gyroaverage operator simplifies to a multiplication by a Bessel function, as will be demonstrated shortly. For the local code version, the fields can be solved for algebraically. For the global code version, a matrix with $n_x * n_x$ entries must be constructed for each y and z coordinate. This matrix is then LU-factored in the initialization phase and solved for every timestep in the simulation.

In order to solve for the fields and the gyrokinetic equation, a numerical implementation of the gyroaveraging procedure must be provided. This is a straightforward procedure for the local flux-tube version of the code. To determine the local gyroaverage operator, one must first write the distribution to be gyroaveraged in Fourier space,

$$\psi(\mathbf{x}_\perp, z, v_\parallel, \mu) = \int d^2k_\perp e^{i\mathbf{k}_\perp \cdot \mathbf{x}_\perp} \psi(\mathbf{k}_\perp, z, v_\parallel, \mu).$$

Using this representation, the gyroaverage operator, Eq. 2.2, can be represented as

$$\int d^2k_\perp e^{i\mathbf{k}_\perp \cdot \mathbf{x}_\perp} \overline{\psi}(\mathbf{k}_\perp, z, v_\parallel, \mu) = \int d^2k_\perp e^{i\mathbf{k}_\perp \cdot \mathbf{x}_\perp} \frac{1}{2\pi} \int d\theta e^{i\mathbf{k}_\perp \cdot \rho_a} \psi(\mathbf{k}_\perp, z, v_\parallel, \mu).$$

The following Bessel function identity (and the orthogonality property of trigonometric functions) is useful for constructing the gyroaverage operator:

$$e^{iz\cos(\theta)} = J_0(z) + 2\sum_{n=1}^{\infty} i^n J_n(z)\cos(n\theta).$$

It is then easy to see that the gyroaverage operation in Fourier space simply corresponds to multiplication by a Bessel function,

$$\overline{\psi}(\mathbf{k}_\perp, z, v_\parallel, \mu) = J_0(k_\perp \rho_a)\psi(\mathbf{k}_\perp, z, v_\parallel, \mu).$$

The other gyroaverage operator, Eq. 2.12, can be derived for the local code in a similar way,

$$\langle \psi \rangle(\mathbf{k}_\perp, z, v_\parallel, \mu) = J_0(k_\perp \rho_a)\psi(\mathbf{k}_\perp, z, v_\parallel, \mu).$$

The gyroaveraging procedure for the global code version is more complicated. To facilitate

this implementation, the distribution to be gyroaveraged is interpolated from a finite element basis,

$$\psi(x) = \sum_m \psi(x_m)\Lambda_m(x) = \sum_m \psi_m \Lambda_m(x). \tag{2.17}$$

The ψ_m values form a vector with a length given by the x resolution,

$$\psi = (\psi(x_1), ..., \psi(x_n))^T.$$

Plugging Eq. 2.17 into Eq. 2.2, the expression for the gyroaverage operator is obtained,

$$\overline{\psi}(X_m, Y, z, v_\parallel, \mu) = \frac{1}{2\pi}\int d\theta \sum_{n,k_y} e^{ik_y(Y+\rho_y)}\psi_n \Lambda_n(X_m + \rho_x).$$

This can be written in a matrix form,

$$\overline{\psi}(X_m, Y, z, v_\parallel, \mu) = \sum_n G_{mn}\psi_n e^{ik_y Y}$$

$$\overline{\psi} = \sum_{ky} e^{ik_y Y}\overleftrightarrow{\mathbf{G}} \cdot \psi,$$

where the gyroaverage matrix, $\overleftrightarrow{\mathbf{G}}$, is given in index notation as

$$G_{mn}(k_y, z, \mu) = \frac{1}{2\pi}\int d\theta e^{ik_y\rho_y}\Lambda_n(X_m + \rho_x).$$

The gyroaverage operator contains no information about the fields or perturbed distribution function, so it can be constructed in the initialization phase of the simulation. The alternative gyroaverage operator that is needed for the construction of the field solver can be expressed as

$$\langle\psi\rangle(x_m, y, z) = \frac{1}{2\pi}\int d^3X d\theta \delta(\mathbf{X} - (\mathbf{x}_m - \rho)) \sum_{m,k_y} e^{ik_y Y}\psi_m \Lambda_m(X),$$

which can be written in a matrix form,

$$\langle \psi \rangle = \sum_{k_y} e^{ik_y y} \overleftrightarrow{\mathbf{G}}^{\text{alt}} \cdot \psi$$

$$G^{\text{alt}}_{mn}(k_y, z, \mu) = \frac{1}{2\pi} \int d\theta e^{-ik_y \rho_y} \Lambda_n(x_m - \rho_x).$$

The details and properties of the finite element basis shall not be discussed here. See ref. [27] for more information on that topic. What is worth noting, however, is that it can be shown that the other gyroaverage matrix needed for the field solver is the adjoint of the original gyroaverage matrix discussed,

$$\overleftrightarrow{\mathbf{G}}^{\text{alt}} = \overleftrightarrow{\mathbf{G}}^{\dagger}.$$

Therefore, only one gyroaverage matrix and its adjoint need be considered. The two gyroaveraging procedures are discretized as

$$\overline{\psi}(X, k_y, z) = \overleftrightarrow{\mathbf{G}} \cdot \psi$$

$$\langle \psi \rangle (x, k_y, z) = \overleftrightarrow{\mathbf{G}}^{\dagger} \cdot \psi.$$

Besides the linear terms and the field solver, the perpendicular nonlinearity also deserves special consideration. The perpendicular nonlinearity of the gyrokinetic equation is expressed as

$$\left(\frac{\partial f_a}{\partial t} \right) \Big|_{\text{nonlin}} = -\frac{c}{C} \frac{B_0}{B^*_{0\|}} \left(\frac{\partial \overline{\chi}}{\partial x} \Gamma_{a,y} - \frac{\partial \overline{\chi}}{\partial y} \Gamma_{a,x} \right).$$

This can be written in a Poisson bracket formalism in the xy space,

$$\left(\frac{\partial f_a}{\partial t}\right)\Big|_{\text{nonlin}} = -\frac{c}{C}\frac{B_0}{B_{0\|}^*}\left(\{\overline{\chi}, f_a\}_{x,y} + \frac{q_a F_{Ma}}{T_{0a}}\{\overline{\chi}, \overline{\phi}\}_{x,y}\right).$$

In the current version of the code, only a single Poisson bracket is used on the gyrokinetic potential, χ, and a modified distribution defined as

$$g_a = f_a + \frac{q_a v_\|}{c}\frac{F_{Ma}}{T_{0a}}\overline{A}_\|.$$

However, this method of analyzing the nonlinearity can lead to numerical difficulties in the nonlinear electromagnetic global version of the code, as will be discussed in chapter 5. A fast Fourier transform (FFT) is performed on the x and y coordinate to evaluate the nonlinearity in the local code version. An FFT is performed on the y coordinate in the global version of the code. Dealiasing accompanies each FFT procedure, and an Arakawa discretization is utilized for evaluating the nonlinearity. This ensures conservation of free energy. For more information on how the nonlinearity is evaluated, see ref. [26].

2.10.5 Hyperdiffusion

Due to the use of finite difference and Arakawa schemes for the numerical evaluation of derivatives, grid-scale oscillations can be present and sometimes cause numerical instabilities. To mitigate this problem, hyperdiffusion terms in the form of finite difference stencils of fourth order derivatives with second order accuracy in the x, y, z, and $v_\|$ dimensions have been implemented [37]. Hyperdiffusion values are set to be high enough to eliminate the grid-scale oscillations, but low enough to have minimal effects on the turbulent dynamics. In the case where the collision operator is active, the hyperdiffusion on $v_\|$ is excluded, since grid scale oscillations in that coordinate would be destroyed by the collisional dissipation. There is also an alternative model called GyroLES which is implemented in GENE and which is designed to mimic the effect of sub-grid scales on the resolved scales and eliminate the need for hyperdiffusion in y [38]. The choice of using hyperdiffusion for that component or GyroLES is left up to the user.

2.11 Chapter summary

In this chapter, the foundations of gyrokinetics have been discussed, and the set of integro-differential equations implemented in the GENE code has been derived starting from the full-f gyrokinetic Vlasov equations. Diagnostic quantities, boundary conditions, and discretization schemes have also been analyzed. However, one important aspect has been left out: Collisional dissipation. This shall be the topic of the next chapter.

CHAPTER 3

Collision operators in delta-f gyrokinetic codes

3.1 The need for including collisions

Any realistic simulation of plasma turbulence near the edge of fusion devices such as tokamaks or stellarators must include more than just the collective motion of particles and the evolution of the electromagnetic fields based on the Maxwell equations. To more realistically model the plasma behavior, one must include discrete particle effects, where the ions and electrons occasionally interact with each other, and not just the fields arising from the bulk motion of particles. These effects act as an important sink of free energy (in the collisionless gyrokinetic equations, free energy is conserved) and contribute to the dampening/growth of certain plasma instabilities. In particular, collisions become more important as one arrives closer to the edge. If particles are at a high enough temperature, then at the point when they cross near each other they typically go by at a high enough speed that they have little time for the interactions to play much of a role. This is not always the case when one encounters lower temperatures and the collisional cross section is higher. For this reason, a collision operator which models the physics of such interactions has been implemented in the GENE code to study plasma turbulence and transport, especially in the edge.

Many different collision operators have been derived in the literature for use with gyrokinetic models [14, 39, 40, 41, 42, 43, 44]. Different codes may use different collision operators depending on whether they are delta-f/full-f and Eulerian/Lagrangian/semi-Lagrangian codes. A full-f code evolves the full distribution rather than a small perturbation, and a typical form of the collision operator utilized for such a task is the nonlinear Landau collision operator. This model is utilized in the XGC code for full-f collisional simulations [45]

with a second-order finite-volume scheme and a particle-mesh interpolator, and evolved in time with an implicit Picard iteration scheme. While this full-f collision model is complete, it is also highly expensive due to the nonlinear and nonlocal nature of the full Landau collision operator. A linearized full-f collision model has been derived in Estéve et al. [46] and implemented in the semi-Lagrangian GYSELA code with a numerical scheme described in [47]. This model has the benefit of being more computationally tractable. The gyrokinetic code, COGENT, which is used specifically for the study of plasma dynamics in the edge, has the option of using several different collision operators, including a drag/diffusion operator in parallel velocity space, a pitch-angle scattering operator, and a linearized Fokker-Planck operator [48]. A fully nonlinear Fokker-Planck operator has also been implemented in the COGENT code, where the Rosenbluth potentials are computed with a finite-difference scheme and multipole-expansion boundary conditions [49].

In delta-f gyrokinetic models, the full distribution is split into a background part and a perturbed part, and the perturbation is evolved in time. The collision operator must then take a different form. The typical model used for this purpose is a linearized Fokker-Planck collision operator to represent the perturbation scattering off of the background, as well as a back reaction term which is used to conserve momentum and energy. A more crude model for the back reaction term is typically utilized to avoid the more complicated convolution integral. This type of model is implemented in the grid-based GKW [50] and GS2 [51] codes. This type of model has also been implemented in the particle-in-cell code, ORB5 [52]. This is done by using random kicks in velocity space to represent the diffusion process, while altering the weights of the marker particles to preserve conservation properties. The GKV code utilizes the collision model developed by Sugama et al. [14]. The Sugama model is the same as the linearized Fokker-Planck model, except that the nonisothermal term in the linearized operator is replaced with a model term which ensures that the collision operator satisfies an appropriate H-theorem in the nonisothermal limit, whereas the linearized Fokker-Planck operator satisfies an H-theorem only in the isothermal case. The Sugama collision model in the GKV code is based on a sixth-order finite difference scheme for a grid-based code [53]. The Sugama model has also been implemented as a pseudospectral operator in

the CGYRO code [54]. In addition to modifications allowing for nonisothermal background profiles, a linearized collision operator allowing for shifted Maxwellian backgrounds with different parallel flows has been implemented in the LOKI code to study the dynamics of interpenetrating plasma streams [55].

Earlier collisional models have been incorporated into GENE [33, 56] such as a Krook model, a pitch-angle scattering operator, and most importantly, a linearized Landau-Boltzmann operator. The standard collision operator included a linearized Landau-Boltzmann operator and a model back-reaction term which was responsible for the conservation of momentum and energy. However, the standard collision operator in use did not analytically satisfy an H-theorem for nonisothermal parameters, did not numerically dissipate free energy for all grid resolutions, did not incorporate FLR corrections into the field-particle part of the collision operator, was not tested for relaxation of flow and temperature fluctuations, and was not adequately benchmarked. The current work in this thesis makes such extensions to the collision operator (except for the extension of FLR corrections in the global version of the code, which is yet to be done).

GENE is a delta-f grid-based code and the collision operator implemented in GENE is based on the model derived by Sugama et al. [14]. This model satisfies appropriate conservation and free energy dissipation properties, and has been adapted for both the local and x-global gyrokinetic model (including with the block-structured grid numerical scheme). The adaptation of the model to the 3D version of GENE shall be left for future work. Also, while FLR corrections have been implemented in the collision operator for the local code version, this is still a work in progress for the global code version. The model contains no velocity-space convolution integrals, and its linear nature allows for optimized time-stepping schemes. Furthermore, the use of the local flux-tube approximation, as well as the recently developed block-structured velocity space grids [57, 58] for the global version of the code, allow for the capability of collisional gyrokinetic simulations without the need for large velocity space resolution. The amount of physics contained within the operator (pitch-angle scattering, energy diffusion, FLR corrections, etc.), as well as its good numerical properties (particle, momentum, and energy conservation, as well as free energy dissipation) and

computational tractability allow for unique, cutting-edge simulations exploring collisional plasma turbulence in the edge.

This chapter is outlined in the following way: First, the general Landau-Boltzmann collision operator is discussed in subsection 3.2. Then, the standard linearized collision operator is derived from the full Landau-Boltzmann operator in subsection 3.3. Then the problems with free energy dissipation in the nonisothermal limit is explained in section 3.4. Afterwards, a proposed solution to the problem is given for the simplified case of ion-electron collisions in section 3.5. Such an operator is generalized to the case of multiple species in section 3.6. This is the same approach that was originally developed by Sugama et al. [14]. Then it is shown that such an operator analytically satisfies the H-theorem in section 3.7. Following that are discussions of the extensions of such an operator to include Finite Larmor Radius (FLR) corrections in section 3.8. Afterwards, the numerical implementation of the operator in GENE is discussed in section 3.9, 3.10, and 3.11, and results are presented demonstrating appropriate conservation and free energy dissipation properties in section 3.12. Afterwards, the effects of collisions on Geodesic Acoustic Mode (GAM) oscillations is discussed in section 3.13. The collision operator is then benchmarked with regards to neoclassical transport, and frequencies and growth rates of microinstabilities in section 3.14. Finally, a summary of the work that has been completed and work that is left to be done on collisions in gyrokinetics is given in section 3.15.

3.2 Landau-Boltzmann collision operator

Collisions are exceedingly rare events occurring in a plasma. Because of the rarity of such events, the dominant collisional interactions are between two species, and collision events between three or more species can safely be neglected. The two species collision operator considered in the remainder of this thesis is expressed as

$$C_a = \sum_b C_{ab}.$$

In the above formula, a and b correspond to different plasma species. In addition, because of the long range of the shielded Coulomb interaction, collisions are mainly characterized by small-angle scattering. Any collision process that can be described by small-angle scattering can be represented by the Fokker-Planck collision operator, which shall now be derived. Afterwards, a popular type of Fokker-Planck operator used in plasma physics, the Landau-Boltzmann collision operator, shall be discussed. Much of this derivation and discussion follows the formulation outlined in ref. [12], and the interested reader may look towards that source for more information on generalized collision operators.

It can safely be assumed that the time-scale associated with a collisional event, $t_{\text{collision}}$, is much shorter than the time-scales of the other processes occurring in a plasma, t. This can be expressed as

$$t \gg t_{\text{collision}}.$$

Since the time-scale describing collisionless dynamics in a plasma is so much larger than the time-scale of collisions, the effect of collisions in a plasma can be modeled with a probability distribution with regard to changes in the larger time-scale, Δt:

$$F_a(\mathbf{x}, \mathbf{v}, t) = \int d^3\Delta v F_a(\mathbf{x}, \mathbf{v} - \Delta\mathbf{v}, t - \Delta t) P(\mathbf{v} - \Delta\mathbf{v}, \Delta\mathbf{v}, \Delta t). \tag{3.1}$$

In Eq. 3.1, $P(\mathbf{v} - \Delta\mathbf{v}, \Delta\mathbf{v}, \Delta t)$ corresponds to the probability that a particle will change its velocity from $\mathbf{v} - \Delta\mathbf{v}$ by $\Delta\mathbf{v}$ within a time window, Δt. In this formula, Δt is a quantity which is taken to be small with regard to the entire time trace of the plasma dynamics, but large compared to $t_{\text{collision}}$. The above expression can now be Taylor expanded to first order in time, and second order in velocity (because for a Fokker-Planck process, the assumption of small-angle scattering applies):

$$F_a(\mathbf{x}, \mathbf{v}, t) = \int d^3\Delta v \Big[F_a(\mathbf{x}, \mathbf{v}, t) P(\mathbf{v}, \Delta\mathbf{v}, \Delta t) - \frac{\partial F_a}{\partial t} \Delta t P(\mathbf{v}, \Delta\mathbf{v}, \Delta t)$$

$$-\Delta\mathbf{v}\cdot\frac{\partial}{\partial\mathbf{v}}\Big(P(\mathbf{v},\Delta\mathbf{v},\Delta t)F_a(\mathbf{x},\mathbf{v},t)\Big)+\frac{1}{2}\Delta\mathbf{v}\cdot\frac{\partial^2}{\partial\mathbf{v}\partial\mathbf{v}}\Big(P(\mathbf{v},\Delta\mathbf{v},\Delta t)F_a(\mathbf{x},\mathbf{v},t)\Big)\cdot\Delta\mathbf{v}\Big].$$

This expression can be simplified in several ways. The term on the LHS cancels with the first term on the RHS because the integral of the probability distribution by itself is 1,

$$\int d^3\Delta v P(\mathbf{v},\Delta\mathbf{v},\Delta t)=1.$$

Also, since only collisions are being considered in this case, $\partial F/\partial t$ can be replaced by the collision operator. So the following expression can be used for the collision operator:

$$C_{ab}=-\frac{1}{m_a}\frac{\partial}{\partial\mathbf{v}}\cdot\Big(\mathbf{r}_{ab}F_a\Big)+\frac{\partial^2}{\partial\mathbf{v}\partial\mathbf{v}}\cdot\Big(\overleftrightarrow{\mathbf{D}}_{ab}F_a\Big). \tag{3.2}$$

In Eq. 3.2, $\mathbf{r}_{ab}$ and $\overleftrightarrow{\mathbf{D}}_{ab}$ are given by the following expressions:

$$\mathbf{r}_{ab}=\frac{m_a}{\Delta t}\int d^3\Delta v P(\mathbf{v},\Delta\mathbf{v},\Delta t)\Delta\mathbf{v}$$

$$\overleftrightarrow{\mathbf{D}}_{ab}=\frac{1}{2\Delta t}\int d^3\Delta v P(\mathbf{v},\Delta\mathbf{v},\Delta t)\Delta\mathbf{v}\Delta\mathbf{v}.$$

To write the Fokker-Planck collision operator in a more traditional form, a new resistive vector shall be defined as

$$\mathbf{r}_{ab}=\mathbf{R}_{ab}+m_a\frac{\partial}{\partial\mathbf{v}}\cdot\overleftrightarrow{\mathbf{D}}_{ab}.$$

So the Fokker-Planck collision operator can be written in the following manner:

$$C_{ab}=-\frac{\partial}{\partial\mathbf{v}}\cdot\mathbf{\Gamma}_{ab}, \tag{3.3}$$

where the collisional flux, Γ_{ab}, is given by

$$\mathbf{\Gamma}_{ab} = \frac{1}{m_a}\mathbf{R}_{ab}F_a - \overleftrightarrow{\mathbf{D}}_{ab} \cdot \frac{\partial F_a}{\partial \mathbf{v}}. \tag{3.4}$$

The collision operator can be expressed as the divergence of a velocity space flux, which contains diffusive and resistive terms. The diffusive term will attempt to spread out the velocity space distribution of particles. The resistive term will attempt to slow down particles until they are at a single uniform velocity. The competition between these two terms will bring the final distribution to a Maxwellian equilibrium (if only collisions are allowed to act). The only remaining task to achieve a refined model of collisions in plasmas is to determine the expressions for the resistive vectors and diffusion tensors, $\mathbf{R}_{ab}$ and $\overleftrightarrow{\mathbf{D}}_{ab}$ respectively. There are several different collision models that can be obtained depending on the assumptions made when solving for these values. Deriving the models for these terms is beyond the scope of this thesis, and the interested reader may consult other references for more information [59, 12].

For this thesis, the Landau-Boltzmann collision operator shall be considered, where the resistive vector and diffusion tensor are given by Eq. 3.5 and 3.6,

$$\overleftrightarrow{\mathbf{D}}_{ab} = \frac{\gamma_{ab}}{m_a^2}\int d^3v' \overleftrightarrow{\mathbf{U}} F_b(\mathbf{v}') \tag{3.5}$$

$$\mathbf{R}_{ab} = \frac{\gamma_{ab}}{m_b}\int d^3v' \overleftrightarrow{\mathbf{U}} \cdot \frac{\partial}{\partial \mathbf{v}'} F_b(\mathbf{v}') \tag{3.6}$$

$$\overleftrightarrow{\mathbf{U}} = \frac{u^2 \overleftrightarrow{\mathbf{I}} - \mathbf{uu}}{u^3}$$

$$\gamma_{ab} = 2\pi e_a^2 e_b^2 \ln(\Lambda).$$

The following identity is also useful:

$$\frac{\partial}{\partial \mathbf{v}} \cdot \overleftrightarrow{\mathbf{U}} = -\frac{\partial}{\partial \mathbf{v}'} \cdot \overleftrightarrow{\mathbf{U}}.$$

This identity, combined with integration by parts, can be used to express the resistive vector in terms of the diffusion tensor for the Landau-Boltzmann collision operator,

$$\mathbf{R}_{ab} = \frac{m_a^2}{m_b} \frac{\partial}{\partial \mathbf{v}} \cdot \overleftrightarrow{\mathbf{D}}_{ab}. \tag{3.7}$$

In the next section, it will be required to analytically compute the diffusion tensor and resistive vector associated with a Maxwellian distribution. For this purpose, it will be convenient to recast the collision operator in terms of Rosenbluth Potentials:

$$G_b(\mathbf{v}) = \int d^3v' F_b(\mathbf{v}')u \tag{3.8}$$

$$H_b(\mathbf{v}) = \int d^3v' F_b(\mathbf{v}') \frac{1}{u} \tag{3.9}$$

$$u = \mid \mathbf{v} - \mathbf{v}' \mid .$$

The tensor $\overleftrightarrow{\mathbf{U}}$ can be expressed as the second derivative of the relative speed,

$$U_{ij} = \frac{\partial^2 u}{\partial u_i \partial u_j},$$

and this can be used to express the diffusion tensor in terms of Rosenbluth potentials:

$$\overleftrightarrow{\mathbf{D}}_{ab} = \frac{\gamma_{ab}}{m_a^2} \frac{\partial^2 G_b(\mathbf{v})}{\partial \mathbf{v} \partial \mathbf{v}}. \tag{3.10}$$

The divergence of the tensor, $\frac{\partial}{\partial \mathbf{u}} \cdot \overleftrightarrow{\mathbf{U}}$, can be expressed as the derivative of the inverse speed,

$$\frac{\partial}{\partial u_j} U_{ij} = 2 \frac{\partial}{\partial u_i} \frac{1}{u},$$

and this identity (along with integration by parts) allows for the expression of the resistance vector in terms of the Rosenbluth potentials:

$$\mathbf{R}_{ab} = \frac{2\gamma_{ab}}{m_b}\frac{\partial H_b(\mathbf{v})}{\partial \mathbf{v}}. \tag{3.11}$$

The above equations for the Rosenbluth potentials have a clear analogy to the equations of electrostatics. For instance, Eq. 3.9 suggests that the Rosenbluth potential, H_b, is analogous to the electrostatic potential. $F_b(\mathbf{v}')$ is analogous to the charge density in configuration space. And the distance in velocity space, u, is analogous to the configuration space distance between a charge and a point where the potential is calculated. This suggests that Laplace's equation can be used to compute the Rosenbluth potentials,

$$\nabla_v^2 H_a = -4\pi F_a.$$

Plugging Eq. 3.10 and 3.11 into Eq. 3.7, the equation for G_a in terms of H_a is obtained:

$$\nabla_v^2 G_a = 2H_a.$$

3.3 Linearization of operator

The delta-f splitting of the full distribution function into a background Maxwellian distribution, F_{Ma}, and a perturbed distribution function, f_a, is applied. Then one can write the full distribution function as $F_a = F_{Ma} + f_a$ and the collision operator as

$$C_{ab}(F_a, F_b) = C_{ab}(F_{Ma}, F_{Mb}) + C_{ab}(f_a, F_{Mb}) + C_{ab}(F_{Ma}, f_b) + C_{ab}(f_a, f_b). \tag{3.12}$$

Now if one had arbitrary distribution functions for an electron-ion plasma, and one were to evolve these distribution functions using only the collision operator, then each distribution function would relax to a local Maxwellian distribution,

$$F_{Ma} = \frac{n_a}{(\sqrt{\pi} v_{Ta})^3} e^{-(\frac{v}{v_{Ta}})^2}. \tag{3.13}$$

Then each Maxwellian distribution would relax into one single Maxwellian distribution for all species given a proper normalization. The second equilibration process would take much longer than the first because of the much larger mass differential between different species rather than similar species in a typical plasma. Billiard balls can exchange energy very efficiently in collisions because they have similar mass. However, if one were to collide ping-pong balls with bowling balls, the ping-pong balls would just bounce off of the bowling balls, and not much energy would be exchanged in the process. A similar case occurs in a plasma, and this allows for a natural separation of time-scales. The time it takes the ion and electron Maxwellian distributions to equilibrate is much longer than the turbulent transport time-scale for a plasma discharge in a magnetic confinement device (the transport timescale in the edge of a magnetic confinement device is $\sim O(100a/c_s)$ and the thermalization timescale is $\sim O(10000a/c_s)$). As such, the equilibration process is neglected. In the gyrokinetic code, GENE, the evolution of the perturbed distribution function, f_a, is modeled. The temperature and density profiles are regarded as fixed, which is a reflection of the fact that the evolution of the background Maxwellian distribution is neglected.

Because the equilibration process is neglected, $C_{ab}(F_{Ma}, F_{Mb})$, which can be interpreted as the term which evolves F_{Ma} due to collisions with the background Maxwellian distribution of species b, can be disregarded. The term should be small due to the large timescale of the process, and it would be inconsistent to include a term which would alter the temperatures of the different species while also keeping the temperature profiles fixed in the remainder of the gyrokinetic equation. However, there may be situations where one must keep this term, and a model for this has been developed [39]. The final term in Eq. 3.12 is also neglected as it is considered to be of higher order in the delta-f ordering. Therefore, the equations are linearized. For global gyrokinetic simulations, a source may be utilized to prevent the perturbation from becoming too large in accordance with the delta-f ordering.

Only two terms remain in the linearized collision operator: $C_{ab}(f_a, F_{Mb})$ and $C_{ab}(F_{Ma}, f_b)$.

The first term, $C^T_{ab}(f_a) = C_{ab}(f_a, F_{Mb})$, represents the evolution of f_a due to collisions with a background Maxwellian distribution of species b. This term should clearly be included in the collision operator. The other term, $C^F_{ab}(f_b) = C_{ab}(F_{Ma}, f_b)$ represents the evolution of a Maxwellian due to collisions with a perturbation. Again, since the background distributions have been regarded as fixed, it is not clear how one should model the effects of such a term. Furthermore, the computation of such a term would be expensive due to the nonlocal velocity space integral (the analytical model for this has been done by [40]). However, if one were to ignore such a term, then the model collision operator would be unable to satisfy the essential conservation laws for momentum and energy in plasma simulations [12]:

$$\int d^3v m_a \mathbf{v} C_{ab} = -\int d^3v m_b \mathbf{v} C_{ba} \tag{3.14}$$

$$\int d^3v \frac{1}{2} m_a v^2 C_{ab} = -\int d^3v \frac{1}{2} m_b v^2 C_{ba}. \tag{3.15}$$

For these reasons, the second term is replaced with a model operator such that the collision operator as a whole conserves momentum and energy,

$$C^F_{ba}(f_a) = -\frac{T_a}{T_b} \frac{C^T_{ba}(\frac{F_{Mb} m_b \mathbf{v}}{T_b}) \cdot \int d^3v \frac{m_a \mathbf{v}}{T_a} C^T_{ab}(f_a)}{\int d^3v \frac{m_b v_\parallel}{T_b} C^T_{ba}(F_{Mb} m_b v_\parallel / T_b)} - \frac{T_a}{T_b} \frac{C^T_{ba}(F_{Mb} x_b^2) \int d^3v x_a^2 C^T_{ab}(f_a)}{\int d^3v x_b^2 C^T_{ba}(F_{Mb} x_b^2)}. \tag{3.16}$$

The complete linearized collision operator can be written as

$$C^{\text{linear}}_{ab}(f_a, f_b) = C^T_{ab}(f_a) + C^F_{ab}(f_b). \tag{3.17}$$

The two component parts shall be called the test-particle operator and the field-particle operator respectively. One can verify that the above model given for the field-particle part enables the entire collision operator to satisfy the above conservation laws for a nearly arbitrary test-particle part. The only constraint on the test-particle part is that it conserves particles. Therefore, only the test-particle operator needs to be evaluated for the entire

linearized collision operator to be determined. The use of the Rosenbluth potentials makes it easier to evaluate the test-particle part of the collision operator, $C_{ab}^T(f_a) = C_{ab}(f_a, F_{Mb})$. One has the following relation for H_{Mb}:

$$H_{Mb} = \int d^3\mathbf{v} F_{Mb}(v') \frac{1}{\mid \mathbf{v} - \mathbf{v}' \mid}.$$

The expansion formula which is familiar from electrostatics shall now be used to evaluate H_{Mb},

$$\frac{1}{\mid \mathbf{v} - \mathbf{v}' \mid} = \frac{1}{v_>} \sum_{m=0} (\frac{v_<}{v_>})^m P_m(cos(\theta)).$$

Where the P_M's are the Legendre polynomials and $v_>$ is the larger of the v and v'. Since the Legendre polynomials are orthogonal, only the zeroth order term for the calculation needs to be kept,

$$H_{Mb} = 4\pi \int_0^\infty dv'(v')^2 F_{Mb}(v') \frac{1}{v_>} = 4\pi \int_0^v dv'(v')^2 F_{Mb}(v') \frac{1}{v} + 4\pi \int_v^\infty dv'(v')^2 F_{Mb}(v') \frac{1}{v'}.$$

Substituting the Maxwellian distribution into the equation yields

$$H_{Mb} = \frac{4n_b}{\sqrt{\pi}} \Bigg(\int_0^{\frac{v}{v_{Tb}}} dx x^2 e^{-x^2} \frac{1}{v} + \int_{\frac{v}{v_{Tb}}}^\infty dx x^2 e^{-x^2} \frac{1}{v_{Tb} x} \Bigg)$$

$$H_{Mb} = \frac{4n_b}{\sqrt{\pi}} \Bigg(-\frac{1}{2} \int_0^{\frac{v}{v_{Tb}}} dx x \frac{d}{dx}(e^{-x^2}) \frac{1}{v} + \int_{(\frac{v}{v_{Tb}})^2}^\infty \frac{dw}{2} e^{-w} \frac{1}{v_{Tb}} \Bigg)$$

$$H_{Mb} = \frac{4n_b}{\sqrt{\pi}} \Bigg(-\frac{1}{2v_{Tb}} e^{-(\frac{v}{v_{Tb}})^2} + \frac{1}{2v} \int_0^{\frac{v}{v_{Tb}}} dx e^{-x^2} + \frac{1}{2v_{Tb}} e^{-(\frac{v}{v_{Tb}})^2} \Bigg)$$

$$H_{Mb} = \frac{n_b}{v} \mathrm{erf}\Bigg(\frac{v}{v_{Tb}} \Bigg), \tag{3.18}$$

where erf is the error function defined as

$$\mathrm{erf}(x) = \Phi(x) = \int_0^x e^{-t^2} dt. \tag{3.19}$$

Now G_{Mb} can be computed from H_{Mb} in a similar way to how the distribution function is used to compute H_{Mb},

$$G_{Mb} = -\frac{1}{3\pi} \int d^3\mathbf{v} H_{Mb}(v') \frac{1}{\mid \mathbf{v} - \mathbf{v}' \mid}$$

$$G_{Mb} = -2 \int_0^v dv' (v')^2 H_{Mb}(v') \frac{1}{v} - 2 \int_v^\infty dv' (v')^2 H_{Mb}(v') \frac{1}{v'}$$

$$G_{Mb} = -2n_b \left(\int_0^v dv' v' \Phi\left(\frac{v'}{v_{Tb}}\right) \frac{1}{v} + \int_v^\infty dv' \Phi\left(\frac{v'}{v_{Tb}}\right) \right)$$

$$G_{Mb} = -2n_b v_{Tb} \left(\int_0^{\frac{v}{v_{Tb}}} du u \Phi(u) \frac{v_{Tb}}{v} + \int_{\frac{v}{v_{Tb}}}^\infty du \Phi(u) \right).$$

The second integral in the above expression diverges. However, the singularity obtained is irrelevant for the physical calculation of the collision operator, since the derivative of the Rosenbluth potentials is taken in the end. Thus it is only the functional form of the Rosenbluth potentials that matters, not the arbitrary constant within the potentials themselves. If one had a similar electrostatics problem with a charge density having a functional form similar to that of H_{Mb}, then the electrostatic potential would also diverge. However, the electric field would not. Integrating by parts (ignoring the singularity in the second integral) and defining $x_b = v/v_{Tb}$, the following is obtained:

$$G_{Mb} = -2n_b v_{Tb} \left(\frac{1}{2} x_b \Phi(x_b) - \frac{2}{\sqrt{\pi}} \int_0^{x_b} du \frac{1}{2} u^2 e^{-u^2} \frac{1}{x_b} - x_b \Phi(x_b) - \frac{2}{\sqrt{\pi}} \int_{x_b}^\infty du u e^{-u^2} \right)$$

$$G_{Mb} = -2n_b v_{Tb}\bigg(-\frac{x_b}{2}\Phi\big(x_b\big) + \frac{1}{\sqrt{\pi}}\int_0^{x_b} duu\frac{1}{2}\frac{d}{du}\big(e^{-u^2}\big)\frac{1}{x_b} - \frac{1}{\sqrt{\pi}}\int_{(x_b)^2}^{\infty} dwe^{-w}\bigg)$$

$$G_{Mb} = -n_b v_{Tb}\bigg(-x_b\Phi\big(x_b\big) - \frac{1}{\sqrt{\pi}}e^{-(x_b)^2} - \frac{1}{\sqrt{\pi}}\int_0^{x_b} due^{-u^2}\frac{1}{x_b}\bigg)$$

$$G_{Mb} = \frac{n_b v_{Tb}}{2x_b}\bigg(2x_b^2\Phi(x_b) + x_b\frac{d}{dx_b}\Phi(x_b) + \Phi(x_b)\bigg). \tag{3.20}$$

Now that the Rosenbluth potentials have been computed, the test-particle part of the collision operator can be obtained. For simplicity, the spherical velocity space coordinates are used in the subsequent analysis,

$$\frac{\partial G_{Mb}}{\partial \mathbf{v}} = \frac{\partial G_{Mb}}{\partial v}\hat{\mathbf{v}} = \frac{1}{v}\frac{\partial G_{Mb}}{\partial v}\mathbf{v}$$

$$\frac{\partial^2 G_{Mb}}{\partial \mathbf{v}\partial \mathbf{v}} = \mathbf{v}\hat{\mathbf{v}}\frac{\partial}{\partial v}\left(\frac{1}{v}\frac{\partial G_{Mb}}{\partial v}\right) + \frac{1}{v}\frac{\partial G_{Mb}}{\partial v}\frac{\partial}{\partial \mathbf{v}}\mathbf{v}$$

$$\frac{\partial^2 G_{Mb}}{\partial \mathbf{v}\partial \mathbf{v}} = \frac{1}{v}\frac{\partial G_{Mb}}{\partial v}\overleftrightarrow{\mathbf{I}} + \mathbf{v}\mathbf{v}\frac{1}{v}\frac{\partial}{\partial v}\left(\frac{1}{v}\frac{\partial G_{Mb}}{\partial v}\right)$$

$$\frac{\partial^2 G_{Mb}}{\partial \mathbf{v}\partial \mathbf{v}} = \frac{1}{v^3}\frac{\partial G_{Mb}}{\partial v}\big(v^2\overleftrightarrow{\mathbf{I}} - \mathbf{v}\mathbf{v}\big) + \frac{\mathbf{v}\mathbf{v}}{v^2}\frac{\partial^2 G_{Mb}}{\partial v^2}$$

$$\frac{\partial^2 G_{Mb}}{\partial \mathbf{v}\partial \mathbf{v}}\cdot\frac{\partial f_a}{\partial \mathbf{v}} = \frac{1}{v^3}\frac{\partial G_{Mb}}{\partial v}\big(v^2\overleftrightarrow{\mathbf{I}} - \mathbf{v}\mathbf{v}\big)\cdot\frac{\partial f_a}{\partial \mathbf{v}} + \frac{\mathbf{v}}{v}\frac{\partial^2 G_{Mb}}{\partial v^2}\frac{\partial f_a}{\partial v}.$$

Using the identities $\nabla\cdot\frac{\mathbf{v}}{v} = \frac{3}{v} + v\frac{\partial}{\partial v}(\frac{1}{v}) = \frac{2}{v}$ and $\mathbf{v}\cdot(v^2\overleftrightarrow{\mathbf{I}} - \mathbf{v}\mathbf{v}) = 0$ gives

$$\frac{\partial}{\partial \mathbf{v}}\cdot\left(\frac{\partial^2 G_{Mb}}{\partial \mathbf{v}\partial \mathbf{v}}\cdot\frac{\partial f_a}{\partial \mathbf{v}}\right) = \frac{2}{v^3}\frac{\partial G_{Mb}}{\partial v}\mathfrak{L}f_a + \frac{2}{v}\frac{\partial^2 G_{Mb}}{\partial v^2}\frac{\partial f_a}{\partial v} + \frac{\partial}{\partial v}\left(\frac{\partial^2 G_{Mb}}{\partial v^2}\frac{\partial f_a}{\partial v}\right).$$

Where $\mathfrak{L}$ represents the traditional pitch-angle scattering operator,

$$\mathfrak{L} = \frac{1}{2}\frac{\partial}{\partial \mathbf{v}} \cdot \left(v^2 \overleftrightarrow{\mathbf{I}} - \mathbf{vv} \right) \cdot \frac{\partial}{\partial \mathbf{v}} = \frac{1}{2}\left(\frac{1}{\sin(\theta)} \frac{\partial}{\partial \theta} \sin(\theta) \frac{\partial}{\partial \theta} + \frac{1}{\sin^2(\theta)} \frac{\partial^2}{\partial \phi^2} \right). \tag{3.21}$$

The previous formula can be easily proven using the definition of the gradient and divergence in spherical coordinates, and the fact that the dot product of the tensor, $(v^2 \overleftrightarrow{\mathbf{I}} - \mathbf{vv})$ with the gradient effectively kills the radial component of the gradient. Now the coefficient of the pitch-angle part of the collision operator can be evaluated as

$$\frac{\partial G_{Mb}}{\partial v} = \frac{n_b}{2}\frac{d}{dx_b}\left[\frac{1}{x_b}\big((2x_b^2 + 1)\Phi(x_b) + x_b \frac{d}{dx_b}\Phi(x_b) \big) \right]$$

$$\frac{\partial G_{Mb}}{\partial v} = \frac{n_b}{2}\big[-2x_b \frac{d}{dx_b}\Phi(x_b) + \frac{1}{x_b}(2x_b^2 + 1)\frac{d}{dx_b}\Phi(x_b) + (2 - 1/x_b^2)\Phi(x_b) \big]$$

$$\frac{\partial G_{Mb}}{\partial v} = \frac{n_b}{2}\left[\frac{1}{x_b}\frac{d}{dx_b}\Phi(x_b) + (2 - 1/x_b^2)\Phi(x_b) \right]$$

$$\frac{\partial G_{Mb}}{\partial v} = n_b[\Phi(x_b) - G(x_b)]. \tag{3.22}$$

Where $G(x) = [\Phi(x) - x\frac{d}{dx}\Phi(x)]/2x^2$ has been defined such that the notation is consistent with that of [14]. The pitch-angle scattering frequency is defined as

$$\nu_D^{ab}(v) = \frac{4\pi n_b}{m_a^2 v^3} e_a^2 e_b^2 \ln(\Lambda)(\Phi(x_b) - G(x_b)). \tag{3.23}$$

The test-particle part can be written as

$$C_{ab}^T(f_a) = \nu_D^{ab}(v)\mathfrak{L}f_a +$$

$$\frac{\gamma_{ab}}{m_a^2}\left(\frac{2}{v}\frac{d^2G_{Mb}}{dv^2}\frac{\partial f_a}{\partial v}+\frac{\partial}{\partial v}\left(\frac{d^2G_{Mb}}{dv^2}\frac{\partial f_a}{\partial v}\right)\right)-\frac{2\gamma_{ab}}{m_a m_b}\left((\nabla_v^2 H_{Mb})f_a+\frac{dH_{Mb}}{dv}\frac{\partial f_a}{\partial v}\right).$$

The terms with the Rosenbluth potentials can be evaluated and substituted into the above equation:

$$\nabla_v^2 H_{Mb}=-4\pi F_{Mb}$$

$$\frac{dH_{Mb}}{dv}=-\frac{n_b}{v^2}\Phi(x_b)+\frac{n_b}{vv_{Tb}}\Phi'(x_b)=\frac{n_b}{v^2}\left(-\Phi(x_b)+x_b\Phi'(x_b)\right)=-\frac{2n_b}{v_{Tb}^2}G(x_b) \tag{3.24}$$

$$\frac{d^2G_{Mb}}{dv^2}=\frac{n_b}{v_{Tb}}\left(\Phi'(x_b)+\frac{(\Phi(x_b)-x_b\Phi'(x_b))}{x_b^3}-\frac{(-x_b\Phi''(x_b))}{2x_b^2}\right)=\frac{2n_b}{v}G(x_b) \tag{3.25}$$

$$C_{ab}^T(f_a)=\nu_D^{ab}(v)\mathfrak{L}f_a+\frac{\gamma_{ab}}{m_a^2}\left(\frac{4n_b}{v^2}G(x_b)\frac{\partial f_a}{\partial v}+\frac{\partial}{\partial v}\left(\frac{2n_b}{v}G(x_b)\frac{\partial f_a}{\partial v}\right)\right)$$

$$+\frac{2\gamma_{ab}}{m_a m_b}\left(4\pi F_{Mb}f_a+\frac{2n_b}{v_{Tb}^2}G(x_b)\frac{\partial f_a}{\partial v}\right).$$

A new frequency is defined (again consistent with [14]) and the expression can be rewritten as

$$\nu_{\parallel}^{ab}(v)=\frac{4\gamma_{ab}n_b}{m_a^2v^3}G(x_b) \tag{3.26}$$

$$C_{ab}^{T}(f_a) = \nu_D^{ab}(v)\mathfrak{L}f_a + v\nu_\parallel^{ab}(v)\frac{\partial f_a}{\partial v} + \frac{\partial}{\partial v}\left(\frac{v^2}{2}\nu_\parallel^{ab}(v)\frac{\partial f_a}{\partial v}\right) + \frac{4n_b\gamma_{ab}}{m_a m_b v_{Tb}^3}\Phi'(x_b)f_a + \frac{m_a}{m_b}\frac{v^3}{v_{Tb}^2}\nu_\parallel^{ab}(v)\frac{\partial f_a}{\partial v}. \tag{3.27}$$

The derivative of the newly defined frequency term can now be evaluated and used to rewrite the test-particle part of the collision operator:

$$\frac{d\nu_\parallel^{ab}(v)}{dv} = \frac{4\gamma_{ab}n_b}{m_a^2}\left(\frac{G'(x_b)}{v_{Tb}v^3} - 3\frac{G(x_b)}{v^4}\right).$$

Given the identity, $G'(x) = \Phi'(x) - 2G(x)/x$, the following expressions can be obtained:

$$\frac{d\nu_\parallel^{ab}(v)}{dv} = \frac{4\gamma_{ab}n_b}{m_a^2}\left(\frac{\Phi'(x_b)}{v_{Tb}v^3} - 5\frac{G(x_b)}{v^4}\right)$$

$$\frac{d\nu_\parallel^{ab}(v)}{dv} = \frac{4\gamma_{ab}n_b}{m_a^2 v_{Tb}}\frac{\Phi'(x_b)}{v^3} - \frac{5\nu_\parallel^{ab}(v)}{v} \tag{3.28}$$

$$\frac{4\gamma_{ab}n_b}{m_a m_b v_{Tb}^3}\Phi'(x_b) = \frac{m_a}{m_b}\frac{v^3}{v_{Tb}^2}\left(\frac{d\nu_\parallel^{ab}(v)}{dv} + \frac{5\nu_\parallel^{ab}(v)}{v}\right).$$

This expression can be substituted into the collision operator:

$$C_{ab}^{T}(f_a) = \nu_D^{ab}(v)\mathfrak{L}f_a + v\nu_\parallel^{ab}(v)\frac{\partial f_a}{\partial v} + \frac{\partial}{\partial v}\left(\frac{v^2}{2}\nu_\parallel^{ab}(v)\frac{\partial f_a}{\partial v}\right)$$

$$+\frac{m_a}{m_b}\frac{v^3}{v_{Tb}^2}\left(\frac{\partial}{\partial v}(\nu_\parallel^{ab}(v)f_a) + \nu_\parallel^{ab}(v)f_a\frac{1}{v^5}\frac{d}{dv}(v^5)\right)$$

$$C_{ab}^{T}(f_a) = \nu_D^{ab}(v)\mathfrak{L}f_a + v\nu_\parallel^{ab}(v)\frac{\partial f_a}{\partial v} + \frac{\partial}{\partial v}\left(\frac{v^2}{2}\nu_\parallel^{ab}(v)\frac{\partial f_a}{\partial v}\right) + \frac{m_a}{T_b}\frac{1}{v^2}\frac{\partial}{\partial v}\left(\frac{\nu_\parallel^{ab}(v)}{2}v^5 f_a\right).$$

The two terms in the middle can be combined into one. Using the chain rule gives

$$\frac{1}{v^2}\frac{\partial}{\partial v}\left[(v^2)(\frac{v^2}{2}\nu_{\parallel}^{ab}(v)\frac{\partial f_a}{\partial v})\right] = v\nu_{\parallel}^{ab}(v)\frac{\partial f_a}{\partial v} + \frac{\partial}{\partial v}\left(\frac{v^2}{2}\nu_{\parallel}^{ab}(v)\frac{\partial f_a}{\partial v}\right).$$

Thus, one obtains

$$C_{ab}^{T}(f_a) = \nu_D^{ab}(v)\mathfrak{L}f_a + \frac{1}{v^2}\frac{\partial}{\partial v}\left(\frac{v^4}{2}\nu_{\parallel}^{ab}(v)\frac{\partial f_a}{\partial v}\right) + \frac{m_a}{T_b}\frac{1}{v^2}\frac{\partial}{\partial v}\left(\frac{\nu_{\parallel}^{ab}(v)}{2}v^5 f_a\right).$$

The following identity is used to rewrite the collision operator:

$$F_{Ma}\frac{\partial}{\partial v}\left(\frac{g}{F_{Ma}}\right) = \frac{\partial g}{\partial v} + \frac{2v}{v_{Ta}^2}g$$

$$\frac{\partial g}{\partial v} = F_{Ma}\frac{\partial}{\partial v}\left(\frac{g}{F_{Ma}}\right) - \frac{m_a v}{T_a}g.$$

The final form of the complete linearized Landau-Boltzmann test-particle part of the collision operator is then obtained:

$$C_{ab}^{T}(f_a) = C_{ab}^{T0}(f_a) + \frac{m_a}{T_b}\left(1 - \frac{T_b}{T_a}\right)\frac{1}{v^2}\frac{\partial}{\partial v}\left(\frac{\nu_{\parallel}^{ab}(v)}{2}v^5 f_a\right), \tag{3.29}$$

where

$$C_{ab}^{T0}(f_a) = \nu_D^{ab}(v)\mathfrak{L}f_a + \frac{1}{v^2}\frac{\partial}{\partial v}\left(\frac{v^4}{2}\nu_{\parallel}^{ab}(v)F_{Ma}\frac{\partial}{\partial v}\left(\frac{f_a}{F_{Ma}}\right)\right). \tag{3.30}$$

The test-particle part has been written in this form such that there is a nonisothermal part and a part which obeys a certain self-adjointness symmetry (to be explained in more detail later). This operator conserves particles since the integral of the entire collision term is equal to zero. And a field-particle term is constructed such that the collision operator as a whole conserves particles, momentum, and energy. However, the collision operator must also dissipate free energy and drive different perturbations toward a common localized distribution function. This is essentially the main feature of the collision operator.

3.4 Problems with free energy dissipation

It is required that the free energy change for each species be negative. Since the Vlasov equation conserves entropy, the free energy change from the collisional term must be negative,

$$\sum_a -T_a \left(\frac{\partial S_a}{\partial t} \right)_{\text{coll}} \leq 0. \tag{3.31}$$

The definition for the entropy associated with a given distribution function is given by [12],

$$S_a = -\int d^3v F_a \ln(F_a). \tag{3.32}$$

Plugging this into the above expression and using the chain rule, one obtains

$$\sum_a T_a \int d^3v \Big(\ln(F_a) C_a + C_a \Big) \leq 0.$$

Because the collision operator conserves particles,

$$\sum_a T_a \int d^3v \ln(F_a) C_a \leq 0.$$

Since the distribution function being considered is linearized ($F_a = F_{Ma} + f_a$), a Taylor expansion can be performed:

$$\sum_a T_a \int d^3v C_a \left[\ln\left(\frac{n_a}{(\sqrt{\pi} v_{Ta})^3} \right) - \left(\frac{v}{v_{Ta}} \right)^2 + \ln\left(1 + \frac{f_a}{F_{Ma}} \right) \right] \leq 0.$$

Due to particle and energy conservation, the first two terms inside of the brackets vanish. Taylor expanding the last term in the bracket gives

$$\sum_a T_a \int d^3v \frac{f_a}{F_{Ma}} C_a \leq 0$$

$$\sum_a T_a \int d^3v \frac{f_a}{F_{Ma}} \sum_b (C_{ab}^T(f_a) + C_{ab}^F(f_b)) \leq 0.$$

Since the collision operator is binary between particles, this relation must hold between any pair of species, so the H-theorem can be written more succinctly as

$$T_a \int d^3v \frac{f_a}{F_{Ma}} (C_{ab}^T(f_a) + C_{ab}^F(f_b)) + T_b \int d^3v \frac{f_b}{F_{Mb}} (C_{ba}^T(f_b) + C_{ba}^F(f_a)) \leq 0. \tag{3.33}$$

Given an isothermal case in which all of the background distributions are at a common temperature, this property is analytically satisfied. However, the nonisothermal part of the test-particle operator breaks a particular symmetry which is contained in $C_{ab}^{T0}(f_a)$ such that the operator is no longer guaranteed to dissipate free energy. This is an unfortunate side effect of the attempt to linearize the collision operator. To more clearly explain how the nonisothermal part breaks the free energy dissipation property, it shall be proven that the other part of the collision operator (C_{ab}^{T0} and the associated field-particle part) satisfies the free energy dissipation property for the isothermal case, and then it shall be explained how the nonisothermal part breaks it.

Self-adjointness relations for the test-particle and field-particle operators can be derived:

$$\int d^3v \frac{f_a}{F_{Ma}} C_{ab}^{T0}(g_a) = \frac{1}{2} \int dv d\theta d\phi \frac{f_a}{F_{Ma}} v^2 \nu_D^{ab}(v) \frac{\partial}{\partial \theta} \left(\sin(\theta) \frac{\partial}{\partial \theta} g_a \right)$$

$$+ \frac{1}{2} \int dv d\theta d\phi \frac{f_a}{F_{Ma}} v^2 \nu_D^{ab}(v) \frac{1}{\sin(\theta)} \frac{\partial^2}{\partial \phi^2} g_a$$

$$+ \int dv d\theta d\phi \frac{f_a}{F_{Ma}} \sin(\theta) \frac{\partial}{\partial v} \left[\frac{\nu_\parallel^{ab}(v)}{2} v^4 F_{Ma} \frac{\partial}{\partial v} \left(\frac{g_a}{F_{Ma}} \right) \right].$$

Integrating by parts for each of these integrals (and using the fact that the distribution functions go to zero infinitely far away):

$$\int d^3v \frac{f_a}{F_{Ma}} C_{ab}^{T0}(g_a) = -\frac{1}{2} \int dv d\theta d\phi \frac{1}{F_{Ma}} v^2 \nu_D^{ab}(v) \sin(\theta) \left(\frac{\partial f_a}{\partial \theta} \right) \left(\frac{\partial g_a}{\partial \theta} \right)$$

$$-\frac{1}{2}\int dvd\theta d\phi \frac{1}{F_{Ma}} v^2 \nu_D^{ab}(v) \frac{1}{\sin(\theta)} \frac{\partial f_a}{\partial \phi} \frac{\partial g_a}{\partial \phi}$$

$$-\int dvd\theta d\phi \sin(\theta) \frac{\nu_\parallel^{ab}(v)}{2} v^4 F_{Ma} \frac{\partial}{\partial v}\left(\frac{f_a}{F_{Ma}}\right) \frac{\partial}{\partial v}\left(\frac{g_a}{F_{Ma}}\right).$$

Since this expression is symmetric in f_a and g_a, a self-adjointness relation for the test particle operator can be written as

$$\int d^3v \frac{f_a}{F_{Ma}} C_{ab}^{T0}(g_a) = \int d^3v \frac{g_a}{F_{Ma}} C_{ab}^{T0}(f_a). \tag{3.34}$$

The previous relation gives an important property:

$$\int d^3v \frac{f_a}{F_{Ma}} C_{ab}^{T0}(f_a) = -\frac{1}{2}\int dvd\theta d\phi \frac{1}{F_{Ma}} v^2 \nu_D^{ab}(v) \sin(\theta) \left(\frac{\partial f_a}{\partial \theta}\right)^2$$

$$-\frac{1}{2}\int dvd\theta d\phi \frac{1}{F_{Ma}} v^2 \nu_D^{ab}(v) \frac{1}{\sin(\theta)} \left(\frac{\partial f_a}{\partial \phi}\right)^2 - \int dvd\theta d\phi \sin(\theta) \frac{\nu_\parallel^{ab}(v)}{2} v^4 F_{Ma} \left[\frac{\partial}{\partial v}\left(\frac{f_a}{F_{Ma}}\right)\right]^2.$$

Both $\nu_D^{ab}(v)$ and $\nu_\parallel^{ab}(v)$ are positive definite, as well as all other quantities under the integrals, so that the following is evident:

$$\int d^3v \frac{f_a}{F_{Ma}} C_{ab}^{T0}(f_a) \leq 0. \tag{3.35}$$

This property is essential for satisfying the H-theorem for arbitrary distributions. In fact, if one of the distributions in the H-theorem is set to zero, the H-theorem and the above expression become exactly the same. So this condition must hold. However, this condition is not ensured when the nonisothermal part in C_{ab}^T is included. The integral of that part is not guaranteed to be negative definite for an arbitrary distribution. This is because when the collision operator was linearized, the background was regarded as fixed compared to the perturbations, and that leads to a complication. In the isothermal case, free energy would

always flow from the perturbation to the Maxwellian background distribution, otherwise the second law of thermodynamics would be violated. However, if the background distributions are at different temperatures, then free energy can flow from the background distribution of one species to the perturbation of another species. For a situation where the background is kept fixed, this can result in free energy flowing into the system.

It is highly desirable to have a collision operator which acts as a pure sink of free energy and satisfies an H-theorem. Otherwise, one may observe artificial instabilities in any simulation which uses collisions. For this reason, the test-particle operator is replaced with a model term which satisfies an H-theorem and has a collisional asymptotic limit which is a generalization of the isothermal one. This is the same model term derived and detailed in ref. [14]. A model collision operator is sought whereby when only collisions act on the system and all perturbations are driven to an asymptotic distribution of the form

$$f_a \to F_{Ma}\left(\frac{\delta n_a}{n_a} + \frac{m_a}{T_a}u_\parallel v_\parallel + \frac{\delta T}{T}\left(\frac{v^2}{v_{Ta}^2} - \frac{3}{2}\right)\right). \tag{3.36}$$

Where $u_\parallel$ and $\delta T/T$ is the same between all species in the relaxed state. This property holds in the isothermal case, and a collisional model is sought whereby this holds also in the nonisothermal case. In creating such a model, the above formula is regarded as the collisional equilibrium for simulations where the background distributions are fixed, even though it is not a true thermal equilibrium. The starting point for the construction of such a model is the modification of the test-particle operator to ensure that the self-adjointness condition holds.

The derivation of the self-adjointness relation suggests a method for modifying the test-particle operator (same method described in ref. [14]). Suppose a self-adjoint operator, Q_{ab}, is given by

$$\int d^3v \frac{f_a}{F_{Ma}} Q_{ab} g_a = \int d^3v \frac{g_a}{F_{Ma}} Q_{ab} f_a \tag{3.37}$$

If a new collision operator, $C_{ab}^{TS}(f_a) = Q_{ab}C_{ab}^{T0}Q_{ab}(f_a)$, is defined, then the following expres-

sion can be derived:

$$\int d^3v \frac{f_a}{F_{Ma}} C_{ab}^{TS}(f_a) = -\frac{1}{2}\int \frac{dv}{F_{Ma}} d\theta d\phi v^2 \nu_D^{ab}(v)\sin(\theta)\left(\frac{\partial(Q_{ab}f_a)}{\partial\theta}\right)^2$$

$$-\frac{1}{2}\int \frac{dv}{F_{Ma}} d\theta d\phi v^2 \nu_D^{ab}(v)\frac{1}{\sin(\theta)}\left(\frac{\partial(Q_{ab}f_a)}{\partial\phi}\right)^2$$

$$-\int dv d\theta d\phi \sin(\theta)\frac{\nu_\parallel^{ab}(v)}{2} v^4 F_{Ma}\left[\frac{\partial}{\partial v}\left(\frac{Q_{ab}f_a}{F_{Ma}}\right)\right]^2 \leq 0.$$

This new operator will be guaranteed to dissipate free energy. All that is needed is some way of modeling the nonisothermal part of the test-particle operator such that the new operator has the form of $C_{ab}^{TS}(f_a)$. To do this, it will be helpful to first look at a simplified case. In typical simulations that are run using GENE, if the species are at different temperatures, they are also at dramatically different mass. If there is an additional impurity ion species, it is often assumed that the impurity species is at the same temperature as the other ion species. This is because there is a lack of measurements that would allow for distinguishing impurity and bulk ion temperatures. Therefore, the ion-electron and electron-ion collision operators shall be examined in the limit of extreme mass ratio for inspiration on how to modify the nonisothermal test-particle part of the collision operator. This will give a derivation for the same operator outlined in Sugama et al. [14] which is incorporated into GENE.

3.5 Ion-electron and electron-ion collision operators

The test-particle part of the ion-electron and electron-ion collision operators shall be examined by Taylor expanding in the limit of small $\sqrt{m_e/m_i}$ to provide inspiration for how to construct a model collision operator to ensure the self-adjointness property. Starting with the Fokker-Plank form for the electron-ion collision operator, the collision operator can be written as

$$C_{ei} = -\frac{\partial}{\partial \mathbf{v}} \cdot \mathbf{\Gamma}_{ei}$$

$$\mathbf{\Gamma}_{ei} = -\overleftrightarrow{D}_{ei} \cdot \frac{\partial f_e}{\partial \mathbf{v}} + \frac{1}{m_e} \mathbf{R}_{ei} f_e.$$

Now, for the Landau-Boltzmann operator, the following identity is used:

$$\mathbf{R}_{ab} = \frac{m_a^2}{m_b} \frac{\partial}{\partial \mathbf{v}} \cdot \overleftrightarrow{D}_{ab}.$$

To see where the above identity comes from, the definition of the resistance vector and diffusion tensor from the Landau-Boltzmann collision operator are utilized,

$$\overleftrightarrow{\mathbf{D}}_{ab} = \frac{\gamma_{ab}}{m_a^2} \int d^3 v' \overleftrightarrow{\mathbf{U}} F_b(\mathbf{v}')$$

$$\mathbf{R}_{ab} = \frac{\gamma_{ab}}{m_b} \int d^3 v' \overleftrightarrow{\mathbf{U}} \cdot \frac{\partial F_b(\mathbf{v}')}{\partial \mathbf{v}'}$$

$$\overleftrightarrow{\mathbf{U}} = \frac{u^2 \overleftrightarrow{\mathbf{I}} - \mathbf{uu}}{u^3}.$$

The previous identity can be proven with these expressions, integration by parts, and the following formula:

$$\frac{\partial}{\partial \mathbf{v}} \cdot \overleftrightarrow{\mathbf{U}} = -\frac{\partial}{\partial \mathbf{v}'} \cdot \overleftrightarrow{\mathbf{U}}.$$

Using the previous form of the resistance vector gives

$$\mathbf{\Gamma}_{ei} = -\overleftrightarrow{D}_{ei} \cdot \frac{\partial f_e}{\partial \mathbf{v}} + \frac{m_e}{m_i} \frac{\partial}{\partial \mathbf{v}} \cdot \overleftrightarrow{D}_{ei} f_e.$$

Assuming that $m_e \ll m_i$ and that the perturbed distributions vary smoothly in velocity space on scales of the ion thermal velocity, the resistive term can be ignored,

$$C_{ei} = \frac{\partial}{\partial \mathbf{v}} \cdot \overleftrightarrow{D}_{ei} \cdot \frac{\partial f_e}{\partial \mathbf{v}}.$$

The diffusion tensor is given by

$$\overleftrightarrow{D}_{ei} = \frac{2\pi e_e^2 e_i^2 \ln(\Lambda)}{m_e^2} \int d^3v' \overleftrightarrow{\mathbf{U}} f_i(v').$$

Consider the case in which the ion distribution is a Maxwellian distribution at rest. In that case, assuming that the electron distribution varies on the scale of the electron thermal velocity and that the temperatures are roughly comparable, the ion Maxwellian distribution should seem very narrow to the electrons. When compared to the normalized electron thermal velocity, the width of the electron distribution should be of order $\sim \frac{v_{Ti}}{v_{Te}} \sim \sqrt{\frac{m_e T_i}{m_i T_e}}$. Assuming that the mass ratio is sufficiently small, the width of the distribution can be neglected and replaced with a delta function: $f_i(v') = n_i \delta(v')$. The diffusion tensor then becomes

$$\overleftrightarrow{\mathbf{D}}_{ei} = \frac{2\pi n_i e_e^2 e_i^2 \ln(\Lambda)}{m_e^2} \frac{v^2 \overleftrightarrow{\mathbf{I}} - \mathbf{vv}}{v^3}.$$

Placing this tensor within the expression for the collision operator, the test-particle part of the electron-ion collision operator is obtained,

$$C_{ei}^T = \frac{2\pi n_i e_e^2 e_i^2 \ln(\Lambda)}{v m_e^2} \left(\nabla_v^2 - \frac{1}{v^2} \frac{\partial}{\partial v} v^2 \frac{\partial}{\partial v} \right) f_e$$

$$C_{ei}^T = \frac{2n_i}{v m_e^2} \mathfrak{L} f_e. \tag{3.38}$$

This is a pitch-angle scattering operator, and should obey the self-adjointness relation described previously. It was assumed earlier that the ion distribution was at rest. If it was not, then the collision operator would contain a moment of the ion distribution function. However, this correction would be part of the field-particle part of the linearized operator.

In whatever way the test-particle operator is constructed, it must be done in such a way

as to match the electron-ion test-particle operator in the small mass ratio limit. So the term which breaks the self-adjointness symmetry must be replaced with a self-adjoint model term which nearly vanishes for electron-ion collisions (but not ion-electron collisions). Now the ion-electron test-particle part of the collision operator must be derived in the limit of small mass ratio. The flux used in the operator can be expressed as

$$\mathbf{\Gamma}_{ie} = -\overleftrightarrow{D}_{ie} \cdot \frac{\partial f_i}{\partial \mathbf{v}} + \frac{1}{m_i}\mathbf{R}_{ie} f_i.$$

Now the expression for the diffusion tensor shall be obtained from the definition based on the Rosenbluth potentials:

$$\overleftrightarrow{\mathbf{D}}_{ie} = \frac{\gamma_{ie}}{m_i^2}\frac{\partial^2 G_{Me}}{\partial \mathbf{v}\partial \mathbf{v}}.$$

Since G_{Me} depends only on the magnitude of the velocity, this expression can be simplified,

$$\overleftrightarrow{\mathbf{D}}_{ie} = \frac{\gamma_{ie}}{m_i^2}\frac{\partial}{\partial \mathbf{v}}\left(\frac{\partial G_{Me}}{\partial v}\hat{\mathbf{v}}\right) = \frac{\gamma_{ie}}{m_i^2}\left(\frac{\partial^2 G_{Me}}{\partial v^2}\hat{\mathbf{v}}\hat{\mathbf{v}} + \frac{\partial G_{Me}}{\partial v}\frac{\partial}{\partial \mathbf{v}}\hat{\mathbf{v}}\right),$$

and Einstein summation notation can be used to evaluate the last term,

$$\frac{\partial}{\partial \mathbf{v}}\hat{\mathbf{v}} = \mathbf{e}_i\partial_i\frac{v_j\mathbf{e}_j}{v} = \frac{\delta_{ij}}{v}\mathbf{e}_i\mathbf{e}_j - \frac{v_i v_j}{v^3}\mathbf{e}_i\mathbf{e}_j = \frac{1}{v}\left(\overleftrightarrow{\mathbf{I}} - \frac{\mathbf{vv}}{v^2}\right)$$

giving

$$\overleftrightarrow{\mathbf{D}}_{ie} = \frac{\gamma_{ie}}{m_i^2}\left(\left(\frac{\partial^2 G_{Me}}{\partial v^2} - \frac{1}{v}\frac{\partial G_{Me}}{\partial v}\right)\hat{\mathbf{v}}\hat{\mathbf{v}} + \frac{1}{v}\frac{\partial G_{Me}}{\partial v}\overleftrightarrow{\mathbf{I}}\right).$$

Earlier, the derivatives of this Rosenbluth potential were calculated in Eq. 3.22 and 3.25. Substituting those expressions into the one above gives

$$\overleftrightarrow{\mathbf{D}}_{ie} = \frac{\gamma_{ie}}{m_i^2}\frac{n_e}{v}\left[\Big(3G(x_e) - \Phi(x_e)\Big)\hat{\mathbf{v}}\hat{\mathbf{v}} + \Big(\Phi(x_e) - G(x_e)\Big)\overleftrightarrow{\mathbf{I}}\right].$$

The structures vary on the ion-thermal velocity scale, which means that a Taylor ex-

pansion based on the small mass ratio can be performed on the coefficients of the tensor elements ($x_e = v_{Ti}\hat{v}/v_{Te} \sim O(\sqrt{m_e/m_i})$). The lowest order term in front of the first tensor is proportional to x_e^3, and the lowest order term in front of the second tensor is proportional to x_e. As such, the first tensor is ignored since it is smaller than the second by a factor of the mass ratio. Taylor expanding the coefficient in front of the second term gives

$$\Phi(x_e) - G(x_e) \simeq \frac{4}{3\sqrt{\pi}} x_e,$$

and

$$\overleftrightarrow{\mathbf{D}}_{ie} \cdot \frac{\partial f_i}{\partial \mathbf{v}} = \frac{4}{3\sqrt{\pi}} \frac{\gamma_{ie}}{m_i^2} \frac{n_e}{v_{Te}} \frac{\partial f_i}{\partial \mathbf{v}}.$$

Now an expression for the resistance vector must be obtained from the Rosenbluth potentials:

$$\mathbf{R}_{ie} = \frac{2\gamma_{ie}}{m_e} \frac{\partial H_{Me}}{\partial \mathbf{v}} = \frac{2\gamma_{ie}}{m_e} \frac{\partial H_{Me}}{\partial v} \hat{\mathbf{v}}.$$

Substituting the expression obtained earlier for the derivative (Eq. 3.24) gives

$$\mathbf{R}_{ie} = -\frac{4\gamma_{ie} n_e}{m_e v_{Te}^2} G(x_e) \hat{\mathbf{v}}.$$

The expression, $G(x_e)$, can also be Taylor expanded,

$$G(x_e) \simeq \frac{2}{3\sqrt{\pi}} x_e,$$

and the expression for the resistance vector is obtained:

$$\mathbf{R}_{ie} = -\frac{8\gamma_{ie} n_e}{3\sqrt{\pi} m_e v_{Te}^3} \mathbf{v}.$$

Substituting this into the expression for the flux gives

$$\mathbf{\Gamma}_{ie} = -\frac{4}{3\sqrt{\pi}}\frac{\gamma_{ie} n_e}{m_i^2 v_{Te}}\frac{\partial f_i}{\partial \mathbf{v}} - \frac{8}{3\sqrt{\pi}}\frac{\gamma_{ie} n_e}{m_i m_e v_{Te}^3}\mathbf{v} f_i = -\frac{4}{3\sqrt{\pi}}\frac{\gamma_{ie} n_e}{m_i v_{Te} T_e}\left[\mathbf{v} f_i + \frac{T_e}{m_i}\frac{\partial f_i}{\partial \mathbf{v}}\right].$$

From this expression, the ion-electron test-particle collision operator in the small mass ratio limit can be obtained,

$$C_{ie}^T(f_i) = \frac{4}{3\sqrt{\pi}}\frac{\gamma_{ie} n_e}{m_i v_{Te} T_e}\frac{\partial}{\partial \mathbf{v}} \cdot \left[\mathbf{v} f_i + \frac{T_e}{m_i}\frac{\partial f_i}{\partial \mathbf{v}}\right].$$

Using the identity,

$$F_{Mi}\frac{\partial}{\partial \mathbf{v}}\left(\frac{f_i}{F_{Mi}}\right) = \frac{\partial f_i}{\partial \mathbf{v}} + \frac{2\mathbf{v}}{v_{Ti}^2} f_i,$$

this expression can be rewritten in a way which clearly separates out the nonisothermal part which breaks self-adjointness,

$$C_{ie}^T(f_i) = \frac{4\gamma_{ie} n_e}{3\sqrt{\pi} m_i v_{Te} T_e}\frac{\partial}{\partial \mathbf{v}} \cdot \left[\frac{T_e}{m_i} F_{Mi}\frac{\partial}{\partial \mathbf{v}}\left(\frac{f_i}{F_{Mi}}\right) + \left(1 - \frac{T_e}{T_i}\right)\mathbf{v} f_i\right]. \tag{3.39}$$

One could achieve a self-adjoint operator by simply neglecting this term. However, for practical purposes, this is too crude of an approximation. It is expected that the linearized collision operator will drive the perturbed distribution, f_i, close to a perturbed Maxwellian (not to a complete Maxwellian, since there are the constraints that the collision operator must conserve momentum and energy). This would not be the case if the nonisothermal term were completely ignored. The momentum and free energy transfer corresponding to that term must be retained.

A better approximation can be obtained by replacing this term with a model term which gives the same momentum and energy transfer as the original term, but also satisfies the self-adjointness relation. It is also required that the new term vanishes when acting on a Maxwellian. One approach to doing this is to replace the divergence term with a quadratic polynomial in v multiplying a simple distribution such as a Maxwellian, and then determining

the coefficients such that one can reproduce the same energy and momentum transfer (one can then verify if this term is self-adjoint):

$$\frac{\partial}{\partial \mathbf{v}} \cdot (\mathbf{v} f_i) \rightarrow \left(a(f_i) + \mathbf{b}(f_i) \cdot \mathbf{v} + c(f_i) x_i^2 \right) F_{Mi}.$$

The integral of this term over velocity space is zero since the distribution function approaches zero as $v \rightarrow \infty$ and since the middle term is odd in v. This gives the constraint:

$$\int d^3v (a + c x_i^2) e^{-x_i^2} = 0$$

$$\int_0^\infty dx x^2 (a + c x^2) e^{-x^2} = 0.$$

The values of these integrals can be found in any standard table of integrals. Evaluating them and solving for a in terms of c gives $a = -3c/2$. The earlier expression can thus be simplified to

$$\frac{\partial}{\partial \mathbf{v}} \cdot \left(\mathbf{v} f_i \right) \rightarrow \left(a(f_i)(x_i^2 - \frac{3}{2}) + \mathbf{b}(f_i) \cdot \mathbf{v} \right) F_{Mi}.$$

The vector, $\mathbf{b}$, can be determined by matching the momentum transfer of the two terms. The momentum transfer of the original term is given by

$$\int d^3v m_i \mathbf{v} \frac{\partial}{\partial \mathbf{v}} \cdot \left(\mathbf{v} f_i \right) = -m_i n_i \mathbf{u}_i(f_i).$$

Where $\mathbf{u}_i(f_i) = (1/n_i) \int d^3v \mathbf{v} f_i$ has been defined so as to use the same notation as Sugama et al. [14]. Now the analogous term on the right hand side is evaluated in cylindrical velocity space coordinates as

$$\int d^3v \mathbf{b} \cdot \mathbf{v} f_{Mi} m_i \mathbf{v} = \int dv_\perp v_\perp d\phi dv_z b v_z m_i F_{Mi} (v_\perp \hat{\mathbf{v}}_\perp + v_z \hat{\mathbf{v}}_z).$$

The expression in front of the first vector vanishes because it is odd in v_z. The other part

becomes

$$\int d^3v \mathbf{b}\cdot\mathbf{v} f_{Mi} m_i \mathbf{v} = \frac{2\pi n_i b m_i}{\pi^{3/2} v_{Ti}^3} \int_0^\infty dv_\perp v_\perp e^{-(v_\perp/v_{Ti})^2} \int_{-\infty}^\infty dv_z v_z^2 e^{-(v_z/v_{Ti})^2} \hat{\mathbf{v}}_z.$$

The expression for the integrals can again be looked up in a table:

$$\int d^3v \mathbf{b}\cdot\mathbf{v} F_{Mi} m_i \mathbf{v} = \frac{\pi n_i b m_i v_{Ti}^2}{\pi^{3/2}} \frac{\sqrt{\pi}}{2} = n_i b T_i \hat{\mathbf{v}}_z = n_i T_i \mathbf{b}.$$

From this equation, one can see

$$\mathbf{b}(f_i) = -\frac{m_i}{T_i}\mathbf{u}_i(f_i).$$

And the earlier expression further simplifies as

$$\frac{\partial}{\partial \mathbf{v}}\cdot\big(\mathbf{v} f_i\big) \to \left(a(f_i)(x_i^2 - \frac{3}{2}) - \frac{m_i}{T_i}\mathbf{u}_i(f_i)\cdot\mathbf{v}\right) F_{Mi}.$$

Now the energy transfer of the final term is examined to determine the final coefficient:

$$\int d^3v \frac{1}{2} m_i v^2 \frac{\partial}{\partial \mathbf{v}}\cdot\big(\mathbf{v} f_i\big) = -\int d^3v m_i v^2 f_i.$$

Evaluating the analogous term on the other side of the equation gives

$$\int d^3v \frac{1}{2} m_i v^2 a\left(x_i^2 - \frac{3}{2}\right) F_{Mi} = a T_i \frac{n_i}{\pi^{3/2} v_{Ti}^3} 4\pi \int_0^\infty dv v^2 x_i^2 \left(x_i^2 - \frac{3}{2}\right) e^{-x_i^2}$$

$$= \frac{4 a T_i n_i}{\sqrt{\pi}} \int_0^\infty dx x^4 \left(x^2 - \frac{3}{2}\right) e^{-x^2}.$$

Again, evaluating the expression using a table of integrals gives

$$\int d^3v \frac{1}{2} m_i v^2 a\left(x_i^2 - \frac{3}{2}\right) f_{Mi} = \frac{4 a T_i n_i}{\sqrt{\pi}} \left(\frac{15}{16}\sqrt{\pi} - \frac{9}{16}\sqrt{\pi}\right) = \frac{3}{2} a T_i n_i,$$

therefore

$$a(f_i) = -\frac{2}{3n_i T_i}\int d^3v m_i v^2 f_i$$

$$\frac{\partial}{\partial \mathbf{v}}\cdot(\mathbf{v}f_i) \rightarrow -\frac{2}{3n_i T_i}\left(\int d^3v m_i v^2 f_i\right)\left(x_i^2 - \frac{3}{2}\right)F_{Mi} - \frac{m_i}{T_i}\mathbf{u}_i(f_i)\cdot\mathbf{v}F_{Mi}.$$

There is a problem with the above expression. It does not vanish for a Maxwellian distribution, whereas the previous term did. This is an essential property of the collision operator, so the model for the term must be further modified. The energy carried by a Maxwellian distribution with arbitrary amplitude in this term should clearly be zero, so a reasonable guess would be to simply add $\frac{2}{3n_i T_i}\frac{\int d^3v f_i}{n_i}(\int d^3v m_i v^2 F_{Mi})(x_i^2 - \frac{3}{2})F_{Mi}$ to the above expression so that it vanishes for a Maxwellian with arbitrary amplitude. So the new expression becomes

$$\frac{\partial}{\partial \mathbf{v}}\cdot(\mathbf{v}f_i) \rightarrow -\frac{4}{3n_i T_i}\left(\int d^3v \frac{1}{2}m_i v^2 f_i - \frac{3}{2}T_i\int d^3v f_i\right)\left(x_i^2 - \frac{3}{2}\right)F_{Mi} - \frac{m_i}{T_i}\mathbf{u}_i(f_i)\cdot\mathbf{v}F_{Mi}.$$

The divergent term breaking self-adjointness has been replaced by a model operator which replicates the same momentum and free energy transfer as the original term. By replicating the same free energy transfer, but not the same total energy transfer, the nonisothermal system is essentially regarded as an equilibrium. While this is not a reasonable assumption for systems where thermalization plays an important role, it should be reasonable for delta-f gyrokinetic simulations where the background profiles are regarded as fixed, and the only concern is replicating gyrokinetic turbulence and transport for a given plasma discharge (the evolution of the background profiles are negligible compared to the perturbed distribution for turbulent time scales). The validity of the final linearized model collision operator shall be discussed in more detail in the next section. For now, it is assumed that the divergent term can be written in the following way:

$$\frac{\partial}{\partial \mathbf{v}} \cdot \left(\mathbf{v} f_i\right) \rightarrow -2\frac{\delta T_i(f_i)}{T_i}\left(x_i^2 - \frac{3}{2}\right)F_{Mi} - \frac{m_i}{T_i}\mathbf{u}_i(f_i)\cdot\mathbf{v}F_{Mi}. \tag{3.40}$$

Where the following integral moment has been introduced to follow the notation used in [14]:

$$\frac{\delta T_i(f_i)}{T_i} = \frac{1}{n_i}\int d^3v f_i\left(\frac{m_i v^2}{3T_i} - 1\right). \tag{3.41}$$

Substituting this term for the term which breaks self-adjointness, the following ion-electron collision operator is obtained:

$$C_{ie}^{TS}(f_i) = \frac{4\gamma_{ie}n_e}{3\sqrt{\pi}m_i T_e v_{Te}}\left(\frac{\partial}{\partial \mathbf{v}}\cdot\left(\frac{T_e}{m_i}F_{Mi}\frac{\partial}{\partial \mathbf{v}}\left(\frac{f_i}{F_{Mi}}\right)\right)\right.$$

$$\left.-\left(1-\frac{T_e}{T_i}\right)F_{Mi}\left(\frac{m_i}{T_i}\mathbf{u}_i(f_i)\cdot\mathbf{v} + 2\frac{\delta T_i(f_i)}{T_i}\left(x_i^2-\frac{3}{2}\right)\right)\right).$$

This can be written in operator notation (same as the Sugama et al.) as

$$C_{ie}^{TS}(f_i) = C_{ie}^{T0}(f_i) - \frac{4\gamma_{ie}n_e}{3\sqrt{\pi}m_i T_e v_{Te}}\left(1-\frac{T_e}{T_i}\right)\left(P_{1i}+2P_{2i}\right)f_i. \tag{3.42}$$

Where P_{1i} and P_{2i} can be viewed as projection operators,

$$P_{1i}(f) = F_{Mi}\frac{m_i}{T_i}\mathbf{v}\cdot\mathbf{u}_i(f) \tag{3.43}$$

$$P_{2i}(f) = F_{Mi}\frac{\delta T_i(f)}{T_i}\left(x_i^2 - \frac{3}{2}\right). \tag{3.44}$$

And the self-adjoint part of the ion-electron collision operator, $C_{ie}^{T0}(f_i)$, is given by

$$C_{ie}^{T0}(f_i) = \frac{4\gamma_{ie}n_e}{3\sqrt{\pi}m_i T_e v_{Te}}\frac{\partial}{\partial \mathbf{v}}\cdot\left(\frac{T_e}{m_i}F_{Mi}\frac{\partial}{\partial \mathbf{v}}\left(\frac{f_i}{F_{Mi}}\right)\right). \tag{3.45}$$

One can verify that P_{1i} and P_{2i} satisfy the self-adjointness relation, $\int d^3v \frac{h}{F_{Mi}}P_i(g) = \int d^3v \frac{g}{F_{Mi}}P_i(h)$ as well as $(P_{1i})^2 = P_{1i}$, $(P_{2i})^2 = P_{2i}$, and $P_{1i}P_{2i} = P_{2i}P_{1i}$. Since the operator is now self-

adjoint, it is desirable to rewrite the collision operator as $C_{ie}^{TS} = Q_{ie} C_{ie}^{T0} Q_{ie}$, so that the free energy dissipation property can be more clearly expressed. The assumption will be made that Q_{ie} takes the following form:

$$Q_{ie}(f) = f + AP_{1i}(f) + BP_{2i}(f).$$

Now $Q_{ie} C_{ie}^{T0} Q_{ie}$ is evaluated, and A and B are solved for by matching the coefficients of the projection operators in the equation $C_{ie}^{TS} = Q_{ie} C_{ie}^{T0} Q_{ie}$:

$$\frac{\partial}{\partial \mathbf{v}} \left(\frac{Q_{ie} f}{F_{Mi}} \right) = \frac{\partial}{\partial \mathbf{v}} \left(\frac{f}{F_{Mi}} \right) + A \frac{m_i}{T_i} \mathbf{u}_i(f) + B \frac{\delta T_i(f)}{T_i} \frac{2\mathbf{v}}{v_{Ti}^2}$$

$$\frac{\partial}{\partial \mathbf{v}} \cdot \left[F_{Mi} \frac{\partial}{\partial \mathbf{v}} \left(\frac{Q_{ie} f}{F_{Mi}} \right) \right] = \frac{\partial}{\partial \mathbf{v}} \cdot \left[F_{Mi} \frac{\partial}{\partial \mathbf{v}} \left(\frac{f}{F_{Mi}} \right) \right]$$

$$-A \frac{m_i}{T_i} \mathbf{u}_i(f) \cdot \left(\frac{2\mathbf{v}}{v_{Ti}^2} \right) F_{Mi} + B \frac{\delta T_i(f)}{T_i} \frac{2}{v_{Ti}^2} F_{Mi} \left(3 - \frac{2v^2}{v_{Ti}^2} \right)$$

$$\frac{T_e}{m_i} \frac{\partial}{\partial \mathbf{v}} \cdot \left[F_{Mi} \frac{\partial}{\partial \mathbf{v}} \left(\frac{Q_{ie} f}{F_{Mi}} \right) \right] = \frac{T_e}{m_i} \frac{\partial}{\partial \mathbf{v}} \cdot \left[F_{Mi} \frac{\partial}{\partial \mathbf{v}} \left(\frac{f}{F_{Mi}} \right) \right] - \frac{T_e}{T_i} A P_{1i}(f) - 2B \frac{T_e}{T_i} P_{2i}(f).$$

Using

$$\mathbf{u}_i \left(\frac{T_e}{m_i} \frac{\partial}{\partial \mathbf{v}} \cdot \left[F_{Mi} \frac{\partial}{\partial \mathbf{v}} \left(\frac{f}{F_{Mi}} \right) \right] \right)$$

$$= -\frac{T_e}{m_i n_i} \int d^3 v F_{Mi} \frac{\partial}{\partial \mathbf{v}} \left(\frac{f}{F_{Mi}} \right) = -\frac{T_e}{m_i n_i} \int d^3 v \frac{2\mathbf{v}}{v_{Ti}^2} f = -\frac{T_e}{T_i} \mathbf{u}_i(f)$$

$$P_{1i} \left(\frac{T_e}{m_i} \frac{\partial}{\partial \mathbf{v}} \cdot \left[F_{Mi} \frac{\partial}{\partial \mathbf{v}} \left(\frac{f}{F_{Mi}} \right) \right] \right) = -\frac{T_e}{T_i} P_{1i}(f)$$

and

$$\frac{\delta T_i}{T_i}\left(\frac{T_e}{m_i}\frac{\partial}{\partial \mathbf{v}}\cdot\left[F_{Mi}\frac{\partial}{\partial \mathbf{v}}\left(\frac{Q_{ie}f}{F_{Mi}}\right)\right]\right) = \frac{T_e}{m_i n_i}\int d^3v\left(\frac{m_i v^2}{3T_i}-1\right)\frac{\partial}{\partial \mathbf{v}}\cdot\left[F_{Mi}\frac{\partial}{\partial \mathbf{v}}\left(\frac{f}{F_{Mi}}\right)\right]$$

$$= -\frac{2T_e}{3m_i n_i}\int d^3v \frac{m_i}{T_i}\mathbf{v}\cdot\left[F_{Mi}\frac{\partial}{\partial \mathbf{v}}\left(\frac{f}{F_{Mi}}\right)\right]$$

$$= \frac{2T_e}{3n_i T_i}\int d^3v \frac{f}{F_{Mi}}\frac{\partial}{\partial \mathbf{v}}\cdot\left(\mathbf{v}F_{Mi}\right)$$

$$= -\frac{2T_e}{n_i T_i}\int d^3v\left(\frac{m_i v^2}{3T_i}-1\right)f = -2\frac{T_e}{T_i}\frac{\delta T_i}{T_i}(f)$$

$$P_{2i}\left(\frac{T_e}{m_i}\frac{\partial}{\partial \mathbf{v}}\cdot\left[F_{Mi}\frac{\partial}{\partial \mathbf{v}}\left(\frac{Q_{ie}f}{F_{Mi}}\right)\right]\right) = -\frac{2T_e}{T_i}P_{2i}(f),$$

the final expression for $Q_{ie}C_{ie}^{T0}Q_{ie}$ is given by

$$Q_{ie}\left(\frac{T_e}{m_i}\frac{\partial}{\partial \mathbf{v}}\cdot\left[F_{Mi}\frac{\partial}{\partial \mathbf{v}}\left(\frac{Q_{ie}f}{F_{Mi}}\right)\right]\right) =$$

$$\frac{T_e}{m_i}\frac{\partial}{\partial \mathbf{v}}\cdot\left[F_{Mi}\frac{\partial}{\partial \mathbf{v}}\left(\frac{f}{F_{Mi}}\right)\right] - \frac{T_e}{T_i}A(2+A)P_{1i}(f) - 2B(2+B)\frac{T_e}{T_i}P_{2i}(f).$$

Matching the coefficients of the projection operators so that the above expression agrees with C_{ie}^{TS}, the following is obtained:

$$A = B$$

$$-\frac{T_e}{T_i}A(2+A) = -\left(1-\frac{T_e}{T_i}\right).$$

Solving this quadratic gives

$$A = \pm\sqrt{\frac{T_i}{T_e}} - 1.$$

The positive root is chosen so that the new term vanishes in the isothermal case, as it should. This gives the final form of the self-adjoint model ion-electron and electron-ion collision operators,

$$C_{ie}^{TS}(f_i) = Q_{ie} C_{ie}^{T0} Q_{ie}(f_i) \tag{3.46}$$

$$Q_{ie}(f) = f + \left(\sqrt{\frac{T_i}{T_e}} - 1\right) P_i(f) \tag{3.47}$$

$$P_i(f) = F_{Mi}\frac{m_i}{n_i T_i}\mathbf{v} \cdot \int d^3v \mathbf{v} f + F_{Mi}\left(x_i^2 - \frac{3}{2}\right)\frac{1}{n_i}\int d^3v \left(\frac{m_i v^2}{3T_i} - 1\right) f \tag{3.48}$$

$$C_{ei}^{TS}(f_e) = C_{ei}^{T0}(f_e). \tag{3.49}$$

3.6 Generalization of self-adjoint collision operator to multiple species

A self-adjoint two species test-particle collision operator has been derived. It is useful to write the collision operator in a generalized form that could be applied to multiple species. This generalized model shall have the same form as in ref. [14],

$$C_{ab}^{TS}(f_a) = Q_{ab} C_{ab}^{T0} Q_{ab}(f_a) \tag{3.50}$$

$$Q_{ab}(f) = f + (\theta_{ab} - 1) P_a(f) \tag{3.51}$$

$$P_a(f) = F_{Ma}\frac{m_a}{T_a}\mathbf{v} \cdot \mathbf{u}_a(f) + F_{Ma}\left(x_a^2 - \frac{3}{2}\right)\frac{\delta T_a(f)}{T_a} \tag{3.52}$$

$$\mathbf{u}_a(f_a) = \frac{1}{n_a}\int d^3v \mathbf{v} f_a \tag{3.53}$$

$$\frac{\delta T_a(f_a)}{T_a} = \frac{1}{n_a}\int d^3v f_a\left(\frac{m_a v^2}{3T_a} - 1\right). \tag{3.54}$$

θ_{ab} should approach unity if $m_a \ll m_b$ and $\sqrt{\frac{T_a}{T_b}}$ if $m_a \gg m_b$. That way, the new self-adjoint collision operator should agree with the one obtained for collisions between ions and electrons. The following form for θ_{ab} shall be chosen, consistent with Sugama et al.:

$$\theta_{ab} = \sqrt{\frac{T_a(m_a + m_b)}{(T_a m_b + T_b m_a)}}. \tag{3.55}$$

This provides a self-adjoint operator that can be applied to any number of species. Furthermore, since Q_{ab} satisfies the self-adjointness property, the following integral moment can be written as

$$\int d^3v \frac{f_a}{F_{Ma}} C_{ab}^{TS}(f_a) = -\frac{1}{2}\int \frac{dv}{F_{Ma}} d\theta d\phi v^2 \nu_D^{ab}(v) sin(\theta)\left(\frac{\partial(Q_{ab}f_a)}{\partial\theta}\right)^2$$

$$-\frac{1}{2}\int \frac{dv}{F_{Ma}} d\theta d\phi v^2 \nu_D^{ab}(v)\frac{1}{sin(\theta)}\left(\frac{\partial(Q_{ab}f_a)}{\partial\phi}\right)^2$$

$$-\int dv d\theta d\phi sin(\theta)\frac{\nu_\parallel^{ab}(v)}{2} v^4 F_{Ma}\left[\frac{\partial}{\partial v}\left(\frac{Q_{ab}f_a}{F_{Ma}}\right)\right]^2.$$

The derivation of this equation is very similar to the one used previously. One simply has to use the self-adjointness relation for Q_{ab}. From this one can see

$$\int d^3v \frac{f_a}{F_{Ma}} C_{ab}^{TS}(f_a) \leq 0.$$

Equality will hold in the above formula only if the quantities $\frac{\partial(Q_{ab}f_a)}{\partial\theta}$, $\frac{\partial(Q_{ab}f_a)}{\partial\phi}$, and $\frac{\partial}{\partial v}\left(\frac{Q_{ab}f_a}{F_{Ma}}\right)$ are all zero everywhere in velocity space (all of the other quantities are positive definite inside of the integral). This will only be true if $Q_{ab}f_a \propto F_{Ma}$. Since $Q_{ab}F_{Ma} = F_{Ma}$, this implies

that the free energy dissipation from the test-particle part vanishes only if the distribution is proportional to a Maxwellian,

$$\int d^3v \frac{f_a}{F_{Ma}} C_{ab}^{TS}(f_a) = 0 \Leftrightarrow f_a = F_{Ma}\frac{\delta n_a}{n_a} \tag{3.56}$$

$$\delta n_a = \int d^3v f_a. \tag{3.57}$$

So the new test-particle part of the collision operator should dissipate free energy for an arbitrary distribution function. The test-particle part of the collision operator can be written more explicitly,

$$C_{ab}^{TS}(f_a) = C_{ab}^{T0}(f_a) + (\theta_{ab}-1)(P_a C_{ab}^{T0}(f_a) + C_{ab}^{T0}P_a(f_a)) + (\theta_{ab}-1)^2 P_a C_{ab}^{T0} P_a(f_a) \tag{3.58}$$

$$P_a C_{ab}^{T0}(f_a) = F_{Ma}\frac{m_a}{n_a T_a}\mathbf{v}\cdot\int d^3v \mathbf{v} C_{ab}^{T0}(f_a) + F_{Ma}\frac{1}{n_a}\left(x_a^2 - \frac{3}{2}\right)\int d^3v\left(\frac{m_a v^2}{3T_a} - 1\right) C_{ab}^{T0}(f_a).$$

The self-adjointness relation and the fact that the collision operator conserves particles can be used to write this expression as

$$P_a C_{ab}^{T0}(f_a) = F_{Ma}\frac{m_a}{n_a T_a}\mathbf{v}\cdot\int d^3v \frac{f_a}{F_{Ma}} C_{ab}^{T0}(F_{Ma}\mathbf{v}) + F_{Ma}\frac{2}{3n_a}\left(x_a^2 - \frac{3}{2}\right)\int d^3v \frac{f_a}{F_{Ma}} C_{ab}^{T0}(F_{Ma}x_a^2). \tag{3.59}$$

In addition,

$$C_{ab}^{T0}P_a(f_a) = \frac{m_a}{T_a}\mathbf{u}_a(f_a)\cdot C_{ab}^{T0}(F_{Ma}\mathbf{v}) + \frac{\delta T_a(f_a)}{T_a} C_{ab}^{T0}(F_{Ma}x_a^2). \tag{3.60}$$

Where the fact that the collision operator vanishes when acting on a Maxwellian has been

utilized. The expression for $P_a C_{ab}^{T0} P_a$ can be written as

$$P_a C_{ab}^{T0} P_a(f_a) = F_{Ma}\left[\frac{m_a}{n_a T_a}\mathbf{v}\cdot\int d^3v \frac{m_a}{T_a}\mathbf{u}(f_a)\cdot C_{ab}^{T0}(F_{Ma}\mathbf{v})\mathbf{v}\right.$$

$$\left. + \frac{1}{n_a}\left(x_a^2 - \frac{3}{2}\right)\int d^3v \frac{\delta T_a(f_a)}{T_a} C_{ab}^{T0}(F_{Ma}x_a^2)\left(\frac{m_a v^2}{3T_a} - 1\right)\right]. \tag{3.61}$$

Using the fact that only the component along $\mathbf{u}_a(f_a)$ survives in the first integral, and the fact that the integral over only the collision operator is zero in the second integral,

$$P_a C_{ab}^{T0} P_a(f_a) = F_{Ma}\left[\frac{m_a}{T_a}\mathbf{u}_a(f_a)\cdot\mathbf{v}\frac{1}{n_a}\int d^3v \frac{m_a\mathbf{v}}{3T_a}\cdot C_{ab}^{T0}(F_{Ma}\mathbf{v})\right.$$

$$\left. + \frac{\delta T_a(f_a)}{T_a}\left(x_a^2 - \frac{3}{2}\right)\frac{1}{n_a}\int d^3v \frac{2}{3}x_a^2 C_{ab}^{T0}(F_{Ma}x_a^2)\right]. \tag{3.62}$$

The field-particle part of the collision operator can also be generalized from Eq. 3.16:

$$C_{ba}^F(f_a) = -\frac{T_a C_{ba}^{TS}\left(\frac{F_{Mb}m_b\mathbf{v}}{T_b}\right)\cdot\int d^3v \frac{m_a\mathbf{v}}{T_a}C_{ab}^{TS}(f_a)}{\gamma_{ba}} - \frac{T_a C_{ba}^{TS}(F_{Mb}x_b^2)\int d^3v x_a^2 C_{ab}^{TS}(f_a)}{\eta_{ba}}. \tag{3.63}$$

Where γ_{ab} and η_{ab} have been defined as

$$\gamma_{ab} = T_a\int d^3v \frac{m_a v_\parallel}{T_a}C_{ab}^{TS}\left(F_{Ma}\frac{m_a v_\parallel}{T_a}\right) \tag{3.64}$$

$$\eta_{ab} = T_a\int d^3v x_a^2 C_{ab}^{TS}(F_{Ma}x_a^2). \tag{3.65}$$

Eq. 3.64 and 3.65 can be written in a more simplified way using the representation $C_{ab}^{TS} = Q_{ab}C_{ab}^{T0}Q_{ab}$, the fact that Q_{ab} is a self-adjoint operator, $Q_{ab}F_{Ma}\frac{m_a v_\parallel}{T_a} = \theta_{ab}F_{Ma}\frac{m_a v_\parallel}{T_a}$, and $Q_{ab}F_{Ma}x_a^2 = \theta_{ab}F_{Ma}x_a^2 - \frac{3}{2}(\theta_{ab}-1)F_{Ma}$:

$$\gamma_{ab} = \theta_{ab}^2 T_a \int d^3v \frac{m_a v_\parallel}{T_a} C_{ab}^{T0}\left(F_{Ma}\frac{m_a v_\parallel}{T_a}\right)$$

$$\eta_{ab} = \theta_{ab}^2 T_a \int d^3v x_a^2 C_{ab}^{T0}(F_{Ma} x_a^2).$$

These integrals can be evaluated in a straightforward manner, and this is done in section 3.8. The result is shown in Eq. 3.84 and 3.85. Using these expressions, γ_{ab} and η_{ab} can be written in very simplified expressions,

$$\gamma_{ab} = -\frac{16\sqrt{\pi}}{3}\frac{n_a n_b q_a^2 q_b^2 ln(\Lambda)}{(v_{Ta}^2 + v_{Tb}^2)^{3/2}}\left(\frac{1}{m_a} + \frac{1}{m_b}\right)$$

$$\eta_{ab} = -8\sqrt{\pi}\ln(\Lambda)\frac{n_a n_b q_a^2 q_b^2 v_{Ta}^2 v_{Tb}^2}{(v_{Ta}^2 + v_{Tb}^2)^{5/2}}\left(\frac{1}{m_a} + \frac{1}{m_b}\right).$$

It can be seen from the above expressions that $\gamma_{ab} = \gamma_{ba}$ and $\eta_{ab} = \eta_{ba}$. When evaluating the integral moment, $T_b \int d^3v \frac{f_b}{F_{Mb}} C_{ab}^F(f_a)$, it is clear (when using the self-adjointness relations corresponding to the test-particle part) that the expression is symmetric in the indices a and b. This gives a self-adjointness relation for the field-particle part,

$$T_a \int d^3v \frac{f_a}{F_{Ma}} C_{ab}^F(f_b) = T_b \int d^3v \frac{f_b}{F_{Mb}} C_{ba}^F(f_a). \tag{3.66}$$

This completes the derivation of the linearized model collision operator in the drift-kinetic limit. The proof that this operator satisfies the H-theorem and acts to drive distributions toward a simple perturbed Maxwellian is given in the following section. The reader may wonder after this derivation whether the construction of such a model operator is truly justified. They may wonder whether any important physics has been lost in the replacement of the field-particle part or the nonisothermal test-particle part with models designed to enforce conservation and symmetry properties.

A key fact in this regard is that more advanced collision models cannot be used in the GENE code because the background profiles must be regarded as fixed. It is furthermore

not clear how one would devise a gyrokinetic model which evolves both the perturbed distribution on the fast turbulence timescale and the background distribution on the slow heating timescale in one simulation with no numerical difficulties. Creating a code or upgrading GENE to a code which does this would be a difficult task.

One could devise a collision operator for a full-f model, and there are plans for creating a version of GENE that would simulate gyrokinetic turbulence in the scrape-off layer of a magnetic confinement device with such a model. However, there are also difficulties in this area. For full-f simulations with a nonlinear Landau-Boltzmann operator, one would be faced with the nonlocal nature of the collisions, and a convolution integral would have to be performed which would be computationally expensive. There are also numerical difficulties that have been encountered in such endeavors, such as the distribution function becoming negative from application of the collision operator. Additionally, incorporating FLR corrections into such an operator would be difficult.

It is not clear that model operators truncate significant physics. It could be that as long as pitch-angle scattering and energy diffusion are retained in the operator, then the other terms, as well as the exact size of the free energy sink are not as important, so long as appropriate conservation and symmetry properties are retained to prevent strange numerical features. To truly determine the validity of the collision model, however, requires a comparison with a more complete collision model. This has already been done for a neoclassical scenario in ref. [60] for an isothermal parameter set.

3.7 Proof of H-theorem

It has been shown that the test-particle part of the collision operator dissipates free energy, but it remains to be shown that the complete operator dissipates free energy. It also remains to be determined what distributions the collisions will drive the system towards. This shall be investigated in this section in the same way it has been investigated in Appendix A of ref. [14]. Consider the following operator acting on pairs of distribution functions:

$$[f_a, f_b|g_a, g_b] = -T_a \int d^3v \frac{f_a}{F_{Ma}} C_{ab}^{TS}(g_a) - T_b \int d^3v \frac{f_b}{F_{Mb}} C_{ba}^{TS}(g_b).$$

From Eq. 3.56 it is clear that this expression is positive definite for certain distributions,

$$[f_a, f_b|f_a, f_b] \geq 0.$$

One can then evaluate $[\lambda f_a - g_a, \lambda f_a - g_a|\lambda f_a - g_a, \lambda f_a - g_a]$ (which must be greater than zero) as a quadratic polynomial in λ, $a\lambda^2 + b\lambda + c$. Since $[\lambda f_a - g_a, \lambda f_a - g_a|\lambda f_a - g_a, \lambda f_a - g_a] \geq 0$ for arbitrary λ, this requires that the discriminant be less than or equal to zero: $b^2 - 4ac \leq 0$. Equating the coefficients with the proper terms gives an essential inequality,

$$[f_a, f_b|f_a, f_b][g_a, g_b|g_a, g_b] \geq [f_a, f_b|g_a, g_b]^2. \tag{3.67}$$

For the derivation of the H-theorem, it is convenient to decompose the distribution function into spherical harmonics,

$$f(\mathbf{v}) = \sum_{l=0}^{\infty} \sum_{m=-l}^{l} F_{l,m}(v) Y_l^m(\theta, \phi) = f^{\text{odd}}(\mathbf{v}) + f^{\text{even}}(\mathbf{v}).$$

First the odd components (odd values of l) shall be considered. Setting $g_a = F_{Ma} m_a v_\parallel / T_a$ and $g_b = F_{Mb} m_b v_\parallel / T_b$ (where $\parallel$ denotes an arbitrary direction in this case, although it shall be taken to parameterize the velocity component along the magnetic field later), Eq. 3.67 gives

$$(\gamma_{ab} + \gamma_{ba}) \left(T_a \int d^3v \frac{f_a^{\text{odd}}}{F_{Ma}} C_{ab}^{TS}(f_a^{\text{odd}}) + T_b \int d^3v \frac{f_b^{\text{odd}}}{F_{Mb}} C_{ba}^{TS}(f_b^{\text{odd}}) \right)$$

$$\geq \left(T_a \int d^3v \frac{f_a^{\text{odd}}}{F_{Ma}} C_{ab}^{TS}\left(F_{Ma} \frac{m_a v_\parallel}{T_a} \right) + T_b \int d^3v \frac{f_b^{\text{odd}}}{F_{Mb}} C_{ba}^{TS}\left(F_{Mb} \frac{m_b v_\parallel}{T_b} \right) \right)^2.$$

The following relation is also useful:

$$\left(T_a \int d^3v \frac{f_a^{\text{odd}}}{F_{Ma}} C_{ab}^{TS}\left(F_{Ma}\frac{m_a v_\parallel}{T_a}\right) - T_b \int d^3v \frac{f_b^{\text{odd}}}{F_{Mb}} C_{ba}^{TS}\left(F_{Mb}\frac{m_b v_\parallel}{T_b}\right)\right)^2 \geq 0.$$

Furthermore

$$\left(T_a \int d^3v \frac{f_a^{\text{odd}}}{F_{Ma}} C_{ab}^{TS}\left(F_{Ma}\frac{m_a v_\parallel}{T_a}\right)\right)^2 + \left(T_b \int d^3v \frac{f_b^{\text{odd}}}{F_{Mb}} C_{ba}^{TS}\left(F_{Mb}\frac{m_b v_\parallel}{T_b}\right)\right)^2$$

$$\geq 2\left(T_a \int d^3v \frac{f_a^{\text{odd}}}{F_{Ma}} C_{ab}^{TS}\left(F_{Ma}\frac{m_a v_\parallel}{T_a}\right)\right)\left(T_b \int d^3v \frac{f_b^{\text{odd}}}{F_{Mb}} C_{ba}^{TS}\left(F_{Mb}\frac{m_b v_\parallel}{T_b}\right)\right),$$

and using the fact that $\gamma_{ab} = \gamma_{ba}$, the previous relation can be rewritten as

$$2\gamma_{ab}\left(T_a \int d^3v \frac{f_a^{\text{odd}}}{F_{Ma}} C_{ab}^{TS}(f_a^{\text{odd}}) + T_b \int d^3v \frac{f_b^{\text{odd}}}{F_{Mb}} C_{ba}^{TS}(f_b^{\text{odd}})\right)$$

$$\geq 4\left(T_a \int d^3v \frac{f_a^{\text{odd}}}{F_{Ma}} C_{ab}^{TS}\left(F_{Ma}\frac{m_a v_\parallel}{T_a}\right)\right)\left(T_b \int d^3v \frac{f_b^{\text{odd}}}{F_{Mb}} C_{ba}^{TS}\left(F_{Mb}\frac{m_b v_\parallel}{T_b}\right)\right).$$

Using the definition of the field-particle part of the collision operator, as well as $\gamma_{ab} < 0$, the H-theorem for the odd spherical harmonic components of the distribution function can be proven,

$$T_a \int d^3v \frac{f_a^{\text{odd}}}{F_{Ma}}\left(C_{ab}^{TS}(f_a^{\text{odd}}) + C_{ab}^{F}(f_b^{\text{odd}})\right) + T_b \int d^3v \frac{f_b^{\text{odd}}}{F_{Mb}}\left(C_{ba}^{TS}(f_b^{\text{odd}}) + C_{ba}^{F}(f_a^{\text{odd}})\right) \leq 0. \quad (3.68)$$

Now that the H-theorem has been proven, the equilibrium solution for which the left-hand side equates to zero remains to be found. Given that $C_{ab}^{TS}\left(F_{Ma}\frac{m_a \mathbf{v}}{T_a}\right) \parallel \mathbf{v}$, and that the spherical harmonics are orthogonal functions, the field-particle part of the collision operator acting on all odd components of the distribution function with $l > 1$ vanishes. So the inequality for the higher order odd spherical harmonics can be written as

$$T_a \int d^3v \frac{f_a^{\text{odd},l>1}}{F_{Ma}} C_{ab}^{TS}(f_a^{\text{odd},l>1}) + T_b \int d^3v \frac{f_b^{\text{odd},l>1}}{F_{Mb}} C_{ba}^{TS}(f_b^{\text{odd},l>1}) \leq 0.$$

All of the above integrals will vanish unless the distributions are proportional to a Maxwellian distribution, which by definition, they never will be. So these higher order spherical harmonics are continuously damped. So the equilibrium distribution for this case will correspond to $l = 1$ and be proportional to $v_\parallel$. One can assume solutions of the following form:

$$f_a^{l=1} = A(v) F_{Ma} \frac{m_a v_\parallel}{T_a}$$

$$f_b^{l=1} = B(v) F_{Mb} \frac{m_b v_\parallel}{T_b}.$$

Plugging these formulas into the H-theorem and imposing equality gives the following equation:

$$\gamma_{ab} T_a \int d^3v A(v) \frac{m_a v_\parallel}{T_a} C_{ab}^{TS} \left(A(v) F_{Ma} \frac{m_a v_\parallel}{T_a} \right) + \gamma_{ab} T_b \int d^3v B(v) \frac{m_b v_\parallel}{T_b} C_{ba}^{TS} \left(B(v) F_{Mb} \frac{m_b v_\parallel}{T_b} \right)$$

$$-2 T_a T_b \left(\int d^3v A(v) \frac{m_a v_\parallel}{T_a} C_{ab}^{TS} \left(F_{Ma} \frac{m_a v_\parallel}{T_a} \right) \right) \left(\int d^3v B(v) \frac{m_b v_\parallel}{T_b} C_{ba}^{TS} \left(F_{Mb} \frac{m_b v_\parallel}{T_b} \right) \right) = 0.$$

The solution to the above equation is $A(v) = B(v) = constant$. The physical interpretation of this constant would be the equilibrium flow of the system,

$$f_a \to u_\parallel F_{Ma} \frac{m_a v_\parallel}{T_a}$$

$$f_b \to u_\parallel F_{Mb} \frac{m_b v_\parallel}{T_b}.$$

Since the parallel direction was chosen arbitrarily, the above two formulas can be generalized,

$$f_a \to \mathbf{u}\cdot\mathbf{v} F_{Ma}\frac{m_a}{T_a} \tag{3.69}$$

$$f_b \to \mathbf{u}\cdot\mathbf{v} F_{Mb}\frac{m_b}{T_b}. \tag{3.70}$$

Now the even components of the spherical harmonics shall be considered. Setting $g_a = F_{Ma}x_a^2$ and $g_b = F_{Mb}x_b^2$ in Eq. 3.67 and following the same procedure as for the odd components gives the H-theorem for the even part of the distribution function:

$$T_a\int d^3v \frac{f_a^{\text{even}}}{F_{Ma}}\left(C_{ab}^{TS}(f_a^{\text{even}}) + C_{ab}^{F}(f_b^{\text{even}})\right) + T_b\int d^3v \frac{f_b^{\text{even}}}{F_{Mb}}\left(C_{ba}^{TS}(f_b^{\text{even}}) + C_{ba}^{F}(f_a^{\text{even}})\right) \leq 0. \tag{3.71}$$

All of the even spherical harmonics with $l > 0$ have a field-particle part which vanishes by the same logic used for the odd components. So only the even components have to be considered. An equilibrium solution of the following form shall be considered:

$$f_a^{l=0} = A(v)F_{Ma}$$

$$f_b^{l=0} = B(v)F_{Mb}.$$

The equation for equilibrium is then given by

$$\eta_{ab}T_a\left(\int d^3v A(v)C_{ab}^{TS}\left(A(v)F_{Ma}\right)\right) + \eta_{ab}T_b\left(\int d^3v B(v)C_{ab}^{TS}\left(B(v)F_{Mb}\right)\right)$$

$$-2T_aT_b\left(\int d^3v A(v)C_{ab}^{TS}\left(F_{Ma}x_a^2\right)\right)\left(\int d^3v B(v)C_{ba}^{TS}\left(F_{Mb}x_b^2\right)\right) = 0.$$

The above set of equations can be solved to give the following solutions:

$$A(v) = \alpha + \beta x_a^2$$

$$B(v) = \gamma + \beta x_a^2.$$

Where α, β, and γ could be any arbitrary value. However, it is convenient to rewrite the above expressions in a way which separates out the density and temperature fluctuations,

$$f_a \rightarrow \left(\frac{\delta n_a}{n_a} + \frac{\delta T}{T} \left(x_a^2 - \frac{3}{2} \right) \right) \tag{3.72}$$

$$f_b \rightarrow \left(\frac{\delta n_b}{n_b} + \frac{\delta T}{T} \left(x_b^2 - \frac{3}{2} \right) \right). \tag{3.73}$$

Putting Eq. 3.68 and 3.71 together, the H-theorem associated with the collision operator is obtained,

$$T_a \int d^3v \frac{f_a}{F_{Ma}} \left(C_{ab}^{TS}(f_a) + C_{ab}^{F}(f_b) \right) + T_b \int d^3v \frac{f_b}{F_{Mb}} \left(C_{ba}^{TS}(f_b) + C_{ba}^{F}(f_a) \right) \leq 0. \tag{3.74}$$

This inequality becomes an equality when the equilibrium state is reached. For the delta-f gyrokinetic simulation model, the equilibrium state is a perturbed Maxwellian (as seen by putting Eq. 3.69, 3.70, 3.72, and 3.73 together) of the following form:

$$f_a \rightarrow F_{Ma} \left(\frac{\delta n_a(f_a)}{n_a} + \frac{m_a}{T_a} \mathbf{u} \cdot \mathbf{v} + \frac{\delta T}{T} \left(x_a^2 - \frac{3}{2} \right) \right). \tag{3.75}$$

In the above formula, a could correspond to any species. Collisions will tend to drive all of them to a distribution of the same form. And $\mathbf{u}$ and $\frac{\delta T}{T}$ will be the same for all species. The effect of the field-particle part of the collision operator can be seen more clearly from this derivation. If the field-particle part is excluded, then collisions would drive all species towards a Maxwellian distribution, and all of the flow and temperature

perturbations would be destroyed by the collision operator, as seen in Eq. 3.56. However, if the field-particle part is included, then the constraints of momentum and energy conservation are imposed, and the asymptotic state of the collision operator is altered to account for these constraints. The asymptotic state represented by Eq. 3.75 is a highly desirable property of the collision operator. The collisions drive arbitrary perturbations to a localized structure in velocity space which is as close to a Maxwellian as possible, while also meeting the essential momentum and energy conservation constraints.

3.8 Gyrokinetic form of the model collision operator

The gyrokinetic form of the new collision operator shall now be derived, as has been in ref. [14]. The gyrokinetic distribution function to first order is given by [15],

$$f_a(\mathbf{r}, v_\parallel, \mu, t) = -F_{Ma}\frac{q_a}{T_a}\langle\phi(\mathbf{r}, t)\rangle + h_a(\mathbf{R}_a, v_\parallel, \mu, t) + O(\epsilon^2). \tag{3.76}$$

Here, the distribution function has been separated into an adiabatic part and a nonadiabatic part. The vector, $\mathbf{r}$, denotes the particle coordinates of the distribution function and $\mathbf{R}_a$ denotes the guiding center coordinates of the particle in the magnetic field. In a gyrokinetic simulation, there is no information about the full six dimensional distribution, only the gyrophase averaged five dimensional distribution. The collision operator also vanishes when acting on a Maxwellian distribution. So the adiabatic part of the distribution need not be included in the collision operator. Since collisions occur in particle space, it will be necessary to transform the nonadiabatic part to particle coordinates, operate with the collision operator, transform back to guiding center coordinates, and then perform the gyrophase-average operation,

$$C_{ab}^{GK} = \oint \frac{d\phi}{2\pi} T_{p\to gc} C_{ab}^{\text{linear}}\left(T_{gc\to p}h_a, T_{gc\to p}h_b\right).$$

For simplicity, this derivation will be done for the local version of gyrokinetics. However, the derivation for the global case would be very similar. But since only local FLR corrections

are implemented in the code, the description of global FLR corrections do not provide any insight into the collision operator in GENE, and is left to future work.

The procedure starts with transforming the distribution into Fourier space,

$$a(\mathbf{r}) = \frac{1}{(2\pi)^{3/2}} \int d^3k a(\mathbf{k}) e^{i\mathbf{k}\cdot\mathbf{r}}.$$

Using $\mathbf{R} = \mathbf{r} - \rho_a$, the perturbed distribution function can be written to first order in the gyrokinetic ordering in Fourier space,

$$\frac{1}{(2\pi)^{3/2}} \int d^3k f_k e^{i\mathbf{k}\cdot\mathbf{r}} = -F_{Ma}\frac{q_a}{T_a}\frac{1}{(2\pi)^{3/2}} \int d^3k \phi_k e^{i\mathbf{k}\cdot\mathbf{r}} + \frac{1}{(2\pi)^{3/2}} \int d^3k h_k e^{i\mathbf{k}\cdot(\mathbf{r}-\rho_a)}$$

$$f_{a\mathbf{k}} = -\frac{q_a}{T_a}\phi_{\mathbf{k}} F_{Ma} + h_{a\mathbf{k}} e^{-i\mathbf{k}\cdot\rho_a}.$$

Since the gyroradius vector, ρ_a, is perpendicular to the magnetic field, the Fourier transform can be limited to the part of configuration space perpendicular to the magnetic field,

$$f_{a\mathbf{k}_\perp} = -\frac{q_a}{T_a}\phi_{\mathbf{k}_\perp} F_{Ma} + h_{a\mathbf{k}_\perp} e^{-i\mathbf{k}_\perp\cdot\rho_a}.$$

Since the collision operator vanishes when acting on a Maxwellian, and since it is necessary to transform the collision operator back from particle coordinates to guiding center coordinates and then gyroaverage, the form for the gyrokinetic test-particle operator can be given as

$$C_{ab}^{(GK)} = \oint \frac{d\phi}{2\pi} e^{i\mathbf{k}_\perp\cdot\rho_a}\left[C_{ab}^{TS}(e^{-i\mathbf{k}_\perp\cdot\rho_a} h_{a\mathbf{k}_\perp}) + C_{ab}^{F}(e^{-\mathbf{k}_\perp\cdot\rho_b} h_{b\mathbf{k}_\perp})\right].$$

The gyrokinetic test-particle part of the collision operator can be written more explicitly as

$$\oint \frac{d\phi}{2\pi} e^{i\mathbf{k}_\perp\cdot\rho_a} C_{ab}^{TS}(e^{-i\mathbf{k}_\perp\cdot\rho_a} h_{a\mathbf{k}_\perp}) = \oint \frac{d\phi}{2\pi} e^{i\mathbf{k}_\perp\cdot\rho_a} C_{ab}^{T0}(e^{-i\mathbf{k}_\perp\cdot\rho_a} h_{a\mathbf{k}_\perp})$$

$$+(\theta_{ab}-1)\oint\frac{d\phi}{2\pi}e^{i\mathbf{k}_\perp\cdot\rho_a}P_aC_{ab}^{T0}(e^{-i\mathbf{k}_\perp\cdot\rho_a}h_{a\mathbf{k}_\perp})$$

$$+(\theta_{ab}-1)\oint\frac{d\phi}{2\pi}e^{i\mathbf{k}_\perp\cdot\rho_a}C_{ab}^{T0}P_a(e^{-i\mathbf{k}_\perp\cdot\rho_a}h_{a\mathbf{k}_\perp})$$

$$+(\theta_{ab}-1)^2\oint\frac{d\phi}{2\pi}e^{i\mathbf{k}_\perp\cdot\rho_a}P_aC_{ab}^{T0}P_a(e^{-i\mathbf{k}_\perp\cdot\rho_a}h_{a\mathbf{k}_\perp}).$$

The first integral term shall be explicitly evaluated using spherical coordinates so that $\mathbf{k}_\perp\cdot\rho_a=\frac{k_\perp v}{\Omega_a}\sin(\theta)\cos(\phi)$. The azimuthal part of the pitch-angle scattering operator (Eq. 3.21) shall be evaluated first,

$$\frac{\partial}{\partial\phi}(e^{-i\mathbf{k}_\perp\cdot\rho_a}h_{a\mathbf{k}_\perp})=\frac{ik_\perp v}{\Omega_a}\sin(\theta)\sin(\phi)e^{-i\mathbf{k}_\perp\cdot\rho_a}h_{a\mathbf{k}_\perp}$$

$$\frac{\partial^2}{\partial\phi^2}(e^{-i\mathbf{k}_\perp\cdot\rho_a}h_{a\mathbf{k}_\perp})=\frac{ik_\perp v}{\Omega_a}\sin(\theta)e^{-i\mathbf{k}_\perp\cdot\rho_a}h_{a\mathbf{k}_\perp}\left(\cos(\phi)+i\frac{k_\perp v}{\Omega_a}\sin(\theta)\sin^2(\phi)\right)$$

$$\oint\frac{d\phi}{2\pi}e^{i\mathbf{k}_\perp\cdot\rho_a}\frac{\nu_D^{ab}(v)}{2\sin^2(\theta)}\frac{\partial^2}{\partial\phi^2}\left(e^{-i\mathbf{k}_\perp\cdot\rho_a}h_{a\mathbf{k}_\perp}\right)=-\frac{k_\perp^2v^2}{4\Omega_a^2}\nu_D^{ab}(v)h_{a\mathbf{k}_\perp}.$$

Now the inclination part of the gyroaveraged pitch-angle scattering operator shall be examined,

$$\frac{\partial}{\partial\theta}(e^{-i\mathbf{k}_\perp\cdot\rho_a}h_{a\mathbf{k}_\perp})=e^{-i\mathbf{k}_\perp\cdot\rho_a}\frac{\partial}{\partial\theta}h_{a\mathbf{k}_\perp}-\frac{ik_\perp v}{\Omega_a}\cos(\theta)\cos(\phi)e^{-i\mathbf{k}_\perp\cdot\rho_a}h_{a\mathbf{k}_\perp}$$

$$\frac{\partial}{\partial\theta}\left(\sin(\theta)\frac{\partial}{\partial\theta}(e^{-i\mathbf{k}_\perp\cdot\rho_a}h_{a\mathbf{k}_\perp})\right)$$

$$=e^{-i\mathbf{k}_\perp\cdot\rho_a}\frac{\partial}{\partial\theta}\left(\sin(\theta)\frac{\partial}{\partial\theta}h_{a\mathbf{k}_\perp}\right)-\frac{2ik_\perp v}{\Omega_a}\cos(\theta)\cos(\phi)e^{-i\mathbf{k}_\perp\cdot\rho_a}\sin(\theta)\frac{\partial h_{a\mathbf{k}_\perp}}{\partial\theta}$$

$$-\frac{ik_\perp v}{\Omega_a}(\cos^2(\theta)-\sin^2(\theta))\cos(\phi)e^{-i\mathbf{k}_\perp\cdot\rho_a}h_{a\mathbf{k}_\perp}-\left(\frac{k_\perp v}{\Omega_a}\cos(\theta)\cos(\phi)\right)^2\sin(\theta)e^{-i\mathbf{k}_\perp\cdot\rho_a}h_{a\mathbf{k}_\perp}.$$

Multiplying by $e^{i\mathbf{k}_\perp\cdot\rho_a}$ and gyroaveraging, all of the terms proportional to $\cos(\phi)$ to the first power will vanish,

$$\oint\frac{d\phi}{2\pi}e^{i\mathbf{k}_\perp\cdot\rho}\frac{\nu_D^{ab}(v)}{2\sin(\theta)}\frac{\partial}{\partial\theta}\left(\sin(\theta)\frac{\partial}{\partial\theta}(e^{-i\mathbf{k}_\perp\cdot\rho_a}h_{a\mathbf{k}_\perp})\right)$$

$$=\frac{\nu_D^{ab}(v)}{2\sin(\theta)}\frac{\partial}{\partial\theta}\left(\sin(\theta)\frac{\partial}{\partial\theta}h_{a\mathbf{k}_\perp}\right)-\frac{k_\perp^2v_\parallel^2}{4\Omega_a^2}\nu_D^{ab}(v)h_{a\mathbf{k}_\perp}.$$

Now the FLR corrections to the energy diffusion part of the test-particle operator (Eq. 3.30) shall be examined,

$$\frac{\partial}{\partial v}\left(\frac{h_{a\mathbf{k}_\perp}}{F_{Ma}}e^{-i\mathbf{k}_\perp\cdot\rho_a}\right)=e^{-i\mathbf{k}_\perp\cdot\rho_a}\frac{\partial}{\partial v}\left(\frac{h_{a\mathbf{k}_\perp}}{F_{Ma}}\right)-\frac{ik_\perp}{\Omega_a}\sin(\theta)\cos(\phi)e^{-i\mathbf{k}_\perp\cdot\rho_a}\frac{h_{a\mathbf{k}_\perp}}{F_{Ma}}$$

$$\frac{\partial}{\partial v}\left(\frac{\nu_\parallel^{ab}(v)}{2}v^4F_{Ma}\frac{\partial}{\partial v}\left(\frac{h_{a\mathbf{k}_\perp}}{F_{Ma}}e^{-i\mathbf{k}_\perp\cdot\rho_a}\right)\right)=e^{-i\mathbf{k}_\perp\cdot\rho_a}\frac{\partial}{\partial v}\left(\frac{\nu_\parallel^{ab}(v)}{2}v^4F_{Ma}\frac{\partial}{\partial v}\left(\frac{h_{a\mathbf{k}_\perp}}{F_{Ma}}\right)\right)$$

$$-\left(\frac{k_\perp}{\Omega_a}\sin(\theta)\cos(\phi)\right)^2e^{-i\mathbf{k}_\perp\cdot\rho_a}\frac{\nu_\parallel^{ab}(v)}{2}v^4h_{a\mathbf{k}_\perp}+...$$

Where the remaining terms are proportional to $\cos(\phi)$ and would vanish under the gyroaveraging operation. So now the following expression is obtained:

$$\oint\frac{d\phi}{2\pi}e^{i\mathbf{k}_\perp\cdot\rho_a}\frac{1}{v^2}\frac{\partial}{\partial v}\left(\frac{\nu_\parallel^{ab}(v)}{2}v^4F_{Ma}\frac{\partial}{\partial v}\left(\frac{h_{a\mathbf{k}_\perp}}{F_{Ma}}e^{-i\mathbf{k}_\perp\cdot\rho_a}\right)\right)$$

$$=\frac{1}{v^2}\frac{\partial}{\partial v}\left(\frac{\nu_\parallel^{ab}(v)}{2}v^4F_{Ma}\frac{\partial}{\partial v}\left(\frac{h_{a\mathbf{k}_\perp}}{F_{Ma}}\right)\right)-\frac{k_\perp^2v_\perp^2}{4\Omega_a^2}\nu_\parallel^{ab}(v)h_{a\mathbf{k}_\perp}.$$

Putting these three expressions together gives

$$\oint \frac{d\phi}{2\pi} e^{i\mathbf{k}_\perp \cdot \rho_a} C_{ab}^{T0}(h_{a\mathbf{k}_\perp} e^{-i\mathbf{k}_\perp \cdot \rho_a}) = C_{ab}^{T0}(h_{a\mathbf{k}_\perp}) - \frac{k_\perp^2 h_{a\mathbf{k}_\perp}}{4\Omega_a^2}(\nu_D^{ab}(v)(2v_\parallel^2 + v_\perp^2) + \nu_\parallel^{ab}(v)v_\perp^2). \quad (3.77)$$

The gyrokinetic form of the pitch-angle scattering and energy diffusion parts of the collision operator are exactly the same except for the addition of a spatial diffusion operator. This term will tend to dampen small-scale configuration space structures perpendicular to the magnetic field. This matches the intuition of what one would expect collisions to do. Another potentially nice feature of this term is that it may reduce the need for ad hoc numerical hyperdiffusion terms in x and y (numerical hyperdiffusion is needed for these terms to prevent grid scale oscillations in those dimensions, although there is also a risk that it may dampen physical structures if set too high). One problematic aspect of this term, however, is that it can dramatically reduce the timestep if high perpendicular wavenumbers are incorporated into a gyrokinetic simulation at high collisionality. For instance, when performing gyrokinetic simulations in the edge, it has been found that for high values of $k_y\rho_s$ (~ 10), the spatial diffusion can shrink the timestep by about an order of magnitude, making studies of high $k_y\rho_s$ gyrokinetic turbulence in the edge impractical until alternative time-stepping schemes can be utilized.

Now the gyroaveraged form of the other parts of the collision operator must be evaluated. Starting with $P_a C_{ab}^{T0}$ (Eq. 3.59),

$$\oint \frac{d\phi}{2\pi} e^{i\mathbf{k}_\perp \cdot \rho_a} P_a C_{ab}^{T0}(h_{a\mathbf{k}_\perp} e^{-i\mathbf{k}_\perp \cdot \rho_a}) =$$

$$\oint \frac{d\phi}{2\pi} e^{i\mathbf{k}_\perp \cdot \rho_a} F_{Ma}\left[\frac{m_a}{T_a}\mathbf{v} \cdot \frac{1}{n_a}\int d^3v \frac{h_{a\mathbf{k}_\perp} e^{-i\mathbf{k}_\perp \cdot \rho_a}}{F_{Ma}} C_{ab}^{T0}(F_{Ma}\mathbf{v})\right.$$

$$\left. + \frac{2}{3n_a}\left(x_a^2 - \frac{3}{2}\right)\int d^3v \frac{h_{a\mathbf{k}_\perp} e^{-i\mathbf{k}_\perp \cdot \rho_a}}{F_{Ma}} C_{ab}^{T0}(F_{Ma}x_a^2)\right],$$

$\mathbf{k}_\perp \cdot \rho_a \propto cos(\phi)$, the Bessel function expansion,

$$e^{izcos(\phi)} = J_0(z) + 2\sum_{n=1}^{\infty} i^n J_1(z)\cos(n\phi),$$

and the orthogonality of trigonometric functions, an expansion of the coefficients in spherical coordinates can be utilized,

$$\oint \frac{d\phi}{2\pi} e^{i\mathbf{k}_\perp\cdot\rho_a} P_a C_{ab}^{T0}(h_{a\mathbf{k}_\perp} e^{-i\mathbf{k}_\perp\cdot\rho_a}) = J_0(k_\perp\rho_a) F_{Ma}\frac{m_a v_\parallel}{n_a T_a}\int d^3v \frac{h_{a\mathbf{k}_\perp} e^{-i\mathbf{k}_\perp\cdot\rho_a}}{F_{Ma}} C_{ab}^{T0}(F_{Ma} v_\parallel)$$

$$+ iJ_1(k_\perp\rho_a) F_{Ma}\frac{m_a v_\perp}{n_a T_a}\int d^3v \frac{h_{a\mathbf{k}_\perp} e^{-i\mathbf{k}_\perp\cdot\rho_a}}{F_{Ma}} C_{ab}^{T0}(F_{Ma} v_x)$$

$$+ J_0(k_\perp\rho_a) F_{Ma}\left(x_a^2 - \frac{3}{2}\right)\frac{1}{n_a}\int d^3v \frac{h_{a\mathbf{k}_\perp} e^{-i\mathbf{k}_\perp\cdot\rho_a}}{F_{Ma}}\frac{2}{3} C_{ab}^{T0}(F_{Ma} x_a^2).$$

One can easily verify that $\mathfrak{L}(\mathbf{v}) \parallel \mathbf{v}$ and the energy diffusion part of the test-particle operator does not depend on any coordinate other than the magnitude of the velocity. So it can be stated that $C_{ab}^{T0}(F_{Ma}\mathbf{v}) = A(v)\mathbf{v}$. Also, $C_{ab}^{T0}(F_{Ma}x_a^2)$ does not depend on the angle coordinates at all. So the Bessel function expansion can be reused,

$$\oint \frac{d\phi}{2\pi} e^{i\mathbf{k}_\perp\cdot\rho_a} P_a C_{ab}^{T0}(h_{a\mathbf{k}_\perp} e^{-i\mathbf{k}_\perp\cdot\rho_a}) = J_0(k_\perp\rho_a) F_{Ma}\frac{m_a v_\parallel}{n_a T_a}\int d^3v \frac{h_{a\mathbf{k}_\perp} J_0(k_\perp\rho_a)}{F_{Ma}} A(v) v_\parallel$$

$$+ J_1(k_\perp\rho_a) F_{Ma}\frac{m_a v_\perp}{n_a T_a}\int d^3v \frac{h_{a\mathbf{k}_\perp} J_1(k_\perp\rho_a)}{F_{Ma}} A(v) v_\perp$$

$$+ J_0(k_\perp\rho_a) F_{Ma}(x_a^2 - \frac{3}{2})\frac{2}{3n_a}\int d^3v \frac{h_{a\mathbf{k}_\perp} J_0(k_\perp\rho_a)}{F_{Ma}} C_{ab}^{T0}(F_{Ma} x_a^2).$$

Now since the orientation of $\hat{\mathbf{v}}_\parallel$ does not depend on the angular coordinates, $C_{ab}^{T0}(F_{Ma}v_\parallel) =$

$A(v)v_\parallel$. But the same cannot be said of the integral involving $v_\perp$ since the orientation of $\hat{\mathbf{v}}_\perp$ does depend on the azimuthal angle. As such, the terms in the second integral are multiplied by $\frac{v_\parallel}{v_\parallel}$,

$$\oint \frac{d\phi}{2\pi} e^{i\mathbf{k}_\perp\cdot\rho_a} P_a C_{ab}^{T0}(h_{a\mathbf{k}_\perp} e^{-i\mathbf{k}_\perp\cdot\rho_a})$$

$$= J_0(k_\perp\rho_a) F_{Ma}\frac{v_\parallel}{n_a}\int d^3v \frac{h_{a\mathbf{k}_\perp} J_0(k_\perp\rho_a)}{F_{Ma}} C_{ab}^{T0}(F_{Ma} m_a v_\parallel/T_a)$$

$$+J_1(k_\perp\rho_a) F_{Ma}\frac{v_\perp}{n_a}\int d^3v \frac{h_{a\mathbf{k}_\perp} J_1(k_\perp\rho_a)}{F_{Ma}}\frac{v_\perp}{v_\parallel} C_{ab}^{T0}(F_{Ma} m_a v_\parallel/T_a)$$

$$+ J_0(k_\perp\rho_a) F_{Ma}(x_a^2-\frac{3}{2})\frac{2}{3n_a}\int d^3v \frac{h_{a\mathbf{k}_\perp} J_0(k_\perp\rho_a)}{F_{Ma}} C_{ab}^{T0}(F_{Ma} x_a^2). \tag{3.78}$$

The same exercise can be done with $C_{ab}^{T0} P_a$ (Eq. 3.60),

$$\oint \frac{d\phi}{2\pi} e^{i\mathbf{k}_\perp\cdot\rho_a} C_{ab}^{T0} P_a(h_{a\mathbf{k}_\perp} e^{-i\mathbf{k}_\perp\cdot\rho_a})$$

$$= J_0(k_\perp\rho_a) C_{ab}^{T0}(F_{Ma} m_a v_\parallel/T_a)\frac{1}{n_a}\int d^3v J_0(k_\perp\rho_a) h_{a\mathbf{k}_\perp} v_\parallel$$

$$+J_1(k_\perp\rho_a)\frac{v_\perp}{v_\parallel} C_{ab}^{T0}(F_{Ma} m_a v_\parallel/T_a)\frac{1}{n_a}\int d^3v J_1(k_\perp\rho_a) h_{a\mathbf{k}_\perp} v_\perp$$

$$+ J_0(k_\perp\rho_a) C_{ab}^{T0}(F_{Ma} x_a^2)\frac{2}{3n_a}\int d^3v J_0(k_\perp\rho_a) h_{a\mathbf{k}_\perp}(x_a^2-\frac{3}{2}), \tag{3.79}$$

as well as for the field-particle operator C_{ab}^F (Eq. 3.63),

$$\oint \frac{d\phi}{2\pi} e^{i\mathbf{k}_\perp\cdot\rho_a} C_{ab}^F(h_{b\mathbf{k}_\perp} e^{-i\mathbf{k}_\perp\cdot\rho_b}) =$$

$$-\frac{T_b}{\gamma_{ab}}C_{ab}^{TS}(F_{Ma}m_a v_\parallel/T_a)J_0(k_\perp\rho_a)\int d^3v J_0(k_\perp\rho_b)\frac{h_{b\mathbf{k}_\perp}}{F_{Mb}}C_{ba}^{TS}(F_{Mb}m_b v_\parallel/T_b)$$

$$-\frac{T_b}{\gamma_{ab}}\frac{v_\perp}{v_\parallel}C_{ab}^{TS}(F_{Ma}m_a v_\parallel/T_a)J_1(k_\perp\rho_a)\int d^3v J_1(k_\perp\rho_b)\frac{v_\perp}{v_\parallel}\frac{h_{b\mathbf{k}_\perp}}{F_{Mb}}C_{ba}^{TS}(F_{Mb}m_b v_\parallel/T_b)$$

$$-\frac{T_b}{\eta_{ab}}C_{ab}^{TS}(F_{Ma}x_a^2)J_0(k_\perp\rho_a)\int d^3v J_0(k_\perp\rho_b)\frac{h_{b\mathbf{k}_\perp}}{F_{Mb}}C_{ba}^{TS}(F_{Mb}x_b^2). \tag{3.80}$$

The gyroaveraged expression for the final part of the test-particle operator, $P_a C_{ab}^{T0} P_a$, is more complicated. First, $C_{ab}^{T0}(F_{Ma}m_a v_\parallel/T_a)$ and $C_{ab}^{T0}(F_{Ma}x_a^2)$ must be evaluated. For the purpose of clarity, the same notation as Sugama et al. will be used,

$$\frac{3\sqrt{\pi}}{4\tau_{ab}} = \frac{2\gamma_{ab}n_b}{m_a^2 v_{Ta}^3} = \frac{4\pi n_b e_a^2 e_b^2 \ln(\Lambda)}{m_a^2 v_{Ta}^3}. \tag{3.81}$$

The pitch-angle scattering operator clearly vanishes when acting on a spherically symmetric distribution, so the following is obtained:

$$C_{ab}^{T0}(F_{Ma}x_a^2) = \frac{1}{v^2}\frac{\partial}{\partial v}\left(\nu_\parallel^{ab}(v)\frac{v^4}{2}F_{Ma}\frac{\partial}{\partial v}(x_a^2)\right) = \frac{4\gamma_{ab}n_b}{m_a^2 v^2}\frac{\partial}{\partial v}\left(G(x_b)x_a^2 F_{Ma}\right)$$

$$C_{ab}^{T0}(F_{Ma}x_a^2) = \frac{3\sqrt{\pi}}{4\tau_{ab}}\frac{v_{Ta}^3}{\alpha_{ab}^2 v^2}\frac{\partial}{\partial v}\left((\Phi(x_b) - x_b\Phi'(x_b))F_{Ma}\right),$$

where $\alpha_{ab} = v_{Ta}/v_{Tb}$. It is straightforward to evaluate the derivative of the above expression. When this is done, one obtains:

$$C_{ab}^{T0}(F_{Ma}x_a^2) = -\frac{3\sqrt{\pi}}{2\tau_{ab}}\frac{F_{Ma}}{\alpha_{ab}x_b}[\Phi(x_b) - x_b(1+\alpha_{ab}^2)\Phi'(x_b)].$$

Now $C_{ab}^{T0}(F_{Ma}m_a v_\parallel/T_a)$ must be considered. Since the pitch angle scattering operator only depends on the angular coordinates, and

$$\frac{1}{2\sin(\theta)}\frac{\partial}{\partial\theta}\left(\sin(\theta)\frac{\partial}{\partial\theta}\left(\cos(\theta)\right)\right) = -\cos(\theta),$$

it follows that

$$\nu_D^{ab}(v)\mathfrak{L}\left(F_{Ma}\frac{m_a v_\parallel}{T_a}\right) = -\nu_D^{ab}(v)F_{Ma}\frac{m_a v_\parallel}{T_a}.$$

Furthermore

$$\frac{1}{v^2}\frac{\partial}{\partial v}\left[\frac{\nu_\parallel^{ab}(v)}{2}v^4 F_{Ma}\frac{\partial}{\partial v}\left(\frac{m_a v_\parallel}{T_a}\right)\right] = \frac{1}{v^3}\frac{\partial}{\partial v}\left[\frac{\nu_\parallel^{ab}(v)}{2}v^4 F_{Ma}\right]\frac{m_a v_\parallel}{T_a},$$

therefore

$$C_{ab}^{T0}\left(F_{Ma}\frac{m_a v_\parallel}{T_a}\right) = \left[\frac{1}{v^3}\left(\frac{\partial}{\partial v}\left(\frac{\nu_\parallel^{ab}(v)}{2}v^4\right) - \frac{v^5\nu_\parallel^{ab}(v)}{v_{Ta}^2}\right) - \nu_D^{ab}(v)\right]F_{Ma}\frac{m_a v_\parallel}{T_a}.$$

From the chain rule,

$$\frac{\partial}{\partial v}\left(\frac{\nu_\parallel^{ab}(v)}{2}v^4\right) = 2v^3\nu_\parallel^{ab}(v) + \frac{1}{2}v^4\frac{\partial}{\partial v}\left(\nu_\parallel^{ab}(v)\right).$$

It was previously determined that the derivative of $\nu_\parallel^{ab}(v)$ is (Eq. 3.28)

$$\frac{d\nu_\parallel^{ab}(v)}{dv} = \frac{4\gamma_{ab}n_b}{m_a^2 v_{Tb}}\frac{\Phi'(x_b)}{v^3} - \frac{5\nu_\parallel^{ab}(v)}{v}.$$

So

$$\frac{1}{v^3}\frac{\partial}{\partial v}\left(\frac{\nu_\parallel^{ab}(v)}{2}v^4\right) = -\frac{1}{2}\nu_\parallel^{ab}(v) + \frac{2\gamma_{ab}n_b}{m_a^2 v^3}x_b\Phi'(x_b).$$

Using this and the definition for $\nu_D^{ab}(v)$ (Eq. 3.23), it follows that

$$C_{ab}^{T0}\left(F_{Ma}\frac{m_a v_\parallel}{T_a}\right) = -F_{Ma}\frac{m_a v_\parallel}{T_a}\left[\left(\frac{1}{2}+x_a^2\right)\nu_\parallel^{ab}(v) + \frac{2\gamma_{ab}n_b}{m_a^2 v^3}\left(\Phi(x_b) - x_b\Phi'(x_b) - G(x_b)\right)\right] \quad (3.82)$$

$$C_{ab}^{T0}\left(F_{Ma}\frac{m_a v_\parallel}{T_a}\right) = -F_{Ma}\frac{m_a v_\parallel}{T_a}\left[x_a^2\nu_\parallel^{ab}(v) + \frac{4\gamma_{ab}n_b}{m_a^2 v^3}x_b^2 G(x_b)\right]$$

$$C_{ab}^{T0}(F_{Ma}\frac{m_a v_\parallel}{T_a}) = -F_{Ma}\frac{m_a v_\parallel}{T_a}(1+\alpha_{ab}^2)x_a^2\nu_\parallel^{ab}(v) = -F_{Ma}\frac{m_a v_\parallel}{T_a}(1+\alpha_{ab}^2)\frac{3\sqrt{\pi}}{2\tau_{ab}}\frac{G(x_b)}{x_a}. \quad (3.83)$$

Now the moments of these quantities, $\int d^3v(m_a v_\parallel/T_a)C_{ab}^{T0}(F_{Ma}v_\parallel)/n_a$ and $2\int d^3v x_a^2 C_{ab}^{T0}(F_{Ma}x_a^2)/(3n_a)$ must be evaluated to obtain an appropriate expression for the gyroaveraged form of $P_a C_{ab}^{T0} P_a$,

$$\frac{1}{n_a}\int d^3v\frac{m_a v_\parallel}{T_a}C_{ab}^{T0}(F_{Ma}v_\parallel) = \frac{1}{n_a}\int d^3v\frac{m_a v_\parallel}{T_a}\left(-\frac{3\sqrt{\pi}}{2\tau_{ab}}\right)(1+\alpha_{ab}^2)F_{Ma}v_\parallel\frac{G(x_b)}{x_a}.$$

This integral can be evaluated using spherical coordinates and the evaluation of the angular parts of the integrand ($\cos(\theta)$) is straightforward. Furthermore, the prefactors from the Maxwellian term are removed and the u-substitution for the radial component of the velocity space integral $x = v/v_{Ta}$ is used:

$$\frac{1}{n_a}\int d^3v\frac{m_a v_\parallel}{T_a}C_{ab}^{T0}(F_{Ma}v_\parallel) = -\frac{2m_a}{T_a}(1+\alpha_{ab}^2)\frac{v_{Ta}^2}{\tau_{ab}}\int_0^\infty dx x^3 e^{-x^2}G(\alpha_{ab}x)$$

$$= -4\frac{(1+\alpha_{ab}^2)}{\alpha_{ab}^2\tau_{ab}}\int_0^\infty dx\frac{1}{2}xe^{-x^2}(\Phi(\alpha_{ab}x) - \alpha_{ab}x\Phi(\alpha_{ab}x))$$

$$= \frac{(1+\alpha_{ab}^2)}{\alpha_{ab}^2\tau_{ab}}\int_0^\infty dx\left(\frac{d}{dx}e^{-x^2}\right)(\Phi(\alpha_{ab}x) - \alpha_{ab}x\Phi'(\alpha_{ab}x))$$

$$= \frac{(1+\alpha_{ab}^2)}{\alpha_{ab}^2\tau_{ab}}\int_0^\infty dx e^{-x^2}\alpha_{ab}x\Phi''(\alpha_{ab}x)\alpha_{ab}$$

$$= -\frac{4}{\sqrt{\pi}}\alpha_{ab}\frac{(1+\alpha_{ab}^2)}{\tau_{ab}}\int_0^\infty dx x^2 e^{-(1+\alpha_{ab}^2)x^2}.$$

Using another u-substitution:

$$\frac{1}{n_a}\int d^3v \frac{m_a v_\parallel}{T_a} C_{ab}^{T0}(F_{Ma} v_\parallel) = -\frac{4\alpha_{ab}}{\tau_{ab}\sqrt{\pi(1+\alpha_{ab}^2)}} \int_0^\infty dx x^2 e^{-x^2}.$$

One can look up the value of this integral from a table,

$$\frac{1}{n_a}\int d^3v \frac{m_a v_\parallel}{T_a} C_{ab}^{T0}(F_{Ma} v_\parallel) = -\frac{\alpha_{ab}}{\tau_{ab}\sqrt{1+\alpha_{ab}^2}}. \tag{3.84}$$

Now the other integral is evaluated,

$$\frac{2}{3n_a}\int d^3v x_a^2 C_{ab}^{T0}(F_{Ma} x_a^2) = -\frac{\sqrt{\pi}}{n_a \tau_{ab}} \int d^3v x_a \frac{F_{Ma}}{\alpha_{ab}^2}\Big[\Phi(\alpha_{ab}x_a) - \alpha_{ab}x_a(1+\alpha_{ab}^2)\Phi'(\alpha_{ab}x_a)\Big].$$

Once again, the prefactors from the Maxwellian term can be removed and the angular integration is trivial,

$$\frac{2}{3n_a}\int d^3v x_a^2 C_{ab}^{T0}(F_{Ma} x_a^2) = -\frac{4}{\tau_{ab}} \int_0^\infty dx x^3 \frac{e^{-x^2}}{\alpha_{ab}^2}\Big[\Phi(\alpha_{ab}x) - \alpha_{ab}(1+\alpha_{ab}^2)x\Phi'(\alpha_{ab}x_a)\Big]$$

$$\frac{2}{3n_a}\int d^3v x_a^2 C_{ab}^{T0}(F_{Ma} x_a^2) = \frac{2}{\tau_{ab}\alpha_{ab}^2} \int_0^\infty dx \frac{d}{dx}\Big((x^2{+}1)e^{-x^2}\Big)\Big[\Phi(\alpha_{ab}x){-}(1{+}\alpha_{ab}^2)\alpha_{ab}x\Phi'(\alpha_{ab}x)\Big]$$

$$\frac{2}{3n_a}\int d^3v x_a^2 C_{ab}^{T0}(F_{Ma} x_a^2) = \frac{2\alpha_{ab}}{\tau_{ab}}\frac{2}{\sqrt{\pi}} \int_0^\infty dx (x^2+1)e^{-(1+\alpha_{ab}^2)x^2}(1-2x^2(1+\alpha_{ab}^2)).$$

Using the change of variables $y = x\sqrt{1+\alpha_{ab}^2}$,

$$\frac{2}{3n_a}\int d^3v x_a^2 C_{ab}^{T0}(F_{Ma}x_a^2) = \frac{4\alpha_{ab}}{\tau_{ab}\sqrt{\pi}(1+\alpha_{ab}^2)^{3/2}}\int_0^\infty dy(y^2+1+\alpha_{ab}^2)(1-2y^2)e^{-y^2}.$$

This leads to an integral of a quartic polynomial multiplying an exponential function. The integral for each term in the polynomial can be evaluated using a table of integrals,

$$\frac{2}{3n_a}\int d^3v x_a^2 C_{ab}^{T0}(F_{Ma}x_a^2) = -\frac{2\alpha_{ab}}{\tau_{ab}(1+\alpha_{ab}^2)^{3/2}}. \tag{3.85}$$

Using these two expressions for the integrals, the expression for $P_a C_{ab}^{T0} P_a$ (Eq. 3.62) can be simplified,

$$P_a C_{ab}^{T0} P_a(f_a) = -\frac{F_{Ma}\alpha_{ab}}{\tau_{ab}\sqrt{1+\alpha_{ab}^2}}\left[\frac{m_a}{T_a}\mathbf{v}\cdot\mathbf{u}_a(f_a) + \frac{2\left(x_a^2-\frac{3}{2}\right)}{1+\alpha_{ab}^2}\frac{\delta T_a(f_a)}{T_a}\right]$$

The gyroaveraged form of $P_a C_{ab}^{T0} P_a$ can now be examined in a way which is very similar to the evaluation of $C_{ab}^{T0} P_a$ and $P_a C_{ab}^{T0}$:

$$\oint \frac{d\phi}{2\pi} e^{i\mathbf{k}_\perp\cdot\rho_a} P_a C_{ab}^{T0} P_a(h_{a\mathbf{k}_\perp} e^{-i\mathbf{k}_\perp\cdot\rho_a}) = -\frac{m_a F_{Ma}\alpha_{ab}}{n_a T_a \tau_{ab}\sqrt{1+\alpha_{ab}^2}}\Bigg[J_0(k_\perp\rho_a)v_\parallel\int d^3v v_\parallel J_0(k_\perp\rho_a)h_{a\mathbf{k}_\perp}$$

$$+ J_1(k_\perp\rho_a)v_\perp\int d^3v v_\perp J_1(k_\perp\rho_a)h_{a\mathbf{k}_\perp} + \frac{2\left(x_a^2-\frac{3}{2}\right)}{1+\alpha_{ab}^2}J_0(k_\perp\rho_a)\int d^3v J_0(k_\perp\rho_a)h_{a\mathbf{k}_\perp}\frac{2}{3}\left(x_a^2-\frac{3}{2}\right)\Bigg]. \tag{3.86}$$

The complete analytical form for the linearized self-adjoint gyrokinetic collision operator is given by

$$C_{ab}^{(\text{Gyrokinetic})}(h_{a\mathbf{k}_\perp}, h_{b\mathbf{k}_\perp}) = C_{ab}^{T0}(h_{a\mathbf{k}_\perp}) - \frac{k_\perp^2 h_{a\mathbf{k}_\perp}}{4\Omega_a^2}(\nu_D^{ab}(v)(2v_\parallel^2+v_\perp^2) + \nu_\parallel^{ab}(v)v_\perp^2)$$

$$+(\theta_{ab}-1)\left(\oint\frac{d\phi}{2\pi}e^{i\mathbf{k}_\perp\cdot\rho_a}P_aC_{ab}^{T0}(h_{a\mathbf{k}_\perp}e^{-i\mathbf{k}_\perp\cdot\rho_a})+\oint\frac{d\phi}{2\pi}e^{i\mathbf{k}_\perp\cdot\rho_a}C_{ab}^{T0}P_a(h_{a\mathbf{k}_\perp}e^{-i\mathbf{k}_\perp\cdot\rho_a})\right)$$

$$+(\theta_{ab}-1)^2\oint\frac{d\phi}{2\pi}e^{i\mathbf{k}_\perp\cdot\rho_a}P_aC_{ab}^{T0}P_a(h_{a\mathbf{k}_\perp}e^{-i\mathbf{k}_\perp\cdot\rho_a})$$

$$+\oint\frac{d\phi}{2\pi}e^{i\mathbf{k}_\perp\cdot\rho_a}C_{ab}^{F}(h_{b\mathbf{k}_\perp}e^{-i\mathbf{k}_\perp\cdot\rho_b}),\tag{3.87}$$

where the gyroaveraged expressions were given earlier in Eqs. 3.78, 3.79, 3.86, and 3.80. This expression is correct, however, it is not in a form which is convenient for numerical discretization and normalization. From the test-particle part of the collision operator, there are only six moments to calculate. Since the field-particle part is based on the test-particle part, there are only the same 6 moments in that part as well. The moments will simply be transposed in the field-particle part. The six coefficients multiplying the moments in the test-particle part shall be derived in a way which is similar to [53]. The six moments in the test-particle part are

$$M_{1\mathbf{k}_\perp}^{ab}=\int d^3v\frac{m_av_\parallel}{T_a}C_{ab}^{T0}(J_0(k_\perp\rho_a)h_{a\mathbf{k}_\perp})\tag{3.88}$$

$$M_{2\mathbf{k}_\perp}^{ab}=\int d^3v\frac{m_av_\parallel}{T_a}C_{ab}^{T0}(J_1(k_\perp\rho_a)h_{a\mathbf{k}_\perp}v_\perp/v_\parallel)\tag{3.89}$$

$$M_{3\mathbf{k}_\perp}^{ab}=\int d^3vx_a^2C_{ab}^{T0}(J_0(k_\perp\rho_a)h_{a\mathbf{k}_\perp})\tag{3.90}$$

$$M_{4\mathbf{k}_\perp}^{ab}=\int d^3vv_\parallel J_0(k_\perp\rho_a)h_{a\mathbf{k}_\perp}\tag{3.91}$$

$$M^{ab}_{5\mathbf{k}_\perp} = \int d^3v v_\perp J_1(k_\perp \rho_a) h_{a\mathbf{k}_\perp} \tag{3.92}$$

$$M^{ab}_{6\mathbf{k}_\perp} = \int d^3v J_0(k_\perp \rho_a) h_{a\mathbf{k}_\perp} \left(x_a^2 - \frac{3}{2} \right). \tag{3.93}$$

The gyrokinetic collision operator shall be rewritten as

$$C^{(\text{Gyrokinetic})}_{ab}(h_{a\mathbf{k}_\perp}, h_{b\mathbf{k}_\perp}) = C^{T0}_{ab}(h_{a\mathbf{k}_\perp}) - \frac{k_\perp^2 h_{a\mathbf{k}_\perp}}{4\Omega_a^2}(\nu_D^{ab}(v)(2v_\parallel^2 + v_\perp^2) + \nu_\parallel^{ab}(v) v_\perp^2)$$

$$+ \sum_{n=1}^{6} (X^{ab}_{n\mathbf{k}_\perp} M^{ab}_{n\mathbf{k}_\perp} + Y^{ab}_{n\mathbf{k}_\perp} M^{ba}_{n\mathbf{k}_\perp}). \tag{3.94}$$

Where $X^{ab}_{n\mathbf{k}_\perp}$ represents the coefficients for the test-particle part and $Y^{ab}_{n\mathbf{k}_\perp}$ represents the coefficients for the field-particle part. Matching the appropriate coefficients with Eq. 3.87 gives

$$X^{ab}_{1\mathbf{k}_\perp} = (\theta_{ab} - 1) J_0(k_\perp \rho_a) F_{Ma} \frac{v_\parallel}{n_a} \tag{3.95}$$

$$X^{ab}_{2\mathbf{k}_\perp} = (\theta_{ab} - 1) J_1(k_\perp \rho_a) F_{Ma} \frac{v_\perp}{n_a} \tag{3.96}$$

$$X^{ab}_{3\mathbf{k}_\perp} = (\theta_{ab} - 1) J_0(k_\perp \rho_a) F_{Ma} (x_a^2 - \frac{3}{2}) \frac{2}{3n_a} \tag{3.97}$$

$$X^{ab}_{4\mathbf{k}_\perp} = (\theta_{ab} - 1) J_0(k_\perp \rho_a) \frac{1}{n_a} \left[C^{T0}_{ab} \left(\frac{F_{Ma} m_a v_\parallel}{T_a} \right) - (\theta_{ab} - 1) \frac{\alpha_{ab}}{\tau_{ab} \sqrt{1 + \alpha_{ab}^2}} \frac{m_a v_\parallel}{T_a} F_{Ma} \right] \tag{3.98}$$

$$X^{ab}_{5\mathbf{k}_\perp} = \frac{J_1(k_\perp\rho_a)v_\perp}{J_0(k_\perp\rho_a)v_\parallel} X^{ab}_{4\mathbf{k}_\perp} \tag{3.99}$$

$$X^{ab}_{6\mathbf{k}_\perp} = (\theta_{ab}-1)J_0(k_\perp\rho_a)\frac{2}{3n_a}\left[C^{T0}_{ab}(F_{Ma}x_a^2) - (\theta_{ab}-1)\frac{2\alpha_{ab}F_{Ma}}{\tau_{ab}(1+\alpha_{ab}^2)^{3/2}}\left(x_a^2-\frac{3}{2}\right)\right]. \tag{3.100}$$

Now the terms for the field-particle operator must be evaluated. To do this, $C^{TS}_{ab}(F_{Ma}m_a v_\parallel/T_a)$ and $C^{TS}_{ab}(F_{Ma}x_a^2)$ must be evaluated. Starting with the first term,

$$\mathbf{u}_a\left(F_{Ma}\frac{m_a v_\parallel}{T_a}\right) = \frac{2\pi}{n_a}\int dv_\parallel dv_\perp v_\perp \frac{m_a v_\parallel^2}{T_a}\frac{n_a}{\pi^{3/2}v_{Ta}^3}e^{-(v/v_{Ta})^2}\hat{\mathbf{v}}_\parallel,$$

and using two u-substitutions,

$$\mathbf{u}_a\left(F_{Ma}\frac{m_a v_\parallel}{T_a}\right) = \frac{4}{\sqrt{\pi}}\int_{-\infty}^{\infty} dy y^2 e^{-y^2}\int_0^\infty dx x e^{-x^2}\hat{\mathbf{v}}_\parallel = \hat{\mathbf{v}}_\parallel,$$

the following expression is obtained:

$$P_{1a}\left(F_{Ma}\frac{m_a v_\parallel}{T_a}\right) = F_{Ma}\frac{m_a v_\parallel}{T_a}.$$

$P_{2a}\left(F_{Ma}\frac{m_a v_\parallel}{T_a}\right) = 0$ because it involves the integral of an odd function over the entire domain. Since $Q_{ab}(f) = f + (\theta_{ab}-1)P_a f$,

$$Q_{ab}(F_{Ma}\frac{m_a v_\parallel}{T_a}) = \theta_{ab}F_{Ma}\frac{m_a v_\parallel}{T_a}$$

$$C^{T0}_{ab}\left(Q_{ab}\left(F_{Ma}\frac{m_a v_\parallel}{T_a}\right)\right) = \theta_{ab}C^{T0}_{ab}\left(F_{Ma}\frac{m_a v_\parallel}{T_a}\right)$$

$$C^{TS}_{ab}\left(F_{Ma}\frac{m_a v_\parallel}{T_a}\right) = Q_{ab}\left(C^{T0}_{ab}\left(Q_{ab}\left(F_{Ma}\frac{m_a v_\parallel}{T_a}\right)\right)\right) =$$

$$\theta_{ab}C_{ab}^{T0}\left(F_{Ma}\frac{m_a v_\parallel}{T_a}\right)+\theta_{ab}(\theta_{ab}-1)P_a\left(C_{ab}^{T0}\left(F_{Ma}\frac{m_a v_\parallel}{T_a}\right)\right).$$

Using Eq. 3.84:

$$C_{ab}^{TS}\left(F_{Ma}\frac{m_a v_\parallel}{T_a}\right)=\theta_{ab}\left(C_{ab}^{T0}\left(F_{Ma}\frac{m_a v_\parallel}{T_a}\right)-\frac{F_{Ma}m_a\alpha_{ab}v_\parallel(\theta_{ab}-1)}{\tau_{ab}T_a\sqrt{1+\alpha_{ab}^2}}\right). \tag{3.101}$$

Now $C_{ab}^{TS}(F_{Ma}x_a^2)$ must be examined,

$$\frac{\delta T_a}{T_a}(F_{Ma}x_a^2)=\frac{1}{n_a}\int d^3v\left(\frac{2}{3}x_a^2-1\right)x_aF_{Ma}=1$$

$$P_a(F_{Ma}x_a^2)=F_{Ma}\left(x_a^2-\frac{3}{2}\right)$$

$$Q_{ab}(F_{Ma}x_a^2)=F_{Ma}\left(x_a^2+\left(\theta_{ab}-1\right)\left(x_a^2-\frac{3}{2}\right)\right).$$

Since C_{ab}^{T0} vanishes when acting on a Maxwellian distribution,

$$C_{ab}^{T0}(Q_{ab}(F_{Ma}x_a^2))=\theta_{ab}C_{ab}^{T0}(F_{Ma}x_a^2).$$

Now, based on the earlier integral that was evaluated in Eq. 3.85,

$$\frac{\delta T_a}{T_a}(C_{ab}^{T0}(F_{Ma}x_a^2))=\frac{1}{n_a}\int d^3v\frac{2}{3}x_a^2C_{ab}^{T0}(F_{Ma}x_a^2)=-\frac{2\alpha_{ab}}{\tau_{ab}(1+\alpha_{ab}^2)^{3/2}}$$

$$P_{2a}(C_{ab}^{T0}(F_{Ma}x_a^2))=-\frac{2F_{Ma}\alpha_{ab}}{\tau_{ab}\left(1+\alpha_{ab}^2\right)^{3/2}}\left(x_a^2-\frac{3}{2}\right).$$

Finally:

$$C_{ab}^{TS}(F_{Ma}x_a^2) = \theta_{ab}\left[C_{ab}^{T0}(F_{Ma}x_a^2) - \frac{2F_{Ma}\alpha_{ab}(\theta_{ab}-1)}{\tau_{ab}(1+\alpha_{ab}^2)^{3/2}}\left(x_a^2 - \frac{3}{2}\right)\right].$$

One can substitute these expressions into the expression for the gyroaveraged field-particle operator (Eq. 3.80), and obtain

$$\oint \frac{d\phi}{2\pi} e^{i\mathbf{k}_\perp\cdot\rho_a} C_{ab}^F(h_{b\mathbf{k}_\perp} e^{-i\mathbf{k}_\perp\cdot\rho_b}) = \sum_{n=1}^{6} Y_{n\mathbf{k}_\perp} M_{n\mathbf{k}_\perp}^{ba} \tag{3.102}$$

$$Y_{1\mathbf{k}_\perp}^{ab} = -\frac{T_b\theta_{ba}}{\gamma_{ab}} C_{ab}^{TS}(F_{Ma}\frac{m_a v_\parallel}{T_a}) J_0(k_\perp\rho_a) \tag{3.103}$$

$$Y_{2\mathbf{k}_\perp}^{ab} = \frac{J_1(k_\perp\rho_a)v_\perp}{J_0(k_\perp\rho_a)v_\parallel} Y_{1\mathbf{k}_\perp}^{ab} \tag{3.104}$$

$$Y_{3\mathbf{k}_\perp}^{ab} = -\frac{T_b\theta_{ba}}{\eta_{ab}} C_{ab}^{TS}(F_{Ma}x_a^2) J_0(k_\perp\rho_a) \tag{3.105}$$

$$Y_{4\mathbf{k}_\perp}^{ab} = -\frac{m_b\alpha_{ba}\theta_{ba}}{\tau_{ba}T_b\sqrt{1+\alpha_{ba}^2}} Y_{1\mathbf{k}_\perp}^{ab} \tag{3.106}$$

$$Y_{5\mathbf{k}_\perp}^{ab} = -\frac{m_b\alpha_{ba}\theta_{ba}}{\tau_{ba}T_b\sqrt{1+\alpha_{ba}^2}} Y_{2\mathbf{k}_\perp}^{ab} \tag{3.107}$$

$$Y_{6\mathbf{k}_\perp}^{ab} = -\frac{2\alpha_{ba}\theta_{ba}}{\tau_{ba}(1+\alpha_{ba}^2)^{3/2}} Y_{3\mathbf{k}_\perp}^{ab}. \tag{3.108}$$

Thus, the final form for the analytical linearized model gyrokinetic collision operator is derived,

$$C_{ab}^{(\text{Gyrokinetic})}(h_{a\mathbf{k}_\perp}, h_{b\mathbf{k}_\perp}) = C_{ab}^{T0}(h_{a\mathbf{k}_\perp}) - \frac{k_\perp^2 h_{a\mathbf{k}_\perp}}{4\Omega_a^2}(\nu_D^{ab}(v)(2v_\parallel^2 + v_\perp^2) + \nu_\parallel^{ab}(v)v_\perp^2)$$

$$+\sum_{n=1}^{6}(X^{ab}_{n\mathbf{k}_\perp}M^{ab}_{n\mathbf{k}_\perp}+Y^{ab}_{n\mathbf{k}_\perp}M^{ba}_{n\mathbf{k}_\perp}). \tag{3.109}$$

The gyrokinetic form of the model collision operator is exactly the same as the drift-kinetic version except for the addition of a spatial diffusion term and the modulation of the integral parts by Bessel functions. The effect of the FLR corrections will be to dampen structures at high perpendicular wavenumber and structures far from the origin in velocity space.

3.9 Numerical implementation of gyrokinetic collision operator

An analytical form for the gyrokinetic collision operator has been obtained. Now the numerical form for the operator must be derived such that it conserves particles, momentum, and energy as well as satisfying the self-adjointness relations to guarantee free energy dissipation. The collision operator shall be discretized such that particles, momentum, and energy are conserved to machine precision in the drift-kinetic limit ($k_\perp \to 0$) where it is simple to write down the appropriate conservation laws. In the gyrokinetic case when FLR corrections are included, the conservation law can be expressed as a divergence of a flux in configuration space as shown in ref. [42]. In order for that property to be satisfied, the operator must be discretized such that the local conservation laws are satisfied numerically in the drift-kinetic limit. It is also important to point out that the numerical form of the collision operator is designed to act on the nonadiabatic part of the distribution function divided by a background Maxwellian. The division by the background Maxwellian is done to numerically ensure the following self-adjointness relation:

$$\int d^3v \frac{f_a}{F_{Ma}} C^{TS}_{ab}(g_a) = \int d^3v \frac{g_a}{F_{Ma}} C^{TS}_{ab}(f_a).$$

The nonadiabatic part of the distribution is used because the rate of change of free energy by collisions, $dF/dt|_{\text{coll}}$, is defined from the nonadiabatic part of the distribution [61],

$$\left.\frac{dF}{dt}\right|_{\text{coll}} = \sum_j n_j T_j \int d^3v \frac{h_j}{F_{Mj}} C_j. \tag{3.110}$$

So to numerically enforce the negative-definite nature of Eq. 3.110, the collision operator must be defined as an operator acting on the nonadiabatic part of the distribution divided by a background Maxwellian.

One other point worth mentioning is that the form of the Sugama collision operator currently implemented in the GENE code utilizes a μ grid which is equidistant in the perpendicular velocity, not the standard Gauss-Laguerre grid. This is because derivatives in μ are taken as part of the evaluation of this term. In the collisionless case, there are no μ derivatives, and the main numerical error pertaining to the magnetic moment dimension is integration error. It then makes to use a discretization scheme that minimizes that type of error to better resolve modes such as trapped electron modes. When the collisionality is higher however, then dissipation of small scale structures in μ can occur, and the main numerical error is associated with the numerical differentiation which smooths out the magnetic moment component of the distribution function. If one were to use a grid which minimized the integration error for this case, then one would run the risk of optimizing for the wrong scenario. So it would make sense to use a μ grid which is equidistant in the perpendicular velocity. As of this writing, the Sugama collision operator has not been implemented with the μ Gauss-Laguerre grids because it was assumed that such a grid was no longer optimal for the case where collisions were active. However, it might make sense to implement the new grids in the collision model, and see if the model has the same necessary numerical free energy dissipation properties. One could then look at how the growth rates and frequencies of the various microinstabilities converge with different collisionalities and different grids. It may make sense for instance to use a Gauss-Laguerre grid for a weakly collisional system with TEMs, and an equidistant perpendicular velocity grid for the highly collisional edge (the Gauss-Laguerre grid may under-resolve the smoothing of the distribution function in certain regions of velocity space).

3.9.1 Numerical implementation of differential test-particle part

The differential part of the collision operator, $C_{ab}^{T0}(h_a)$, is evaluated with a second-order finite volume scheme on a grid which is equidistant in parallel and perpendicular velocity (this is very similar to the discretization applied to the full Landau-Boltzmann collision operator described in ref. [45]). The collisional fluxes are evaluated on a staggered velocity space grid from the nonadiabatic part of the distribution function divided by a background Maxwellian distribution. This scheme is used to allow for improved self-adjointness properties. To do this, C_{ab}^{T0} (Eq. 3.30) shall be written in a form more amenable to a finite volume discretization,

$$C_{ab}^{T0}(h_a) = \nabla_v \cdot \mathbf{J}_{ab}. \tag{3.111}$$

Where the collisional velocity space flux, $\mathbf{J}_{ab}$, can be split into a pitch-angle scattering part and an energy diffusion part,

$$\mathbf{J}_{ab} = \mathbf{J}_{ab,pa} + \mathbf{J}_{ab,ed}$$

$$\mathbf{J}_{ab,pa} = \frac{\nu_D(v)}{2}\left(v^2 \overleftrightarrow{\mathbf{I}} - \mathbf{vv}\right) F_{Ma} \cdot \frac{\partial}{\partial \mathbf{v}}\left(\frac{h_a}{F_{Ma}}\right)$$

$$\mathbf{J}_{ab,ed} = \frac{v}{2}\nu_{\parallel}^{ab}(v) F_{Ma} \frac{\partial}{\partial v}\left(\frac{h_a}{F_{Ma}}\right)\mathbf{v}.$$

From the above expression it is straightforward to split the collisional flux into a parallel and a perpendicular part,

$$J_{ab}^{\parallel} = \frac{1}{2}\left(v_{\parallel}^2 \nu_{\parallel}^{ab}(v) + v_{\perp}^2 \nu_D^{ab}(v)\right) F_{Ma} \frac{\partial}{\partial v_{\parallel}}\left(\frac{h_a}{F_{Ma}}\right) + \frac{1}{2}\left(\nu_{\parallel}^{ab}(v) - \nu_D^{ab}(v)\right) v_{\parallel} v_{\perp} F_{Ma} \frac{\partial}{\partial v_{\perp}}\left(\frac{h_a}{F_{Ma}}\right)$$

$$J_{ab}^{\perp} = \frac{1}{2}\left(\nu_{\parallel}^{ab}(v) - \nu_{D}^{ab}(v)\right) v_{\parallel} v_{\perp} F_{Ma} \frac{\partial}{\partial v_{\parallel}}\left(\frac{h_a}{F_{Ma}}\right) + \frac{1}{2}\left(v_{\perp}^2 \nu_{\parallel}^{ab}(v) + v_{\parallel}^2 \nu_{D}^{ab}(v)\right) F_{Ma} \frac{\partial}{\partial v_{\perp}}\left(\frac{h_a}{F_{Ma}}\right).$$

All of the frequencies and the background distribution are evaluated on the staggered grid (if the standard velocity space coordinates are evaluated from the indices 0, 1, 2, etc., then the staggered velocity space coordinates are evaluated from the indices 0.5, 1.5, 2.5, etc.) and the derivatives are interpolated to the staggered grid,

$$\left.\frac{\partial g}{\partial v_{\parallel}}\right|_{(l+1/2),(m+1/2)} = \frac{1}{2\Delta v_{\parallel}}\left(g(l+1,m) - g(l,m)\right) + \frac{1}{2\Delta v_{\parallel}}\left(g(l+1,m+1) - g(l,m+1)\right).$$

The use of the staggered grid is part of the second-order finite volume implementation. In the above expression, $v_{\parallel}$ is indexed by l and $v_{\perp}$ is indexed by m. The derivatives with respect to $v_{\perp}$ are defined in an analogous manner. The collision operator on the standard grid is then evaluated numerically from the staggered fluxes as

$$C_{ab}^{T0}(h_a) = \left(J_{ab}^{\parallel}(l+1/2,m) - J_{ab}^{\parallel}(l-1/2,m)\right)/\Delta v_{\parallel} + \left(J_{ab}^{\perp}(l,m+1/2) - J_{ab}^{\perp}(l,m-1/2)\right)/\Delta v_{\perp}.$$

Where the parallel and perpendicular flux elements in the above equation are calculated from the velocity space integration weights and the flux on the staggered grid via

$$J_{ab}^{\perp}(l, m \pm 1/2) = \frac{\Delta V_a(m \pm 1/2)}{2\Delta V_a(m)} J_{ab}^{\perp}(l - 1/2, m \pm 1/2) + \frac{\Delta V_a(m \pm 1/2)}{\Delta V_a(m)} J_{ab}^{\perp}(l + 1/2, m \pm 1/2)$$

$$J_{ab}^{\parallel}(l \pm 1/2, m) = \frac{\Delta V_a(m + 1/2)}{\Delta V_a(m)} J_{ab}^{\parallel}(l \pm 1/2, m + 1/2) + \frac{\Delta V_a(m - 1/2)}{\Delta V_a(m)} J_{ab}^{\parallel}(l \pm 1/2, m - 1/2).$$

All of the fluxes on the staggered grid that fall outside of the simulated velocity space box are set to zero. This enforces the conservation of particles for the differential part of the collision operator.

3.9.2 Numerical implementation of the moment parts of the collision operator

All of the moments are evaluated with the same numerical integration in velocity space that is used in the rest of the code,

$$M^{ab}_{1\mathbf{k}_\perp} = \int d^3v \frac{m_a v_\parallel}{T_a} C^{T0}_{ab}(h_{a\mathbf{k}_\perp} J_0(k_\perp \rho_a)) = \sum_l \sum_m \mathfrak{J} \Delta v_\parallel \Delta v_\perp \frac{m_a v_\parallel}{T_a} C^{T0}_{ab}(h_{a\mathbf{k}_\perp} J_0(k_\perp \rho_a))$$

$$M^{ab}_{2\mathbf{k}_\perp} = \int d^3v \frac{m_a v_\parallel}{T_a} C^{T0}_{ab}(h_{a\mathbf{k}_\perp} J_1(k_\perp \rho_a) \frac{v_\perp}{v_\parallel}) = \sum_l \sum_m \mathfrak{J} \Delta v_\parallel \Delta v_\perp \frac{m_a v_\parallel}{T_a} C^{T0}_{ab}(h_{a\mathbf{k}_\perp} J_1(k_\perp \rho_a) v_\perp / v_\parallel)$$

$$M^{ab}_{3\mathbf{k}_\perp} = \int d^3v x_a^2 C^{T0}_{ab}(h_{a\mathbf{k}_\perp} J_0(k_\perp \rho_a)) = \sum_l \sum_m \mathfrak{J} \Delta v_\parallel \Delta v_\perp x_a^2 C^{T0}_{ab}(h_{a\mathbf{k}_\perp} J_0(k_\perp \rho_a))$$

$$M^{ab}_{4\mathbf{k}_\perp} = \int d^3v v_\parallel J_0(k_\perp \rho_a) h_{a\mathbf{k}_\perp} = \sum_l \sum_m \mathfrak{J} \Delta v_\parallel \Delta v_\perp v_\parallel J_0(k_\perp \rho_a) h_{a\mathbf{k}_\perp}$$

$$M^{ab}_{5\mathbf{k}_\perp} = \int d^3v v_\perp J_1(k_\perp \rho_a) h_{a\mathbf{k}_\perp} = \sum_l \sum_m \mathfrak{J} \Delta v_\parallel \Delta v_\perp v_\perp J_1(k_\perp \rho_a) h_{a\mathbf{k}_\perp}$$

$$M^{ab}_{6\mathbf{k}_\perp} = \int d^3v \left(x_a^2 - \frac{3}{2} \right) J_0(k_\perp \rho_a) h_{a\mathbf{k}_\perp} = \sum_l \sum_m \mathfrak{J} \Delta v_\parallel \Delta v_\perp \left(x_a^2 - \frac{3}{2} \right) J_0(k_\perp \rho_a) h_{a\mathbf{k}_\perp}.$$

Here, $\mathfrak{J}$ represents the Jacobian of the gyrophase-integrated 2D velocity space integration ($\mathfrak{J} = 2\pi dv_\parallel v_\perp dv_\perp$). The indices which denote the discrete grid in $v_\parallel$ and μ are denoted by l and m. To evaluate these moments, the numerical implementation of C_{ab}^{T0} defined earlier is utilized. This allows for the conservation of momentum and energy to machine precision. In order to more effectively evaluate these moments at every time step, all of the terms which multiply the distribution and Bessel functions shall be grouped into one set of coefficients. So in the end, in order to evaluate the moments, one simply multiplies the distribution functions, the Bessel functions, and the coefficients, and sums over velocity space.

Now the coefficients of the moments must be considered. To begin with, the coefficients responsible for maintaining conservation of parallel momentum shall be examined,

$$X_1^{ab} = \frac{(\theta_{ab} - 1)}{n_a} F_{Ma} J_0(k_\perp \rho_a) v_\parallel$$

$$X_4^{ab} = \frac{(\theta_{ab} - 1)}{n_a \theta_{ab}} J_0(k_\perp \rho_a) C_{ab}^{TS}(F_{Ma} m_a v_\parallel / T_a)$$

$$Y_1^{ab} = -J_0(k_\perp \rho_a) \frac{T_b}{T_a} \theta_{ba} \frac{C_{ab}^{TS}(F_{Ma} m_a v_\parallel / T_a)}{\int d^3v C_{ab}^{TS}(F_{Ma} m_a v_\parallel / T_a) m_a v_\parallel / T_a}$$

$$Y_4^{ab} = -\frac{m_b}{T_b \tau_{ba}} \frac{\alpha_{ba}}{\sqrt{1 + \alpha_{ba}^2}} (\theta_{ba} - 1) Y_1^{ba}.$$

The coefficients must be discretized such that momentum is conserved to machine precision,

$$\int d^3v m_a v_\parallel C_{ab}^T(f_a) + \int d^3v m_b v_\parallel C_{ba}^F(f_a) = 0. \tag{3.112}$$

To do this, the following identities are utilized:

$$\frac{1}{n_a} = \frac{T_a}{m_a \int d^3v F_{Ma} v_\parallel^2}$$

$$\frac{1}{\theta_{ab} n_a} = -\frac{\theta_{ab}\alpha_{ab}}{\tau_{ab}\sqrt{1+\alpha_{ab}^2}\int d^3v v_\parallel C_{ab}^{TS}(F_{Ma} m_a v_\parallel / T_a)}.$$

The above identities can be shown from the definition of the Maxwellian distribution (Eq. 3.13), the definition of $C_{ab}^{TS}(F_{Ma} m_a v_\parallel / T_a)$ (Eq. 3.101), the expression for the integral moment of $C_{ab}^{T0}(F_{Ma} m_a v_\parallel / T_a)$ (Eq. 3.84), and a table of exponential integral identities. The following discretization is then obtained for X_1^{ab}, X_4^{ab}, Y_1^{ab}, and Y_4^{ab}:

$$X_1^{ab} = (\theta_{ab} - 1) J_0(k_\perp \rho_a) \frac{T_a F_{Ma} v_\parallel}{m_a \int d^3v F_{Ma} v_\parallel^2} \tag{3.113}$$

$$X_4^{ab} = -(\theta_{ab} - 1) \frac{\theta_{ab}\alpha_{ab}}{\tau_{ab}\sqrt{1+\alpha_{ab}^2}} \frac{J_0(k_\perp \rho_a) C_{ab}^{TS}(F_{Ma} m_a v_\parallel / T_a)}{\int d^3v v_\parallel C_{ab}^{TS}(F_{Ma} m_a v_\parallel / T_a)} \tag{3.114}$$

$$Y_1^{ab} = -J_0(k_\perp \rho_a) \frac{T_b}{T_a} \theta_{ba} \frac{C_{ab}^{TS}(F_{Ma} m_a v_\parallel / T_a)}{\int d^3v C_{ab}^{TS}(F_{Ma} m_a v_\parallel / T_a) m_a v_\parallel / T_a} \tag{3.115}$$

$$Y_4^{ab} = -\frac{m_b}{T_b \tau_{ba}} \frac{\alpha_{ba}}{\sqrt{1+\alpha_{ba}^2}} (\theta_{ba} - 1) Y_1^{ab}. \tag{3.116}$$

Provided that the integrations in the above expressions are carried out numerically, and the numerical form of C_{ab}^{T0} is used, momentum will be conserved to machine precision in the drift-kinetic limit. This can be verified by noting that the coefficients of M_1^{ab} and M_4^{ab} cancel when plugged into Eq. 3.112 (the integral of the differential test-particle part must also be considered when the examining the coefficients of M_1^{ab}). Particles and energy are conserved to machine precision by virtue of the fact that the integration of any term which is odd in $v_\parallel$ is zero. The coefficients responsible for perpendicular momentum conservation are obtained from the parallel momentum coefficients by replacing the $J_0(k_\perp \rho_a)$ Bessel function terms with $J_1(k_\perp \rho_a) v_\perp / v_\parallel$,

$$X_2^{ab} = (\theta_{ab} - 1) J_1(k_\perp \rho_a) \frac{T_a F_{Ma} v_\perp}{m_a \int d^3v F_{Ma} v_\parallel^2} \tag{3.117}$$

$$X_5^{ab} = -(\theta_{ab} - 1)\frac{\theta_{ab}\alpha_{ab}}{\tau_{ab}\sqrt{1+\alpha_{ab}^2}}\frac{J_1(k_\perp\rho_a)v_\perp C_{ab}^{TS}(F_{Ma}m_a v_\parallel/T_a)}{v_\parallel \int d^3v v_\parallel C_{ab}^{TS}(F_{Ma}m_a v_\parallel/T_a)} \tag{3.118}$$

$$Y_2^{ab} = -J_1(k_\perp\rho_a)\frac{T_b}{T_a}\theta_{ba}\frac{v_\perp C_{ab}^{TS}(F_{Ma}m_a v_\parallel/T_a)}{v_\parallel \int d^3v C_{ab}^{TS}(F_{Ma}m_a v_\parallel/T_a)m_a v_\parallel/T_a} \tag{3.119}$$

$$Y_5^{ab} = -\frac{m_b}{T_b\tau_{ba}}\frac{\alpha_{ba}}{\sqrt{1+\alpha_{ba}^2}}(\theta_{ba}-1)Y_2^{ab}. \tag{3.120}$$

Finally, the coefficients responsible for energy conservation must be discretized,

$$X_3^{ab} = \frac{2}{3n_a}(\theta_{ab}-1)F_{Ma}J_0(k_\perp\rho_a)\left(x_a^2 - \frac{3}{2}\right)$$

$$X_6^{ab} = \frac{2}{3n_a}\frac{(\theta_{ab}-1)}{\theta_{ab}}C_{ab}^{TS}(F_{Ma}x_a^2)J_0(k_\perp\rho_a)$$

$$Y_3^{ab} = -J_0(k_\perp\rho_a)\frac{T_b}{T_a}\theta_{ba}\frac{C_{ab}^{TS}(F_{Ma}x_a^2)}{\int d^3v x_a^2 C_{ab}^{TS}(F_{Ma}x_a^2)}$$

$$Y_6^{ab} = -\frac{2\alpha_{ba}}{\tau_{ba}(1+\alpha_{ba}^2)^{3/2}}(\theta_{ba}-1)Y_3^{ab}.$$

Where the energy conservation relation for collisions is given by

$$\int \frac{1}{2}m_a v^2 C_{ab}^T(f_a) + \int d^3v \frac{1}{2}m_b v^2 C_{ba}^F(f_b) = 0. \tag{3.121}$$

The following identities are utilized for the discretization:

$$\frac{2}{3n_a} = \frac{1}{\int d^3v F_{Ma}x_a^2(x_a^2 - 3/2)}$$

$$\frac{2}{3n_a\theta_{ab}} = \frac{-2\theta_{ab}\alpha_{ab}}{\tau_{ab}(1+\alpha_{ab}^2)^{3/2}\int d^3v x_a^2 C_{ab}^{TS}(F_{Ma}x_a^2)}.$$

The four coefficients needed for energy conservation can be written as

$$X_3^{ab} = (\theta_{ab} - 1)\frac{F_{Ma}(x_a^2 - 3/2)J_0(k_\perp \rho_a)}{\int d^3v F_{Ma} x_a^2 (x_a^2 - 3/2)}$$

$$X_6^{ab} = -(\theta_{ab} - 1)\frac{2\theta_{ab}\alpha_{ab} C_{ab}^{TS}(F_{Ma}x_a^2)J_0(k_\perp \rho_a)}{\tau_{ab}(1+\alpha_{ab}^2)^{3/2}\int d^3v x_a^2 C_{ab}^{TS}(F_{Ma}x_a^2)}$$

$$Y_3^{ab} = -J_0(k_\perp \rho_a)\frac{T_b}{T_a}\theta_{ba}\frac{C_{ab}^{TS}(F_{Ma}x_a^2)}{\int d^3v x_a^2 C_{ab}^{TS}(F_{Ma}x_a^2)}$$

$$Y_6^{ab} = -\frac{2\alpha_{ba}}{\tau_{ba}(1+\alpha_{ba}^2)^{3/2}}(\theta_{ba} - 1)Y_3^{ab}.$$

To make sure particles are conserved to machine precision, the following numerical replacements are made:

$$F_{Ma}(x_a^2 - 3/2) \to F_{Ma}\widetilde{(x_a^2 - 3/2)} = \left(F_{Ma}(x_a^2 - 3/2) - \frac{F_{Ma}}{\int d^3v F_{Ma}}\int d^3v F_{Ma}(x_a^2 - 3/2)\right) \tag{3.122}$$

$$C_{ab}^{TS}(F_{Ma}x_a^2) \to C_{ab}^{TS}\widetilde{(F_{Ma}x_a^2)} = \left(C_{ab}^{TS}(F_{Ma}x_a^2) - \frac{F_{Ma}}{\int d^3v F_{Ma}}\int d^3v C_{ab}^{TS}(F_{Ma}x_a^2)\right). \tag{3.123}$$

The following form is then obtained for the energy conservation coefficients:

$$X_3^{ab} = (\theta_{ab} - 1)\frac{F_{Ma}\widetilde{(x_a^2 - 3/2)}J_0(k_\perp \rho_a)}{\int d^3v x_a^2 F_{Ma}\widetilde{(x_a^2 - 3/2)}} \tag{3.124}$$

$$X_6^{ab} = -(\theta_{ab} - 1)\frac{2\theta_{ab}\alpha_{ab} C_{ab}^{TS}\widetilde{(F_{Ma}x_a^2)}J_0(k_\perp \rho_a)}{\tau_{ab}(1+\alpha_{ab}^2)^{3/2}\int d^3v x_a^2 C_{ab}^{TS}\widetilde{(F_{Ma}x_a^2)}} \tag{3.125}$$

$$Y_3^{ab} = -J_0(k_\perp \rho_a)\frac{T_b}{T_a}\theta_{ba}\frac{\widetilde{C_{ab}^{TS}(F_{Ma}x_a^2)}}{\int d^3v x_a^2 \widetilde{C_{ab}^{TS}(F_{Ma}x_a^2)}} \tag{3.126}$$

$$Y_6^{ab} = -\frac{2\alpha_{ba}}{\tau_{ba}(1+\alpha_{ba}^2)^{3/2}}(\theta_{ba}-1)Y_3^{ab}. \tag{3.127}$$

It is straightforward to show that when the same numerical integration scheme is consistently used, then the above choice of coefficients will conserve energy and particles to machine precision (The proof that energy conservation is numerically satisfied is similar to the proof of momentum conservation). Momentum will be conserved to machine precision, because all terms are even in $v_\parallel$. In the above formulas, the following form for $C_{ab}^{TS}(F_{Ma}m_a v_\parallel/T_a)$ and $C_{ab}^{TS}(F_{Ma}x_a^2)$ are used:

$$C_{ab}^{TS}(F_{Ma}m_a v_\parallel/T_a) = \theta_{ab}\left(C_{ab}^{T0}(F_{Ma}m_a v_\parallel/T_a) - \frac{F_{Ma}m_a\alpha_{ab}v_\parallel(\theta_{ab}-1)}{\tau_{ab}T_a\sqrt{1+\alpha_{ab}^2}}\right)$$

$$C_{ab}^{TS}(F_{Ma}x_a^2) = \theta_{ab}\left(C_{ab}^{T0}(F_{Ma}x_a^2) - \frac{2F_{Ma}\alpha_{ab}(\theta_{ab}-1)}{\tau_{ab}(1+\alpha_{ab}^2)^{3/2}}(x_a^2-3/2)\right).$$

In the above formulas, $C_{ab}^{T0}(F_{Ma}m_a v_\parallel/T_a)$ and $C_{ab}^{T0}(F_{Ma}x_a^2)$ are evaluated numerically using the scheme outlined in subsection 3.9.1 in order to have improved self-adjointness and conservation properties.

3.9.3 Normalization and summary of collision operator incorporated into GENE

Now that the numerical form of the collision operator in GENE has been obtained, the only thing left to be done is normalization. The collision operator shall be normalized according to the same protocol of the Vlasov gyrokinetic equation. For this, the following collisionality parameter has been defined based on other GENE parameters:

$$\nu_c = \frac{\pi e^4 n_{\mathrm{ref}} L_{\mathrm{ref}} \ln(\Lambda)}{2^{3/2} T_{\mathrm{ref}}^2}. \tag{3.128}$$

ν_c is a term which is labeled as "coll", and specified in the general namelist for a GENE simulation. It is also convenient to define the following normalized collision frequencies (based on Eq. 3.23, 3.26, and 3.81),

$$\hat{\nu}_D^{ab}(v) = \frac{L_{\text{ref}}}{c_{\text{ref}}}\nu_D^{ab}(v) = \frac{4\nu_c \hat{n}_{0b}\hat{n}_{pb}\hat{e}_a^2\hat{e}_b^2}{\sqrt{2^3\hat{m}_a\hat{T}_{0a}^3}\hat{v}^3}(\Phi(x_b) - G(x_b)) \tag{3.129}$$

$$\hat{\nu}_\parallel^{ab}(v) = \frac{L_{\text{ref}}}{c_{\text{ref}}}\nu_\parallel^{ab}(v) = \frac{8\nu_c \hat{n}_{0b}\hat{n}_{pb}\hat{e}_a^2\hat{e}_b^2}{\sqrt{2^3\hat{m}_a\hat{T}_{0a}^3}\hat{v}^3}G(x_b) \tag{3.130}$$

$$x_b = \hat{v}\sqrt{\frac{\hat{m}_b\hat{T}_{0a}}{\hat{m}_a\hat{T}_{0b}\hat{T}_{pb}}}$$

$$\frac{1}{\hat{\tau}_{ab}} = \frac{L_{\text{ref}}}{c_{\text{ref}}\tau_{ab}} = \frac{8}{3\sqrt{\pi}}\frac{\hat{n}_{0b}\hat{n}_{pb}\hat{e}_a^2\hat{e}_b^2}{\sqrt{2\hat{m}_a\hat{T}_{0a}^3\hat{T}_{pa}^3}}. \tag{3.131}$$

The final normalized collision operator can then be written in the following form:

$$C_{ab}^{(\text{Gyrokinetic})}(h_{a\mathbf{k}_\perp}, h_{b\mathbf{k}_\perp}) = C_{ab}^{T0}(h_{a\mathbf{k}_\perp}) + C_{ab}^{SD}(h_{a\mathbf{k}_\perp}) + \sum_{n=1}^{6}(X_{n\mathbf{k}_\perp}^{ab}M_{n\mathbf{k}_\perp}^{ab} + Y_{n\mathbf{k}_\perp}^{ab}M_{n\mathbf{k}_\perp}^{ab}). \tag{3.132}$$

$C_{ab}^{T0}(h_{a\mathbf{k}_\perp})$ is computed from the staggered velocity space grid,

$$C_{ab}^{T0}(h_a) = \Big(J_{ab}^{\parallel}(l+1/2,m) - J_{ab}^{\parallel}(l-1/2,m)\Big)/\Delta\hat{v}_\parallel + \Big(J_{ab}^{\perp}(l,m+1/2) - J_{ab}^{\perp}(l,m-1/2)\Big)/\Delta\hat{v}_\perp$$

$$J_{ab}^{\perp}(l,m\pm1/2) = \frac{\Delta V_a(m\pm1/2)}{2\Delta V_a(m)}J_{ab}^{\perp}(l-1/2,m\pm1/2) + \frac{\Delta V_a(m\pm1/2)}{\Delta V_a(m)}J_{ab}^{\perp}(l+1/2,m\pm1/2)$$

$$J_{ab}^{\parallel}(l\pm 1/2,m)=\frac{\Delta V_a(m+1/2)}{\Delta V_a(m)}J_{ab}^{\parallel}(l\pm 1/2,m+1/2)+\frac{\Delta V_a(m-1/2)}{\Delta V_a(m)}J_{ab}^{\parallel}(l\pm 1/2,m-1/2).$$

Where the collisional flux components are normalized as

$$J_{ab}^{\parallel}=\frac{1}{2}\left(\hat{v}_{\parallel}^2\hat{\nu}_{\parallel}^{ab}(v)+\hat{v}_{\perp}^2\hat{\nu}_D^{ab}(v)\right)\hat{F}_{Ma}\frac{\partial}{\partial\hat{v}_{\parallel}}\left(\frac{\hat{h}_{a\mathbf{k}_\perp}}{\hat{F}_{Ma}}\right)+\frac{1}{2}\left(\hat{\nu}_{\parallel}^{ab}(v)-\hat{\nu}_D^{ab}(v)\right)\hat{v}_{\parallel}\hat{v}_{\perp}\hat{F}_{Ma}\frac{\partial}{\partial\hat{v}_{\perp}}\left(\frac{\hat{h}_{a\mathbf{k}_\perp}}{\hat{F}_{Ma}}\right)$$

$$J_{ab}^{\perp}=\frac{1}{2}\left(\hat{\nu}_{\parallel}^{ab}(v)-\hat{\nu}_D^{ab}(v)\right)\hat{v}_{\parallel}\hat{v}_{\perp}\hat{F}_{Ma}\frac{\partial}{\partial\hat{v}_{\parallel}}\left(\frac{\hat{h}_{a\mathbf{k}_\perp}}{\hat{F}_{Ma}}\right)+\frac{1}{2}\left(\hat{v}_{\perp}^2\hat{\nu}_{\parallel}^{ab}(v)+\hat{v}_{\parallel}^2\hat{\nu}_D^{ab}(v)\right)\hat{F}_{Ma}\frac{\partial}{\partial\hat{v}_{\perp}}\left(\frac{\hat{h}_{a\mathbf{k}_\perp}}{\hat{F}_{Ma}}\right).$$

The spatial diffusion operator is normalized as

$$C_{ab}^{SD}(h_{a\mathbf{k}_\perp})=-\frac{\hat{k}_{\perp}^2\hat{h}_{a\mathbf{k}_\perp}\hat{m}_a\hat{T}_{0a}}{2\hat{e}_a^2\hat{B}_0^2}(\hat{\nu}_D^{ab}(v)(2\hat{v}_{\parallel}^2+\hat{v}_{\perp}^2)+\hat{\nu}_{\parallel}^{ab}(v)\hat{v}_{\perp}^2). \tag{3.133}$$

The moments for the nonisothermal test-particle part and field-particle part are written in normalized form as

$$M_{1\mathbf{k}_\perp}^{ab}=\int d^3\hat{v}\hat{n}_{0a}\sqrt{\frac{2\hat{T}_{0a}}{\hat{m}_a}}\frac{\hat{m}_a\hat{v}_{\parallel}}{\hat{T}_{0a}\hat{T}_{pa}}C_{ab}^{T0}(\hat{h}_{a\mathbf{k}_\perp}J_0(k_{\perp}\rho_a))$$

$$M_{2\mathbf{k}_\perp}^{ab}=\int d^3\hat{v}\hat{n}_{0a}\sqrt{\frac{2\hat{T}_{0a}}{\hat{m}_a}}\frac{\hat{m}_a\hat{v}_{\parallel}}{\hat{T}_{0a}\hat{T}_{pa}}C_{ab}^{T0}(\hat{h}_{a\mathbf{k}_\perp}J_1(k_{\perp}\rho_a)\hat{v}_{\perp}/\hat{v}_{\parallel})$$

$$M_{3\mathbf{k}_\perp}^{ab}=\int d^3\hat{v}\hat{n}_{0a}\frac{\hat{v}^2}{\hat{T}_{pa}}C_{ab}^{T0}(\hat{h}_{a\mathbf{k}_\perp}J_0(k_{\perp}\rho_a))$$

$$M_{4\mathbf{k}_\perp}^{ab}=\int d^3\hat{v}\hat{n}_{0a}\sqrt{\frac{2\hat{T}_{0a}}{\hat{m}_a}}\hat{v}_{\parallel}\hat{h}_{a\mathbf{k}_\perp}J_0(k_{\perp}\rho_a)$$

$$M^{ab}_{5\mathbf{k}_\perp} = \int d^3\hat{v}\hat{n}_{0a}\sqrt{\frac{2\hat{T}_{0a}}{\hat{m}_a}}\hat{v}_\perp \hat{h}_{a\mathbf{k}_\perp} J_1(k_\perp\rho_a)$$

$$M^{ab}_{6\mathbf{k}_\perp} = \int d^3\hat{v}\hat{n}_{0a}\left(\frac{\hat{v}^2}{\hat{T}_{pa}} - \frac{3}{2}\right)\hat{h}_{a\mathbf{k}_\perp} J_0(k_\perp\rho_a).$$

The coefficients for the nonisothermal test-particle part are written in normalized form as

$$X^{ab}_{1\boldsymbol{k}_\perp} = (\theta_{ab}-1)J_0(k_\perp\rho_a)\frac{\hat{T}_{0a}\hat{T}_{pa}\hat{F}_{Ma}\hat{v}_\parallel}{\hat{n}_{0a}\sqrt{2\hat{m}_a\hat{T}_{0a}}\int d^3\hat{v}\hat{F}_{Ma}\hat{v}_\parallel^2}$$

$$X^{ab}_{2\boldsymbol{k}_\perp} = (\theta_{ab}-1)J_1(k_\perp\rho_a)\frac{\hat{T}_{0a}\hat{T}_{pa}\hat{F}_{Ma}\hat{v}_\perp}{\hat{n}_{0a}\sqrt{2\hat{m}_a\hat{T}_{0a}}\int d^3\hat{v}\hat{F}_{Ma}\hat{v}_\parallel^2}$$

$$X^{ab}_{3\mathbf{k}_\perp} = (\theta_{ab}-1)\frac{J_0(k_\perp\rho_a)\widetilde{\hat{F}_{Ma}(\hat{v}^2/\hat{T}_{pa}-3/2)}}{\hat{n}_{0a}\int d^3\hat{v}(\hat{v}^2/\hat{T}_{pa})\widetilde{\hat{F}_{Ma}(\hat{v}^2/\hat{T}_{pa}-3/2)}}$$

$$X^{ab}_{4\mathbf{k}_\perp} = -(\theta_{ab}-1)\frac{\theta_{ab}\alpha_{ab}}{\hat{\tau}_{ab}\sqrt{1+\alpha_{ab}^2}}\frac{J_0(k_\perp\rho_a)C^{TS}_{ab}(\widehat{F_{Ma}m_a}v_\parallel/T_a)}{\hat{n}_{0a}\sqrt{2\hat{T}_{0a}/\hat{m}_a}\int d^3\hat{v}\hat{v}_\parallel C^{TS}_{ab}(\widehat{F_{Ma}m_a}v_\parallel/T_a)}$$

$$X^{ab}_{5\mathbf{k}_\perp} = -(\theta_{ab}-1)\frac{\theta_{ab}\alpha_{ab}}{\hat{\tau}_{ab}\sqrt{1+\alpha_{ab}^2}}\frac{\hat{v}_\perp J_1(k_\perp\rho_a)C^{TS}_{ab}(\widehat{F_{Ma}m_a}v_\parallel/T_a)}{\hat{n}_{0a}\hat{v}_\parallel\sqrt{2\hat{T}_{0a}/\hat{m}_a}\int d^3\hat{v}\hat{v}_\parallel C^{TS}_{ab}(\widehat{F_{Ma}m_a}v_\parallel/T_a)}$$

$$X^{ab}_{6\mathbf{k}_\perp} = -(\theta_{ab}-1)\frac{2\theta_{ab}\alpha_{ab}}{\hat{\tau}_{ab}(1+\alpha_{ab}^2)^{3/2}}\frac{\widetilde{C^{TS}_{ab}(F_{Ma}x_a^2)}}{\hat{n}_{0a}\int d^3\hat{v}(\hat{v}^2/\hat{T}_{pa})\widetilde{C^{TS}_{ab}(F_{Ma}x_a^2)}}.$$

The coefficients for the field-particle part are written in normalized form as

$$Y^{ab}_{1\mathbf{k}_\perp} = -\theta_{ba}\hat{T}_{0b}\hat{T}_{pb}\frac{J_0(k_\perp\rho_a)C^{TS}_{ab}(\widehat{F_{Ma}m_a}v_\parallel/T_a)}{\hat{n}_{0a}\sqrt{2\hat{m}_a\hat{T}_{0a}}\int d^3\hat{v}C^{TS}_{ab}(\widehat{F_{Ma}m_a}v_\parallel/T_a)}$$

$$Y^{ab}_{2\mathbf{k}_\perp} = -\theta_{ba}\hat{T}_{0b}\hat{T}_{pb}\frac{\hat{v}_\perp J_1(k_\perp\rho_a)C^{TS}_{ab}(\widehat{F_{Ma}m_a}v_\parallel/T_a)}{\hat{n}_{0a}\hat{v}_\parallel\sqrt{2\hat{m}_a\hat{T}_{0a}}\int d^3\hat{v}C^{TS}_{ab}(\widehat{F_{Ma}m_a}v_\parallel/T_a)}$$

$$Y^{ab}_{3\mathbf{k}_\perp} = -J_0(k_\perp\rho_a)\frac{\hat{T}_{0b}\hat{T}_{pb}}{\hat{n}_{0a}\hat{T}_{0a}}\theta_{ba}\frac{\widetilde{C^{TS}_{ab}(F_{Ma}x_a^2)}}{\int d^3\hat{v}\hat{v}^2\widetilde{C^{TS}_{ab}(F_{Ma}x_a^2)}}$$

$$Y^{ab}_{4\mathbf{k}_\perp} = -\frac{\hat{m}_b}{\hat{T}_{0b}\hat{T}_{pb}\hat{\tau}_{ba}}\frac{\alpha_{ba}(\theta_{ba}-1)}{\sqrt{1+\alpha_{ba}^2}}Y^{ab}_{1\mathbf{k}_\perp}$$

$$Y^{ab}_{5\mathbf{k}_\perp} = -\frac{\hat{m}_b}{\hat{T}_{0b}\hat{T}_{pb}\hat{\tau}_{ba}}\frac{\alpha_{ba}(\theta_{ba}-1)}{\sqrt{1+\alpha_{ba}^2}}Y^{ab}_{2\mathbf{k}_\perp}$$

$$Y^{ab}_{6\mathbf{k}_\perp} = -\frac{2\alpha_{ba}(\theta_{ba}-1)}{\hat{\tau}_{ba}(1+\alpha_{ba}^2)^{3/2}}(\theta_{ba}-1)Y^{ab}_{3\mathbf{k}_\perp}.$$

For the above coefficients, $C^{TS}_{ab}(\widehat{F_{Ma}m_a}v_\parallel/T_a)$ and $C^{TS}_{ab}(\widehat{F_{Ma}}x_a^2)$ are given by

$$C^{TS}_{ab}(\widehat{F_{Ma}m_a}v_\parallel/T_a) = \theta_{ab}\Bigg(C^{T0}_{ab}\Bigg(\sqrt{2\hat{m}_a\hat{T}_{0a}}\hat{F}_{Ma}\hat{m}_a\hat{v}_\parallel/\Bigg(\hat{T}_{0a}\hat{T}_{pa}\Bigg)\Bigg)$$

$$-\frac{\hat{F}_{Ma}\sqrt{2\hat{m}_a\hat{T}_{0a}}\alpha_{ab}\hat{v}_\parallel(\theta_{ab}-1)}{\hat{\tau}_{ab}\hat{T}_{0a}\hat{T}_{pa}\sqrt{1+\alpha_{ab}^2}}\Bigg)$$

$$C^{TS}_{ab}(\widehat{F_{Ma}}x_a^2) = \theta_{ab}\Bigg(C^{T0}_{ab}(\hat{F}_{Ma}\hat{v}^2/\hat{T}_{pa}) - \frac{2\hat{F}_{Ma}\alpha_{ab}(\theta_{ab}-1)}{\hat{\tau}_{ab}(1+\alpha_{ab}^2)^{3/2}}\Bigg(\frac{\hat{v}^2}{\hat{T}_{pa}}-\frac{3}{2}\Bigg)\Bigg).$$

And the tilde is used to designate the following scheme to ensure conservation of particles:

$$\widetilde{a(v)} = a(v) - \frac{\hat{F}_{Ma}}{\int d^3\hat{v}\hat{F}_{Ma}}\int d^3\hat{v}a(v).$$

3.10 Collision spectra and time-stepping

Since it is computationally expensive to evaluate the collision operator term, and since the collisionality can dramatically limit the timestep in gyrokinetic simulations (especially in the edge), it is desirable to optimize the code by evolving the collision operator with a separate

numerical time scheme than the other terms in the gyrokinetic equation. Currently a first order Runge-Kutta-Chebyshev (RKC) method is employed to evolve the collision operator as opposed to the default 4th order Runge-Kutta schemes used with the other terms [62]. There are four different RKC schemes available in GENE to use with the collision operator, each with a different number of stages (RKC1, RKC2, RKC3, and RKC4). The higher stage schemes require more evaluations and are more expensive to employ. However, they allow for a larger timestep. The lower stage schemes require fewer evaluations. However, they require a smaller timestep. By default, each collisional time-stepping scheme is tested in the initialization phase, and the least computationally expensive scheme is chosen (this method is employed by setting coll_split_scheme = 'RKCa' in the general namelist, which is done by default).

Since the collision operator is linear, the eigenvalue spectra of the collision operator can be precomputed and used to determine the maximum possible time step for a given scheme. All of the eigenvalues of the operator must fit within the stability contour for the corresponding time-stepping scheme. Fig. 3.1 shows a plot of the stability contours for the various time-stepping schemes associated with the collision operator (in the drift-kinetic limit).

Since the contours scale with the timestep, one can optimize the timestep value by ensuring that all of the eigenvalues just barely fit within the stability contours. In all cases, it is the most negative real eigenvalue which determines the timestep. So for a given stage scheme, the most negative real eigenvalue is determined with SLEPC, then the stability contour is adjusted (by adjusting the timestep) such that that eigenvalue barely falls within. The corresponding timestep is the optimized one. There is then a comparison of the computational effort associated with an RKC1, RKC2, RKC3, and RKC4 scheme, and the more optimal choice is used. While this splitting scheme can speed up the code by a factor of ~ 3, future time-stepping schemes may have to be developed to further speed up the code because collisions can dramatically limit the value of the time-step in the edge of a device, especially the spatial diffusion from the FLR corrections. For more information on alternative time-stepping schemes, see ref. [51, 63] for details on the time-stepping schemes utilized

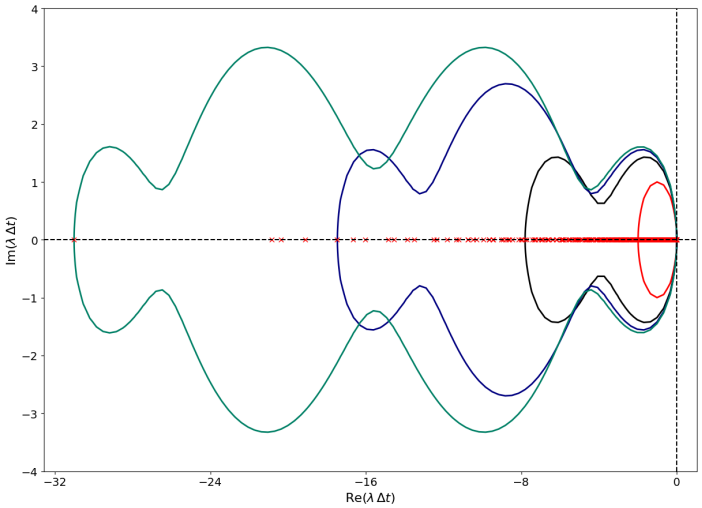

Figure 3.1: Shapes of stability contours for different stage schemes for a given timestep. The eigenvalues of the collision operator (in the drift-kinetic limit) are shown by the red crosses. They lie purely along the negative real axis. The stability contours are shown by the curves, and they represent the RKC1 (red), RKC2 (black), RKC3 (blue), and RKC4 (green) time-stepping schemes. As one goes to higher stage schemes, the number of evaluations of the collision operator is increased, and the timestep is also increased. The computational effort associated with all schemes is then evaluated, and the optimal choice is taken [62].

in the GS2 and GKV gyrokinetic codes respectively.

3.11 Implementation of collisions with block-structured grids in velocity space

In addition to the timestep optimization scheme, the collision operator has been adapted to be compatible with the block-structured grid numerical scheme in GENE [57, 58]. Block-structured grids are used to optimize global gyrokinetic simulations (particularly nonlinear simulations) with steep temperature gradients. In turbulent simulations, the perturbed distribution function typically varies on scales of the thermal velocity, $v_T = \sqrt{2T/m}$ in velocity space. So for standard grids, one would need a large velocity-space domain to capture all of the physics in the core, and one would also need a fine velocity space grid to resolve the physics in the edge. This would lead to very expensive high-resolution simulations. One could get around this problem by having a velocity space grid which continuously varied with the radial position as the temperature varied, but this would severely complicate the gyrokinetic equations and numerical model. To get around this problem, the velocity space domain is made to discretely vary with radial position. A typical simulation setup with block-structured grids is shown in Fig. 3.2.

Block-structured grids are a convenient tool to use with collisions. With block-structured grids, global simulations can be run with fewer velocity space points, which is very convenient for collisional runs, because the computational time to evaluate the collisions increases and the value of the timestep in collisional runs decreases as the number of velocity space points is increased. Furthermore, collisions also help to enforce the assumptions that are made in using the block-structured grid model. The block-structured grid model is predicated on the assumption that the turbulent perturbed distribution function is localized to a structure that varies on the thermal velocity scale (when the background distribution is taken to be a Maxwellian structure, as is always the case when collisions are active). The collisional dissipation function actively drives the perturbation to that sort of structure, providing more confidence that the underlying assumption behind block-structured grids is satisfied.

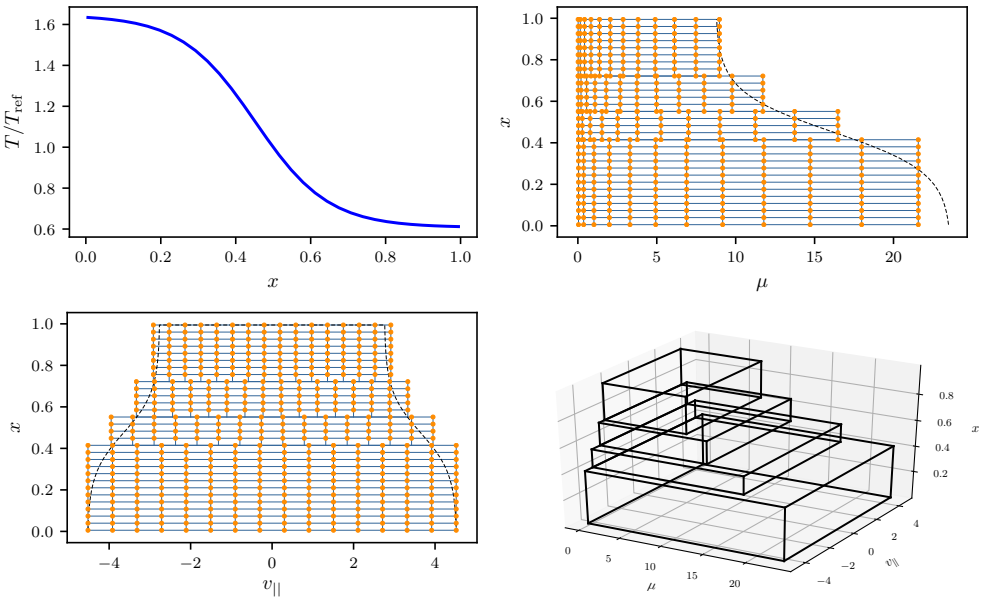

Figure 3.2: Block-structured grid setup for a typical global simulation with varying temperature profile. The upper-left graph depicts the variation of temperature with radial position. The lower-right plot shows the variation of block sizes with radial position. The larger velocity space boxes are near the core where the thermal velocity is higher, and the smaller velocity space boxes are near the edge where the thermal velocity is lower. The lower left plot depicts the variation of the parallel velocity space domain with radial position, and the upper right plot depicts the variation of the magnetic moment velocity space domain with radial position. The above plots used 30 points in the radial position, 24 points in the parallel velocity, and 12 points in the magnetic moment. Typical simulations would require much higher resolution, but the above setup was presented with lower resolution for purposes of clarity. This same figure is also shown in ref. [**?**].

In this way, the two numerical models work to complement each other. It should also be pointed out that adapting global FLR corrections to the global gyrokinetic model, as well as the block-structured grid numerical scheme, shall be left for future work.

3.12 Relaxation and conservation tests

One of the fundamental consequences of the derived collision operator is the relaxation of an arbitrary distribution function towards a perturbed Maxwellian structure of the following form:

Species	Mass	Temperature	Density	Charge
Deuterium	1	1	1	1
Boron	5	0.5	0.2	5
Electrons	0.0002778	2	2	-1

Table 3.1: Parameter set for the relaxation tests. All values in the table are normalized with respect to Deuterium values.

$$f_a \to F_{Ma}\left(\frac{\delta n_a}{n_a} + \frac{m_a}{T_a}u_\parallel v_\parallel + \frac{\delta T}{T}\left(x_a^2 - \frac{3}{2}\right)\right).$$

Where $u_\parallel$ and $\delta T/T$ are the same between all species after a sufficiently long time. This suggests convenient tests for verifying the correct implementation of the collision operator. One could initialize different species to distributions of the form, $f_a = A_a F_{Ma} v_\parallel$, evolve the species using only the collision operator, and see if all species are driven towards a smooth distribution with the same final flow while verifying that momentum is conserved and the change in free energy is negative definite. Similarly, one could initialize different species to distributions of the form, $f_a = A_a F_{Ma}(x_a^2 - 3/2)$, evolve the species using only the collision operator, and see if all species are driven towards a smooth distribution with the same final perturbed temperature while verifying that particles and energy are conserved and the change in free energy is negative definite. Finally, one can also initialize distributions to arbitrary structures, and verify that the collisions relax such structures to perturbed Maxwellians while maintaining negative definite changes in free energy. These tasks have been done in subsections 3.12.1, 3.12.2, and 3.12.3 respectively. These tests have also been done for nonisothermal parameter sets to verify the correct implementation of the Sugama operator. The standard linear Landau-Boltzmann collision operator will not pass these tests in the nonisothermal case. The parameters for these three tests are shown in Table 3.1.

For the following tests, the rate of change of free energy at a point in configuration space is defined as follows:

$$\left.\frac{dF}{dt}\right|_{\text{coll}} = \sum_j \hat{n}_{0j}\hat{T}_{0j}\int d^3\hat{v}\,\frac{\hat{h}_j}{\hat{F}_{Ma}}C_j.$$

3.12.1 Relaxation of flow fluctuations

The derived collision model should act to drive flow perturbations of the form $u_{a\parallel} = \int d^3v v_\parallel f_a / n_a$ towards the same value. To test this property, deuterium, boron, and electron species were initialized to distributions of the form, $f_a = F_{Ma} m_a u_{a\parallel} v_\parallel / T_a$ (where $u_{a\parallel}$ is different for different species), and evolved using only the collision operator in the drift-kinetic limit ($k_\perp \to 0$). The time trace of the flow velocities, free energy dissipation, and momentum conservation error were then examined to verify correct behavior of the collision operator.

The results of the test are shown in Fig. 3.3, 3.4, and 3.5. Fig. 3.3 shows that the flows for different species all relax to the same value and that the free energy change is negative definite. It can also be seen that the electron flow relaxes much quicker than the ion flows, which is consistent with physical intuition for flow relaxation. Fig. 3.4 shows that the collision operator drives the species towards a smooth final state consistent with the perturbed Maxwellian shape expected. Fig. 3.5 shows that the momentum conservation error remains bounded within reasonable values for a realistic mass ratio system ($< 10^{-10}$). The expression for the momentum conservation error is given in Eq. 3.134,

$$\Delta_M = \frac{\sum_a m_a \int d^3v v_\parallel f_a - \left(\sum_a m_a \int d^3v v_\parallel f_a \right)\Big|_{t=t_{\text{start}}}}{\left(\sum_a \int d^3v v_\parallel f_a \right)\Big|_{t=t_{\text{start}}}}. \tag{3.134}$$

These tests confirm that the collision operator behaves as it should.

3.12.2 Relaxation of thermal fluctuations

The derived collision model should act to drive temperature perturbations of the form $\delta T_a / T_a = \int d^3v m_a v^2 f_a / 2 n_a$ towards the same value. To test this property, deuterium, boron, and electron species were initialized to distributions of the form shown in Eq. 3.135,

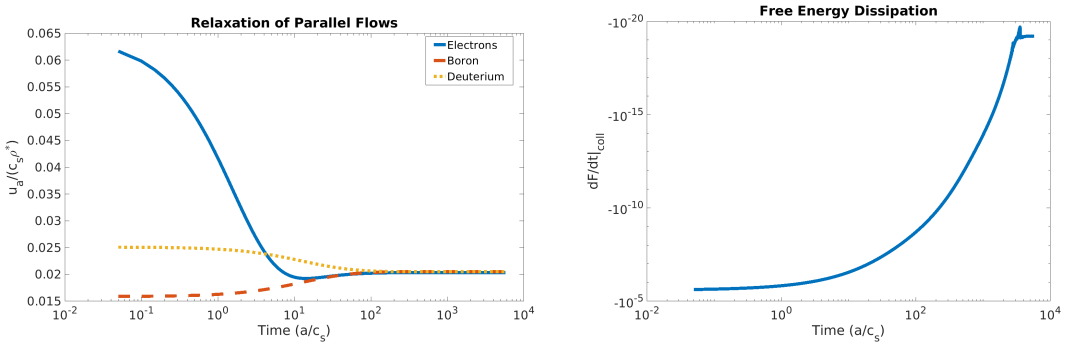

Figure 3.3: The graph on the left depicts flow equilibration for the relaxation test. Collisions drive all species towards the same parallel flow velocity. The graph on the right depicts free energy dissipation vs. time for the flow relaxation test. The change in free energy by collisions is negative definite, consistent with the second law of thermodynamics.

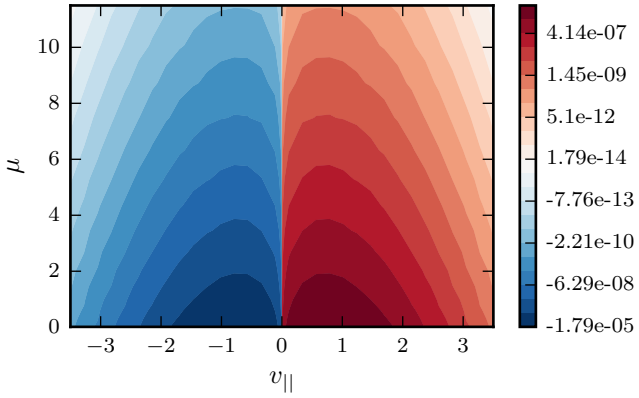

Figure 3.4: Electron velocity distribution function for the flow relaxation test. Collisions drive all species towards a smooth velocity space distribution resembling the one shown above. The distribution for Deuterium and Boron look similar .

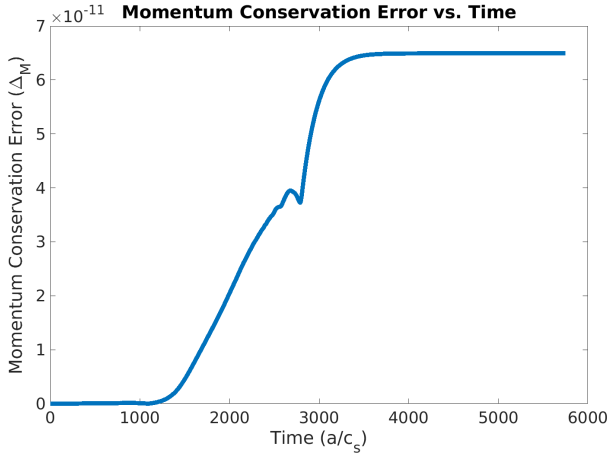

Figure 3.5: Momentum conservation error vs. time for the flow relaxation test. Collisions conserve momentum to nearly machine precision.

$$f_n = \frac{\delta T_n}{T_n} F_{Mn}\left(\frac{m_n v^2}{2T_n} - \frac{3}{2}\right). \tag{3.135}$$

In this test, $\delta T_n/T_n$ is different for different species. The system was then evolved using only the collision operator in the drift-kinetic limit ($k_\perp \to 0$). The time trace of the temperature fluctuation amplitudes, free energy dissipation, particle conservation error, and energy conservation error were then examined to verify correct behavior of the collision operator. The results of the test are shown in Fig. 3.6, 3.7, and 3.8.

Fig. 3.6 shows that the temperature fluctuations for different species all relax to the same value and that the free energy change is negative definite. Also, the ions equilibrate much faster than the electrons due to the much higher mass ratio between the electrons and ions, which is consistent with analytical estimates. The time has been normalized with respect to the ion-ion collision frequency defined by $\nu_{ii} = 8\pi q^4 n_i \ln(\Lambda)/\sqrt{8 m_i T_i^3}$. It can be seen that the ions equilibrate on the order of the inverse ion-ion collision frequency, whereas the electrons equilibrate with the ions on time scales about two orders of magnitude longer. Typical transport time scales are $O(\nu_{ii}^{-1})$, so on the scale of the ion equilibration time-scale. The electron equilibration time is roughly 100 times larger than the transport time-scales, which is important if the ion and electron temperatures are regarded as separate and fixed throughout a simulation.

Fig. 3.8 shows that the collision operator drives the species towards a smooth final state consistent with the perturbed Maxwellian shape expected. Fig. 3.7 shows that the particle and energy conservation error remain bounded within reasonable values for a realistic mass ratio system ($< 10^{-10}$) over very long time scales. The expressions for the particle conservation error, Δ_P, energy conservation error, Δ_E, and temperature fluctuation amplitude, $\delta T_a/T_a$, are given in Eq. 3.136, 3.137, and 3.138 respectively,

$$\Delta_P = \frac{\int d^3v f_a - \left(\int d^3v f_a\right)\Big|_{t=t_{\text{start}}}}{\left(\int d^3v f_a\right)\Big|_{t=t_{\text{start}}}} \tag{3.136}$$

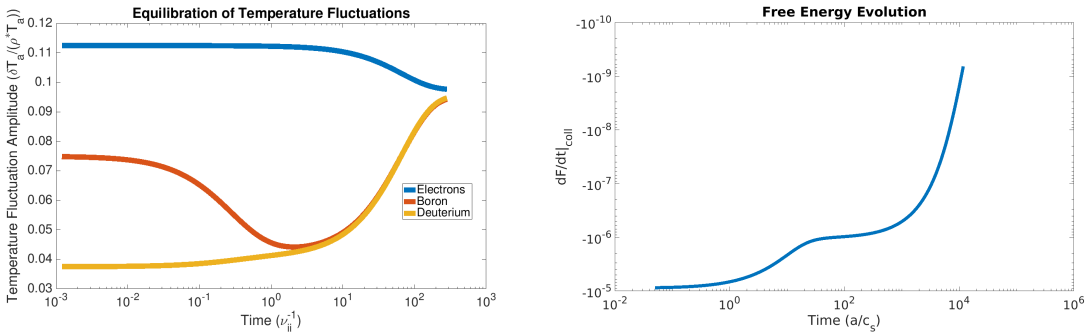

Figure 3.6: The graph on the left depicts relaxation of temperature fluctuations. The graph on the right depicts free energy dissipation during the relaxation test. The change in free energy due to collisions is negative definite, consistent with the H-theorem.

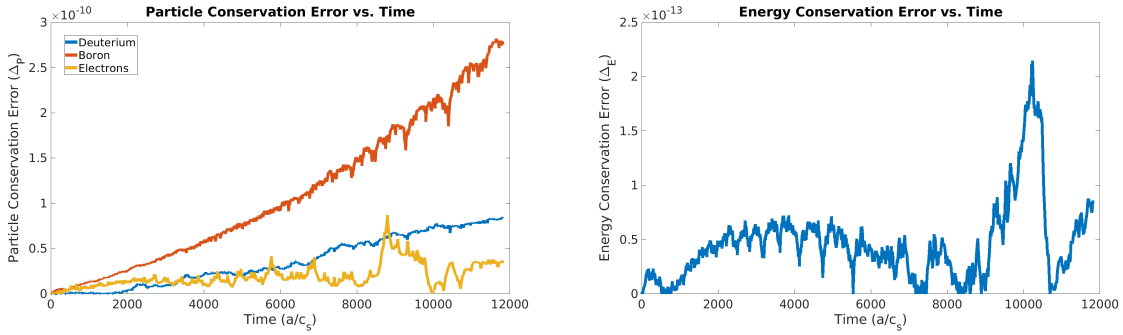

Figure 3.7: Particle and energy conservation error during the relaxation test. Particles and energy are conserved to nearly machine precision over very long simulation times.

$$\Delta_E = \frac{\sum_a \frac{1}{2} m_a \int d^3v v^2 f_a - \left(\sum_a \frac{1}{2} m_a \int d^3v v^2 f_a \right)\Big|_{t=t_{\text{start}}}}{\left(\sum_a \frac{1}{2} m_a \int d^3v v^2 f_a \right)\Big|_{t=t_{\text{start}}}} \tag{3.137}$$

$$\frac{\delta T_a}{T_a} = \frac{m_a}{2 n_{a0}} \int d^3v v^2 f_a / T_{0a}. \tag{3.138}$$

These tests confirm that the collision operator behaves as it should.

3.12.3 Relaxation from an arbitrary distribution

In addition to satisfying the simplistic relaxation tests from simple perturbed Maxwellian structures, a relaxation test has been performed where the velocity space profiles for different species have been initialized to shifted Maxwellian structures and it has been observed that

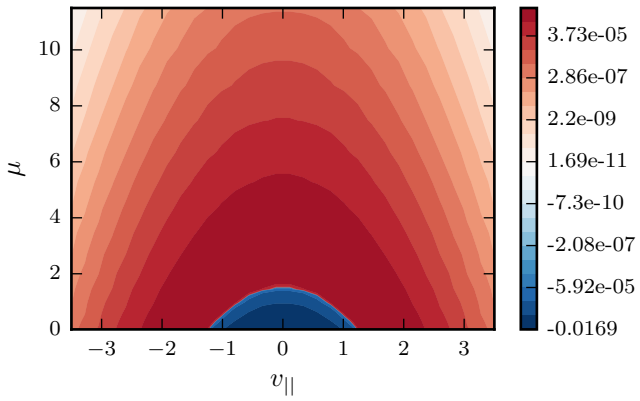

Figure 3.8: Electron velocity space profile for temperature fluctuation relaxation test. A similar distribution is obtained for all species.

the H-theorem remains satisfied for this more general scenario, and that the profiles relax to more simple perturbed Maxwellians. Fig. 3.9 and 3.10 show the velocity space distributions and the free energy dissipation vs. time for this test.

3.13 Effect of collisions on geodesic acoustic mode (GAM) oscillations

An essential test for the correct implementation of the collision operator is the Rosenbluth-Hinton test. The zeroth toroidal mode number ($k_y = 0$) must not be linearly unstable, and it must be damped by collisions. The mode that exists at $k_y = 0$ is called the geodesic acoustic mode (GAM) and there is a well established theory of how these modes are dampened by collisions [64]. According to the Rosenbluth-Hinton theory, the short-time behavior of the residual potential in the collisional limit is given by the following formula:

$$\frac{\phi_k(t)}{\phi_k(0)} \cong A_k(t) + B_k(t)$$

$$A_k(t) = \Big(1 - \Lambda\Big) \exp\Big(- \exp(-q^2)t/(\tau_{ii}R)\Big) \cos(t/(\tau_{ii}R))$$

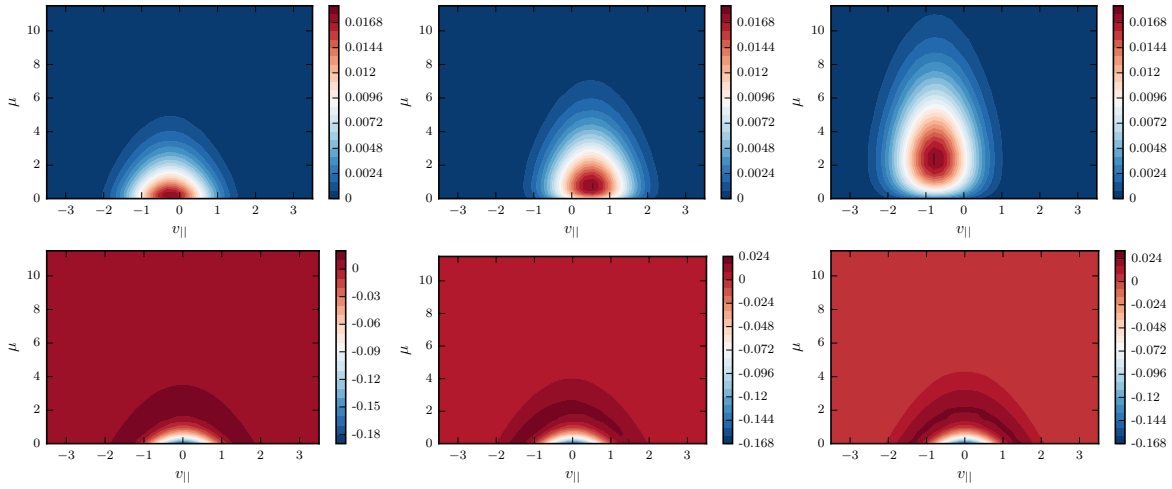

Figure 3.9: Velocity space distribution at the beginning and end of the relaxation test. The graphs at the top are of the initialized distribution, and the graphs at the bottom are of the corresponding final distribution. The graphs on the left, middle, and right correspond to deuterium, boron, and electrons respectively. Collisions relax the distributions to a more localized perturbed Maxwellian.

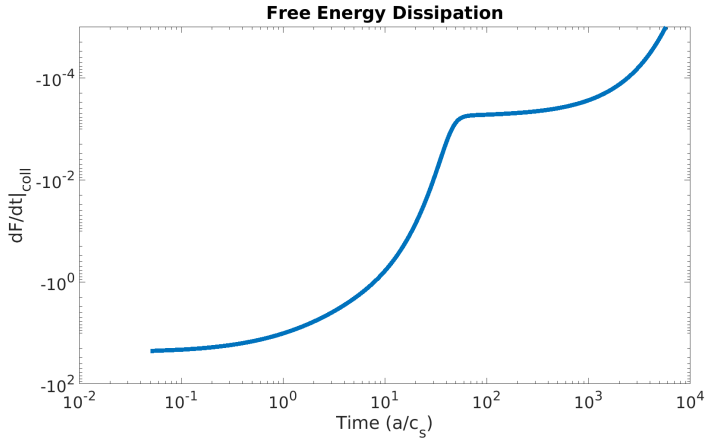

Figure 3.10: Free energy dissipation for the relaxation test. Free energy dissipation is once again negative definite.

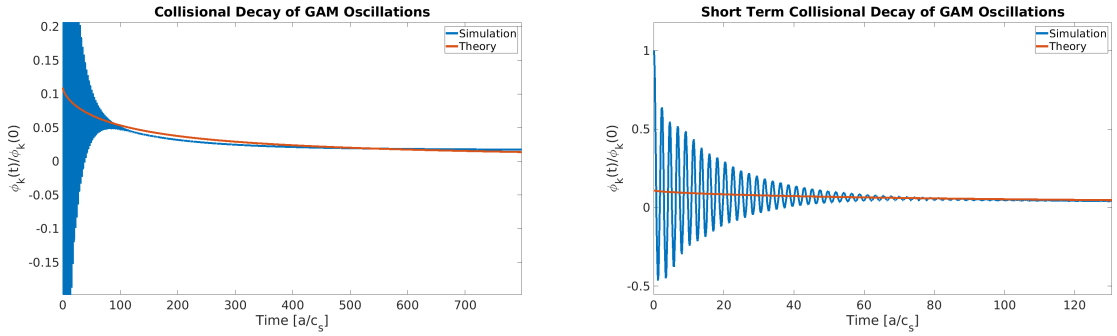

Figure 3.11: Simulations of collisional GAM oscillations are performed and compared to the short-term decay of the non-oscillatory part of the mode. The above plot shows fairly good agreement between GENE simulations and the theory of Rosenbluth and Hinton [65]. The data for the above graph was taken from a one species simulation with 48 points in z, 100 points in μ, and 200 points in the parallel velocity at $k_x = 0.01$. The size of the velocity space box was 4 and 16 in the parallel velocity and μ. The mass, temperature, and density were all set to 1.0 in GENE units. The magnetic geometry was circular with a safety factor of 1.4, an inverse aspect ratio of 0.18, and a major radius of 1.0. The collisionality for the simulation was 0.001 in GENE units.

$$B_k(t) = \Lambda \exp(\Lambda^2 \beta) \mathrm{erfc}(\Lambda \sqrt{\beta})$$

$$\beta = \frac{9\pi^2 q^4 0.61}{\epsilon^2 \ln(16\epsilon\tau_{ii}/(0.61t))} \frac{t}{\tau_{ii}}.$$

In the above formulas, Λ is the residual value of the potential in the collisionless limit, q is the safety factor, R is the major radius of the tokamak, ϵ is the inverse aspect ratio for the magnetic geometry, t is time, and τ_{ii} is the ion-ion collision time [65],

$$\tau_{ii} = \frac{3\sqrt{m_i T_i^3}}{4ne^4\sqrt{\pi}\ln(\Lambda)}.$$

In the above formula, m_i is the ion mass, T_i is the ion temperature, n is the plasma density, e is the magnitude of the electron charge, and $\ln(\Lambda)$ is the Coulomb logarithm. A collisional simulation of GAM oscillations has been performed and the averaged value of the electrostatic potential has been plotted vs. time and compared to $B_k(t)$ to see if the short term collisional decay resembles the prediction by Rosenbluth and Hinton. The results are shown in Fig. 3.11.

r/a=0.5	R/a=3	$\hat{s}$=1.0	α=0	q=2.0
$a/L_{Te} = 3$	$a/L_{Ti} = 3$	$a/L_n = 1$	$T_i/T_e = 1$	$m_e/m_i = 0.0002732$

Table 3.2: General Atomics standard case parameter set for neoclassical benchmark in $\hat{s} - \alpha$ geometry for 2 species case

3.14 Collision operator benchmarks

3.14.1 Local neoclassical benchmark

In an effort to further verify the collision operator, local neoclassical simulations have been performed, and the results have been benchmarked with another neoclassical code, NEO [60, 66]. This code evaluates the neoclassical transport fluxes with the option of using either the full linearized Landau-Boltzmann collision operator (so it does not use approximate model terms in the field-particle part of the operator), or the linearized Landau-Boltzmann collision operator with the ad-hoc model field-particle part (Eq. 3.16). A comparison between these two collision models has already been performed in [60]. For this benchmark, the difference in the transport between the GENE collision model and the NEO model with the full linearized collision operator has been compared to the difference in transport between the model collision operator in NEO and the full collision operator in NEO. These differences should be approximately the same, and this enables a verification test across a large range of collisionalities. The analysis is performed on the same General Atomics parameter set with $\hat{s} - \alpha$ geometry outlined in [60, 33] and displayed in Table 3.2. The original results from the NEO code have been published in [60].

For the following simulations, the neoclassical energy and particle flux, as well as the bootstrap current were evaluated with a neoclassical solver that makes use of a PETSC library [67] that is available in GENE. The collisionality was scanned logarithmically. The comparison could not be extended to higher collisionality ($\nu_c \sim 0.3$) due to the computational expense of the neoclassical solver at higher collision frequencies. In practice however, the collision frequency rarely goes to much higher values before the separatrix of the device is encountered. The results of the simulations are displayed in Fig. 3.12 and 3.13. Both GENE and the ad-hoc Fokker Planck model give close agreement, which again suggests that the

collision operator in GENE has been implemented correctly. In addition, the ad-hoc model gives relatively close agreement with the full model (the heat and particle fluxes are within $\sim$ 20%). A 20% discrepancy in neoclassical heat transport is relatively small compared to the normal level of turbulent transport, and neoclassical transport is highly sensitive to collisions, which suggests that the ad-hoc collision model could be justifiably used for studies of collisional plasma turbulence and transport. However, to truly justify the use of such models, a comparison of the microinstabilities and the nonlinear transport between different collision models should be done.

By examining the neoclassical equilibrium velocity space distribution at the outboard midplane, one can see the effects of higher collisionality on the ions and electrons. The distributions are displayed in Fig. 3.14. At low collisionality, the contours of the trapped/passing particle boundary are clearly visible. As the collisionality is raised, the contours are extinguished, which is what is to be expected from intuition, as collisions tend to drive perturbations down towards a perturbed Maxwellian distribution. The collisionality used in the plots is defined in Eq. 3.139,

$$\nu_c = \frac{\pi e^4 n_i a \ln(\Lambda)}{2^{3/2} T_i^2}. \tag{3.139}$$

3.14.2 Global neoclassical benchmark

In addition to the local neoclassical test, a global one-species neoclassical benchmark between GENE and ORB5 [52] has been performed to ensure correct implementation of the collision operator for the global version of the code. The benchmark was performed for a one-species case using a magnetic geometry consisting of concentric circular flux surfaces. The safety factor profile, temperature gradient profile, and density gradient profile are given by Eq. 3.140, 3.141, and 3.142 respectively,

$$q(r) = \left[0.845 + 2.184(r/a)^2\right] \Big/ \sqrt{1-(r/R)^2} \tag{3.140}$$

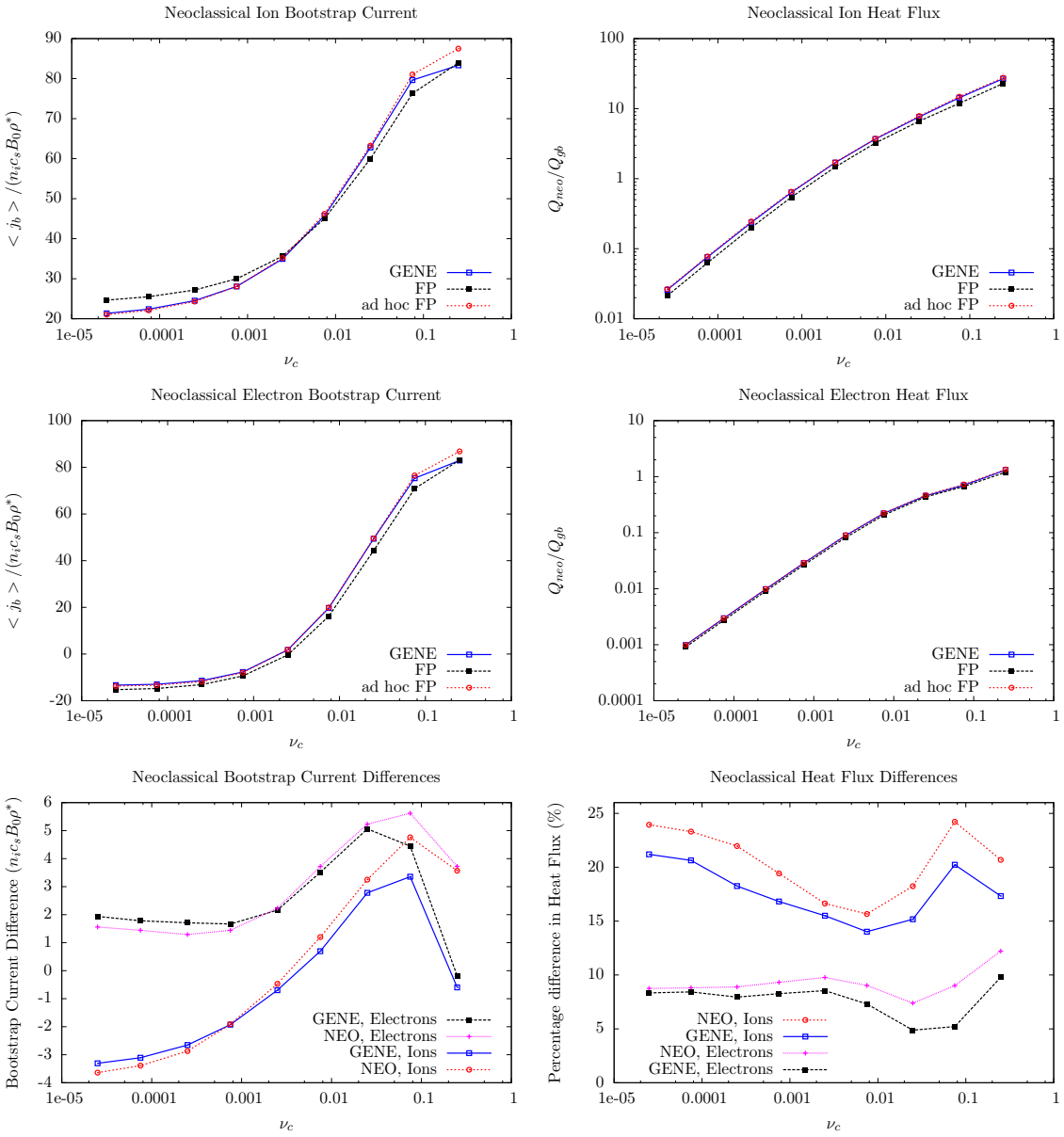

Figure 3.12: Comparison of neoclassical bootstrap current and heat flux between GENE, ad-hoc Fokker-Planck model in NEO, and full Fokker-Planck model in NEO [60]. The bottom plots show the difference of the bootstrap current and heat flux between the model operators and the full operator. GENE predicts a slightly smaller heat flux for ions and electrons, but the agreement is still fairly good. The bootstrap current between the two codes also agree fairly well. Q_{gb} is the gyrobohm heat flux.

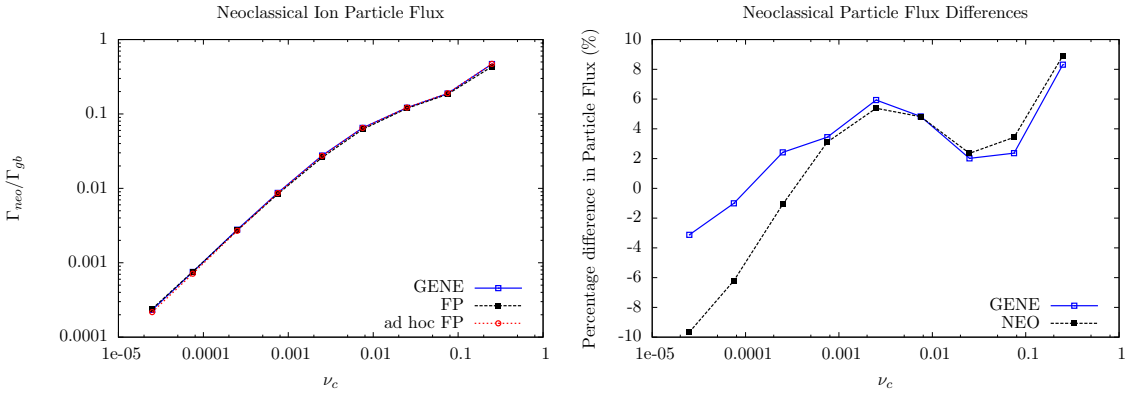

Figure 3.13: Comparison of neoclassical ion particle flux between GENE, ad-hoc Fokker–Planck model in NEO, and full Fokker-Planck model in NEO [60]. The plot on the right shows the difference in the particle flux between the model operators and the full operator. The electron flux has not been shown because it closely resembles the ion flux. Γ_{gb} is the gyrobohm particle flux.

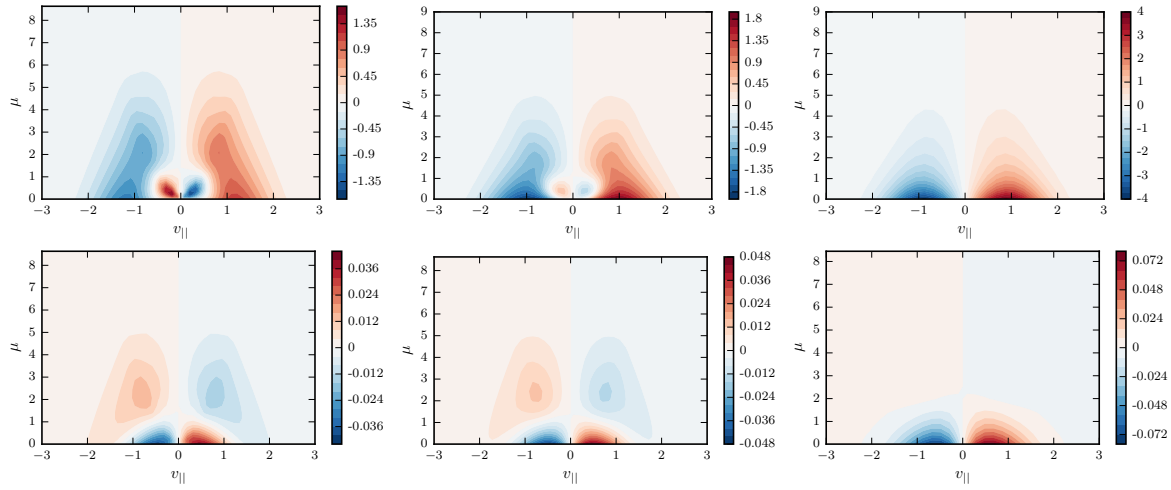

Figure 3.14: Neoclassical Equilibrium Ion and Electron velocity space distribution at the outboard midplane for ν_c=0.00001 (left), ν_c=0.001 (middle), and ν_c=0.1 (right). The graphs on the top correspond to ions, and the graphs on the bottom correspond to electrons. For low collisionality, one can clearly see the complex velocity space contours associated with the trapped-passing boundary. As collisionality is increased, one can see these structures fade as collisions inhibit the trapped particle resonance. At very large collisionality, the contours resemble a simple perturbed Maxwellian structure.

$$\frac{d\ln(T)}{d(r/a)} = -2.49\Big(\cosh(5(r/a-0.5))\Big)^{-2} \tag{3.141}$$

$$\frac{d\ln(n)}{d(r/a)} = -0.79\Big(\cosh(5(r/a-0.5))\Big)^{-2}. \tag{3.142}$$

This benchmark was run with $\nu_i^* = 0.5$ and $\rho^* = 1/180$ with identical analytical collision models, but different numerical implementations. This benchmark was already performed in [33], but since that time, the collision operator has been refactored, and better agreement has been obtained. The results are shown in Fig. 3.15. There is fairly good agreement between GENE and ORB5 for both neoclassical moments, suggesting the collisions were implemented correctly in both codes, at least for the one-species case. The ORB5 collision model is documented in [52]. Future benchmarks testing the implementation of collisions between multiple species for nonisothermal parameters shall be left for future work.

In addition to the benchmark between GENE and ORB5, a two species neoclassical benchmark has been performed between the version of GENE with the standard velocity space grids, and the version of GENE with the block-structured grids. The setup for this case is the same as the previous one, except that an additional electron species is considered in the simulation. The heat flux and bootstrap current output is displayed in Fig. 3.16 and 3.17 respectively. The neoclassical time traces and profiles agree fairly well between both versions of the code, suggesting that the block-structured grids have been implemented correctly, and provide no significant numerical challenges.

3.14.3 Local microinstability benchmark

In addition to studying the effects of collisions on the damping of zonal flows, the collision operator has also been benchmarked in a local microinstability analysis against the operator in another gyrokinetic code, CGYRO [54]. The $k_y\rho_s$ scan displayed in Fig. 5 of ref. [68] depicting a trapped electron mode (TEM) has been repeated in GENE. The collisionality scan displayed in Fig. 1 of ref. [68] depicting an ion temperature gradient driven

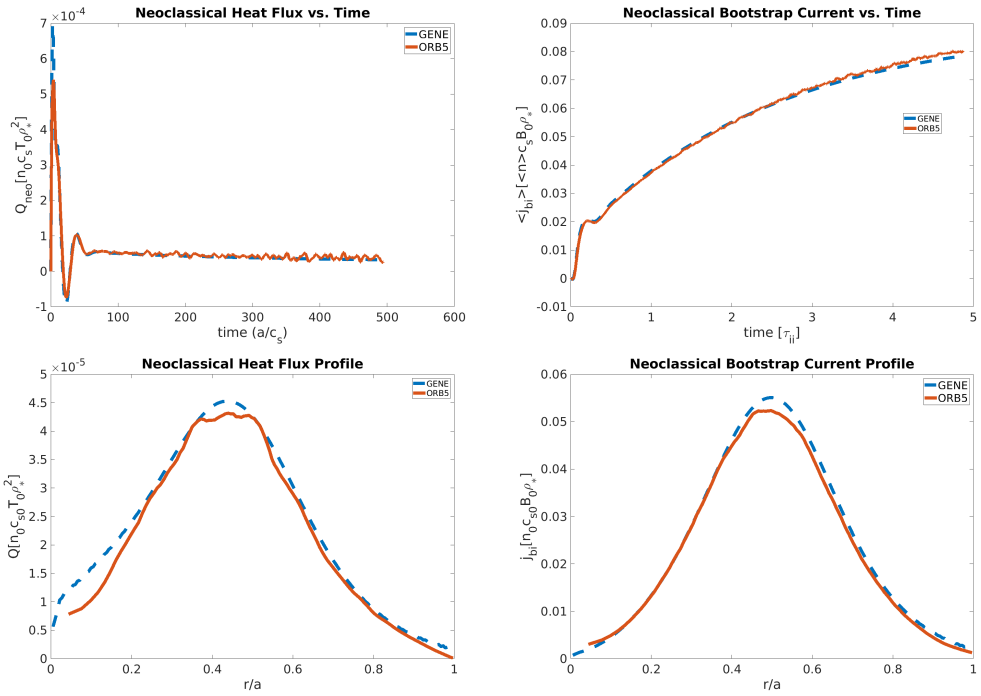

Figure 3.15: Global Neoclassic Benchmark between GENE and ORB5 [52]. The graphs on the left depict the heat flux, and the graphs on the right depict the ion contribution to the bootstrap current (the electron contribution cannot be included in the one species scenario). The middle radial position was taken for the time trace (r/a=0.5) and the profile measurements were taken at $t = 2\tau_{ii}$.

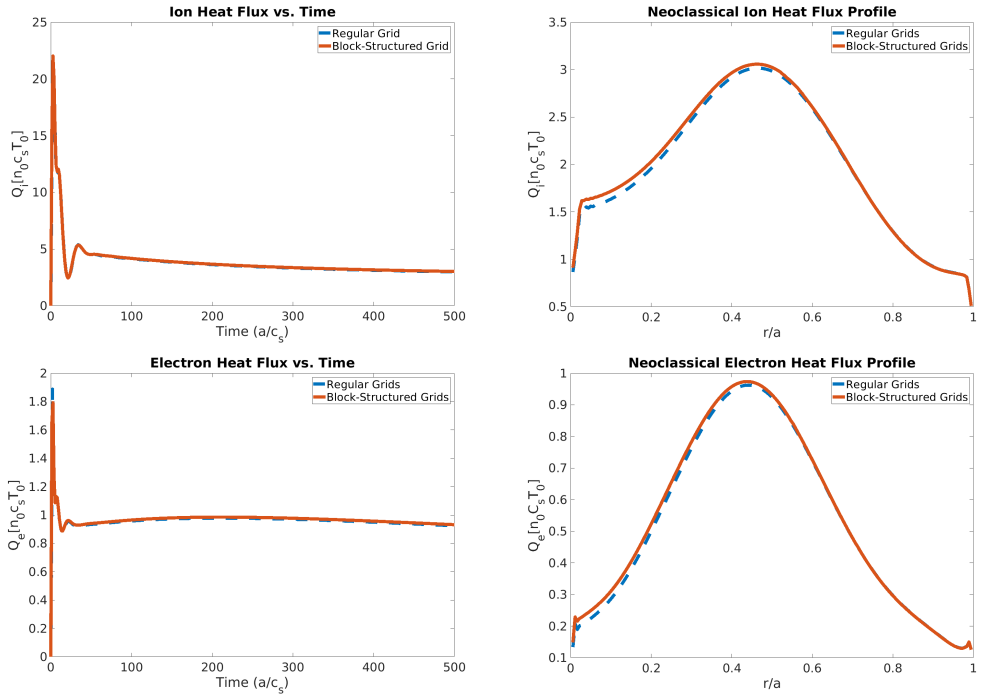

Figure 3.16: Neoclassical heat flux time trace and profiles for regular and block-structured grids. The graphs on the top and bottom depict the ion and electron species respectively. The time trace depicts the flux-surface averaged heat flux at r/a=0.5, and the profiles were observed at the end of the time trace ($t = 500a/c_s$).

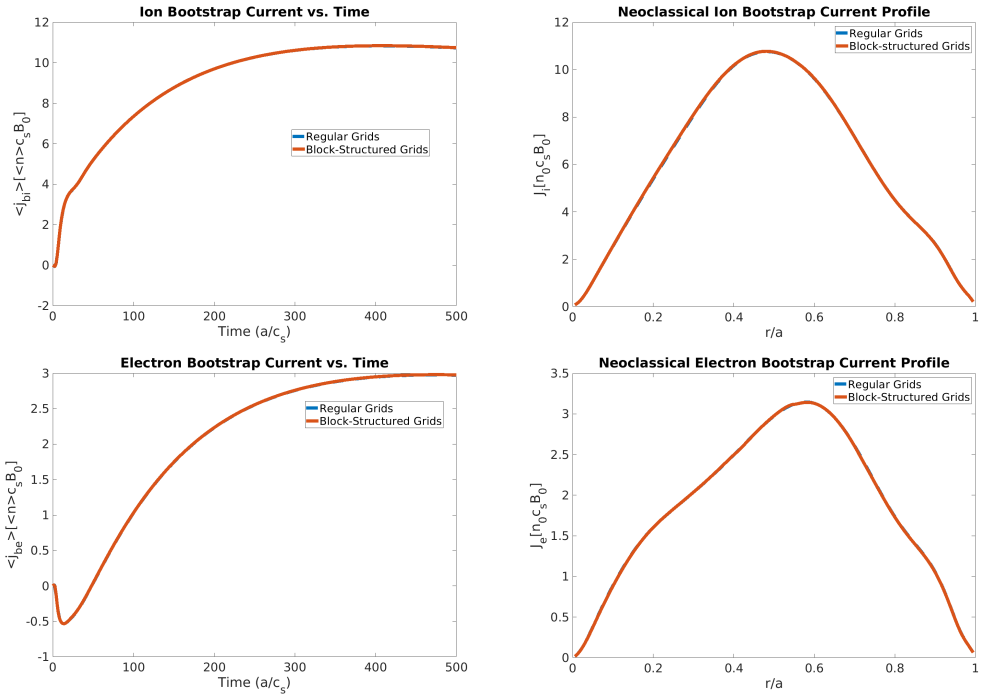

Figure 3.17: Neoclassical bootstrap current time trace and profiles for regular and block--structured grids. The graphs on the top and bottom depict the ion and electron species respectively. The time trace depicts the flux-surface averaged bootstrap current at r/a=0.5, and the profiles were observed at the end of the time trace ($t = 500a/c_s$).

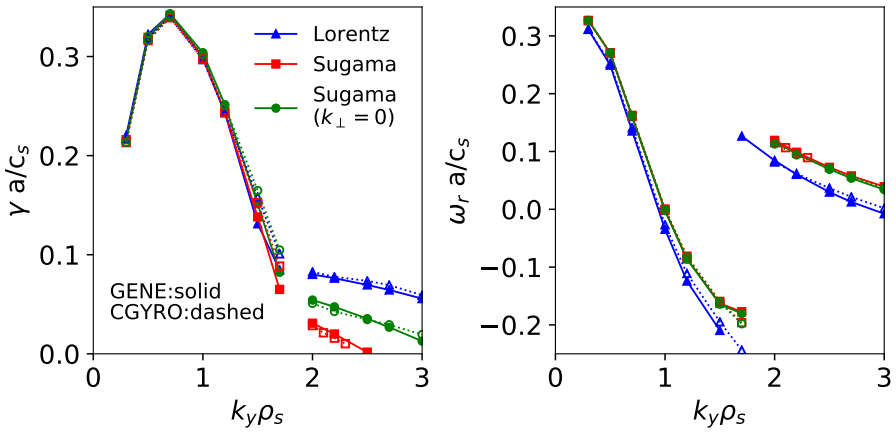

Figure 3.18: Comparison between GENE and CGYRO of frequencies and growth rates for a TEM microinstability.

mode (ITG) has also been repeated. This scenario was based on the General Atomics standard test case, and was run with two species (deuterium and electrons) with no temperature gradients, $a/L_{ni} = a/L_{ne} = 3$, $R/a = 3$, $r/a = 0.5$, $q = 2$, $\hat{s} = 1$, $T_i = T_e$, and $\bar{\nu}_e = \sqrt{2}\pi e^4 a n_e \ln(\Lambda)/(c_s\sqrt{m_e T_e^3}) = 0.2$. The geometry for this scenario is an unshifted miller equilibrium [69, 70]. The results are displayed in Fig. 3.18 and Fig. 3.19. Very good agreement was obtained between the codes. This benchmark in particular, validates the implementation of the FLR correction terms. The CGYRO results are publicly available in ref. [54].

3.15 Chapter summary

A linearized model collision operator which incorporates robust conservation and free energy dissipation properties (even in the nonisothermal scenario) and finite Larmor radius effects (for the local model) has been implemented in the gyrokinetic code, GENE. The conservation and dissipation properties have been ensured through extensive relaxation tests. The collision operator has also been adapted for the use of block-structured grids, allowing for affordable, global, collisional simulations. The implementation has been well benchmarked with neoclassical models as well.

Despite these accomplishments, there are also numerous possibilities for future work to

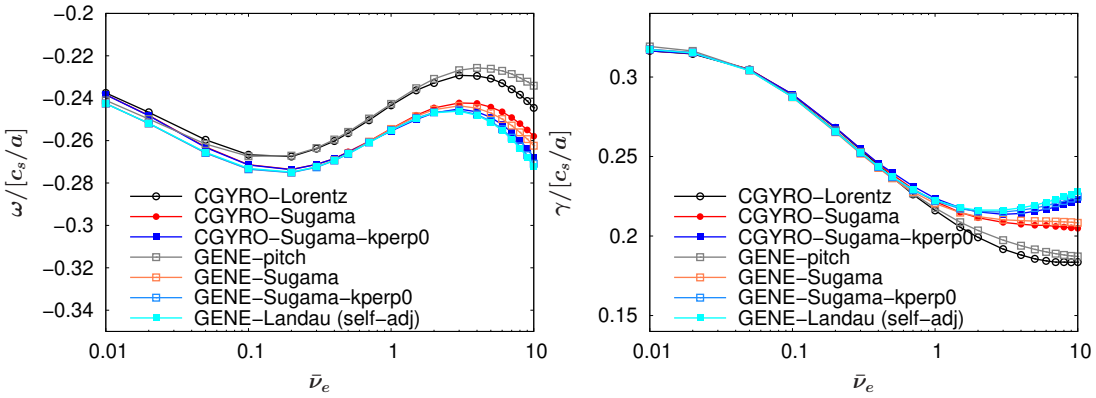

Figure 3.19: Comparison between GENE and CGYRO of frequencies and growth rates for an ITG microinstability. Comparisons were made between the Lorentz operators, the Sugama operators with no FLR correction terms, and the Sugama operators with FLR correction terms. The results from the original drift-kinetic form of the Landau collision operator that was utilized in GENE has also been shown for reference.

be done with collision models. Some of these are listed below:

- Developing an implicit time-stepping scheme which is more optimized for the GENE collision model.
- Implementation of the spatial diffusion and finite Larmor radius effects (incorporated as Bessel functions for the local code) for the global code.
- Implementation of a collision model which includes collisions with neutral species (such as charge exchange or ionization).
- Implementation of a full nonlinear collision operator for use with full-f simulations in the Scrape-Off Layer version of GENE.
- Porting of the collision operator to the 3D global version of GENE.

These extensions will allow many new opportunities for the study of plasma turbulence and transport at high collisionality.

CHAPTER 4

Characterization of the L-mode plasma edge

Gyrokinetic models have achieved good success at simulating the plasma turbulence and transport within the core of magnetic confinement fusion devices [71, 72]. However, it is still a subject of some debate as to whether or not those models can be extrapolated to study the plasma edge of those same devices, as well as whether or not one can reproduce the same experimental fluxes and fluctuation amplitudes. Furthermore, it is an open question as to which features of gyrokinetic turbulence in the core persist out to the edge (such as the correlation between linear and nonlinear cross-phases, and ballooning mode structure) [73, 74, 75, 76].

One of the most commonly used gyrokinetic simulation models is the delta-f localized flux-tube model, and that shall be the model used for the work discussed in this chapter. It is commonly argued that a delta-f flux-tube model has limited use for the study of edge plasma turbulence due to the larger ρ^* values there. However, given the success of the model for the study of physics in the core, it makes sense to see how such a model would behave when taken to a more extreme parameter range. It is meaningful to see if the predictions made by the local model still hold. And if such predictions break down, then it is worthwhile to understand when and how they break down. It is important to understand the limitations and capabilities of the flux-tube gyrokinetic model. Such an investigation can provide confidence in the use of this model, or provide motivation for the use of the global, or full-f model, or additional terms. Such an investigation can also provide insight into what mechanisms are important in the edge, what problems are encountered, and also what solutions could work to mitigate such problems. Understanding the challenges one would face in the study of the edge is crucial before attempting far more complicated global

or full-f studies. For this reason, an L-mode discharge that was previously analyzed in [73] with a large degree of success has been selected for the study of how gyrokinetics fares as one probes deeper into the edge.

Conducting a flux-tube simulation in the plasma edge seems like a deceptively simple problem. Carrying out simulations in the edge is far more difficult than in the core of a discharge. The collisional and electromagnetic models which are relatively well behaved or considered negligible in the core, can cause serious difficulties if not properly handled in the modeling of the edge.

In previous simulations, when the self-adjointness symmetry of the collision operator was not properly numerically handled, the collision term could artificially create free energy which would drive numerical instabilities at low toroidal mode numbers. If one ran a nonlinear simulation with such a model, the heat fluxes could appear to be stable for long periods of simulation time and then blow up, rendering very long and expensive simulations useless. If one used a collision model with FLR correction terms, but no implicit time-stepping scheme, the time-step would shrink by orders of magnitude when studying large toroidal mode numbers, making even linear simulations of large toroidal mode numbers in the edge impossible. Even if collisions are handled correctly and only relatively low toroidal mode numbers are considered, using collisional models would still make simulations far more expensive due to limitations in the time-step and an inability to completely parallelize along the magnetic moment in simulations.

If one attempted to incorporate electromagnetic effects into a nonlinear simulation in the edge, one would notice that the simulation would probably blow up unless very low toroidal mode numbers were included in the simulation, and very large box sizes (perhaps even going outside of the separatrix) were utilized. This would require higher resolution in k_x and k_y, which would make the edge simulation even more expensive. Furthermore, the existence of large $A_\parallel$ structures creates some questions concerning the use of the local flux-tube approximation.

Finally, the shaping of the flux-surface in the edge is far more complicated than in the core.

This would necessitate the use of either a very large resolution in the poloidal dimension, or the use of a grid where the poloidal points are more clustered at the outboard midplane, where the dominant microinstabilities generally (but not always) peak, and where the main plasma transport occurs.

This chapter is outlined as follows: First, a description of the plasma discharge and a summary of the physical parameters at the radial positions of interest shall be given in section 4.1. Following that, an analysis of the linear microinstabilities which exist at those same radial positions shall be given in sections 4.2 and 4.3. Section 4.2 shall describe the setup to the linear investigations while the results are detailed in section 4.3. Afterwards, the results from the nonlinear simulation at $\rho_{\text{tor}} = 0.9$ shall be discussed in section 4.4. That section contains a description of the numerical setup of the simulation in subsection 4.4.1, a comparison of the experimental and simulated transport in subsection 4.4.2, an analysis of the heat flux spectra in subsection 4.4.3, a description of the contours of the fields and moments in subsection 4.4.4, and an analysis of the linear and nonlinear cross-phases in subsection 4.4.5. Finally, conclusions are drawn in section 4.6.

4.1 Physical scenario under investigation

An important scenario which deserves study is the edge of the L-mode plasma discharge. While it is generally desired to have the tokamak operate in the H-mode regime, analyzing the L-mode discharge is still important. Characterizing the L-mode is necessary for understanding the L-H transition and simulating an L-mode plasma discharge is important for validation of the gyrokinetic model (additionally, fluctuation measurements are more accessible for an L-mode discharge).

For the work conducted in this chapter, the ASDEX Upgrade discharge 28132 was analyzed. This discharge was an L-mode plasma with a magnetic field on axis of 2.221 T and a plasma current of 400 kA. The heating of the plasma was predominantly electron cyclotron heating with additional ohmic heating. During the high power phase of the discharge (the phase during which the following simulations seek to model), the electron cyclotron heating

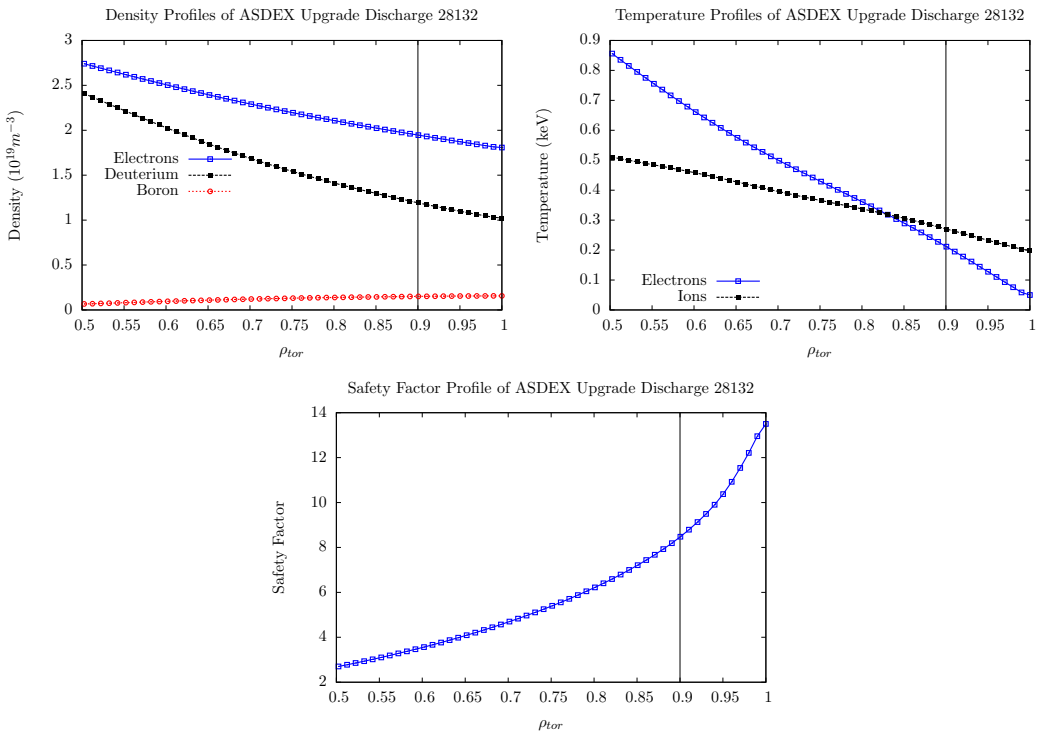

Figure 4.1: Density, temperature, and safety factor profiles for ASDEX Upgrade L-mode discharge being investigated. The black vertical in the graphs indicate where the nonlinear flux-tube simulation took place in the discharge.

had a magnitude of 1.16 MW. The density, temperature, and safety factor profiles for all of the different species, measured during the phase of interest, are displayed in Fig. 4.1. Because of the relatively high density of boron impurities, a three species model was used for accurate modeling of the edge. It can also be seen that the safety factor goes to very high values in the edge, so one could expect strong electromagnetic effects in that region even for relatively low values of the plasma β.

Two radial positions were considered for this discharge, $\rho_{\rm tor} = 0.90$, and $\rho_{\rm tor} = 0.96$, where $\rho_{\rm tor}$ is related to the magnetic flux-surface label, x, as in Eq. 4.1:

$$x = \sqrt{\frac{\Phi}{\pi B_{\rm ref}}} = \sqrt{\frac{\Phi}{\Phi_{\rm edge}}}\sqrt{\frac{\Phi_{\rm edge}}{\pi B_{\rm ref}}} = \rho_{\rm tor} L_{\rm ref} \tag{4.1}$$

Here, Φ is the toroidal magnetic flux divided by 2π, $B_{\rm ref}$ is the reference magnetic field on axis, and $L_{\rm ref}$ is the reference scale length. These two radial positions were chosen in

ρ_{tor}	0.90	0.96
I_p/kA	400	400
B_{ref}/T	2.221	2.221
L_{ref}/m	0.662	0.662
R_{axis}/m	1.710	1.710
a/m	0.501	0.501
ρ^*	0.144%	0.104%
$n_e/10^{19}\text{m}^{-3}$	1.947	1.858
T_e/keV	0.212	0.111
T_i/T_e	1.276	2.037
Z_{eff}	2.550	2.672
$\beta/10^{-4}$	3.373	1.679
$\hat{s}$	3.112	4.439
ω_{Ti}	2.775	3.346
ω_{Te}	7.684	15.67
ω_n	0.780	0.776
q	8.479	10.92

Table 4.1: Physical parameters for the two simulated ASDEX Upgrade L-mode cases

the far edge so as to study how local flux-tube based gyrokinetic simulations fared as one approached the separatrix in an L-mode discharge. This experimental discharge has been well diagnosed and previous GENE simulations were able to match the experimental ion and electron heat flux at two other radial positions within the error bars [73]. One can be confident in the validation of the model for the core of the plasma discharge as observations are made regarding the behavior of the model when extrapolated farther to the edge of the discharge. The other details associated with the two radial positions studied in this paper, such as the density and temperature, are listed in table 4.1.

In this table, R_{axis} is the major radius of the tokamak and a is the minor radius. T_i and T_e represent the ion and electron temperatures respectively, n_e denotes the electron density, and q is the safety factor. Z_{eff} represents the effective ion charge due to impurities, and is defined in Eq. 4.2,

$$Z_{\text{eff}} = \frac{\sum_j Z_j^2 n_j}{n_e}. \tag{4.2}$$

Here the summation is over all ion species. The magnetic shear $\hat{s}$ is defined in Eq. 4.3,

$$\hat{s} = \frac{\rho_{\text{tor}}}{q}\frac{dq}{d\rho_{\text{tor}}}. \tag{4.3}$$

The logarithmic gradients, ω_a (with a corresponding to the temperature or density of a given species) are defined in Eq. 4.4,

$$\omega_a = -\frac{1}{a}\frac{da}{d\rho_{\text{tor}}}. \tag{4.4}$$

And the electron β is defined in Eq. 4.5,

$$\beta = 2\mu_0 n_e T_e / B_{\text{ref}}^2. \tag{4.5}$$

For the following linear and nonlinear simulations, the flux-tube geometry representing the magnetic equilibrium has been extracted via a TRACER-EFIT interface (the development of which is described in [77, 29], and a first application of which is described in [78]) from a SPIDER equilibrium [79, 80]. For further information about this discharge, see ref. [73].

4.2 Setup of linear investigation of plasma microinstabilities

Before investigating the nonlinear dynamics of the plasma discharge, it is worthwhile to examine the linear microinstabilities that are present at the radial positions of interest. These are often the dominant microinstabilities which drive transport in a nonlinear simulation. Furthermore, it is important to ensure that simulations are fully resolved in terms of the number of grid points in each dimension, and it is much less computationally expensive to run convergence tests and parameter scans for linear simulations than it is for nonlinear simulations. It is also often the case in the core of a plasma discharge that features of the plasma turbulence (such as cross-phases and frequencies) closely follow those of the dominant linear microinstabilities. It is worthwhile to investigate if these features are retained as one goes farther into the edge. There is a large effort underway to develop quasilinear models to simulate transport in magnetic confinement devices [81, 82, 83]. Such models

require complete information about the linear physics and an empirical nonlinear saturation rule as inputs to the model. The advantage of such models is that they are much faster than nonlinear simulations, and unlike linear models, they can provide transport values. Such models utilize the cross-phases between the electrostatic potential and the perturbed temperature and density fluctuations to replicate the transport of heat and particles. It is worthwhile to see if these features are retained in nonlinear edge physics, because if so, then quasilinear modeling may be applicable to the edge.

Many different microinstabilities have been considered as potentially significant for the transport in the edge. Ref. [84] has suggested that Ion Temperature Gradient Modes (ITGs), Trapped Electron Modes (TEMs), and Kinetic Ballooning Modes (KBMs) could be significant in this regime. Ref. [78, 84, 85] has suggested that ETGs and Microtearing Modes (MTMs) could be significant contributors to the plasma turbulence in the edge. Ref. [75, 86, 87, 88] have suggested that Resistive Ballooning Modes (RBMs) can become significant in this area. Electron drift waves have been considered as significant to the edge turbulence by ref. [89, 75, 90, 86].

In the following linear simulations, different k_y values were scanned from around $k_y\rho_s = 0.028$ to $k_y\rho_s = 0.1$ in increments of the integer toroidal mode number ($\Delta k_y\rho_s = 0.014$). A scan was also performed over k_y values from a range of $k_y\rho_s = 0.1$ to $k_y\rho_s = 1.0$. These two scans effectively resolve the variation of large scale and moderate scale microinstabilities. The scan could not be extended much farther to greater toroidal mode numbers due to limited computational resources. At higher toroidal mode numbers (small scale microinstabilities) the spatial diffusion part from the FLR corrections in the collision operator can limit the time-step by nearly two orders of magnitude. The nonlinear simulations that follow only go up to about $k_y\rho_s = 1.35$, and higher toroidal mode numbers can certainly not be included in nonlinear simulations (even single-scale nonlinear simulations are extremely expensive), so there is little motivation to study higher toroidal mode numbers. One could also run without FLR corrections in the collision operator. However, it can be reasonably expected that such effects are very important for electron-scale dynamics in the edge. It has been found that at large collisionality, the growth rates of Electron Temperature Gradient Modes (ETGs)

are heavily damped [68], which could be expected to influence the electron scale transport in the edge. If one wishes to study higher toroidal mode numbers in the edge, either in electron-scale or multi-scale simulations, then it is necessary to develop an improved implicit time-stepping scheme for the collision operator. Until then, linear and nonlinear studies in the edge must be limited to a single-scale analysis.

After identifying the dominant linear microinstabilites at the radial position of interest, a convergence test was performed to ensure each mode was adequately resolved. It was found that a resolution of $(n_{kx}, n_z, n_v, n_\mu) = (32, 32, 32, 20)$ was sufficient with the standard velocity space domain (see chapter 2). However, a specialized poloidal grid was required to resolve the modes. Because of the complex shaping of the flux-tube geometry in the edge of the plasma, a higher number of points in the poloidal direction would traditionally be needed to resolve the turbulence in the edge. However, since the dominant microinstabilities typically peak at the outboard midplane of the flux-surface, the poloidal grid points can be discretized such that the points are more clustered in that region, and at points where the curvature of the device is very high, rather than being equally spaced from $-\pi$ to π. This can allow one to simulate the edge with a lower number of poloidal grid points, saving computational resources. The option can be selected in the GENE code by setting edge_opt=2 in the parameter file (first implemented in ref. [26]). The placement of the grid points using this option is displayed in Fig. 4.2. It should be noted that this option is not appropriate when there are modes that peak far away from the outboard midplane. However, that has not been found for the system under review.

4.3 Results of linear investigation of plasma microinstabilities

The dominant plasma microinstabilities at $\rho_{\text{tor}} = 0.90$ ($r/a = 0.93$) for this discharge are MTMs at low toroidal mode numbers ($k_y\rho_s < 0.1$) and electron drift waves destabilized by collisions at moderate toroidal mode numbers (at least up to $k_y\rho_s \sim 1$). Very weak ITGs also seem to exist at very low toroidal mode numbers. A plot of the growth rates and frequencies at various toroidal mode numbers are displayed in Fig. 4.3. The microinstabilities

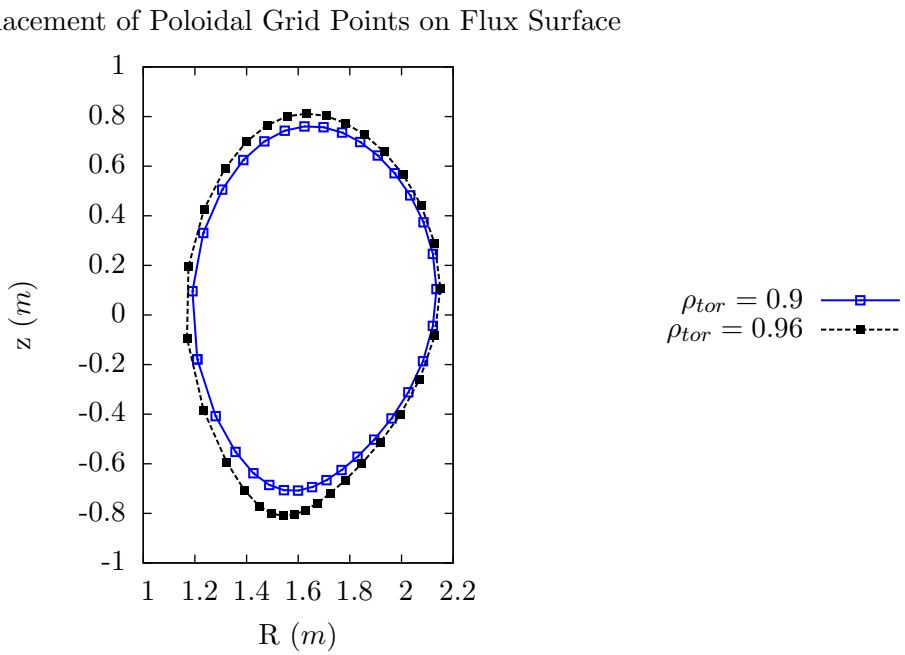

Figure 4.2: Spacing of poloidal grid points on the flux-surface in the corresponding simulations

in the absence of collisions are also displayed in Fig. 4.3. It can clearly be seen that collisions have a dramatic effect on the microinstabilities in the simulation. Collisions act to strongly stabilize the modes at low toroidal mode number, and act to destabilize the modes at moderate toroidal mode number. The linear analysis suggests any accurate description of edge transport must have an appropriately defined collision operator. A comparison between the linear modes for the electrostatic and electromagnetic case has also been displayed in Fig. 4.4. It can be seen that electromagnetic effects result in microtearing modes at low toroidal mode number, mildly destabilize the electron drift waves, and have no discernible effect on the ITGs (which are extremely weak in any case).

The ITGs have been identified by the fact that they drift in the positive direction, have an even parity in the ballooning mode representation, and are stabilized by collisions and β. The MTMs have been identified by the odd parity in the ballooning mode representation and the fact that they drift in the negative (electron diamagnetic drift) direction. The electron drift waves have been identified by the fact that they drift in the negative direction, are destabilized by collisions, and have a cross-phase which is less than $\pi/2$, unlike interchange

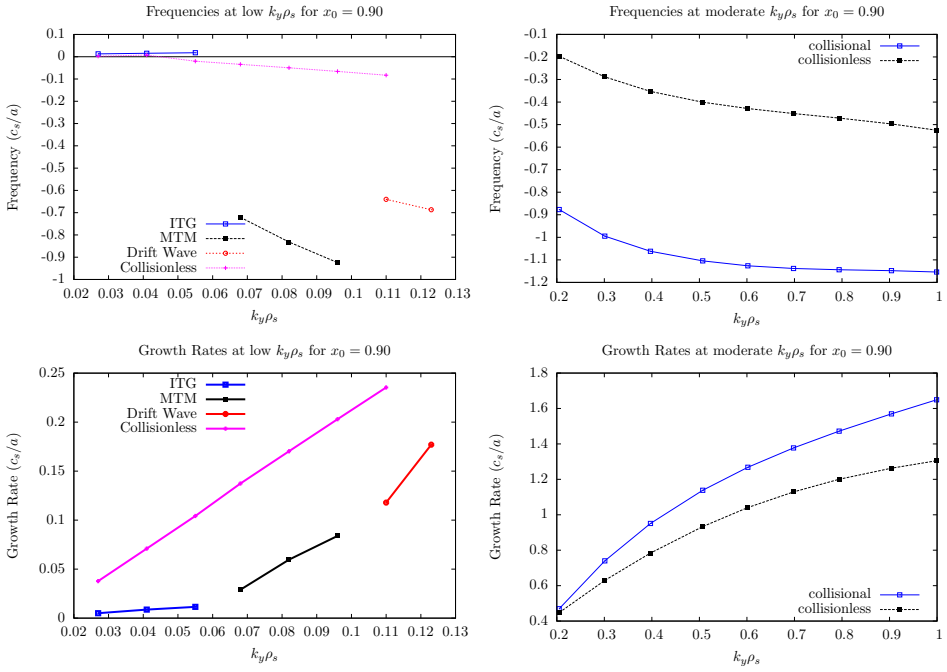

Figure 4.3: Growth rates and frequencies of dominant microinstabilities at $\rho_{\text{tor}} = 0.90$

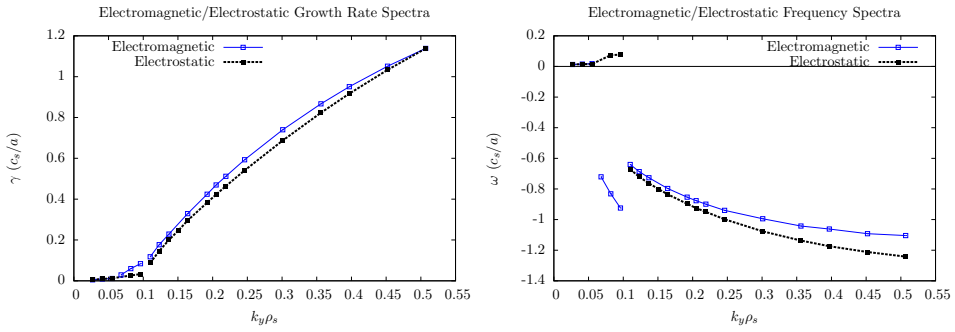

Figure 4.4: Growth rate and frequency spectra of dominant microinstabilities at $\rho_{\text{tor}} = 0.9$ for the electromagnetic and electrostatic case

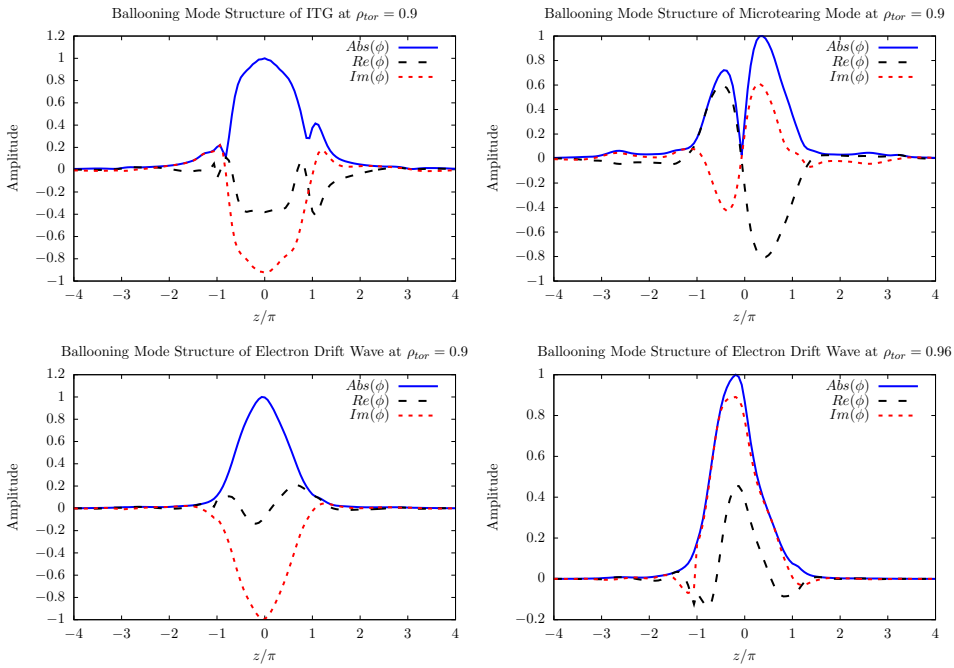

Figure 4.5: Mode structure of ϕ for the dominant microinstabilities at $\rho_{\text{tor}} = 0.90$ and $\rho_{\text{tor}} = 0.96$. The ITG mode structure was evaluated for $k_y\rho_s = 0.055$ and the microtearing mode structure was evaluated for $k_y\rho_s = 0.082$. The electron drift wave mode structure at $\rho_{\text{tor}} = 0.9$ was evaluated at $k_y\rho_s = 0.219$. The electron drift wave mode structure at $\rho_{\text{tor}} = 0.96$ was evaluated at $k_y\rho_s = 0.203$.

instabilities. The ballooning mode structure of the various microinstabilities are displayed in Fig. 4.5. It is worth noting that the ballooning structure at $\rho_{\text{tor}} = 0.96$ is slightly shifted from the outboard mid-plane. This is most likely due to the more extreme geometry of the magnetic field as one goes farther out to the edge of the tokamak.

Table 4.2 illustrates how varying the different plasma parameters in the simulation changes the frequency and growth rate of the dominant electron drift wave mode at $k_y\rho_s = 0.3$. The heat flux in the nonlinear simulations studied at this radial position also seemed to peak near this value of k_y, and electron drift waves end up playing a large role in the nonlinear simulations, as seen in the next section. So understanding how varying the different plasma parameters for this toroidal mode number changes the frequencies and growth rates of the mode of interest is useful information. The parameter which has the biggest effect on the growth rate and frequency is the electron temperature gradient. This is no surprise since that is the driving force behind the mode. After that, the mode seems to be

	$\Delta\omega(\%)$	$\Delta\gamma(\%)$
$\omega_{Te} \times 0.8$	-11.59	-21.29
$\omega_{Te} \times 1.2$	+9.64	+18.82
$\omega_{Ti} \times 0.8$	+4.44	-0.41
$\omega_{Ti} \times 1.2$	-4.48	+0.55
$T_i/T_e \times 0.8$	+3.63	-4.95
$T_i/T_e \times 1.2$	-3.27	+4.46
$\nu_{\text{coll}} \times 0.8$	-2.89	-4.40
$\nu_{\text{coll}} \times 1.2$	+1.83	+3.98
$Z_{\text{eff}} \times 0.8$	-2.77	+1.59
$Z_{\text{eff}} \times 1.2$	+2.75	-1.58
$\omega_n \times 0.8$	+2.33	-1.95
$\omega_n \times 1.2$	-2.28	+1.92
$\beta \times 0.8$	+2.42	-0.71
$\beta \times 1.2$	-2.72	+0.69

Table 4.2: Sensitivity tests for $k_y\rho_s = 0.30$ mode at $\rho_{\text{tor}} = 0.90$

primarily sensitive to the ion/electron temperature ratio and the collisionality. The growth rates and frequencies of the dominant modes at $\rho_{\text{tor}} = 0.96$ are shown in Fig. 4.6. At this radial position, the dominant microinstability appears to be electron drift waves, and the growth rates appear to be much larger than the growth rates at $\rho_{\text{tor}} = 0.90$.

4.4 Nonlinear gyrokinetic simulations

Nonlinear flux-tube simulations at $\rho_{\text{tor}} = 0.9$ ($r/a = 0.93$) were conducted. Previous nonlinear simulations conducted at more inner points in the discharge were documented in ref. [73]. In that analysis, local GENE simulations were able to match the experimental heat flux within the error bars, and it was found that properties of the nonlinear system maintained close correlation with properties of the linear system, such as cross-phases and frequencies. It was also concluded in that analysis that there was no significant difficulty for quasilinear analysis in L-mode discharges, at least out to the radial position of $r/a = 0.9$. While that analysis was very thorough and expertly conducted, such an analysis was also constrained to more inner radial positions, due to a numerical deficiency in the earlier collision model which caused it to artificially create free energy, leading to numerical instabilities at low

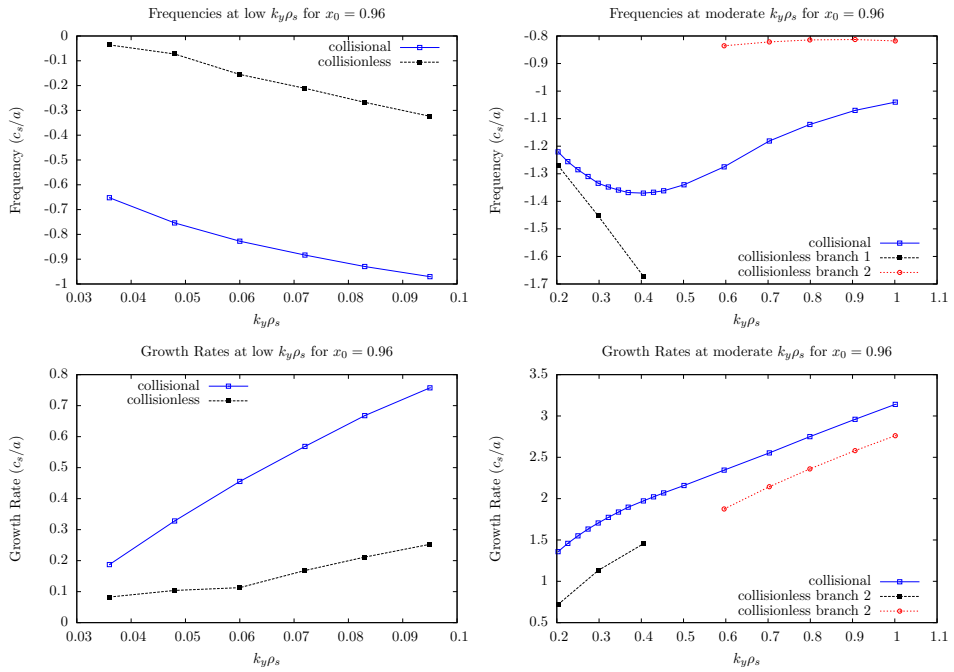

Figure 4.6: Growth rates and frequencies of dominant microinstabilities at $\rho_{\text{tor}} = 0.96$

toroidal mode numbers. This is very important because the linear and nonlinear dynamics of the edge are strongly influenced by the collisional dissipation term. This reinforces the importance of making sure that the collision operator in use conserves particles, momentum, and energy, and numerically dissipates free energy and relaxes perturbations to a smooth localized final state. Neoclassical benchmarking is also important to make sure that there are no bugs in the collision operator.

The present analysis looks at the same discharge at $\rho_{\text{tor}} = 0.9$ $(r/a = 0.93)$, to see how the gyrokinetic model behaves when extrapolated to the edge. For this radial position, the ion and electron heat flux can be matched by lowering the electron temperature gradient by 40%. This suggests that there may be a slight error on the electron temperature profile (or some other input) in the simulation, or that global, full-f, or neutral particle effects are significant to the discharge, and should be taken into account. It does also signify however, that gyrokinetics can closely reproduce the experimental transport quantities, even in the edge. It is also found at this radial position that there is a large electromagnetic effect in the simulation which causes the heat flux to flare up and shift to lower toroidal mode numbers.

The heat flux is still nearly entirely electrostatic. Earlier results from ref. [75, 76, 91] reported a strong nonlinear electromagnetic effect which couples drift wave and MHD turbulence in the edge. For this case, it is found that the cross-phases between electrostatic potential and temperature fluctuations no longer agree at small scales ($k_y\rho_s \gtrsim 0.5$) or large scales ($k_y\rho_s \lesssim 0.1$), however, they still agree in the regime for which the main plasma transport occurs ($0.1 \lesssim k_y\rho_s \lesssim 0.5$). Also, it is found that the increase in heat flux could potentially be attributed to an increase in the electron drift wave growth rates with higher β in linear simulations. However, this result is particular to the case under review. Higher β values have not been investigated, as the focus for this work has been on the experimental parameters. Farther radial positions (where electron drift waves become linearly dominant at $k_y\rho_s \lesssim 0.1$) have also not been looked at because of the computational expense of nonlinear simulations in the far edge for realistic parameters. A detailed description of the findings from the nonlinear simulations is presented in this section.

4.4.1 Numerical setup

Three types of nonlinear flux-tube gyrokinetic simulations were run at the radial position of interest: An electromagnetic collisional simulation with the nominal input parameters taken from the experiment, an electrostatic version of the same simulation, and an electromagnetic collisional simulation with the experimentally obtained logarithmic electron temperature gradient lowered by 40% (with the aim of matching the experimentally measured heat transport). A couple of things are worth clarifying in the following description. Electrostatic simulations correspond to simulations where the plasma β has been set to zero. So this would also mitigate one of the electrostatic drive terms in addition to deleting the electromagnetic corrections. Also, electromagnetic/electrostatic can refer to simulations that were run with and without β respectively. However, electromagnetic simulations also contain electrostatic and electromagnetic heat flux components. This is important to keep in mind to avoid confusion with what is meant by electrostatic.

For the following nonlinear simulations, a resolution of $(n_z, n_v, n_\mu) = (32 \times 32 \times 20)$ was

used for the poloidal and velocity space grids (the poloidal direction was discretized with the scheme described earlier). This was enough to resolve the linear modes at low and moderate toroidal mode numbers. The nonlinear simulations use the same resolution in z, $v_\parallel$, and μ as the linear simulations. This is justified by the fact that the only nonlinear term in the system is the perpendicular nonlinearity, which only contains derivatives in the radial and binormal direction. So it is not expected that the nonlinear simulations would require higher resolution in any dimension besides the radial and binormal directions. The collisionless terms were handled via Arakawa discretization schemes for the linear terms with z and $v_\parallel$ derivatives, and for the nonlinear term with x and y derivatives, as in any standard GENE flux-tube simulation.

A resolution of $(n_{kx}, n_{ky}) = (1024, 48)$ was used to simulate the radial and binormal directions. For the binormal discretization, the second integer toroidal mode number has been chosen as the minimum nonzero mode number in the simulation ($k_{y,\min}\rho_s = 0.028$). This is also the spacing between the different k_y modes in the simulation. This corresponds to a binormal box size of 224.4 gyroradii ($L_y = 224.4\rho_{\rm ref}$). For the radial direction, a box size of 459 gyroradii was used ($L_x = 459\rho_{\rm ref}$). This high resolution was used to resolve the electromagnetic fields in the edge, as will be discussed in more detail in the following sections. For the electrostatic simulations, a lower resolution $(n_{kx}, n_{ky}) = (256, 48)$ and radial domain size ($L_x = 114.75\rho_{\rm ref}$) were utilized. Also, an external $\mathbf{E} \times \mathbf{B}$ shearing rate of $\gamma_{\mathbf{E}\times\mathbf{B}} = 0.04$ was used in an attempt to break up large scale structures. This can be justified because the $\mathbf{E} \times \mathbf{B}$ shearing rate is an external physical parameter in the delta-f gyrokinetic model which is ascertained from the radial derivative of the zonal flows. However, the experimental measurements for such quantities are extremely noisy, and it is very difficult to ascertain the correct value for the shearing rate. A value of $\gamma_{\mathbf{E}\times\mathbf{B}} = 0.04 c_{\rm ref}/L_{\rm ref}$ was considered to be reasonable for the upper bound of the shearing rate, and hence, was chosen as the value in nonlinear simulations. The collision model in use was a linearized Sugama collision operator of the type described in Chapter 3.

4.4.2 Comparison of simulated heat transport with experimental measurements

The heat flux measurements for the nonlinear simulations are displayed in Fig. 4.7. They are based on the time traces shown in Fig. 4.8. The simulations with nominal parameters overestimate the experimentally obtained heat fluxes by a factor of about 4 for the electrons and 2 for the ions. The heat fluxes obtained for the parameter set where the electron temperature gradient was lowered by 40% agree very well with the experimentally measured transport levels. This suggests that perhaps the electron temperature profiles constructed from experimental data happened to give values of the electron temperature gradient at the given radial position that overestimated the true value at $\rho_{\mathrm{tor}} = 0.9$ ($r/a = 0.93$). The experimental electron temperature values reconstructed from experimental measurements, as well as the electron temperature profiles taken for the simulations are displayed in Fig. 4.9. By comparing the profiles used for the simulation with the experimental measurements, it can be seen that it is plausible that the electron temperature gradient could be off by 40%, justifying the use of the altered simulation. It is also possible that there are some other effects in the plasma, such as global effects, full-f effects, and/or collisions with neutral particles which are not being taken into account which would lower the ion and electron heat fluxes.

Nevertheless, gyrokinetic simulations still seem to provide very good agreement with experimental transport levels despite being highly sensitive to the error bars on numerous input parameters. In the electrostatic case, the nominal heat fluxes align very well with the experimental value. This indicates that there is a very strong electromagnetic effect which raises the heat fluxes.

4.4.3 Heat flux spectra

The heat flux spectra of the simulations for the binormal and radial dimension are displayed in Fig. 4.10 and Fig. 4.11 respectively. The electrostatic heat flux seems to peak at the 12th toroidal mode number ($k_y\rho_s = 0.168$) for the simulations with the nominal parameter set, and the 16th toroidal mode number ($k_y\rho_s = 0.224$) for the simulation with the electron temperature gradient lowered by 40% and the electrostatic simulation. The electromagnetic

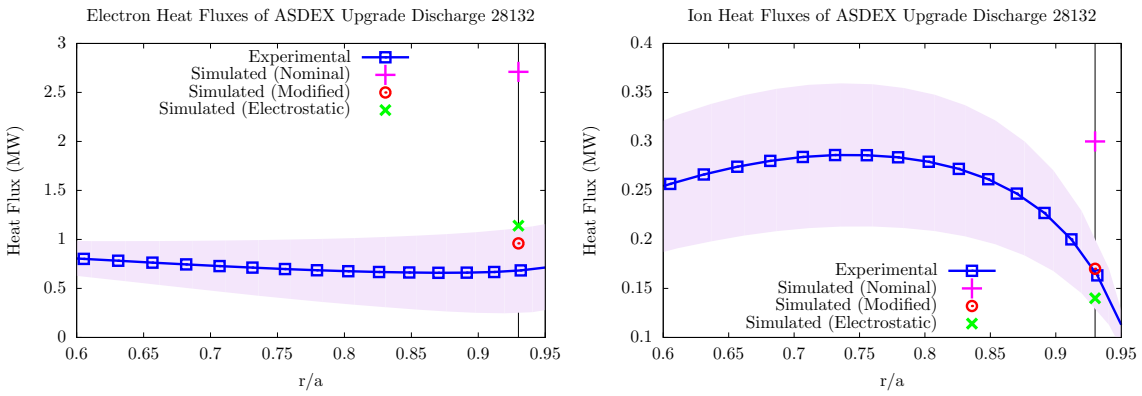

Figure 4.7: Experimental and simulated heat transport for ASDEX Upgrade Discharge 28132. The blue line with the square data points indicate the experimentally measured heat fluxes obtained from the ASTRA code. The shaded area around the line indicates the uncertainty for the ASTRA fitting of the experimental measurements. The flux-tube simulations attempted to model the plasma turbulence in the far edge region indicated by the black vertical line around $r/a = 0.93$. The values obtained for the heat fluxes with the nominal experimental input parameters are indicated by the pink crosses. The values for the heat fluxes associated with the nonlinear simulations where the electron temperature gradient was lowered by 40% are indicated by the red circles. The values obtained for this parameter set agree very well with the experimentally measured transport levels. The heat fluxes for the electrostatic case are displayed by the green circles. These are also close to the experimental values.

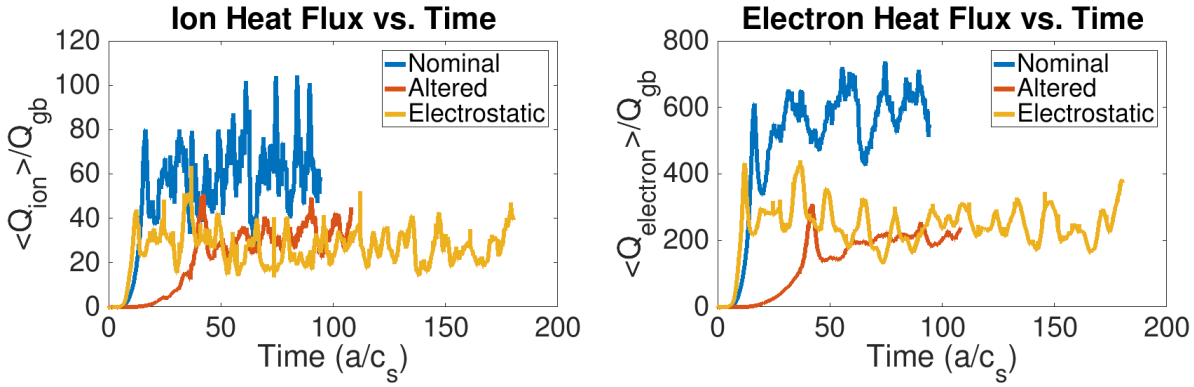

Figure 4.8: Ion and electron heat flux time-traces. The ion heat fluxes are displayed on the left and the electron heat fluxes are displayed on the right. The heat fluxes for the simulation with the nominal input parameters are displayed by the blue lines, and have higher values for both the ions and electrons than the other simulations. The heat fluxes for the simulation with the electron temperature gradient lowered by 40% are displayed by the red lines. The heat fluxes for the electrostatic simulation are displayed by the yellow lines and extend to longer times than the other time-traces. The electromagnetic heat fluxes are negligible and have not been shown. The ion heat fluxes include the deuterium species, but not the boron species (the boron heat flux is small compared to the deuterium heat flux). The heat fluxes are in gyrobohm units.

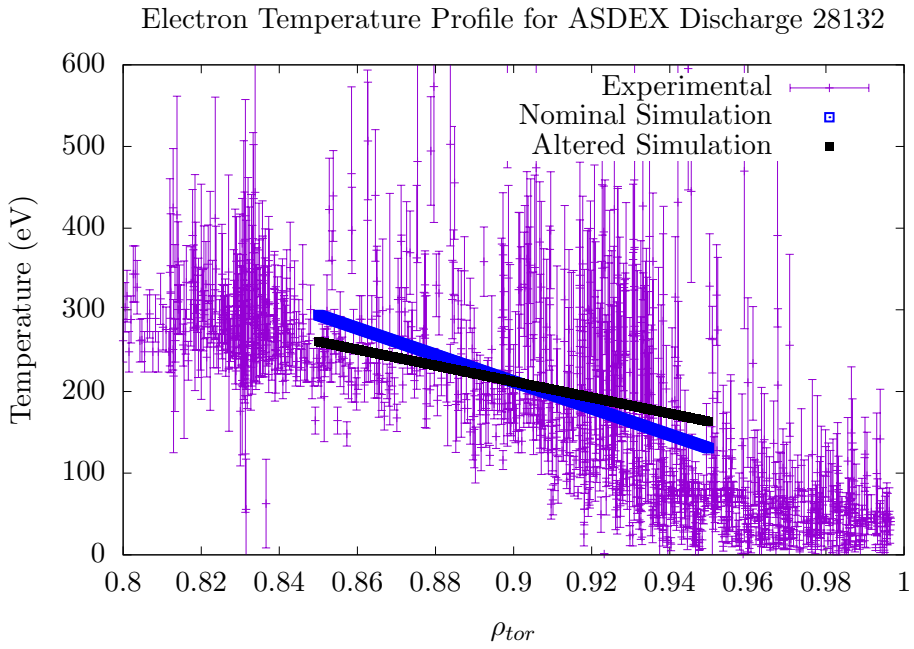

Figure 4.9: Display of experimental and simulated electron temperature values at the radial position of interest. The purple data points indicate nominal electron temperature values reconstructed through Thompson scattering measurements. The thin purple lines indicate the error bars associated with the experimental measurements. The two thicker lines are meant to represent the electron temperature profile taken for the local simulations centered at $\rho_{\text{tor}} = 0.9$. The temperature was taken to be 212 eV throughout all simulations, and the electron temperature gradients (which are assumed to be constant, and are a completely separate entity from the electron temperature value in a localized flux-tube simulation) are represented by the slopes of the lines. The steeper blue line indicates the simulation based on the nominal experimental values, and the flatter black line indicates the simulation with the electron temperature gradient lowered by 40%.

contribution appears at very low toroidal mode number. The electromagnetic heat flux peaks at the 6th toroidal mode number ($k_y\rho_s = 0.084$) for the nominal parameter set and the 10th toroidal mode number ($k_y\rho_s = 0.14$) for the parameter set with the lower electron temperature gradient. Although the electromagnetic heat flux makes a very small contribution compared to the electrostatic heat flux. The flux spectra for the nominal, lowered electron temperature gradient, and electrostatic cases were averaged over the time windows $t = 61.5 - 94.0a/c_s$, $t = 77.4 - 107.9a/c_s$, and $t = 100 - 180.1a/c_s$ respectively.

When conducting nonlinear simulations in the edge, it is necessary to go to very low toroidal mode number to ensure that the electromagnetic electron heat flux is stable. It has been found that if a higher toroidal mode number is chosen for the minimum nonzero value in the simulation, the electromagnetic heat flux will peak at that value, and continually increase. It makes sense that this would be the case because $A_\parallel$ is derived from a 2D Laplace equation, $A_\parallel = 4\pi J/(ck_\perp^2)$. Because of the $k_\perp^2$ in the denominator, it makes sense that the electromagnetic contribution, when present, would appear at low toroidal mode number and with large structures in the radial domain. For these simulations, the 2nd toroidal mode number ($k_{y,\min}\rho_s = 0.028$) has been chosen. This is also the spacing between the different k_y modes in the simulation.

What is interesting to note when comparing the heat fluxes for the electrostatic and electromagnetic simulations is that while even though the electromagnetic heat flux makes minimal contribution to the total heat flux, there is a large surge in the electrostatic heat flux at lower toroidal mode number. This is consistent with what has been reported in ref. [75, 76, 91]. It has been found in these references that as the plasma β is increased, the heat flux increases dramatically, and the increase is associated with the nonlinear coupling of the electron drift wave turbulence with MHD interchange instabilities at scales of $k_y\rho_s < 0.1$. At these higher values of plasma β, it has been found that the system is highly nonlinear, and that the underlying linear instabilities are no longer useful for characterizing the nonlinear system. It shall be seen in subsection 4.4.5 that the physics at scales of $k_y\rho_s < 0.1$ is indeed highly nonlinear when electromagnetic effects are taken into account. However, it is not clear that the large surge in heat flux can be attributed to a coupling between the electron

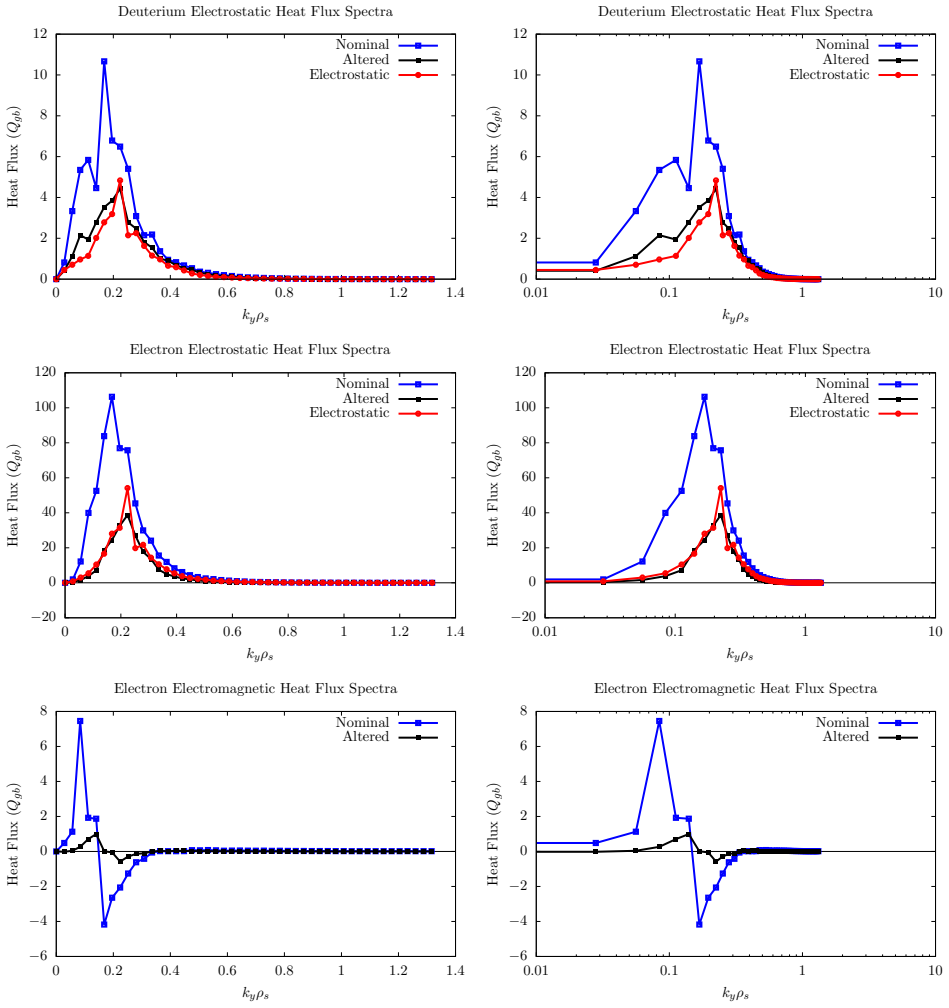

Figure 4.10: Time-averaged heat flux spectra in the binormal coordinate. The graphs on the left and right present the same data, but the graphs on the left have a linear scaling in $k_y\rho_s$ and the graphs on the right have a logarithmic scaling in $k_y\rho_s$. The spectra for the nonlinear simulations with nominal electron temperature gradient are shown, along with the spectra for nonlinear simulations with reduced electron temperature gradient where the heat fluxes match the experimental values, as well as the spectra for the electrostatic nonlinear simulation. The deuterium electrostatic heat flux spectra are shown on the top. The boron heat flux, as well as the electromagnetic ion heat flux, made negligible contributions to the total ion heat flux. The electrostatic electron heat flux spectra are displayed in the center. This is the bulk of the contribution to the heat flux. The electromagnetic electron heat flux spectra are displayed on the bottom.

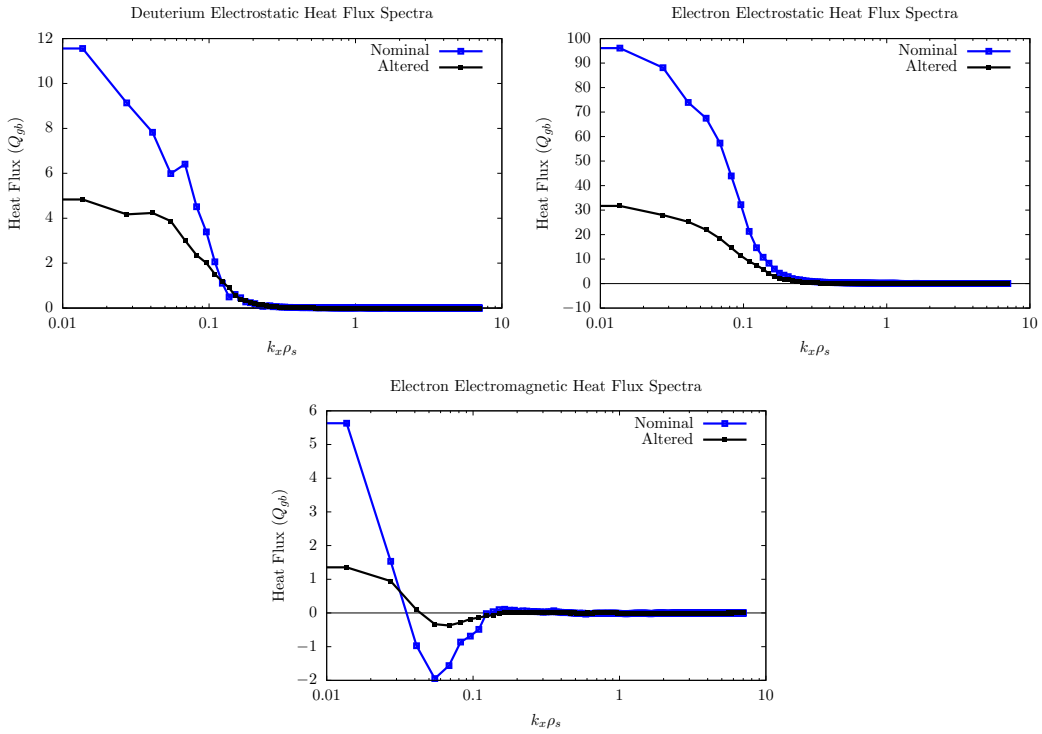

Figure 4.11: Time-averaged heat flux spectra in the radial coordinate. The graphs on the top left, top right, and bottom center represent the electrostatic deuterium, electrostatic electron, and electromagnetic electron radial heat flux spectra respectively. The spectra for the nonlinear simulations with nominal electron temperature gradient are shown, along with the spectra for nonlinear simulations with reduced electron temperature gradient where the heat fluxes match the experimental values.

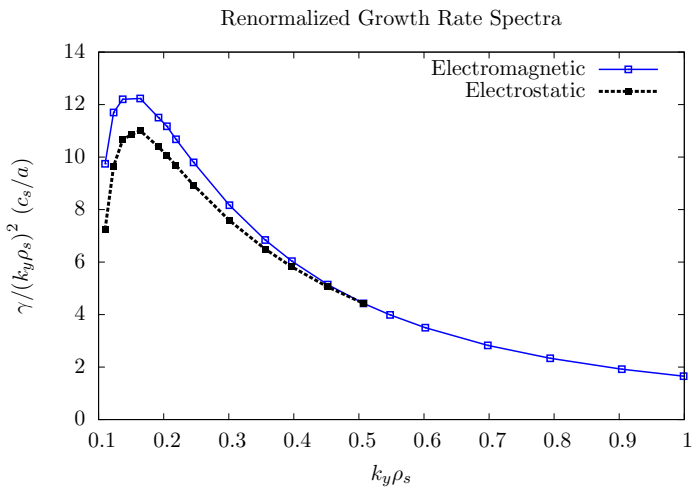

Figure 4.12: Renormalized growth rate spectra in the binormal direction for the electromagnetic and electrostatic case.

drift wave turbulence and highly nonlinear MHD at scales of $k_y\rho_s < 0.1$ for the system with the nominal plasma β value under consideration. Electromagnetic effects also destabilize the linear drift wave physics at the lower end of the k_y spectrum to a significant degree, as shown in Fig. 4.12. In this figure, the growth rates have been weighted by a factor of $1/(k_y\rho_s)^2$ to better mimic the effect that the mode should have in a nonlinear simulation, assuming that the linear physics is a good indication for how the nonlinear system will behave. Lower toroidal mode numbers play a more significant role in the simulation for a given growth rate because they are less strongly affected by the perpendicular nonlinearity than higher mode numbers. While nonlinear coupling to large-scale MHD is a reasonable theory to explain the large surge in the heat flux and the shift in the peak to lower toroidal mode numbers, this could potentially also be explained to some degree by the increase in the growth rate of the electron drift wave instabilities for the radial position under review.

4.4.4 Contour plots at outboard midplane

Contour plots of the electromagnetic fields and the density and flow fluctuations which drive the field perturbations at the outboard midplane are shown in Fig. 4.13 and Fig. 4.14 respectively. It can be seen that the fields and moments are well resolved at the outboard midplane in the simulation. The domain is 459 gyroradii in the radial dimension, and 224.4

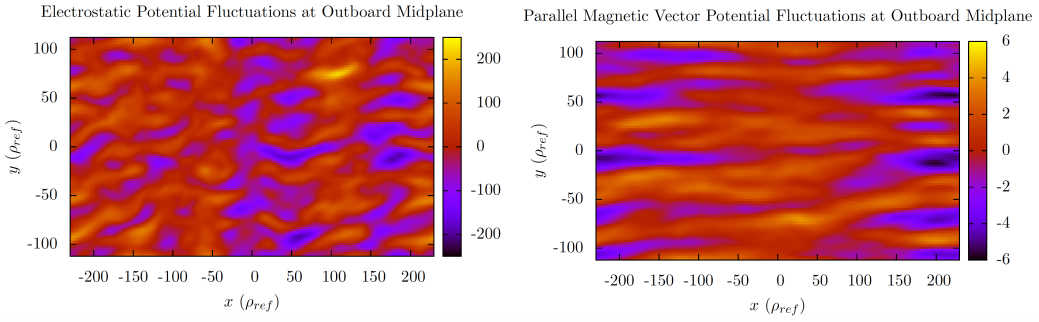

Figure 4.13: Contour plots of electrostatic (left) and parallel magnetic vector (right) potential at the outboard midplane of the simulation domain. The data shown was taken from the simulation with the nominal input parameters at time, $t = 106 L_{\rm ref}/c_{\rm ref}$.

gyroradii in the binormal dimension. Such a box size is very large in the radial domain, and if centered at the position of interest ($\rho_{\rm tor} = 0.9$), would extend beyond the separatrix into the scrape-off layer. The large box size was used to prevent streamers of $A_\parallel$ in the radial domain, and ensure that the fields were well-resolved in the simulation. Some may wonder about the validity of the flux-tube approximation when it is necessary to construct a radial domain extending into a regime where the flux-tube approximation is clearly not valid. But it is important to point out that it is not the size of the radial domain in the flux-tube simulation that is physically significant (in principle, such domains could extend to infinitely large ranges while giving converged results, since the boundary conditions are periodic). What is truly important is the size of the physical structures. The size of the density and flow fluctuations compared to the gradient length scales are meaningful, not the size of the radial domain needed to resolve the larger scale electrostatic potential and magnetic vector potential fluctuations. For flux-tube simulations, $A_\parallel$ is proportional to the charge current density divided by $k_\perp^2$, so the charge current density structures map to larger structures in the xy-plane for $A_\parallel$. When these large $A_\parallel$ structures are used to evolve the perturbed distribution function, the density and flow moments should still retain their standard size in the xy-plane for a saturated nonlinear simulation. So a large radial domain was utilized only to mitigate concerns about $A_\parallel$ streamers, and the use of a large radial domain is not necessarily a cause for concern.

When the problem related to $A_\parallel$ streamers has been encountered in previous simulations

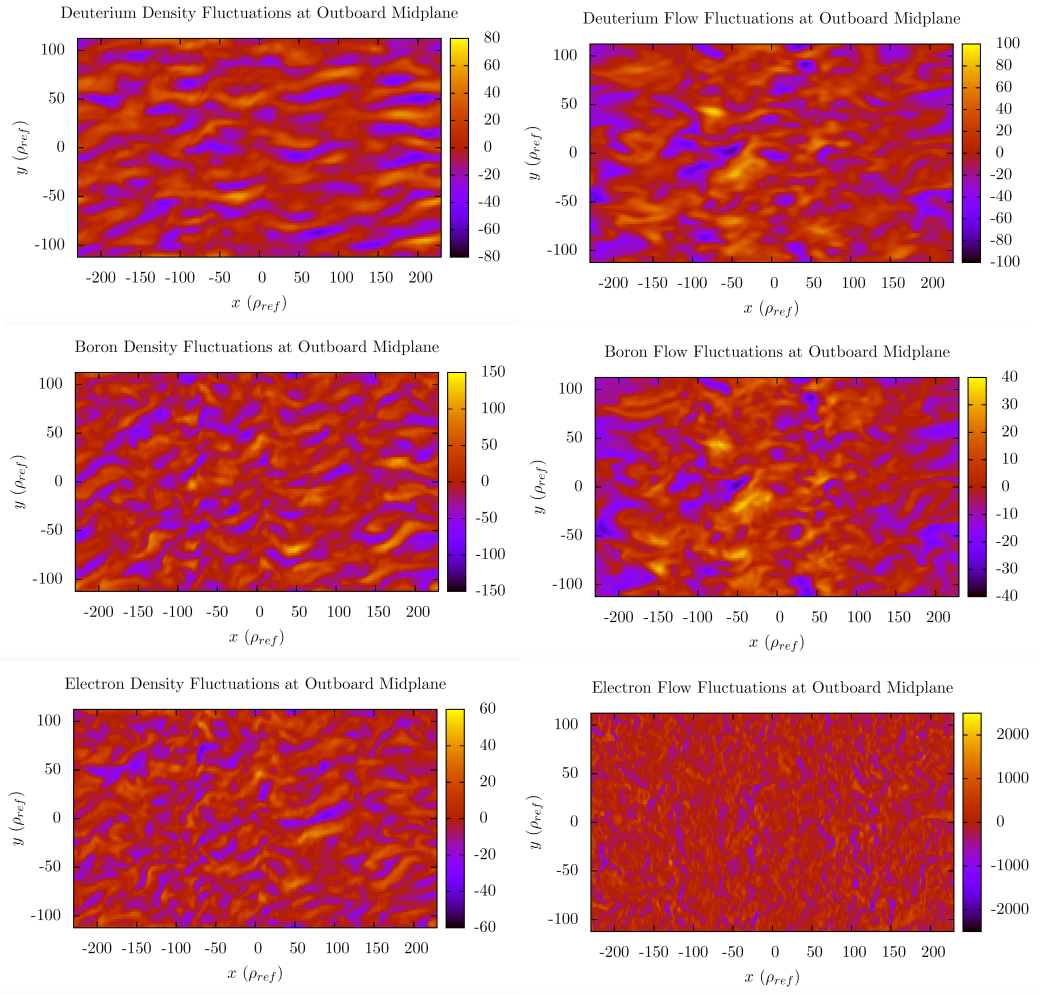

Figure 4.14: Contour plots of deuterium (top), boron (center), and electron (bottom) density (left) and flow (right) fluctuation amplitudes at the outboard midplane of the simulation domain. The data shown was taken from the simulation with the nominal input parameters at time, $t = 106 L_{\text{ref}}/c_{\text{ref}}$.

of the edge, the typical approach has been to use the LILO version of GENE. The LILO version of GENE is the same as the global version of the code, but uses constant profiles. So the equations being solved are the same as in the flux-tube version of the code, except that the radial coordinate is evaluated in real space, as opposed to Fourier space. Dirichlet boundary conditions can then be applied and are used to kill elongated structures, rather than periodic boundary conditions. The motivation for such an approach was that one could confine the length of the box and reduce the resolution requirements for gyrokinetic simulations. However, since smaller structures in the density and flow perturbations map to larger structures in the parallel magnetic vector potential, killing $A_{\parallel}$ structures artificially alters the self-consistent electromagnetic interactions in the plasma. It may be equally suitable, or even preferable, to resolve the electromagnetic fields in the simulation, rather than to artificially truncate them out of computational convenience and reluctance to justify the use of a large radial domain in the edge. Also, in future investigations of the edge, one should examine contour plots of the magnetic field components rather than the parallel magnetic vector potential to gauge if a simulation is resolved. The magnetic field components are the ones which are actually Fourier transformed and evaluated in the perpendicular nonlinearity. Furthermore, since the magnetic field components are related to the derivatives of the vector potential, they are less likely to resemble streamers at the outboard midplane. It is not necessary to prevent streamers in $A_{\parallel}$ if the magnetic field perturbations are localized within the simulation domain and the transport is stable. Keeping this in mind could save on resolution in the radial dimension in future investigations.

The poloidal cross-sections of the electrostatic potential for the electrostatic and electromagnetic nonlinear simulations are displayed in Fig. 4.15. The larger width of the flux-surface for the electromagnetic simulation is due to the larger box size utilized to handle the streamers in the $A_{\parallel}$ structures. The strange deformations occurring on the top and bottom of the inner radius of the electromagnetic flux-surface can be attributed to a breakdown of the local limit assumed for the metric coefficients in the course of the mapping of a box extending beyond the separatrix onto a closed surface, and thus, are not a cause for concern. Both figures show turbulence that is primarily localized at the outboard midplane of the device.

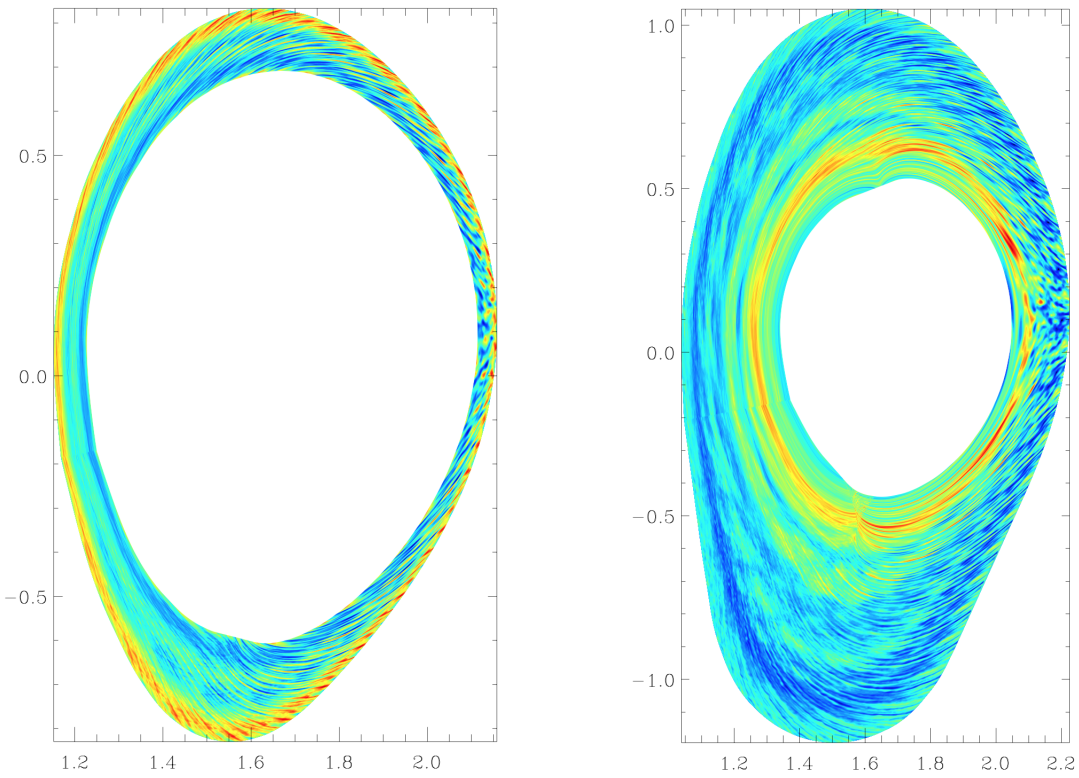

Figure 4.15: Poloidal cross-section of the electrostatic potential for the electrostatic (left) and electromagnetic (right) nonlinear simulations.

This coincides with intuition, and is a desirable feature considering that the poloidal grid points are more concentrated at the outboard midplane, and thus, better suited to resolve turbulence focused around that area. It should be noted however, that as one goes farther into the edge, the ballooning structure of the modes can peak at areas other than the outboard midplane, and the poloidal resolution and discretization of the grid points should be adjusted for such a scenario.

4.4.5 Cross-phase analysis

In addition to the saturation amplitudes of the fields and moments, one of the major determinants of the heat and particle fluxes is the cross-phases between those fields and moments. The transport fluxes are products of fields and moments, as shown in Eqs. 2.13, 2.14, and 2.15. When the fields and moments are in phase, the transport is at a maximum, and when

they are out of phase, the transport is at a minimum. If one had complete information about the saturation amplitudes and cross-phases, one could replicate the transport. In the core of a plasma discharge, the nonlinear cross-phases between the electrostatic potential and the density and temperature fluctuations are strongly correlated to the linear cross-phases. This strong correlation has been used to justify the construction of fast quasilinear models [81, 82, 83] which rely on this correlation to predict plasma transport more quickly than full nonlinear gyrokinetic simulations. These fast quasilinear transport prediction models would be especially useful in the edge, where gyrokinetic simulations are more expensive. There is therefore a strong motivation to understand if the linear and nonlinear cross-phases exhibit strong correlation in the plasma edge. Here, the cross-phase for each k_y mode is defined as in Eq. 4.6,

$$\alpha_{A,B}(k_y) = \left[\sum_{k_x,z} \arg\Big(A(k_x,k_y,z)/B(k_x,k_y,z)\Big) W(k_x,k_y,z)\right] / \sum_{k_x,z} W(k_x,k_y,z). \tag{4.6}$$

In the above expression, A and B are the quantities of interest, such as the fields and moments. W is a weighting factor designed to emphasized high amplitude fluctuations, and is defined as

$$W(k_x,k_y,z) = \frac{\mid A(k_x,k_y,z) \mid * \mid B(k_x,k_y,z) \mid}{<\mid A(k_x,k_y,z) \mid>_{k_x,z} <\mid B(k_x,k_y,z) \mid>_{k_x,z}}.$$

In the above expression, the angle brackets and subscript denotes an average over all k_x modes and poloidal grid points. The function arg is defined in Eq. 4.7,

$$\arg(x) = \tan^{-1}(\mathrm{Im}(x)/\mathrm{Re}(x)). \tag{4.7}$$

The cross-phases between the electrostatic potential and the perpendicular temperature fluctuations at the outboard midplane are displayed in Fig. 4.16. Results are displayed for the nominal and electrostatic scenario, and data has been time-averaged over the intervals, $t = 76.6 - 93.9a/c_s$ and $t = 100 - 180.1a/c_s$ for the two scenarios respectively. If the

weighting factors, W, were set equal to one, then the amplitudes in the contour plots could be interpreted as the probability that a particular cross-phase was observed for a given binormal wave number. Because of the weighting factors, the amplitudes in the contour plot are shifted to dramatically lower values then would be expected from a probability distribution.

It can be seen that there is generally good agreement between the linear and nonlinear phases in the range $0.1 \lesssim k_y\rho_s \lesssim 0.5$, which is the range of the spectrum for which the bulk of the heat transport occurs. For small scales ($k_y\rho_s \gtrsim 0.5$) and large scales ($k_y\rho_s \lesssim 0.1$) there is very little agreement between the linear and nonlinear phases. The electromagnetic and electrostatic cases have also been shown side-by-side to allow for comparison. It has been found previously in ref. [75, 91] that increasing the plasma β leads to a greater contribution from low toroidal mode numbers, and cross-phases that are closer to $\pi/2$. This would suggest that MHD-like instabilities become relevant to the system, and result in the elevated heat fluxes in electromagnetic nonlinear simulations. The cross-phases do not match the dominant linear microinstabilities for both the electrostatic and electromagnetic scenario in this regime (however, the transport is also weaker here). Nevertheless it can clearly be seen that electromagnetic effects result in a spreading out of the cross-phases for the part of the binormal spectrom, $k_y\rho_s \lesssim 0.1$. Movement of the cross-phases towards $\pi/2$ have not been observed for the nominal parameters, however higher β values have not been investigated. A shift in the heat flux towards lower mode numbers has been observed, but not far into the $k_y\rho_s \lesssim 0.1$ regime, and this could also be potentially explained by the electromagnetic effect on the linear microinstabilities (see Fig. 4.12).

The cross-phases between electrostatic potential and density fluctuations for the nominal parameter set are displayed in Fig. 4.17. These are the relevant data for assessing whether or not particle transport is quasilinear (the electromagnetic particle transport was found to be negligible in the simulation). The cross-phases seem to give very good agreement for the ions. There are two different cross–phase branches around $k_y\rho_s \sim 0.2$ and $k_y\rho_s \sim -\pi$, and the nonlinear physics switches branches in accordance with the linear physics. For the electrons, there is very good agreement in the regime where the transport occurs, $0.1 \lesssim k_y\rho_s \lesssim 0.5$,

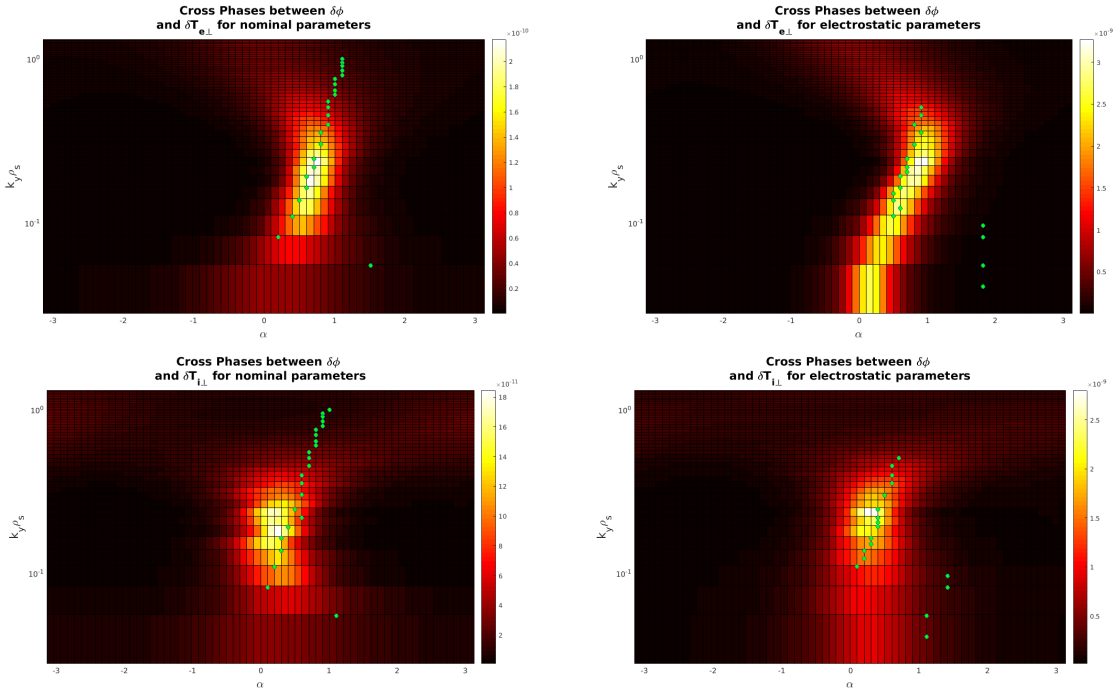

Figure 4.16: Time-averaged cross-phases between electrostatic potential and perpendicular temperature fluctuations for each toroidal mode number in the simulation. The cross-phases for electrons are shown on the top and the cross-phases for the ions are shown on the bottom. The cross-phases for the nominal parameters are displayed on the left, and the cross-phases for the electrostatic parameters are displayed on the right. The contour plots display the cross-phases for the nonlinear simulations, and the green markers indicate the dominant cross-phases for each toroidal mode number in the linear simulations. The cross-phases between the electrostatic potential and parallel temperature fluctuations are highly similar to the data displayed here. The data for the parameters where the electron temperature gradient was lowered also qualitatively resemble the data for the nominal electromagnetic parameters.

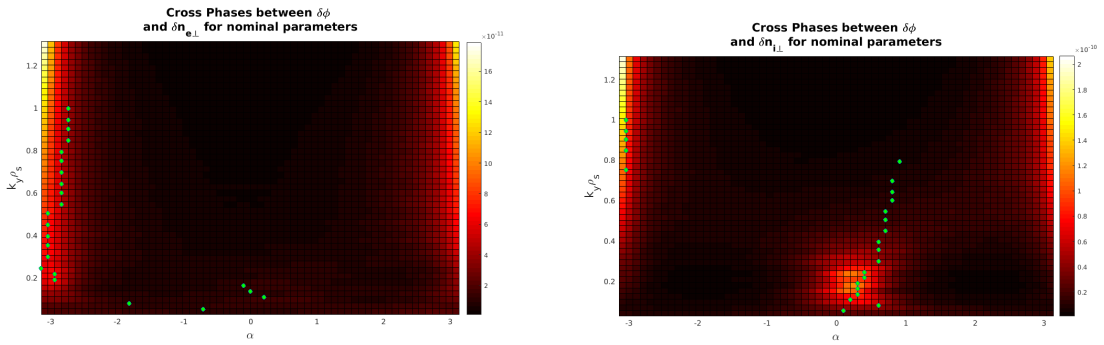

Figure 4.17: Cross-phases between electrostatic potential and density fluctuations. The plots for the electrons are shown on the left, and the plots for the ions are shown on the right. The contour plots display the cross-phases for the nonlinear simulations, and the green markers indicate the dominant cross-phases for each toroidal mode number in the linear simulations.

although the agreement is slightly worse at smaller scales, and very poor at large scales, $k_y\rho_s \lesssim 0.1$.

4.5 Extrapolation of the model farther in the edge

A statement of caution is worth mentioning. The findings presented here are specific to the scenario and radial position under study. These findings cannot necessarily be extrapolated farther into the edge. As one goes closer to the separatrix, the electron drift wave microinstabilities begin to become dominant at very low toroidal mode number ($k_y\rho_s \lesssim 0.1$). The renormalized growth rate spectra would then indicate a massive surge in the heat flux in that region, as shown in Fig. 4.18. It was already found at $\rho_{\text{tor}} = 0.9$ that the physics of the region $k_y\rho_s \lesssim 0.1$ is highly nonlinear, and this region exhibits little resemblance to the modes located there. This didn't seem to impact the transport levels observed for $\rho_{\text{tor}} = 0.9$ because the transport was dominated by higher binormal wavenumbers. However, if this region retains its nonlinear nature as one goes farther to the edge where electron drift waves become much stronger at lower binormal wavenumbers, then one would expect the transport in that region to be highly nonlinear, and for the cross-phases to exhibit little correspondence, as found in [75, 76].

An attempt was made to model the transport at the radial position $\rho_{\text{tor}} = 0.96$. Unfortu-

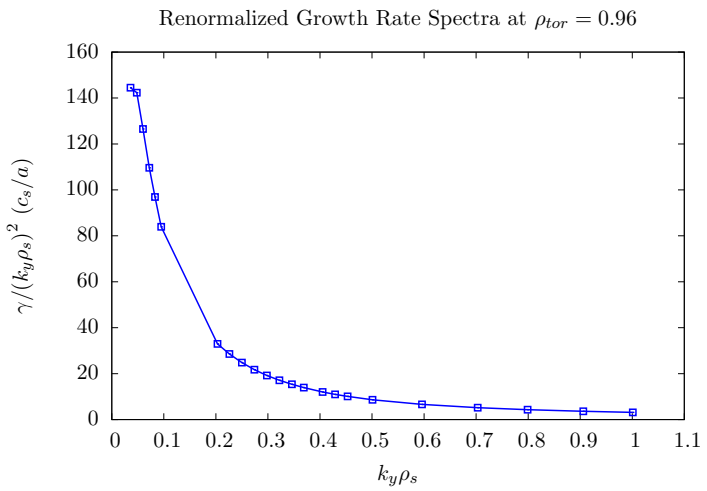

Figure 4.18: Renormalized growth rate spectra in the binormal direction for the linear microinstabilities at $\rho_{\text{tor}} = 0.96$.

nately, such an attempt was unsuccessful due to the enormously computationally expensive nature of such simulations. In this region, the collisionality places severe restrictions on the timestep, especially for a simulation with Boron impurities, which should be included in this discharge to realistically model the physics. Additionally, a higher resolution in the binormal dimension is needed to resolve the modes in the region $k_y\rho_s \lesssim 0.1$, and a higher z resolution is needed to resolve the low toroidal mode numbers, which increases the time per timestep and decreases the timestep in the simulation.

An implicit collisional time-stepping scheme should be developed to allow for more computationally tractable simulations of the plasma edge. Also, nonlinear simulations at farther radial positions where the electron drift waves become unstable in the $k_y\rho_s \lesssim 0.1$ region should be investigated to see if the transport remains attached to the underlying linear instabilities or if the transport becomes highly nonlinear. If the transport becomes highly nonlinear, then there seems to be a natural point at which the nonlinear physics departs from the linear physics: when the electron drift waves in the edge become unstable in $k_y\rho_s \lesssim 0.1$ region. If the transport remains quasilinear, then it would prove that the underlying microinstabilities remain a useful guide for characterizing transport in gyrokinetic simulations even in the extreme parameter regime of the edge.

4.6 Chapter summary

After conducting a thorough linear and nonlinear examination with the delta-f flux-tube gyrokinetic model at $\rho_{\text{tor}} = 0.9$ ($r/a = 0.93$), it can be seen that the transport in this region is dominated by electron drift wave turbulence. The transport is nearly entirely electrostatic heat and particle flux. For the nominal parameters, the simulated heat flux is higher than the experimental measurements by a factor of ~ 4 for the electrons and ~ 2 for the ions. This discrepancy can be mitigated by lowering the electron temperature gradient by 40%. It is not clear that this parameter was incorrectly provided by the experimentalists, but it's possible, and matching the heat fluxes by lowering the electron temperature gradient by 40% demonstrates that the delta-f gyrokinetic model can reproduce the transport in the edge by varying the input parameters within their error bars. It was also found at this radial position that the cross-phases between electrostatic potential and temperature and density fluctuations remain highly correlated between linear and nonlinear simulations in the regime for which the transport dominates ($0.1 \lesssim k_y\rho_s \lesssim 0.5$). Outside of this regime, there is little correlation (although, there is also minimal transport).

It has also been found that there is a large electromagnetic effect on transport in the edge. The electrostatic parameter set gives heat transport which very closely agrees with the experimental measurements. When electromagnetic effects are included, the electrostatic heat flux roughly doubles for the ions and quadruples for the electrons. This boost is nearly entirely at low toroidal mode number, and could also potentially be attributed to the linear physics, as shown in Fig. 4.12. It was also found that electromagnetic effects lead to a large spreading out of the cross-phases at large scales ($k_y\rho_s \lesssim 0.1$). Nevertheless, the transport in the regime ($0.1 \lesssim k_y\rho_s \lesssim 0.5$) appears to be mostly quasilinear, suggesting that such models should be able to replicate the transport found here reasonably well.

CHAPTER 5

Electromagnetic gyrokinetic models

The plasma β is considered to be one of the most fundamental dimensionless parameters in plasma physics,

$$\beta = \frac{8\pi p}{B_0^2} = \frac{8\pi n_{\rm ref} T_{\rm ref}}{B_{\rm ref}^2}.$$

This parameter is traditionally used as an indicator for the confinement quality of a given device. The logic behind this philosophy is the idea that the background magnetic field is to a large extent determined independently of the plasma (for instance, by the amount of current being driven through the external coils) and a higher plasma pressure is obviously one of the desired outcomes of a fusion device. Furthermore, the fusion reaction rates are proportional to β^2 and the bootstrap fraction (fraction of plasma current driven by trapped plasma particles) is proportional to β. The plasma β is also an important parameter for the consideration as to whether or not a system is MHD stable or not. While β is certainly not the only relevant plasma parameter (the confinement time, τ_E, is also an extremely important parameter for the confinement quality of the system), it has a certain relevance in gyrokinetic models as well. In gyrokinetic models, the plasma β is an indicator for the relevance of electromagnetic effects in the system (It can be seen in the normalized gyrokinetic equations that the electromagnetic fields vanish in the limit $\beta \to 0$). This is similar to how ν_c and ρ^* represent the relevance of collisional effects and finite size effects respectively (although there is also a pressure drive term independent of electromagnetic effects, but proportional to β). And in various cases, these electromagnetic effects are important.

Many investigations using gyrokinetics must include not only electrostatic fluctuations

against a strong background magnetic field, but also perturbed electromagnetic fields to facilitate an accurate and comprehensive description of plasma microturbulence and transport. Under certain circumstances, electromagnetic effects such as stochastic magnetic fields and plasma induction, can give rise to diverse and important transport mechanisms. Many important microinstabilities such as the Microtearing Mode (MTM), Kinetic Ballooning Mode (KBM), and Toroidal Alfvén Eigenmode (TAE) exist only in the presence of finite β (which would mean non-negligible electromagnetic effects). Other microinstabilities such as Ion Temperature Gradient (ITG) instabilities can be strongly damped by these effects.

However, previous attempts at conducting electromagnetic gyrokinetic simulations have encountered severe difficulties. For local gyrokinetic simulations, it has been found that at high enough plasma β, the heat fluxes saturate at an exceptionally high level of transport not found in realistic experiments, and this is a result of magnetic perturbations shorting out flux surfaces and destroying zonal flows. This phenomena has been termed the nonzonal transition (NZT), and sets an upper bound to the value of the plasma β that can be studied with flux-tube gyrokinetic simulations (which is generally lower than the critical β value for MHD stability) [92, 93, 94, 95, 96].

Global gyrokinetic simulations have also suffered from numerical problems, primarily, the cancellation problem [97], first observed in particle-in-cell codes in ref. [98]. This problem limited electromagnetic gyrokinetic investigations to extremely low β parameter sets [99]. The cancellation problem has been examined with particle-in-cell methods in refs. [100, 101, 102] and with Eulerian methods in ref. [103]. A recent approach to solving the cancellation problem has been published in ref. [104] using a new mixed variable formulation of gyrokinetics [105, 106]. A good review of the cancellation problem and it's mitigation can be found in ref. [107]. For global gyrokinetic GENE simulations, the electromagnetic model could also become outright numerically unstable for certain scenarios, even at relatively low values of β. This problem shall be investigated in this chapter.

Also, in addition to delta-f gyrokinetic simulations for core and edge plasma turbulence, there is a desire to develop a full-f version of GENE to study scrape-off layer turbulence, and it is not immediately clear how to analyze the nonlinear plasma induction term. An alternative

scheme for evaluating the electromagnetic fields has been developed within this thesis with the hope of mitigating these problems. This scheme is discussed in this chapter, as well as tests of the implementation of this scheme. For more information on the implementation of electromagnetic fields in GENE, see refs. [108, 27, 35].

This chapter is outlined in the following way. First, a discussion of the original and alternative implementation of the electromagnetic fields in the GENE code is discussed in section 5.1. This includes a linear benchmark for local and global microinstabilities at finite β. Following this, the Rosenbluth-Hinton test is applied to examine the numerical stability of the magnetic induction of these different implementations in section 5.2. Afterwards, the numerical instability for the global electromagnetic version of GENE is analyzed in section 5.3. Conclusions are drawn in section 5.4.

5.1 Implementation of electromagnetic fields in GENE code

The collisionless gyrokinetic equation is given as

$$\frac{\partial F_a}{\partial t} = \frac{q_a}{m_a c}\frac{\partial \overline{A_\parallel}}{\partial t}\frac{\partial F_a}{\partial v_\parallel}$$

$$-\left[\frac{c\hat{\mathbf{b}}}{qB^*_\parallel}\times\nabla(\mu B + q\bar{\chi}) + v_\parallel\hat{\mathbf{b}} + \frac{B}{B^*_\parallel}\mathbf{v}_c\right]\cdot\nabla F_a$$

$$+\frac{1}{m_a v_\parallel}\left[\frac{c\hat{\mathbf{b}}}{qB^*_\parallel}\times\nabla(\mu B + q\bar{\chi}) + v_\parallel\hat{\mathbf{b}} + \frac{B}{B^*_\parallel}\mathbf{v}_c\right]\cdot(\mu\nabla B + q\nabla\overline{\psi})\frac{\partial F_a}{\partial v_\parallel}. \tag{5.1}$$

The first term in Eq. 5.1 proportional to $\partial\overline{A_\parallel}/\partial t$ representing the plasma induction poses a numerical difficulty. It is not immediately clear how one could evaluate this equation using a simple fourth-order Runge-Kutta time-stepping scheme because of the two time derivatives. If the higher order parallel nonlinearities are neglected (which can be justified in a delta-f framework), then $\partial F_a/\partial v_\parallel$ becomes $\partial F_{0a}/\partial v_\parallel$ which is constant in time. So one could define a new distribution, g_a,

$$g_a = f_a - \frac{q_a}{m_a c}\frac{\partial F_{0a}}{\partial v_\parallel}\overline{A_\parallel}. \tag{5.2}$$

One could then numerically evaluate the delta-f gyrokinetic equation by using a fourth-order Runge-Kutta time-stepping scheme to evolve g_a as opposed to f_a. The Ampére's law field equation would then also have to be modified from a Poisson equation to a Helmholtz equation so that $A_\parallel$ could be evaluated from g_a as opposed to f_a, but this is a trivial task. However, this scheme could not be extrapolated to the full-f case, because $\partial F_a/\partial v_\parallel$ is not constant in the full-f model. In the remainder of this section, an alternative scheme for numerically evaluating the electromagnetic fields is devised with the hope of creating a model which could be extended to full-f electromagnetic gyrokinetic simulations. This scheme has similarities to the one outlined in [109].

The original equations for the $A_\parallel$ fluctuations and the plasma induction are given by

$$\nabla_\perp^2 A_\parallel = -\frac{4\pi}{c} j = -\frac{4\pi}{c}\sum_b q_b \int d^3 v \mathcal{G}^\dagger\{v_\parallel F_b\} \tag{5.3}$$

$$\frac{\partial F_a}{\partial t} - \frac{q_a}{m_a c}\frac{\partial}{\partial t}(\mathcal{G}\{A_\parallel\})\frac{\partial F_a}{\partial v_\parallel} = R_a. \tag{5.4}$$

In Eq. 5.4, R_a represents the entire right hand side of the gyrokinetic equation that excludes the plasma induction. Now the following formalism will be used:

$$E_\parallel^{\text{ind}} = -\frac{1}{c}\frac{\partial A_\parallel}{\partial t}. \tag{5.5}$$

And the gyrokinetic equation shall be rewritten as

$$\frac{\partial F_a}{\partial t} = R_a - \frac{q_a}{m_a}\mathcal{G}\{E_\parallel^{\text{ind}}\}\frac{\partial F_a}{\partial v_\parallel}. \tag{5.6}$$

Taking the time derivative of Eq. 5.3, and using the definition of $E_\parallel^{\text{ind}}$ in Eq. 5.5, the following is obtained:

$$\nabla_\perp^2 E_\parallel^{\rm ind} - \frac{4\pi}{c^2}\sum_b q_b \int d^3v \mathcal{G}^\dagger \left\{ v_\parallel \frac{\partial F_b}{\partial t} \right\} = 0. \tag{5.7}$$

Plugging Eq. 5.6 into Eq. 5.7, one can arrive at an equation for the induced electric field,

$$\left(\nabla_\perp^2 + \frac{4\pi}{c^2}\sum_b \frac{q_b^2}{m_b} \int d^3v \mathcal{G}^\dagger v_\parallel \frac{\partial F_b}{\partial v_\parallel} \mathcal{G} \right) E_\parallel^{\rm ind} = \frac{4\pi}{c^2}\sum_b q_b \int d^3v \mathcal{G}^\dagger \{ v_\parallel R_b \} = \frac{4\pi}{c^2}\frac{\partial j}{\partial t}. \tag{5.8}$$

In principle, since the right-hand side of the gyrokinetic equation is stored in an array in a GENE simulation, one could use Eq. 5.8 to solve for the induced electric field, and then use this together with Eq. 5.6 to evolve the gyrokinetic equation with induction without changing the explicit time scheme used by the code. One could furthermore adapt this scheme to a delta-f model by modifying the full distribution, F_a, to include only the background effects from F_{0a}, and not the lower order terms. In this case, one could also avoid taking numerical derivatives if the background distribution is a Maxwellian,

$$\frac{\partial f_a}{\partial t} = R_a + \frac{q_a}{T_a}\mathcal{G}\{E_\parallel^{\rm ind}\} v_\parallel F_{Ma} \tag{5.9}$$

$$\left(\nabla_\perp^2 - \frac{4\pi}{c^2}\sum_b \frac{q_b^2}{T_b} \int d^3v \mathcal{G}^\dagger v_\parallel^2 F_{Mb} \mathcal{G} \right) E_\parallel^{\rm ind} = \frac{4\pi}{c^2}\frac{\partial j}{\partial t} = \frac{4\pi}{c^2}\sum_b q_b \int d^3v \mathcal{G}^\dagger \{ v_\parallel R_b \}. \tag{5.10}$$

By comparing the delta-f (Eq. 5.6 and 5.8) and full-f (Eq. 5.9 and 5.10) equations, it can be seen that there are two nonlinearities associated with the induction. There is the nonlinear contribution to the plasma induction, which can be incorporated into a gyrokinetic model by modifying the matrix for the $E_\parallel^{\rm ind}$ solver continuously with time. There is also the nonlinear response to the induced electric field, which could be incorporated into a gyrokinetic model by simply modifying the term on the right hand side so that the derivative of the full distribution is used, as opposed to the derivative of the background distribution.

If one was to use a more advanced form of the 2D full-f Ampére equation where the flow moment was calculated using the full-f pull back operator, then the equation for the induced electric field would be more complex. Such an equation, however, could be found and would still be linear. One could derive a linear equation for $E_{\parallel}^{\mathrm{ind}}$ by taking the time derivative of the Ampére equation. Because of the chain rule, the time derivative of any nonlinear quantity is linear in time derivatives. One could then substitute Eq. 5.9 for $\partial f_a/\partial t$ and Eq. 5.5 for $\partial A_{\parallel}/\partial t$. This equation would be linear in $E_{\parallel}^{\mathrm{ind}}$ and $\partial\phi/\partial t$. One could then take the time derivative of the Poisson equation to obtain two coupled linear equations for $E_{\parallel}^{\mathrm{ind}}$ and $\partial\phi/\partial t$, which could be solved. This technique for evaluating the parallel nonlinearity can therefore be generalized to a full-f gyrokinetic model.

One could simplify the equation for the determination of the induced electric field using integration by parts for the integral on the left hand side. In the drift-kinetic limit, such an integral can be interpreted as the squared plasma frequency,

$$\left(\nabla_{\perp}^2 - \left(\frac{\omega_p}{c}\right)^2\right) E_{\parallel}^{\mathrm{ind}} = \frac{4\pi}{c^2}\frac{\partial j}{\partial t}.$$

However, it has been found that applying integration by parts before numerical integration results in worse convergence properties for the study of electromagnetic microinstabilities. This makes sense, because consistent numerical schemes should be used throughout to ensure good conservation and symmetry properties. While integrating by parts results in a more appealing looking formula, maintaining the consistency and symmetry of the equations is more important. This is related to the cancellation problem observed in earlier particle-in-cell codes, where numerically evaluating the derivatives in the field matrix is a more difficult task.

A natural choice of normalization for the induced electric field is

$$E_{\parallel}^{\mathrm{ind}} = \frac{T_{\mathrm{ref}}}{eL_{\mathrm{ref}}}\frac{\rho_{\mathrm{ref}}}{L_{\mathrm{ref}}}\hat{E_{\parallel}^{\mathrm{ind}}}.$$

The normalized field equation for the plasma induction then becomes

$$\left(\nabla_\perp^2 + \frac{\beta}{2}\sum_b n_{0b}\frac{q_b^2}{m_b}\int d^3v\mathcal{G}^\dagger v_\parallel \frac{\partial}{\partial v_\parallel}\left(F_{0b} + \frac{\rho_{\rm ref}}{L_{\rm ref}}f_b\right)\mathcal{G}\right)E_\parallel^{\rm ind} \tag{5.11}$$

$$= \frac{\beta}{2}\sum_b q_b n_{0b}\sqrt{\frac{2T_{0b}}{m_b}}\int d^3v\mathcal{G}^\dagger(v_\parallel R_b),$$

and the normalized gyrokinetic equation then becomes

$$\frac{\partial F_a}{\partial t} = R_a - \frac{q_a}{\sqrt{2m_aT_{0a}}}\mathcal{G}\{E_\parallel^{\rm ind}\}\frac{\partial}{\partial v_\parallel}\left(F_{0a} + \frac{\rho_{\rm ref}}{L_{\rm ref}}f_a\right).$$

The delta-f approximation can be applied by taking $\rho_{\rm ref}/L_{\rm ref} \to 0$. The normalized Ampére's law can also be written as

$$\nabla_\perp^2 A_\parallel = -\frac{\beta}{2}\sum_b q_b n_{0b}\sqrt{\frac{2T_{0b}}{m_b}}\int d^3v\mathcal{G}^\dagger\{v_\parallel f_b\}.$$

As can be seen above, the magnetic field perturbations and the plasma induction vanish in the limit $\beta \to 0$, as discussed earlier.

There is one important aspect of the global delta-f gyrokinetic model that should be discussed. To reiterate, the delta-f gyrokinetic model is given by

$$\frac{\partial f_a}{\partial t} = \frac{c}{C_{xy}}\frac{B_0}{B_{0\parallel}^*}\left[\frac{\partial_x n_{0a}}{n_{0a}} + \frac{\partial_x T_{0a}}{T_{0a}}\left(\frac{m_a v^2}{2T_{0a}} - \frac{3}{2}\right)\right]F_{0a}\frac{\partial\bar{\chi}}{\partial y}$$

$$+\frac{c}{C_{xy}}\frac{B_0}{B_{0\parallel}^*}\frac{\mu B_0 + m_a v_\parallel^2}{q_a B_0}\left(\partial_y B_0 + \frac{g^{xx}g^{yz} - g^{yx}g^{xz}}{g^{xx}g^{yy} - g^{xy}g^{yx}}\partial_z B_0\right)\Gamma_{a,x}$$

$$-\frac{c}{C_{xy}}\frac{B_0}{B_{0\parallel}^*}\left[\frac{\mu B_0 + m_a v_\parallel^2}{q_a B_0}\left(\partial_x B_0 - \frac{g^{xy}g^{yz} - g^{yy}g^{xz}}{g^{xx}g^{yy} - g^{xy}g^{yx}}\partial_z B_0\right) + \frac{m_a v_\parallel^2}{2q_a}\beta\frac{\partial_x p_0}{p_0}\right]\Gamma_{a,y}$$

$$-\frac{c}{C_{xy}}\frac{B_0}{B_{0\parallel}^*}\left(\frac{\partial\overline{\chi}}{\partial x}\Gamma_{a,y} - \frac{\partial\overline{\chi}}{\partial y}\Gamma_{a,x}\right)$$

$$-\frac{C_{xy}}{JB_0}v_\parallel\Gamma_{a,z}+\frac{C_{xy}}{JB_0}\frac{\mu}{m_a}\partial_z B_0\frac{\partial f_a}{\partial v_\parallel}$$

$$+\frac{c}{C_{xy}}\frac{B_0}{B^*_{0\parallel}}\frac{m_a v_\parallel^2+\mu B_0}{q_a B_0}\left(\partial_z B_0+\frac{g^{xx}g^{yz}-g^{yx}g^{xz}}{g^{xx}g^{yy}-g^{xy}g^{yx}}\partial_z B_0\right)\left[\frac{\partial n_{0a}}{n_{0a}}+\frac{\partial T_{0a}}{T_{0a}}\left(\frac{m_a v_\parallel^2}{2T_{0a}}-\frac{3}{2}\right)\right]F_{0a}$$

$$+\frac{q_a}{T_a}\overline{E_\parallel^{\mathrm{ind}}}v_\parallel F_{0a}. \tag{5.12}$$

In Eq. 5.12, $\Gamma_{a,i}$ (where i can represent x, y, or z) is given by (as of this writing, $B_\parallel$ fluctuations are neglected in the global version of the code)

$$\Gamma_{a,i}=\partial_i f_a+q_a\frac{F_{0a}}{T_{0a}}\partial_i\overline{\phi}.$$

In the previous gyrokinetic model, since g_a was evolved explicitly in time, and since $\chi=\phi-v_\parallel A_\parallel/c$ was a commonly used parameter, it was natural to rewrite the expression for $\Gamma_{a,i}$ as

$$\Gamma_{a,i}=\partial_i g_a+q_a\frac{F_{0a}}{T_{0a}}\partial_i\overline{\chi}-\frac{q_a v_\parallel}{cT_{0a}}\overline{A_\parallel}\partial_i F_{0a}. \tag{5.13}$$

In Eq. 5.13 the last term was regarded as insignificant and neglected, so that the following expression for $\Gamma_{a,i}$ was used:

$$\Gamma_{a,i}\simeq\partial_i g_a+q_a\frac{F_{0a}}{T_{0a}}\partial_i\overline{\chi}.$$

While this is a convenient approximation, it also introduces electromagnetic dependence into a term which generally has none in the global version of the code. This can create problems, as will be seen later in this chapter.

To help verify that the alternative schemes to be used for electromagnetic gyrokinetic simulations have been implemented correctly, linear benchmarks have been performed with

both the local and the global versions of the GENE code. The results of the local benchmark are shown in Fig. 5.1. The standard version of the GENE code has been benchmarked against the GS2 code for this case, with very good agreement being shown in [94]. Two different alternative schemes are compared against the standard version of GENE. These schemes are described in the present section, with the only difference between the schemes being the numerical implementation of the field matrix. In alternative scheme 1, Eq. 5.1 has been used to solve for the induced electric field. Numerical differentiation is used in the field matrix, similar to how it is used in the calculation of the parallel nonlinearity. In alternative scheme 2, integration by parts is utilized to prevent having to use numerical differentiation in the field matrix. So the analytical form for the field matrix is simpler. All versions of the codes give very good agreement for the frequencies. However, alternative scheme 2 (the scheme which uses integration by parts) results in lower growth rates for the KBM branch. Since the standard version of GENE has been well benchmarked with GS2, this suggests that the integration by parts trick (which is tempting by virtue of the fact that it makes the underlying field equation is simpler) results in an error in the growth rates relating to the cancellation problem (since the consistency of the field matrix has been altered). This means that alternative scheme 1 should be utilized to maintain the consistency of the numerical schemes, and that is the scheme which shall be used in the rest of the discussion of electromagnetic simulations. The results of the global benchmark are shown in Fig. 5.2. The standard version of the GENE code has been benchmarked against the GKW, EUTERPE, and ORB5 codes in [110]. In this case, the alternative version of GENE refers to the implementation described in the previous section (without using integration by parts for the field solver) and the original version of GENE is the version used in [110]. All code versions give good agreement, and the two versions of GENE give very good agreement.

The benchmarks show very good agreement between the original and alternative version of the GENE code for the linear growth rates and frequencies. While this new scheme was developed particularly with the hope of resolving issues occurring in nonlinear simulations, the linear benchmarks inspire confidence that the implementation has been done correctly, at least as far as the linear modes are concerned. A nonlinear benchmark is difficult, because

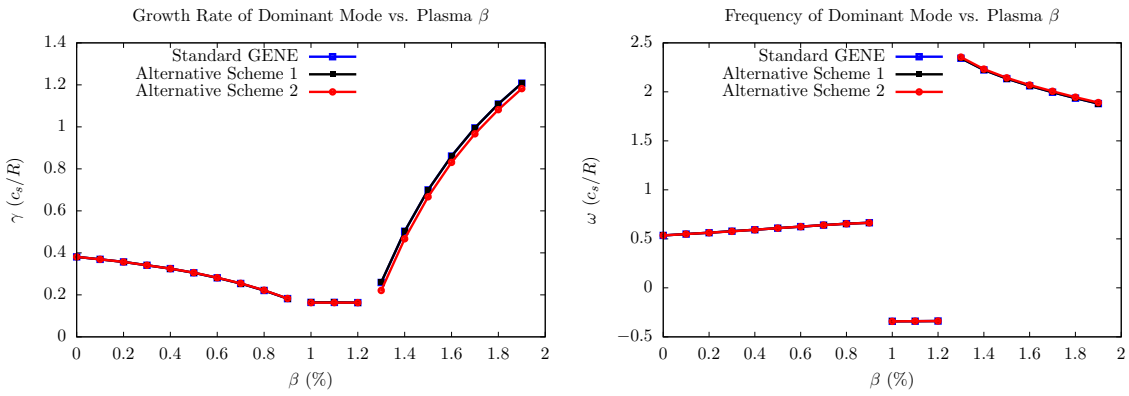

Figure 5.1: Local β scan for the $k_y\rho_s = 0.2$ mode of the CBC parameter set. As β is increased from 0% to 2%, the dominant microinstability changes from an ITG, to a TEM, and finally to a KBM.

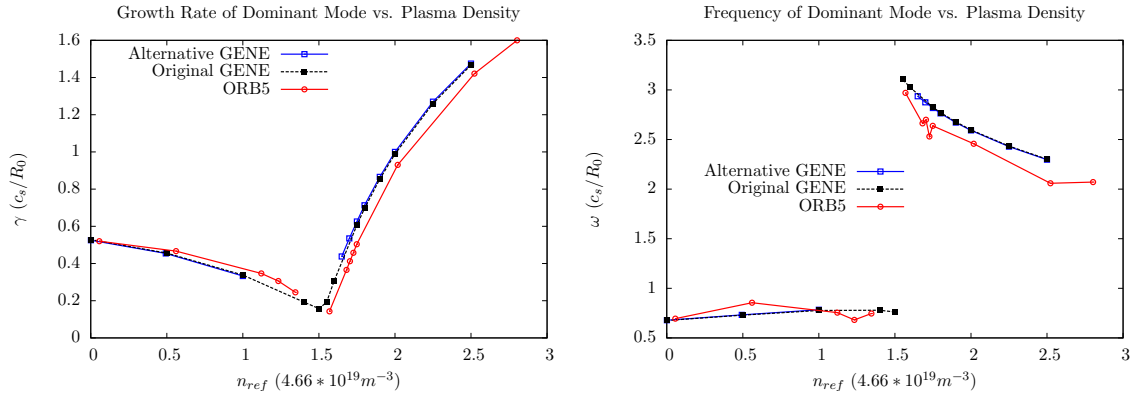

Figure 5.2: Global β scan for the $n_0 = 19$ toroidal mode number of the CBC parameter set. As the reference density, n_{ref}, is increased from $5 \cdot 10^{16} m^{-3}$ to $14 \cdot 10^{19} m^{-3}$, the dominant mode changes from an ITG to a KBM.

such tests can be highly expensive, and the original code can become unstable for different scenarios, making comparisons difficult. However, some insights can be gained by studying zonal flows (the main candidate for saturation of ITG modes), and a Rosenbluth-Hinton test must also be performed to ensure the numerical stability of the code implementations.

5.2 Rosenbluth-Hinton test for electromagnetic field implementation

One of the fundamental tests of the numerical stability of a code is the Rosenbluth-Hinton test. The $k_y = 0$ mode in a simulation must not be unstable, and this feature has been used to study the numerical stability of the various schemes proposed in section 5.1. Perpendicular magnetic field fluctuations do not appear in the $k_y = 0$ part of the electromagnetic gyrokinetic equation. However, the magnetic induction, $E_{\parallel}^{\mathrm{ind}}$, does appear, and simulations of $k_y = 0$ can be used to examine the stability of different induction schemes as well as the parallel nonlinearities for both the local and global versions of the code. The tests performed for this case have been done with CBC parameters at different values of β, ρ^*, and mass ratio.

For the local version of the code, both the linear and nonlinear electromagnetic schemes appear to be stable, as shown in Fig. 5.3, although the nonlinearities do not seem to change the results significantly. The difference in the electromagnetic implementation is that the induction is solved for explicitly. In the nonlinear electromagnetic model, the electrostatic parallel nonlinearity, the nonlinear contribution to the induction, and the nonlinear response to the induction are all included. This test seems to indicate that the electromagnetic model with nonlinear terms can be used in gyrokinetic flux-tube simulations.

The Rosenbluth-Hinton test has also been performed for the global electromagnetic case. When the parallel nonlinearities are excluded, then the test is passed and the zonal flows are stable. The results of this test are displayed in Fig. 5.4. However, it is not straightforward to implement the nonlinear contribution to the plasma induction in the GENE code. GENE uses an LU decomposition method to solve for the fields. The matrix is constructed, and decomposed into an upper and lower matrix in the initialization. The field equations are then solved with this decomposed matrix for each time-step in the simulation. If one wished to run gyrokinetic simulations with the nonlinear induction contribution included, one would have to rewrite the code so that the field matrix is constructed each time-step. One would then need to factor this matrix each time-step, or use an alternative field solver besides LU-decomposition. This would require too much time in code development and computational

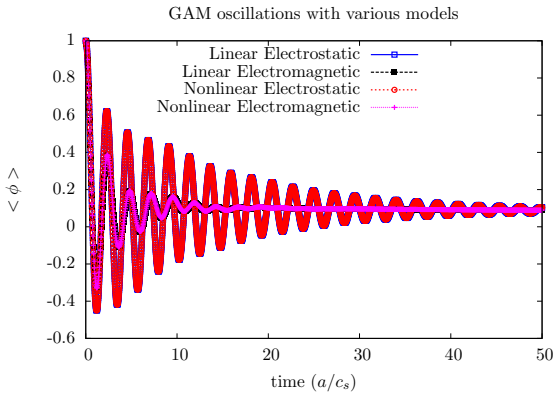

Figure 5.3: Oscillations in electrostatic potential vs. time for the $k_y = 0$ mode. This local simulation was run with $k_x\rho_s = 0.01$. The electromagnetic simulations were performed with $\beta = 2\%$. The nonlinear simulations were performed with $\rho^* = 5\%$. All of the runs were performed with $\nu_c = 0.025\%$ to reduce grid-sized features in the electron dynamics (such a collisionality is near the nominal value). These runs were performed with a grid resolution of $64 \times 256 \times 64$ in $(z, v_\parallel, \mu)$. Very high values for these parameters were chosen so as to test the stability of the model in extreme parameter regimes. It can be seen in the plot that the oscillations decay in time, and ϕ tends toward a finite residual value.

resources. Nevertheless, one could still add the nonlinear response of the plasma to the induced electric field and neglect the nonlinear contribution. This is analogous to the way that the electrostatic parallel nonlinearity is sometimes studied in GENE simulations, even though the electrostatic nonlinear field solver is never considered. However, the gyrokinetic model with the nonlinear induction response seems to be numerically unstable after very short time intervals. This numerical instability seems to exist mainly for realistic mass ratio. The distinguishing feature of the numerical instability is that the potential becomes very sharp at a single point in z before the point of blowing up. This feature cannot be destroyed with any value of hyperdiffusion in z, regardless of whether the hyperdiffusion term contributes to the plasma induction or not. It also seems to persist independent of the resolution in $(x, z, v_\parallel, \mu)$. When the electrons are 100 times heavier, the simulations seem to be stable, as shown in Fig. 5.5. It is possible that this numerical instability is related to the cancellation problem. When the nonlinearity is included in the plasma response to the induced field, but excluded from the field solver, it creates an imbalance that perhaps manifests itself as the observed numerical instability. This could be tested in future full-f scrape-off layer versions of GENE, but it is too difficult to test in the current delta-f version

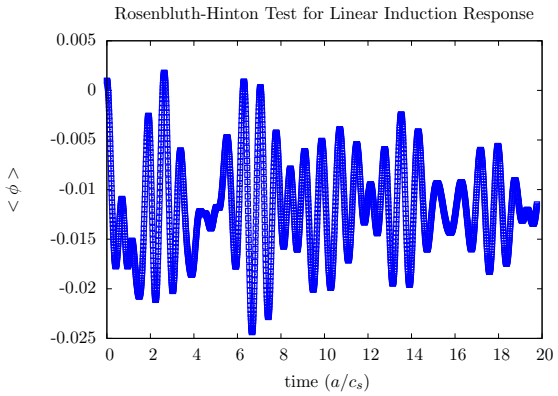

Figure 5.4: Oscillations in electrostatic potential vs. time for the $k_y = 0$ mode. This global simulation was run with $\beta = 1.5\%$ and $\rho^* = 0.1\%$. These runs were performed with a grid resolution of $128 \times 24 \times 64 \times 32$ in $(x, z, v_\parallel, \mu)$. This run was performed with a z-hyperdiffusion of 2.0 and a parallel velocity hyperdiffusion of 0.2. The nonlinear induction terms have been excluded from this simulation. This result shows that the global gyrokinetic model with linear induction is stable.

of the code. It is also possible that the instability is the result of numerical schemes which are not fully conservative.

5.3 Global electromagnetic runaway

One of the major problems associated with the global version of the GENE code is the global EM runaway. It has been found that if the plasma β is too high, the simulation becomes numerically unstable and the moments of the simulation explode. This is displayed in Fig. 5.6 for a global nonlinear simulation with the cyclone base case parameter set and a plasma β of 2%.

These nonlinear simulations were conducted with a resolution of $(n_x, n_{ky}, n_z, n_v, n_\mu) = 320 \times 32 \times 20 \times 50 \times 16$. The first toroidal mode number was taken as the minimum toroidal mode number for this simulation. The first 10% and last 10% of the radial domain were acted on by Krook type buffer terms of the form $-\nu_{\text{Krook}}(x) f_a$. The Krook operator had an amplitude of 20 for $x \leq 0.1$ and $x \geq 0.9$ where the radial domain extended from 0 to 1. This was done in an attempt to make sure the fluxes went down to zero relatively smoothly at the Dirichlet boundary. Additionally, Krook-type particle and heat sources were in place in

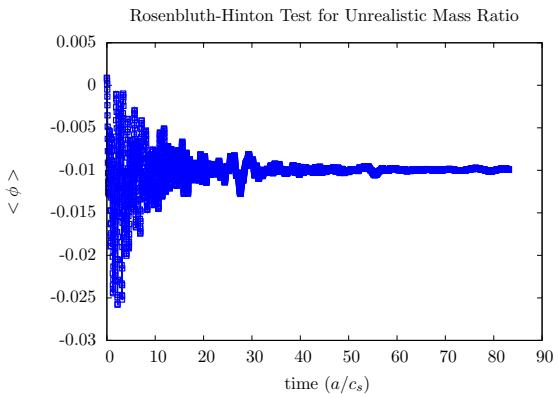

Figure 5.5: Rosenbluth-Hinton test for the global gyrokinetic model with a nonlinear response to the induction and unrealistic mass ratio (the electrons are 100 times heavier). This global simulation was run with $\beta = 1.5\%$ and $\rho^* = 0.1\%$. This model appears to be stable, unlike the model with realistic mass ratio.

order to maintain a fixed temperature and density profile. The amplitudes were chosen to be $0.08 c_{\text{ref}}/L_{\text{ref}}$. See ref. [18, 26] for more information on particle and heat sources. Circular geometry was utilized with a minor radius of $r = 0.36$ and a major radius of $R = 1$. The safety factor profile was set to $q(x) = 1.15 - 0.16x + 2.52x^2$, and ρ^* was set to 0.00555. The temperature and density profiles for the ion and electron species assumed the following form:

$$T(x) = \left(\frac{\cosh\left((x - x_0 + \Delta_T)/\omega_T\right)}{\cosh\left((x - x_0 - \Delta_T)/\omega_T\right)} \right)^{-\kappa_T r \omega_T/2}$$

$$n(x) = \left(\frac{\cosh\left((x - x_0 + \Delta_n)/\omega_n\right)}{\cosh\left((x - x_0 - \Delta_n)/\omega_n\right)} \right)^{-\kappa_n r \omega_n/2}.$$

Where $x_0 = 0.5$, $\omega_T = \omega_n = 0.05$, $\Delta_T = \Delta_n = 0.3$, $\kappa_n = 2.23$, $\kappa_{T,\text{ions}} = 6.96$, and $\kappa_{T,\text{electrons}} = 3.0$ for the case under review. Collisions were not considered in this case. It must be stressed however, that β is the relevant parameter for investigations of the global EM runaway. The buffer terms, sources, and profiles were less important as far as this numerical instability was concerned.

In this case, the β value is extremely high, and the simulations explode after less than half of a time unit. However, simulations have been found to become unstable at much lower values of β as well. At these lower values, the simulations may still be numerically unstable,

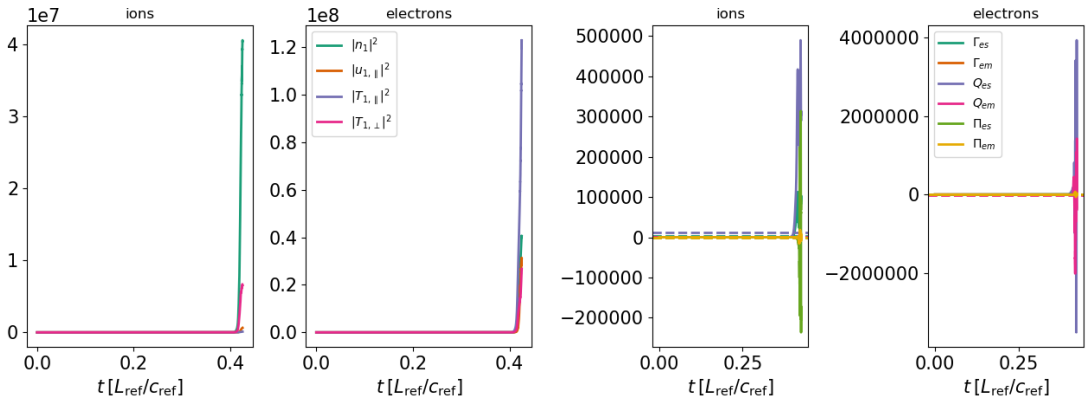

Figure 5.6: The above plots show the time traces for the moments (left) and fluxes (right) in the higher β CBC parameter set for the standard version of the GENE code.

but it would only become apparent after a much longer simulation time. This could then be a very frustrating problem for users of the global code version, because the instability could render very long and expensive simulations useless, and it was never clear at what threshold of the plasma β the simulations failed to stabilize.

With the alternative code version developed in this thesis, the global EM runaway problem appears to be solved. The same parameter set was run with the alternative code, which was very well benchmarked with the earlier GENE code in terms of linear physics. The nonlinear results seem to be numerically stable, at least out to about 60 time units (the simulations cannot be run indefinitely) as shown in Fig. 5.7. This case has an artificially high β for a circular geometry parameter set, so not much physics information can be obtained from these results besides numerical stability. However, characterizing the behavior of the model at extreme values of β is still worthwhile. It can be seen that for high β, the electron heat flux is predominantly electromagnetic and the spectra tends to peak at extremely low toroidal mode number, as shown in Fig. 5.8. It seems that even noninteger toroidal mode numbers might be needed to resolve the flux spectra, although this may not hold for lower values of β. The radial heat flux profiles are shown in Fig. 5.9. It seems to be relatively smooth, except that the electron electromagnetic heat flux rises rapidly from the boundaries. This phenomena seems to exist even with relatively high amplitude buffer terms (~ 20). But again, this could be related to the artificially high plasma β. The ion

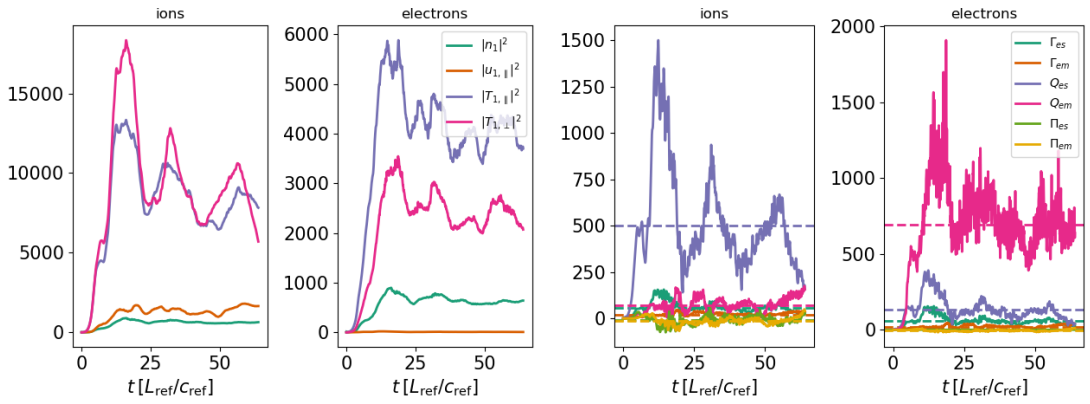

Figure 5.7: The above plots show the time traces for the moments (left) and fluxes (right) in the higher β CBC parameter set for the newly developed version of the GENE code.

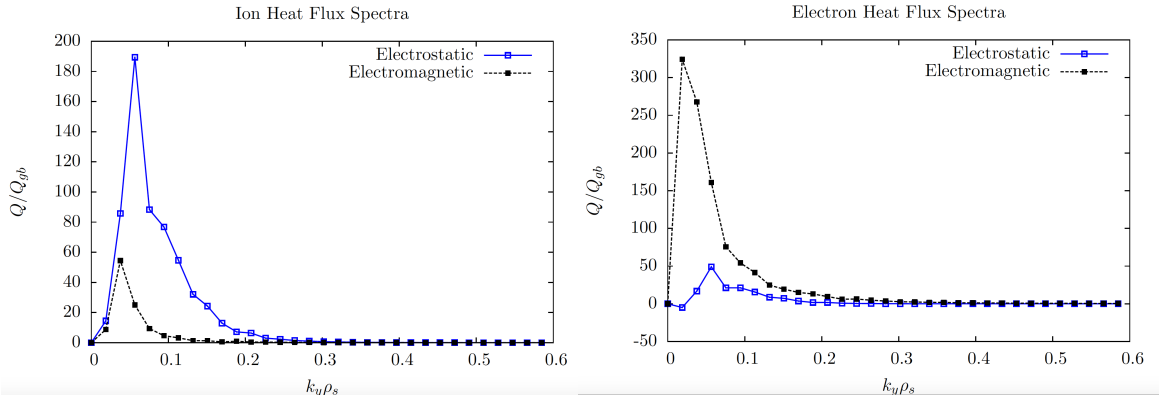

Figure 5.8: Heat flux spectra of the ions (left) and electrons (right) for the higher β CBC parameter set for the newly developed version of the GENE code.

heat flux remains nearly entirely electrostatic.

As of this writing, the newly developed electromagnetic code exists solely on a separate branch in the git repository. This branch is based off of an earlier version of the code, and not the newly refactored version with additional features, such as the block-structured grids. This alternative scheme shall soon be ported to the newly refactored x-global code, as well as GENE-3D. While this modified code version is numerically stable for the x-global code, and the spectra and profiles seem to be mostly well-behaved, one should still be careful regarding numerical conservation properties and numerical gauge invariance. Additionally, one should be careful to ensure that the field matrix is Hermitian, and that the magnetic field is divergence-free. While it is assumed that the use of the magnetic vector potential

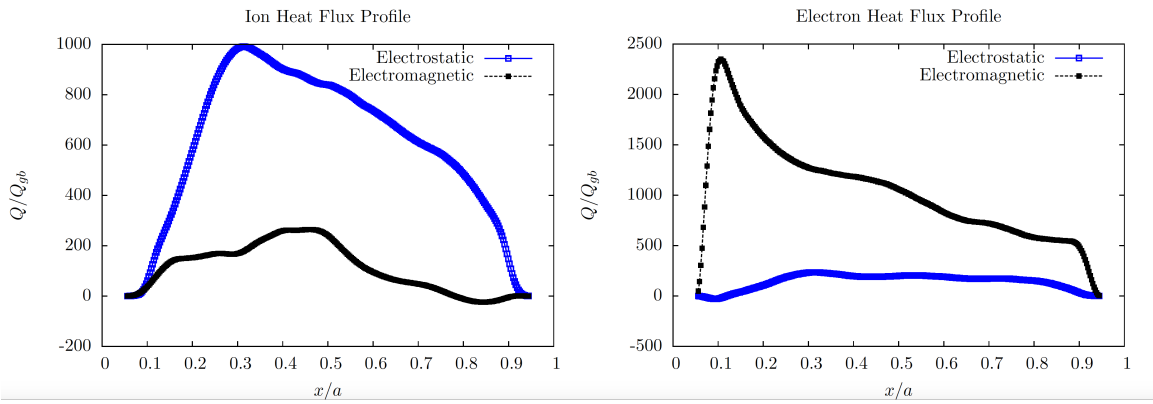

Figure 5.9: Radial heat flux profiles of the ions (left) and electrons (right) for the higher β CBC parameter set for the newly developed version of the GENE code.

automatically ensures a divergence-free magnetic field, this is only true if the discretization schemes are designed such that $\nabla \cdot (\nabla \times \mathbf{A}) = 0$ is numerically satisfied for the field aligned coordinate system. These considerations are important to keep in mind in case one comes across other numerical issues in simulations.

It should also be pointed out that while this revised scheme seems to mitigate the global instability, the revised scheme seems to have no effect on the NZT that occurs at high β in the flux-tube code. This is plausible, because while the global EM runaway considered above clearly resembled an artificial instability, the NZT could be well resolved and seemed like a normal system that evolved in the absence of zonal flows (which were destroyed by magnetic field perturbations) as reported in ref. [92, 93]. Both advanced collision operators and the electromagnetic parallel nonlinearity were tested on a CBC case with $\beta = 1\%$, and in both cases, the heat flux failed to saturate at reasonable values for local simulations. Neither the cubic electromagnetic parallel nonlinearity nor the nonlinear corrections to the field equations were tested, and it is plausible that these terms could have an effect. However, the NZT does appear to be a robust physical feature of the delta-f gyrokinetic model.

5.4 Chapter summary

In this chapter, a new electromagnetic implementation for gyrokinetic codes has been devised. While such an implementation is still subject to the Non-Zonal Transition for the local code version, it seems to no longer be subject to global numerical instabilities previously occurring in high β simulations. With the global instability problem solved, global electromagnetic simulations will now be far easier to perform, and many new scientific investigations will be possible. These include global investigations of kinetic ballooning mode (KBM) and toroidal Alfvén eigenmode (TAE) turbulence, and global simulations of high β devices, such as spherical tokamaks. Since the new electromagnetic scheme is stable, it can also be implemented in GENE 3D, and allow for an investigation of global electromagnetic turbulence in stellarators. This capability, when combined with the many other features of GENE, such as advanced multi-species collision operators, block-structured grids, non-Maxwellian backgrounds, etc., shall make GENE uniquely qualified for many scientific investigations of global electromagnetic plasma turbulence.

Additionally, the new electromagnetic scheme can be appropriately generalized to allow for full-f electromagnetic gyrokinetic simulations. However, a new field solver where the matrix can be changed every time-step must be utilized in order to avoid the cancellation problem. Such an implementation is planned for a new full-f version of GENE capable of studying turbulence and transport in the scrape-off layer.

CHAPTER 6

Conclusion

Computational gyrokinetic models have achieved great success in the study of the transport and turbulence characteristics of many different magnetic confinement scenarios. However, such models have encountered difficulties when tested in extreme parameter regimes. At higher collisionalities, the previous collision operator in use was found to artificially create free energy (in violation of the second law of thermodynamics) leading to numerical instabilities. At higher values of the plasma β, the local gyrokinetic model failed to replicate the experimental transport level by orders of magnitude due to a mitigation of the zonal flows by magnetic field perturbations, and the global gyrokinetic model became outright numerically unstable. In the course of this work, significant progress has been made in the development of collisional and electromagnetic models in the GENE code. With the developments made in this thesis, it is now possible to explore local and global (including with the use of block-structured grids) gyrokinetic plasma turbulence in regions of higher collisionality, such as the edge. It is also now possible to explore global plasma turbulence for scenarios with higher plasma β, such as spherical tokamaks. Since these models have been shown to work in the x-global code, this thesis also provides a preliminary roadmap for the implementation of collisions and electromagnetic fields in GENE 3D and investigations of collisional and electromagnetic plasma turbulence in stellarators.

In addition to the expansions made to the code, GENE has been used (along with the newly developed collision operator) to characterize the plasma behavior in the edge of an L-mode discharge. Gyrokinetic models are frequently utilized for studying the core of the plasma discharge, but only very rarely are attempts made to study how such models behave when applied to a parameter regime with such extreme collisionality and magnetic geometry.

Such an investigation has been conducted in this work. It has been found that the nature of turbulence in the edge is primarily electron drift wave turbulence which is expected to shift to lower binormal wave-numbers as one goes farther out to the edge. At the radial position of $r/a = 0.93$, the heat transport for both the ions and electrons was higher than the experimentally measured values, but were brought into agreement by lowering the electron temperature gradient by 40%. A summary of the results described in the last three chapters shall be given, along with an outline of future work that can be done relating to collisions, electromagnetic fields, and investigations of edge plasmas.

6.1 Key developments

6.1.1 Collisions

The linearized Sugama collision operator (analytically derived in ref. [14]) was implemented in GENE using a second-order finite-volume scheme. The model was shown to conserve particles, momentum, and energy to machine precision, while also dissipating free energy and relaxing an arbitrary distribution to a perturbed Maxwellian in the drift-kinetic limit, even for a nonisothermal parameter set (which is not a property of the original linearized Landau-Boltzmann operator). The implementation has been carried out for both local and global code versions. This is a significant improvement over the previous collision operator, which could artificially create free energy, leading to numerical instabilities. Finite Larmor Radius (FLR) corrections were implemented for the new operator in the local code. Previously, the FLR corrections were incorporated only into the spatial diffusion term, and not the terms with the velocity space moments. In addition, the global version of the collision operator was developed in such a way as to be compatible with the block-structured grid implementation, allowing for more computationally affordable, collisional, global simulations. Neoclassical and microinstability benchmarks were also performed to verify that the implementation of the collision operator was done correctly. The developments made in this thesis allow for new, reliable, and computationally affordable simulations of the plasma edge and lower temperature magnetic confinement scenarios.

6.1.2 Edge Physics

The ASDEX Upgrade L-mode discharge 28132 was examined with the local GENE code at a radial position of $r/a = 0.93$. This is one of the first quantitative gyrokinetic studies of L-mode edge transport so close to the separatrix. Such studies are of great importance in eventually addressing the physics of the L-H transition. This discharge was diagnosed with earlier GENE simulations at the radial positions $r/a = 0.75$ and $r/a = 0.85$. At these radial positions, the heat fluxes from the simulations matched the experimental values very closely with the nominal input parameters. At $r/a = 0.93$, the simulated heat flux was higher for the electrons by about a factor of 4, and higher for the ions by about a factor of 2. When the electron temperature gradient was lowered by 40%, the heat fluxes for both species matched the experimental measurements. 40% is a moderately large assessment for an error bar on the electron temperature gradient, but a comparison to the experimental measurements shows that it is certainly possible. It may also be the case that global, full-f, or neutral particle effects would lower the transport. Nevertheless, this does indicate that the gyrokinetic model can reproduce the experimentally obtained transport. Additionally, it was found at the radial position under consideration that the turbulence was predominantly electron drift wave turbulence. The cross-phases between electrostatic potential and temperature fluctuations gave fairly good agreement in the part of the binormal spectrum for which significant transport occurred ($0.1 \lesssim k_y\rho_s \lesssim 0.5$). The agreement was fairly poor outside of this range, however, there was not significant transport in this region. It was also observed that electromagnetic effects lead to a large increase in the electrostatic heat flux at lower toroidal mode numbers. This could be attributed to electromagnetic effects on the linear spectra. However, electromagnetic effects also lead to a significant change in the cross-phases in the region ($k_y\rho_s \lesssim 0.1$). This is consistent with the findings in ref. [75, 76]. While nonlinear simulations at farther radial positions were too expensive to perform with the current explicit time-stepping scheme, the linear simulations at $\rho_{\text{tor}} = 0.96$ indicate that the transport peak should shift to lower toroidal mode numbers at farther radial positions. However, this prediction is based on linear physics, and it remains to be seen if this holds true in nonlinear simulations.

6.1.3 Electromagnetic Fields

A new scheme to evaluate the electromagnetic fields has been devised and implemented in the GENE code. The purpose of this development was to solve the violent numerical instability which occurs in global electromagnetic simulations at high plasma β. Such a scheme has been shown to satisfy the essential Rosenbluth-Hinton test and is well benchmarked with the linear physics. The new implementation solves the global electromagnetic instability, as confirmed by a global simulation with cyclone base case parameters and a plasma β of 2% (well beyond any practical value of β in a realistic simulation). This scheme has been tested for high β local simulations as well (with and without the higher-order parallel nonlinear induction term), but the nonzonal transition seems to still occur, adding further evidence that the nonzonal transition is a physics phenomenon associated with the local gyrokinetic model.

This implementation also has the potential of being generalized to allow for full-f electromagnetic simulations, although it would require changing the matrix for the field-solver every time-step in order to avoid the cancellation problem. However, implementing the electrostatic full-f field equation would also require updating the field matrix every time-step, so no new barrier is introduced for full-f gyrokinetic simulations. The capability of conducting high β global electromagnetic simulations, when combined with the many other features of GENE, such as advanced multi-species collision operators, block-structured grids, non-Maxwellian backgrounds, etc., make GENE a unique and powerful tool for scientific investigations of global plasma turbulence and transport.

6.2 Future work

6.2.1 Collisions

While the Sugama collision operator implemented in GENE has well tested conservation and dissipation properties, it can be very expensive to utilize when the collisionality is high due to a dramatic shrinking of the time-step. This problem can become especially bad when

FLR corrections are utilized. It has been found in the ASDEX simulations in the edge that the spatial diffusion part of the collision operator can shrink the value of the time-step by two orders of magnitude, making such simulations intractable, even linearly. This problem would also make investigations of the scrape-off layer, where collisionality is extremely high, infeasible. To mitigate this problem, implicit time-stepping schemes should be investigated for use with collision operators.

Additionally, the linearized Sugama collision operator should also be ported to GENE-3D, and FLR corrections should be implemented for both the x-global and 3D code versions. However, an implicit time-stepping scheme should perhaps be prioritized, because simulations with FLR corrections may be intractable until such a scheme is implemented. Neutral particle collision operators should also be considered. These collisional effects may become important for discharges with high impurity content.

Finally, a full-f collision operator should be developed for use with the scrape-off layer version of the GENE code. This however, is a challenging task compared to the implementation of the delta-f collision operator. The full-f nonlinear collision operator is fundamentally nonlocal in velocity space, meaning that a convolution integral would need to be performed in this subspace, leading to more memory usage, and more floating point operations. Furthermore, it has been found that such an operator can lead to the full distribution function becoming negative in numerical implementations, a problem that would ultimately have to be resolved. Additionally, implementing FLR corrections into the nonlinear operator is a much more difficult task than with the delta-f operator.

6.2.2 Edge Physics

At the radial position under consideration ($\rho_{\text{tor}} = 0.9$), it was found that the heat fluxes could match experimental values, and the linear and nonlinear cross phases mostly agreed in the part of the spectrum for which significant transport occurred ($0.1 \lesssim k_y\rho_s \lesssim 0.5$), and disagreed outside of that range ($k_y\rho_s \lesssim 0.1$). As one goes further towards the edge, the transport from electron drift waves is expected to peak at larger scales in the ($k_y\rho_s \lesssim$

0.1) region. Previous studies of the edge (ref. [75, 76]) have found that the transport is highly nonlinear because electron drift wave turbulence nonlinearly couples to MHD in this large wavelength region through electromagnetic interactions. It is worthwhile to investigate farther radial positions where electron drift wave transport in the long wavelength regime is expected to dominate, to see if this nonlinear electromagnetic coupling is observed with GENE. Attempts to conduct nonlinear simulations at farther radial positions during this thesis were hampered because of limited computational resources. There were constraints put on the time-step due to collisions, as well as higher required resolution in configuration space to resolve the $A_{\|}$ structures. Nevertheless, such simulations would be worthwhile. Investigations of the edge of I-mode and H-mode discharges are also crucial, and the next logical step after analyzing the L-mode discharge.

6.2.3 Electromagnetic Fields

While the global electromagnetic instability has been solved, the developments done in this thesis were conducted on an earlier version of the GENE code before major refactoring of the code was performed. The most important work to be done is to implement the appropriate changes that resolve the electromagnetic instability in the newly refactored version of GENE. Electromagnetic effects should also be implemented in GENE-3D as well as the new full-f scrape-off layer version of GENE under development. New simulations of high β devices, such as spherical tokamaks, should also be investigated.

References

[1] U.S. Energy Information Administration, *Monthly Energy Review*, Table 1.3, April 2018

[2] The National Resources Defense Council, www.nrdc.org/issues/climate-change

[3] The National Aeronaoutics and Space Adminstration, climate.nasa.gov

[4] The Intergovernmental Panel on Climate Change, www.ipcc.ch

[5] IRENA (2018), Renewable Power Generation Costs in 2017, International Renewable Energy Agency, Abu Dhabi

[6] J. Wesson, *Tokamaks*, 3rd edition (Clarendon Press-Oxford, 2004)

[7] M. Wakatani, *Stellarator and Heliotron Devices* (Oxford University Press, 1998)

[8] L.D. Landau and E.M. Lifshitz, *Fluid Mechanics* (Elsevier, 1959)

[9] F. Wagner et al., Physical Review Letter **49**, 1408 (1982)

[10] F. Wagner, Plasma Physics of Controlled Fusion **49**, (2007) B1-B33

[11] P.T. Lang et al., Nuclear Fusion **53**, 043004 (2013)

[12] R. Hazeltine and F. Waelbroeck, *The Framework of Plasma Physics* (Perseus Books, 1998)

[13] NRL Plasma Formulary (2009)

[14] H. Sugama, T.-H. Watanabe, and M. Nunami, Physics of Plasmas **16**, 112503 (2009)

[15] G. Howes, S. Cowley, W. Dorland, G. Hammett, E. Quataert, and A. Schekochihin, The Astrophysical Journal, 651:590-614, 2006

[16] F. Jenko, W. Dorland, M. Kotschenreuther, and B. N. Rogers, Physics of Plasmas, 7:1904–1910, (2000)

[17] T. Dannert and F. Jenko, Physics of Plasmas, 12(7):072309, (2005)

[18] T. Görler, X. Lapillonne, S. Brunner, T. Dannert, F. Jenko, F. Merz, and D. Told, Journal of Computational Physics, 230:7053–7071, (2011)

[19] D.H.E. Dubin, J.A. Krommes, C. Oberman, and W.W. Lee, Physics of Fluids **26**, 3524 (1983)

[20] T.S. Hahm, W.W. Lee, and A. Brizard, Physics of Fluids **31**, 1940 (1988)

[21] T.S. Hahm, Physics of Fluids **31**, 2670 (1988)

[22] A. Brizard, Journal of Plasma Physics **41**, 541 (1989)

[23] A.J. Brizard and T.S. Hahm, Reviews of Modern Physics **79**, 421 (2007)

[24] J. R. Cary and R. G. Littlejohn, Annals of Physics **151**, 1 (1983)

[25] R.G. Littlejohn, Journal of Mathematical Physics **23**, 742 (1982)

[26] D. Told, *Gyrokinetic Microturbulence in Transport Barriers*, Universität Ulm (2012)

[27] T. Görler, *Mulitscale Effects in Plasma Microturbulence*, Universität Ulm (2009)

[28] V.D. Shafranov, Soviet Journal of Experimental and Theoretical Physics **6**, 545 (1958)

[29] P. Xanthopoulos and F. Jenko, Physics of Plasmas **13**, 092301 (2006)

[30] X. Lapillonne, S. Brunner, T. Dannert, S. Jolliet, A. Marioni, L. Villard, T. Görler, F. Jenko, and F. Merz, Physics of Plasmas **16**, 032308 (2009)

[31] A. Di Siena, T. Görler, H. Doerk, R. Bilato, J. Citrin, T. Johnson, M. Schneider, E. Poli, and Jet Contributors, Physics of Plasmas 25, 042304 (2018)

[32] W. D'Haeseleer, *Flux Coordinates and Magnetic Field Structure: A Guide to a Fundamental Tool for Plasma Theory* (Springer Verlag, 1991)

[33] H. Doerk, *Gyrokinetic Simulation of Microtearing Turbulence,* Ph.D. thesis, Universität Ulm (2012)

[34] M. Oberparleiter, *Interaction between the neoclassical equilibrium and microturbulence in gyrokinetic simulations*, Universität Ulm (2015)

[35] T. Dannert, *Gyrokinetische Simulation von Plasmaturbulenz mit gefangenen Teilchen und elektromagnetischen Effekten*, Ph.D. thesis, Techniche Universität München (2004)

[36] A. Arakawa, Journal of Computational Physics 1, 119 (1966), Repr. vol 135 (1997) 103

[37] M. J. Pueschel, T. Dannert, and F. Jenko, Computer Physics Communications 181, 1428 (2010)

[38] P. Morel, A. Bañón Navarro, M. Albrecht-Marc, D. Carati, F. Merz, T. Görler, and F. Jenko, Physics of Plasmas 18, 072301 (2011)

[39] J. Madsen, Phys. Rev. E **87**, 011101 (2013)

[40] B. Li and D.R. Ernst, Physical Review Letters **106**, 195002 (2011)

[41] V. Grandgirard, J. Abiteboul, J. Bigot, T.Cartier-Michaud, N. Crouseilles, G. Dif-Pradalier, Ch. Ehrlacher, D. Esteve, X. Garbet, Ph. Ghendrih, G. Latu, M. Mehrenberger, C. Norscini, Ch. Passeron, F. Rozar, Y. Sarazin, E. Sonnendrücker, A. Strugarek, D. Zarzoso, Computer Physics Communications **207** (2016) 35-68

[42] I.G. Abel, M. Barnes, S.C. Cowley, W.Dorland, A.A. Schekochihin, Physics of Plasmas **15** (12) (2008) 122509

[43] F.L. Hinton, R.D. Hazeltine, Review of Modern Physics **48** (1976) 239-308

[44] S.P. Hirshman, D.J. Sigmar, Physics of Fluids **19** (10) (1976) 1532-1540

[45] R. Hager, E.S. Yoon, S. Ku, E.F. D'Azevedo, P.H. Worley, C.S. Chang, Journal of Computational Physics **315** (2016) 644-660

[46] D. Estéve, X. Garbet, Y. Sarazin, V. Grandgirard, T. Cartier-Michaud, G. Dif-Pradalier, P. Ghendrih, G. Latu, C. Norscini , Phys. Plasmas 22, 122506 (2015)

[47] P. Donnel, X. Garbet, Y. Sarazin, V. Grandgirard, Y. Asahi, N. Bouzat, E. Caschera, G. Dif-Pradalier, C. Ehrlacher, P. Ghendrih, C. Gillot, G. Latu, and C. Passeron, Computer Physics Communications **234** (2019) 1-13

[48] M. Dorf, R. H. Cohen, J. C. Compton, M. Dorr, T. D. Rognlien, J. Angus, S. Krasheninnikov, P. Colella, D. Martin, and P. McCorquodale, Contributions to Plasma Physics 52, (2012) 518-522

[49] M. Dorf, R. Cohen, M. Dorr, J. Hittinger, and T.D. Rognlien, Contributions to Plasma Physics 54, (2014) 517-523

[50] P. Manas, Y. Camenen, S. Benkadda, W.A. Hornsby, A.G. Peeters, Physics of Plasmas **22** (6) (2015) 062302

[51] M. Barnes, I.G. Abel, W. Dorland, D.R. Ernst, G.W. Hammett, P. Ricci, B.N. Rogers, A.A. Schekochihin, T. Tatsuno, Physics of Plasmas **16** (7) (2009) 072107

[52] T. Vernay, S. Brunner, L. Villard, B. Mcmillan, S. Jolliet, T.M. Tran, A. Bottino, and J. P. Graves, Phys. Plasmas, 19, 042301 (2012)

[53] M. Nakata, M. Nunami, T.-H. Watanabe, H. Sugama, Computer Physics Communications 197 (2015) 61-72

[54] J. Candy, E. Belli, R. Bravenec, Journal of Computational Physics, **324**, 73 (2016)

[55] A. M. Dimits, J. W. Banks, R. L. Berger, S. Brunner, T. Chapman, D. Copeland, D. Ghosh, W. J. Arrighi, J. Hittinger, and I. Joseph, IEEE Transactions on Plasma Science, 47, (2019) 2074-2080

[56] F. Merz, *Gyrokinetic Simulation of Multimode Plasma Turbulence,* Ph.D. thesis, Westfaelische Wilhelms-Universität Münster (2008)

[57] D. Jarema, H.J. Bungartz, T. Görler, F. Jenko, T. Neckel, D. Told, Computer Physics Communications **215** (2017) 49-62

[58] D. Jarema, H.J. Bungartz, T. Görler, F. Jenko, T. Neckel, D. Told, Computer Physics Communciations **198** (2016) 105-117

[59] R. Balescu, *Transport Processes in Plasmas*, Vol 11. North-Holland, Amsterdam (1988)

[60] E.A. Belli and J. Candy, Plasma Physics of Controlled Fusion **54**, 015015 (2012)

[61] A. Bañón Navarro, P. Morel, M. Albrecht-Marc, D. Carati, F. Merz, T. Görler, F. Jenko, Physics of Plasmas **24**, 092303 (2011)

[62] H. Doerk, F. Jenko, Computer Physics Communications 185 (2014) 1938-1946

[63] S. Maeyama, T.-H. Watanabe, Y. Idomura, M. Nakata, and M. Nunami, Comput. Phys. Comm. 235, (2019) 9-15

[64] F.L. Hinton and M.N. Rosenbluth, *Dynamics of axisymmetric (E x B) and poloidal flows in tokamaks,* Plasma Physics of Control. Fusion **41** (1999)

[65] Braginskii S I 1965 *Reviews of Plasma Physics* vol 1, ed M A Leontovich (New York: Consultants Bureau) p 205

[66] E.A. Belli and J. Candy, Plasma Physics of Controlled Fusion **50**, 095010 (2008)

[67] Portable, Extensible Toolkit for Scientific Computation (PETSC), http://www.mcs.anl.gov/petsc/ (2012)

[68] E.A. Belli and J. Candy, Plasma Physics of Controlled Fusion **59**, 045005 (2017)

[69] R. Miller, M. Chu, J. Greene, Y. Lin-Liu, R. Waltz, Physics of Plasmas, **5**, 973 (1998)

[70] J. Candy, C. Holland, R. Waltz, M. Fahey, E. Belli, Physics of Plasmas, **16**, 060704 (2009)

[71] A. White and T. Görler, Plasma Physics of Control. Fusion **59**, 050101 (2017)

[72] J. Candy and R.E. Waltz, Physical Review Letters **91**, 045001 (2003)

[73] D. Told, F. Jenko, T. Görler, F.J. Casson, E. Fable, and ASDEX Upgrade Team, Physics of Plasmas **20**, 122312 (2013)

[74] B.D. Scott, Plasma Physics of Controlled Fusion **45**, A385 (2003)

[75] B.D. Scott, Plasma Physics of Controlled Fusion **12**, 062314 (2005)

[76] B. Scott, A. Kendl, and T. Ribeiro, Contributions to Plasma Physics **50**, 228 (2010)

[77] P. Xanthopoulos, W.A. Cooper, F. Jenko, Yu. Turkin, A. Runov, and J. Geiger, Physics of Plasmas **16**, 082303 (2009)

[78] D. Told, F. Jenko, P. Xanthopoulos, L. Horton, E. Wolfrum, and ASDEX Upgrade Team, Physics of Plasmas **15**, 102306 (2008)

[79] E. Fable, C. Angioni, J. Hobirk, G. Pereverzev, S. Fietz, T. Hein, and ASDEX Upgrade Team, Nuclear Fusion **51**, 043006 (2011)

[80] A. Ivanov, R. Khayrutdinov, S. Y. Medvedev, and Y.Y. Poshekhonov, in *Proceedings of 32nd EPS Conference on Plasma Phys., Tarragona, 27 June-1 July 2005, ECA,* (2005), Vol. 29, p.5-063

[81] C. Bourdelle, X. Garbet, F. Imbeaux, A. Casati, N. Dubuit, R. Guirlet, and T. Parisot, Physics of Plasmas **14**, 112501 (2007)

[82] Clarisse Bourdelle, *Turbulent Transport in Tokamak Plasmas: bridging theory and experiment*, Ph.D. thesis (Aix-Marseille University, 2015)

[83] https://github.com/QuaLiKiz-group/QuaLiKiz/wiki

[84] D.R. Hatch, D. Told, F. Jenko, H. Doerk, M.G. Dunne, E. Wolfrum, E. Viezzer, The ASDEX Upgrade Team and M.J. Pueschel, Nuclear Fusion **55**, 063028 (2015)

[85] D.R. Hatch, M. Kotschenreuther, S. Mahajan, P. Valanju, F. Jenko, D. Told, T. Görler and S. Saarelma, Nuclear Fusion **56**, 104003 (2016)

[86] A. Zeiler, D. Biskamp, J.F. Drake, and P.N. Guzdar, Physics of Plasmas **3**, 2951 (1996)

[87] C. Bourdelle C.F. Maggi, L. Chôné, P. Beyer, G. Fuhr, X. Garbet, A. Loarte, F. Millitello, A. Monnier, M. Romanelli, S. Saarelma, Y. Sarazin and JET EFDA Contributors, Nuclear Fusion **54**, 022001 (2014)

[88] C. Bourdelle, X. Garbet, R. Singh, and L. Schmitz, Plasma Physics of Controlled Fusion **54**, 115003 (2012)

[89] B.D. Scott, Physics of Fluids B 4, 2468 (1992)

[90] B.D. Scott, Plasma Physics of Controlled Fusion **49**, S25 (2007)

[91] N. Bonanomi, C. Angioni, P.C. Crandall, A. Di Siena, C.F. Maggi, P.A. Schneider, the ASDEX Upgrade Team, the EUROFusion MST1 Team, and JET Contributors, Nuclear Fusion, **59**, 126025 (2019)

[92] M.J. Pueschel, P.W. Terry, F. Jenko, D.R. Hatch, W.M. Nevins, T. Görler, and D. Told, Physical Review Letters, **110**, 155005 (2013)

[93] M.J. Pueschel, D.R. Hatch, T. Görler, W.M. Nevins, F. Jenko, P.W. Terry, and D. Told, Physics of Plasmas, **20**, 102301 (2013)

[94] M.J. Pueschel, M. Kammerer, and F. Jenko, Physics of Plasmas, **15**, 102310 (2008)

[95] R.E. Waltz, Physics of Plasmas **17**, 072501 (2010)

[96] M.J. Pueschel and F. Jenko, Physics of Plasmas **17**, 062307 (2010)

[97] Y. Chen and S. Parker, Physics of Plasmas, **8**, 2095 (2001)

[98] J. C. Cummings, *Gyrokinetic simulation of finite-beta and self-generated sheared-flow effects on pressure-gradient-driven instabilities*, Ph.D. thesis (Princeton University, 1995)

[99] H. Naitou, K. Tsuda, W.W. Lee, and R.D. Sydora, Physics of Plasmas, **2**, 4257 (1995)

[100] Y. Chen and S. Parker, Journal of Computational Physics, **189**, 463 (2003)

[101] A. Mishchenko, R. Hatzky, and A. Könies, Physics of Plasmas, **11**, 5480 (2004)

[102] R. Hatzky, A. Könies, and A. Mishchenko, Journal of Computational Physics, **225**, 568 (2007)

[103] J. Candy and R.E. Waltz, Journal of Computational Physics, **186**, 545 (2003)

[104] A. Mishchenko, A. Könies, R. Kleiber, and M. Cole, Physics of Plasmas, **21**, 092110 (2014)

[105] A. Mishchenko, M. Cole, R. Kleiber, and A. Könies, Physics of Plasmas **21**, 052113 (2014)

[106] R. Kleiber, R. Hatzky, A. Könies, A. Mishchenko, and E. Sonnendrücker, Physics of Plasmas **23**, 032501 (2016)

[107] A. Mishchenko, A. Bottino, R. Hatzky, E. Sonnendrücker, R. Kleiber, and A. Könies, Physics of Plasmas, **24**, 081206 (2017)

[108] Moritz Pueschel, *Electromagnetic Effects in Gyrokinetic Simulations of Plasma Turbulence*, Ph.D. thesis (Universität Münster, 2009)

[109] J.V.W. Reynders, *Gyrokinetic simulation of finite-beta plasmas on parallel architectures*, Ph.D. thesis (Princeton University, 1992)

[110] T. Görler, N. Tronko, W.A. Hornsby, A. Bottino, R. Kleiber, C. Norscini, V. Grandgirard, F. Jenko, and E. Sonnendrücker, Physics of Plasmas, **23**, 072503 (2016)